KINEMATICS & STELLAR POPULATIONS OF NEARBY BULGES

JESÚS FALCÓN BARROSO

Thesis submitted to the University of Nottingham
for the degree of Doctor of Philosophy, December 2002

Supervisor:

Dr. R. F. Peletier

Co-Supervisors:

Dr. M. Balcells
Prof. M. Merrifield

Examiners:

Dr. A. Aragón-Salamanca
Prof. J. Gorgas

A mis padres,

To see what is in front of one's nose requires a constant struggle.
George Orwell, 1946

Abstract

In this thesis, we investigate the internal kinematics and stellar populations of a subsample of the bulges of nearby galaxies defined by Balcells & Peletier (1994). To do that we have analysed minor axis spectroscopic data of the sample together with Integral Field observations of one the most interesting galaxies in it (NGC 7332).

We introduce, for the first time, the use of single-burst stellar population models to obtain stellar velocities, velocity dispersions and higher order Gauss-Hermite moments (h_3, h_4) from galaxy spectra in the near-infrared Ca II triplet region. We detect small-amplitude minor-axis rotation, generally due to inner isophotal twists as a result of slightly triaxial bulges or misaligned inner disks. Velocity dispersion profiles, which extend well into the disk region, show a wide range of slopes. Flattened bulges tend to have shallower velocity dispersion profiles. The inferred similarity of *radial* velocity dispersion profiles of bulge and disk supports the interpretation of these bulges as thickened disks.

We also investigate the position of our sample on the fundamental plane of early-type galaxies. We find that bulges, both in the B and K band, lie close to but slightly below the relation defined by ellipticals and S0s. The most deviant point is NGC 7332, whose offset w.r.t the FP cannot be explained by measurement errors. Besides, there are hints that bulges of later morphological type are situated below the other bulges in our sample. The fact that bulges lie so close to the FP of ellipticals and S0s implies that their formation epoch must have been similar to that of cluster Es and S0s.

We then proceed to present measurements of near-IR Ca triplet (CaT, CaT*), Paschen (PaT) and Magnesium (Mg I) indices for the same sample. We find that CaT* decreases with central velocity dispersion σ with small scatter, unlike other metal indices that generally increase. Our result shows that the CaT* – σ relation is independent of galaxy type from ellipticals to intermediate-type spirals.

Finally we have made use of SAURON observations to unravel the origin of peculiar features in the S0 galaxy NGC 7332. We have discovered a Kinematically Decoupled Core, found kinematic evidence for a central disk and mapped a rather disturbed gas distribution counter-rotating w.r.t the stellar body of the galaxy. 2D stellar populations maps reveal that NGC 7332 is young everywhere. The fact that we see gas inflow now, together with many features indicates that there must have been gas infall for Gyrs in a row, leading to a continuum formation of this galaxy.

Contents

Chapter 1

Introduction

1.1 The definition of a 'bulge'

Galaxies as we know them today have been discovered a long time ago. Evidence for such objects comes from the Greeks who looked at our own Milky Way, which at that time was thought to be a fuzzy fluid rather than a concentration of stars. It was Galileo who, for the first time and with the help of a telescope, resolved this band of material into individual stars. Our understanding of the universe in general and galaxies in particular has suffered many turnovers and it has not been until the late 1880s that our conception of a *galaxy* showing different morphologies came to live thanks to the extensive 'collection' of observations by Dreyer (1888) in the form of what we know today as the *New General Catalogue*. The catalogue contains observations of open and globular star clusters, diffuse and planetary nebulae, supernova remnants and galaxies of all types. The design of better telescopes was crucial to make these morphological distinctions possible. It was not until the time of Hubble that such a thing as a 'bulge' was defined. In Hubble's eyes the things that we nowadays know as bulges were '*dominating non-stellar nuclei*' (Hubble 1927), or '*the nucleus*' as he referred to later on (i.e. Hubble 1936). Terms have changed: the word *the nucleus* is nowadays only used to define the very inner part of the galaxy. He defined a classification system of galaxies in which bulges play a crucial role and define the whole sequence (Hubble 1936).

Many other galactic classification schemes arose as refinements from Hubble's 'Tuning Fork' (de Vaucouleurs 1959; van den Bergh 1960a,b; Morgan 1971) and more recently Kormendy & Bender (1996) (see Fig 1.1). All of them use the bulge

as a key element in their schemes. Classification of galaxies is a very difficult task. In the Hubble system, for example, a galaxy is classified using its morphology, elliptical or spiral, the presence of spiral arms or a bar. A good classification scheme has to be able to accommodate the largest number of galaxies as well as describe the properties of galaxies with as few parameters as possible. In practice it is very difficult to make a good classification system. The scatter of many physical parameters as a function of morphological type is still high. The problem is that galaxies look different depending on the waveband used to look at them. That is probably one of the major difficulties to overcome. What is the right band to use? For the same reason one could also argue that maybe photometry alone is not the way to go. It might be possible that the shape of light profiles or the dynamics of galaxies have an important role to play. It could well be that a combination of them is in place.

Several definitions have been proposed for the bulge component in galaxies. Photometrically a bulge has been defined as '*any light that is in excess of an inward extrapolation of a constant scale-length exponential disk*' (Wyse, Gilmore & Franx 1997) or '*the inner component of the galaxy which appears to be superimposed onto an exponential disk*' (Fathi & Peletier 2003). Dynamically, on the other hand, bulges could be defined as *the randomised region in the centre of galaxies showing an almost isotropic velocity distribution*. Given the fact that bulges are less kinematically studied than photometrically, in the present work I feel more inclined to adopt the rather similar definition Yiannis Andredakis used in his thesis '*a flattened spheroidal system of stars in the centre of spiral galaxies*'. Although I will extend the definition to the S0 galaxies also.

Given our definition of a bulge it is necessary to remember that the bulge is **not** necessarily everything found in the centre of the S0 and spiral galaxies, and room for other types of structures is also needed. In that respect high resolution photometric observations are providing new insights of complicated structures embedded in the bulge, like cuspy cores or central disks (Lauer et al. 1995; Carollo et al. 2002), that we are not considering to be part of it .

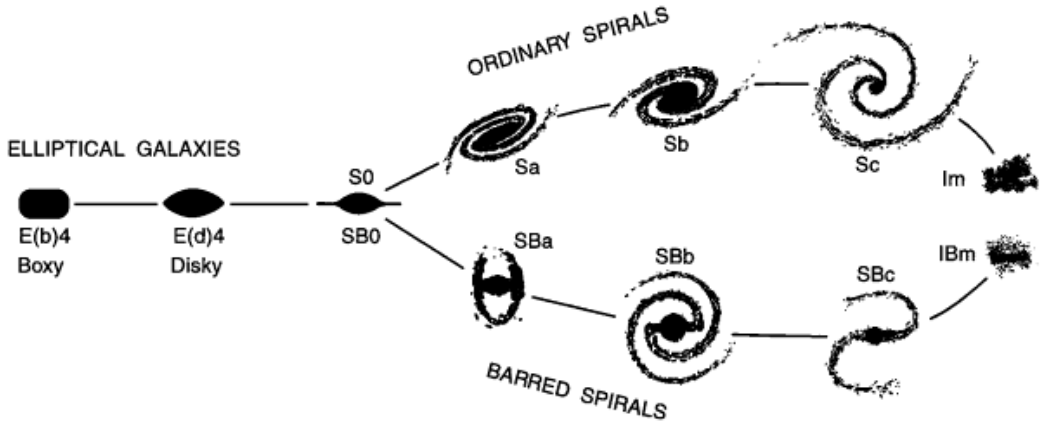

Figure 1.1: Revised Hubble's 'Tuning Fork' as described by Kormendy & Bender (1996).

1.2 Properties of bulges:

Throughout history bulges of galaxies have been considered scaled-down versions of ellipticals and therefore were supposed to share their properties. The last decade has seen the arrival of new telescopes and instrumentation and with them a new world of differences between elliptical galaxies and bulges of S0 and spiral galaxies. In the following sections we will summarise the main properties of bulges and their comparison with those of ellipticals.

1.2.1 Morphology

From the first, ground based, sets of data, radial surface brightness profiles of bulges were considered to follow the $r^{1/4}$ law (de Vaucouleurs 1948) reasonably well (Binney, Kormendy & White 1982). Following results showed evidence of a continuum of shapes of bulges, changing as we move towards later types (Andredakis, Peletier & Balcells 1995) when fitted with a Sersic law (Sersic 1968). The latest high spatial resolution observations indicate that bulges do not follow the $r^{1/4}$ law after all, and that the high-n value from ground observations are the result of nuclear point sources blending with the bulge extended light due to seeing (Balcells et al. 2003). Therefore our current knowledge shows that early-type bulges (S0-Sa) present surface brightness profiles similar to those of ellipticals with $n \approx 4$, whereas late-type bulges (Sb and beyond) tend to show val-

ues of n<4. Indeed some works reveal that later-types could be better fitted with an exponential profile (Andredakis & Sanders 1994; Carollo 1999) rather than a $r^{1/4}$ law.

In terms of luminosity, bulges appear to be as luminous as ellipticals of the same velocity dispersion. However their characteristic colors are somewhat bluer than those of elliptical galaxies (Balcells & Peletier 1994). This offset can be attributted either to a lower age or a lower metallicity. When compared with their surrounding disks, bulges show a range in color similar to that of their disks. Careful photometric analysis (Terndrup et al. 1994; Peletier & Balcells 1996; de Jong 1996), reveal that, far from what it was traditionally thought, bulges are generally as blue or red as inner disks and viceversa.

1.2.2 Kinematics

The measurement of kinematics in galaxies has been one of the major achievements in galactic astrophysics in the last century. Our understanding of kinematics in galaxies has been crucial to learn and model intrinsic properties of this kind of objects. The first studies on kinematics of galaxies in general started in the early 1900's by analysing asymmetries in the line profiles in spectra of M31 and the Sombrero galaxy (Slipher 1914; Wolf 1914), the first indication that galaxies rotate was found[1]. From that moment new observations were developed to unravel the detailed kinematics of different structures within galaxies. Unfortunately up to the mid-seventies no methods had been developed to accurately measure rotation velocities in galaxies from absorption line spectra. In appendix A we summarise the most relevant methods developed from the late 1970's up to date to determine accurate galactic kinematics.

Luminous elliptical galaxies are found to be slow-rotators (Davies et al. 1983). If the movement of the stars in an elliptical galaxy were purely due to random motions, one should expect it to be a perfect sphere. However, under the presence of some systematic rotation around a certain axis, on top of the random motions, it would be natural to see the galaxy flattened perpendicular to this axis. Observations of rotation velocities in ellipticals, however, are found to be orders of magnitude smaller (14 ± 12 km s^{-1} for NGC 5044, Caon, Macchetto &

[1]We refer the reader to Rubin (2000) for a fantastic historical review about rotation in galaxies.

Pastoriza 2000) than what it is expected for oblate isotropic rotators. A different mechanism therefore had to be the able to explain the flattening of ellipticals. In 1976 Binney showed that the flattened shape of bright elliptical galaxies could be explained in terms of anisotropies in the velocity distribution.

Bulges in nearby galaxies, contrary to bright ellipticals, are found to be faster rotators (V_{max} $\sim$150 km s^{-1}, Kormendy & Illingworth 1982). Rotation in Es seems to be correlated with luminosity in the sense that bright Es show almost no rotation, whereas low luminosity Es rotate as much as bulges (Davies et al. 1983). However, taking it to the extremes very low luminosity ellipticals (low surface brightness dwarfs) show no significant rotation (Bender & Nieto 1990).

Elliptical galaxies are often thought to be triaxial. Bulges can also be triaxial, although the origin of this triaxiality might be different than that of ellipticals. Triaxiality in Es can be explained in terms of misalignments between the projected photometric and kinematic minor axis. In bulges rotation is rapid enough to account for the flattening. Signatures of triaxiality in bulges are found, i.e. in M31 (Lindblad 1956), where the misalignment between the disk and the bulge ($\sim$10^{o}) is impossible to explain if both the disk and the bulge are oblate systems. More evidence of triaxiality in bulges has been found by Bertola, Zeilinger & Rubin (1989) or Bertola, Vietri & Zeilinger (1991).

A third kind of triaxial objects are bars. These can be distinguished from ellipticals or bulges by their large ellipticity, a flat surface brightness profile along the major axis and a steep minor axis light profile (Binney, Kormendy & White 1982). Bars were initially found in around 30% of disk galaxies (Sellwood & Wilkinson 1993), however the statistics are not clear yet. The real fraction of barred galaxies has been recently found to be significantly higher because some apparently normal spirals show a bar feature in the near-IR that was not visible in their optical images (70%, Knapen, Shlosman & Peletier 2000). Bars are easily detected photometrically, e.g. in face-on spiral galaxies, however the situation worsens as we look at more edge-on systems. A large fraction of edge-on S0 and spiral galaxies show boxy or peanut-shaped bulges. Kuijken & Merrifield (1995) discovered an unequivocal spectroscopic signature that can identify bars on edge-on systems. They made used of the *Position-Velocity Diagram* (PVD) to look for a double-peaked LOSVD with a characteristic '*figure of eight*' (see Fig. 1.2) variation with radius. Recent works have extended this type of analysis to larger and more diverse samples (Merrifield & Kuijken 1999; Bureau & Freeman 1999;

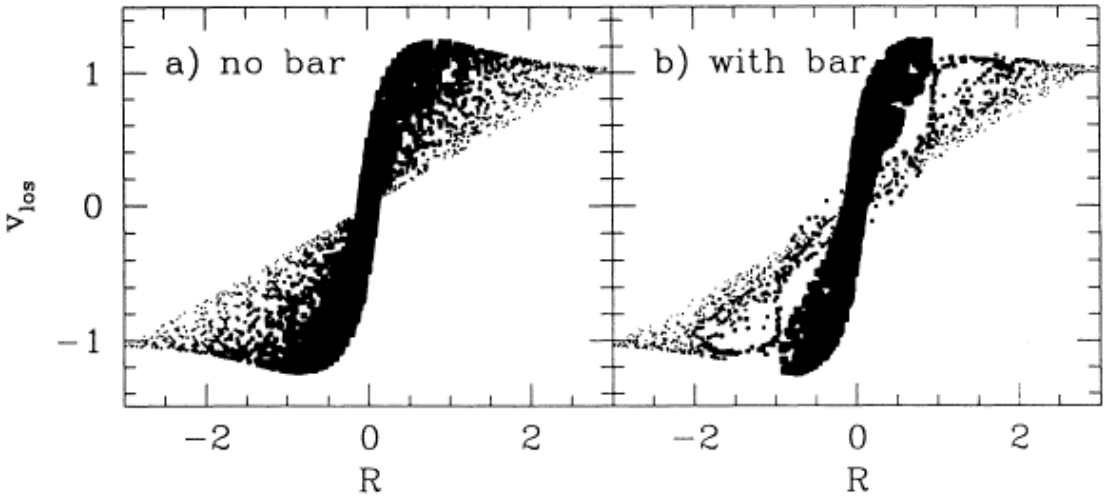

Figure 1.2: Characteristic Position-Velocity diagram (PVD) of a non-barred and a barred galaxy (Kuijken & Merrifield 1995).

Athanassoula & Bureau 1999; Bureau & Athanassoula 1999).

In recent years new observations have revealed that many galaxies contain central structures that, although looking like bulges photometrically (i.e. following the $r^{1/4}$ law), present dynamical signatures of disks. Such behaviour is reflected in a *flat* radial velocity dispersion profile, which might be considered as an extrapolation of the disk velocity dispersion to the inner regions of those galaxies. Therefore, in those cases, it seems more appropriate to talk about thickened disks rather than bulges. The disky nature of bulges is usually discussed in relation to late-type, low-mass bulges (Kormendy 1993), although in this thesis we found evidence for *flat* radial velocity dispersion profiles in all type of galaxies.

It has been found that around 20% of giant E galaxies exhibit kinematically decoupled cores (KDC), or even counter-rotating cores (Franx & Illingworth 1988; Hau 1998). However this picture can also be extended to bulges, where examples of counter-rotating bulges (i.e. NGC 7331, Prada et al. 1996) or even non-rotating bulges (i.e. NGC 4550, Rix et al. 1992) are found.

1.2.3 Stellar Populations

Understanding the stellar populations in galaxies is crucial for the analysis of their formation and evolution. Our understanding of the properties, i.e. ages and metallicities, of the stellar populations in galaxies is a long-standing problem.

Since the integrated light from millions of stars in these galaxies needs to be analysed, and since velocity broadening makes it difficult to study weak absorption features, it has up to now been impossible to uniquely determine the average age and metallicity in any type of galaxies.

A major drawback to investigating stellar populations photometrically is that data suffer from the inherent limitations of the populations diagnostics. More specifically optical broadband colors cannot be used to distinguish the effects of age and metallicity on an integrated stellar population (Worthey et al. 1994), although IR colours provide a way out (Peletier, Valentijn & Jameson 1990; Peletier et al. 1999a). The use of spectroscopic absorption line-strengths provides a solution that alleviates the problems encountered by photometry.

Stellar Population studies started in the early 1960's with the pioneering work of Spinrad (1961), and followed later on by O'Connell (1976) who study absorption features (i.e. Mg I, Na I) in the central regions of elliptical galaxies. The following decade saw the apogee of population studies, thanks to the discoveries like a correlation between the Mg_2 index and the central velocity dispersion of elliptical galaxies (Terlevich et al. 1981), or the definition of the, still nowadays most commonly used, Lick/IDS system (Burstein et al. 1984). In the early 1990's González (1993), using absorption lines measured in the Lick/IDS system, found that the age/metallicity degeneracy could be broken due to the fact that certain absorption lines were more sensitive to age or metallicity than others. Later on a number of groups started to develop a comprehensive set of stellar population models that helped to break the age/metallicity degeneracy (Bruzual A. & Charlot 1993; Worthey et al. 1994; Weiss, Peletier & Matteucci 1995; Vazdekis et al. 1996). However the libraries of stellar spectra used in those models suffer from narrow spectral coverage, limited resolution, limitations in the range of stellar types observed, and often poor data quality. Therefore more and better stellar libraries are essential to learn more about stellar populations in galaxies. The Ca II triplet offers an opportunity to help in that respect. Recently, a new stellar library has been developed to produce an extensive and thorough calibration of a number of features in this region of the spectrum (i.e. CaT*, CaT, PaT and Mg I, Cenarro et al. 2001a; Cenarro 2002). Stellar population models using this library have also been developed by Vazdekis et al. (2003). This new set of indices, together with the ones previously defined at optical wavelengths, is a useful tool to investigate the stellar content of early-type galaxies (Cenarro et al. 2001a,b,

2002; Vazdekis et al. 2003).

The first studies on stellar populations were performed on early-type galaxies and found that they were old or intermediate age systems (Tinsley & Gunn 1976; O'Connell 1980; Pickles 1985). For example, the analysis of the Hβ absorption line also indicates that they are not as old as globular clusters (Burstein et al. 1984). The picture was not clear because the results depended on which method people used. Schweizer et al. (1990) investigated a sample of Es and S0s for the signatures of *fine* structure, by means of ripples, jets, etc. Their comparison of the Hβ or Mg_2 index with σ revealed that the galaxies with those disturbances were younger than the rest. On the other hand González (1993) found evidence of a wide range of ages (from 2 Gyr to 17 Gyr) measured from the integrated light of nearby galaxies, even for galaxies without any *fine* structure.

Stellar population studies in bulges have seen some major improvement in the last decade. Initial works focussed on the analysis of S0 galaxies. The main question to address, which at present remains unsolved, was whether S0 galaxies are primordial or have formed as a result of some evolutionary process (i.e. from gas stripped spirals). Their transitional position along the Hubble sequence makes them the most likely objects to have experienced substantial morphological and population changes. The situation of the S0 galaxies is somewhat similar to that of the Es in terms of the stellar populations. In general S0 galaxies seem to be old, however, similar to the Es. In 1992 Schweizer & Seitzer found evidence for young populations based on the degree of *fine* structure, i.e. shells and dust features, in those galaxies. The central Mg/Fe in the luminous S0 galaxies share similar overabundance of Mg to Fe w.r.t. solar element ratios (Fisher, Franx & Illingworth 1996). Results based on IR photometry, suggested that the disks of S0s would be 3-5 Gyr younger than their bulges (Bothun & Gregg 1990). However, this finding appears to be in contradiction with a more recent studies (Terndrup et al. 1994; Peletier & Balcells 1996) in which no significant age gradients and very shallow metallicity gradients along the major axis are found in a sample of early-type spirals and between bulge and disk. On the other hand, a controversial result is reported by Bender & Paquet (1999), who found evidence of bulges younger than disks in several cases in their sample of S0 galaxies.

Contrary to S0 galaxies, bulges of *spiral* galaxies are much more difficult to analyse in the context of populations as disk light starts affecting the light coming from the centre of the galaxy. Particularly important is the effect of nebular emission

on the measurement of absorption lines traditionally used in index-index diagrams to disentangle the age/metallicity degeneracy (i.e. Hβ vs <Mgb ·Fe5270>, Goudfrooij & Emsellem 1996; Goudfrooij, Gorgas & Jablonka 1999). The Mg_2 index in these galaxies shows a strong correlation with the intrinsic luminosity of the bulge (Jablonka, Martin & Arimoto 1996), and the slope of the Mg_2 gradient coincides with the values found in ellipticals (Gorgas et al. 1997; Proctor & Sansom 2002).

1.2.4 Scaling Relations

Scaling relations are one of the most powerful tools in modern astrophysics due to their ability to link physical properties in galaxies. Although the origin of such relations mainly started with elliptical galaxies, more and more work is being devoted to the study of the role of bulges and their connection to ellipticals. As discussed in previous subsections elliptical, S0 and spiral galaxies emerge as complex individuals when we analyse their detailed structure, internal kinematics and stellar populations. However, they seem to behave highly uniformly when viewed from the perspective of global scaling relations.

More luminous ellipticals have large central velocity dispersions. The Luminosity - σ_0 relation was the first to be discovered by Faber & Jackson (1976) and is mostly referred as the **Faber-Jackson relation**. This relation is of great importance since it is the first one that links photometric and dynamical properties. Just a year later Visvanathan & Sandage (1977) discovered the **Color - Magnitude relation** (CMR) showing that more luminous galaxies, in a sample of Es and S0s in the Virgo cluster, are redder. From such a result it is usually assumed that brighter galaxies are more metal rich. This is because more metal rich stellar populations are redder. Based on the idea that galaxies formed from a monolithic collapse that generates a huge burst of star formation and evolved passively afterwards, one can explain the higher metallicity of larger galaxies by assuming that they are able to retain the products of nucleosynthesis due to their deeper potential. The colors of bulges lie along the CMR of old elliptical galaxies, with a slight, but significant offset to bluer colors (Balcells & Peletier 1994). With the definition of spectral indices (Faber, Burstein & Dressler 1977; Worthey et al. 1994) new correlations appeared linking the stellar populations and dynamical properties. The most widely used is the **Mg_2 - σ relation** (Terlevich et al.

1981). The scatter in the relation is very small. The tight correlation found is interpreted as a mass-metallicity relation, although observations of bulges of S0 and spiral galaxies reveal that for later-type galaxies the relation might be steeper (Jablonka, Martin & Arimoto 1996; Prugniel, Maubon & Simien 2001). This steeping seems to indicate that the Mg_2 - σ relation is a mass-metallicity relation for bright ellipticals, along which the relative fraction of young stars becomes more and more important as we move towards fainter objects (Prugniel, Maubon & Simien 2001).

The best known, and probably most widely used scaling relation nowadays is the **Fundamental Plane** (FP) (Djorgovski & Davis 1987; Dressler et al. 1987). The FP relation defines a thin plane in three dimensional space described by the central velocity dispersion (σ_0), the effective radius (r_e) and the mean effective surface brightness ($< \mu >_e$). Similar to the other scaling relations, the FP has been extensively studied in elliptical galaxies, and particularly in Es in clusters. The work initiated by Jørgensen, Franx & Kjærgaard (1996) has set the reference in the FP studies. Bulges of S0 and spiral galaxies follow a very similar FP as the one defined by ellipticals (Bender, Burstein & Faber 1992; Saglia, Bender & Dressler 1993).

The tightness, small scatter and apparent independence of morphological type (at least among Es, S0s and spirals) of the FP relation has made it an important method for distance determinations. Typical uncertainties in distance estimations from the FP are $\approx 10\%$ (Jørgensen, Franx & Kjærgaard 1996).

Finally the **Tully-Fisher relation** (TFR) (Tully & Fisher 1977) relates the absolute magnitude of a galaxy to its mass through the rotation velocity. This relation is tight in nearby spiral galaxies. Most of the work on this relation has been done using spiral galaxies, for which rotation curves can be accurately measured from the 21 cm line. However it becomes increasingly more difficult as we move to early-type galaxies (Es and S0s) as their gas content is scarce, and with rotation velocities much more complicated to determine.

1.3 Formation theories for bulges

To study the formation of galaxies, galactic bulges are the ideal objects to investigate. Located in the centre of a spiral disk, they closely resemble elliptical

galaxies. Two paradigms are commonly used to explain the formation of the central bulges of disk galaxies. In the first, the bulge forms prior to the disk, perhaps as part or as a consequence of the formation of the stellar halo (Eggen, Lynden-Bell & Sandage 1962; Gilmore & Wyse 1998), or as a result of early merging resulting in an $r^{1/4}$ spheroid around which a new thin disk forms from surrounding gas (e.g. Kauffmann, Guiderdoni & White 1994). In the second scenario, a bar, formed from instabilities of dynamically cold disks, starts buckling through vertical orbital resonances. Material is fuelled towards the centre of the galaxy. Bulges are then formed from the vanishing bar due to a mass concentration in the centre of the galaxy, initially taking an triaxial shape and later on a spheroidal one (Pfenniger & Norman 1990; Pfenniger 1993).

In recent years, significant progress has been made towards understanding the formation of bulges. It is now thought that bulges of early-type spirals form first, before the disk. They seem to have many properties in common with ellipticals: their surface brightness, and profile shapes (Andredakis, Peletier & Balcells 1995). They also share similar behaviour of the scaling relations (CMR, FP). These similarities, together with the fact that elliptical galaxies are old, lead to the conclusion that those bulges are also old. The latest results from their stellar populations confirm so (Peletier et al. 1999a; Carollo et al. 2001). Therefore a monolithic-like collapse (Eggen, Lynden-Bell & Sandage 1962) or a sequence of hierarchical mergers (Kauffmann, Guiderdoni & White 1994), resulting in the formation of the bulge followed by accretion of a disc, are the most likely formation scenarios for these type of galaxies. In such a picture dissipation plays a key role during the formation.

On the other hand bulges of spirals of type later than Sb generally have exponential bulges (Andredakis, Peletier & Balcells 1995; de Jong 1996; Carollo 1999; Graham 2001), and they often contain recent star formation. 'Disklike' bulges, as defined by Kormendy (1993), are more common for later Hubble types. Kormendy (1993) mentions the dynamical resemblance, shown by a flat velocity dispersion profile, of some bulges to their surrounding disks supports the claims of secular evolution for those objects. Indeed bar-driven gas inward transport can produce a dramatically increase of the disk's central concentration, and can induce bursts of star formation. This formation process is supported by observations showing nuclear hot spots of young stars and gas. Those are mainly found in late type galaxies (i.e. NGC 4321, Arsenault et al. 1988), although star formation

is also found in some S0 galaxies.

Despite this progress in all areas, theoretical and observational, important questions remain unanswered and it is not clear whether a breakdown in formation scenarios depending on galaxy type is in place or not.

1.4 Bulges at high-redshift

The study of bulges at high redshift is a difficult task. As the distance to the redshifted galaxy increases our spatial resolution is reduced and therefore it is much more complicated to distinguish between structural components (i.e. disk and bulge) in a galaxy. Such identification problem becomes even more evident when one discoveries that Hubble's 'tuning fork' classification breaks down at redshifts beyond $z>0.5$ (van den Bergh 2002) and that only big spiral galaxies are still identifiable up to $z\approx1$ (van den Bergh et al. 2000; Ellis, Abraham & Dickinson 2001). The literature regarding this topic, despite the fact that it is growing, is quite limited yet. Considering this important setback the question is: is it possible to look back in time and find the progenitors of today's bulges?. The answers to this question, although uncertain, is of great importance since it could help towards our understanding of formation scenarios of spiral bulges. At present, studies at high redshift ($z\sim1$) show that the fraction of barred galaxies at high redshift is much smaller than at low-redshift (Abraham et al. 1999). It is unclear what the physical processes for such a deficit are. On the other hand, hierarchical models predict, on average, older population for bulges than their surrounding disks (Baugh, Cole & Frenk 1996). This pictures is confirmed at all redshifts (Abraham et al. 1999). In a recent work Ellis, Abraham & Dickinson (2001) revise all these issues and find that despite being redder than their disks, bulges are significantly bluer than the bulk of elliptical galaxies at the same redshift. They conclude that those bulges, especially at intermediate redshift, may have occurred some kind of rejuvenation of their stellar populations and that it is more likely to be burstlike.

1.5 The need for Integral Field Spectroscopy

The first IFUs appeared in 1980. The first concept was the use of an array of optical fibers to transform the bidimensional field into a pseudo-slit at the entrance

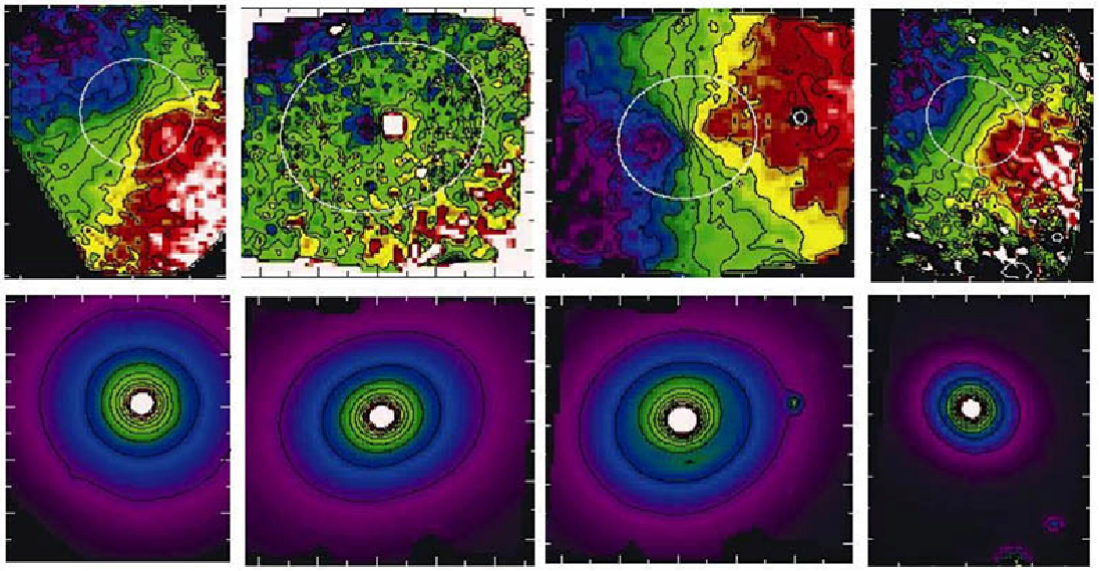

Figure 1.3: Example of how Integral Field Spectroscopy improves our knowledge of galaxies. Figure from Bacon et al. (2002). Top row shows velocity maps for a set of 4 elliptical galaxies, whereas bottom panels show the associated intensity maps.

of a classical long-slit spectrograph (Vanderriest 1980). Further implementations used a microlenses array as the spatial sampler instead (Courtès 1982). The first IFU using the Courtès concept was called TIGER (Bacon et al. 1995) and operated at the CFHT[2]. Since then, more and better IFUs have been developed, aiming to understand the nature of galaxies (i.e. it OASIS, *SAURON*[3], VIMOS)

Understanding the formation and evolution of elliptical galaxies and spiral bulges is complicated by the fact that many of these systems reveal signatures of triaxiality or have multiple kinematic components. Both lead to rich velocity structures which are difficult to understand with long-slit spectroscopy (Statler 1991, 1994). The literature is plenty of examples of counter-rotation in the inner parts of galaxies (i.e. Peletier et al. 2001), central disks (Seifert & Scorza 1996). This makes Integral Field Spectroscopy of stars and gas essential for determining the dynamical structure and stellar populations distribution of these galaxies. The advantage of IFUs (Integral Field Units) is the possibility of producing two-dimensional stel-

[2]The Canada-France-Hawaii Telescope, operated by the National Research Council of Canada, the Centre National de la Recherche Scientifique of France and the University of Hawaii

[3]Spectrographic Areal Unit for Research on Optical Nebulae (Bacon et al. 2001; de Zeeuw et al. 2002)

lar and gas kinematics as well as line-strength maps. This instrumentation serves as the perfect benchmark to test novel techniques, i.e. optimal template fitting to decouple the gas contribution from the galaxy spectra (see §5.4.1 in chapter 5) or three-integral axisymmetric dynamical models (Verolme et al. 2002). Making use of those tools, the *SAURON* survey is revealing a whole set of peculiarities in early-type galaxies. In Fig. 1.3, as an example, the bottom row shows the reconstructed total intensity maps of 4 early-type galaxies from *SAURON* observations. Whereas the photometry is similar, the stellar velocity fields (top row) are very different. From the figure it becomes clear that IFUs open a new world of possibilities to explore the nature of galaxies in general.

In the present thesis we enter in the world of IFUs by making use of *SAURON* observations to study in detail the stellar, gas kinematics and line-strength of the S0 galaxy NGC 7332. Results of our analysis can be found in chapter 5.

1.6 Aims of this thesis

This thesis is born with the idea of providing more clues to understand the nature of bulges and the formation mechanisms involved (see Sec. 1.3). In order to address these questions we have analysed a subset of an optically selected, complete, sample of ≈50 bulges of type S0-Sbc defined by Balcells & Peletier (1994). The galaxies were required to have an inclination $>50^{o}$ to minimize the influence of the disk light on the bulge. We have made use of minor axis long-slit spectroscopy to derive kinematic parameters, as well as line-strength indices. We have determined the location of bulges on the FP of early-type galaxies as well as on the Mg_2 - σ relation. We study the near-IR Ca II triplet - σ relation and discuss their implications in the formation and evolution of bulges. Finally we have also made use of *SAURON* observations for our study of the S0 galaxy NGC 7332. More specifically we want to address the following questions:

(1) **Internal kinematics of bulges in 2D:** Although bulges generally are supported by rotation (Davies et al. 1983), their kinematics has not been studied in as much detail as that of ellipticals. It is not well known whether bulges are triaxial or simply oblate. Studies of 2D spectroscopy, including line profiles are necessary to study the distribution function, and to understand counter-rotation (i.e. Merrifield & Kuijken 1994; Prada et al. 1996).

(2) **Stellar populations in bulges:** Observations of nearby clusters have shown that the fraction of S0 galaxies in clusters at z$\sim$0.5 is much smaller than in nearby clusters, indicating that many S0 galaxies in the nearby universe are relatively young (Dressler et al. 1997). This is in apparent contradiction with recent studies (e.g. Peletier et al. 1999a) that find that early-type bulges are old. On the other hand line-strength studies of bulges are scarce in the literature and a detailed line-strength analysis may provide information of the abundance ratios in bulges and give information about star-formation time scales.

The following section summarises with more detail the results contained in each chapter.

1.7 Outline of the Thesis

1.7.1 Overview

This thesis contains 4 main chapters (Chap. 2, 3, 4, 5) that contain the main results of my research during the last three years. The main results of chapter 2 have been accepted for publication to the Journal *Astronomy & Astrophysics*. Chapter 3 has led to the publication of a paper in *Monthly Notices of the Royal Astronomical Society* (Falcón-Barroso, Peletier & Balcells 2002). Finally, we are on the verge of submitting two more papers summarising the results in chapters 4 and 5. Most of the results presented in this thesis have been obtained by the author.

1.7.2 Chapters content

Chapter 2: Minor-axis kinematics of bulges

This chapter analyses the minor axis kinematics of a well-studied sample of nearby bulges defined by Balcells & Peletier (1994). We have made use of SSP (single-age, single-metallicity population) models from Vazdekis et al. (2003) to derive kinematic parameters (mean radial velocity, velocity dispersion, h_3 and h_4) in the Ca II triplet region. We show that with model templates the same results can be obtained as with observed stars or better. Our sample reveals small amounts

of minor axis rotation, generally due to inner isophotal twists of slightly triaxial bulges or misaligned inner disks. The presence of these features does not seem to correlate with the CaT* index. We also discuss the nature of some bulges based on the shape of their velocity dispersion profiles.

Chapter 3: Bulges on the Fundamental Plane of Early-Type galaxies

Chapter 3 presents the results of our study of the location of bulges on the Fundamental Plane (FP) of Early-type galaxies. We analyse the relation in 2 wavebands, the B-band and the K-band, and conclude that bulges in our sample lie close but slightly below the FP defined by Es and S0s. The result is consistent with the picture of bulges being old. We have also revisited the Mg_2 - σ relation for our sample and compared them with several samples of bulges and early-type galaxies in the literature.

Chapter 4: The CaT-σ relation in bulges

In this chapter we present new results on the relation between the Ca triplet line strength and the velocity dispersion for our sample of bulges. We made use of a new set of near-IR line indices by Cenarro et al. (2001a). We find that the CaT* index decreases as a function of σ with a very small scatter. The implications of this result are very important since it is the first time an anti-correlation is found between velocity dispersion and a metal line index in bulges. The same result, however, was discovered by Saglia et al. (2002) and Cenarro et al. (2003) for elliptical galaxies. On the other hand we also corroborate the positive correlation found between Mg and σ from the Mg I - σ relation. We discuss the origin of these relations and what it implies for stellar populations in galaxies.

Chapter 5: Study of the peculiar galaxy NGC7332

This final chapter presents a new set of state-of-the art observations designed to study in detailed the peculiar galaxy NGC 7332. As it was shown in chapter 3 this galaxy departs from the FP relation beyond the observational uncertainties. We have made use of Integral Field data, part of the *SAURON* project, to obtain 2D kinematical maps (radial velocity, velocity dispersion, h_3 and h_4), gas kinematics (from [O III], Hβ and [N I] emission) and line-strength maps (Hβ, Mgb, Fe5015,

Fe5270). Our analysis reveals a KDC in the stellar velocity field, a central disk, and 2 different gas systems present in [O III].

Chapter 2

Minor axis kinematics of 19 S0-Sbc bulges*

* Falcón-Barroso,J., Balcells, M., Peletier, R.F., Vazdekis, A., 2002, to appear in *Astronomy & Astrophysics*

2.1 Introduction

The measurement of kinematics in galaxies has been one of the major achievements in astrophysics in the second half of the last century. Our knowledge in this field has evolved from crude kinematic determinations from photographic plates (Burbidge & Burbidge 1968), to high-resolution, detailed measurements of the line-of-sight velocity distributions (hereafter LOSVDs; i.e. Bender, Saglia & Gerhard 1994; Fisher 1997; Vega Beltrán et al. 2001).

In the seventies, methods were devised to measure velocity dispersions in addition to radial velocities, i.e. cross-correlation (Tonry & Davis 1979), Fourier Quotient (Sargent et al. 1977). In the past decade, with the improved quality of the data, a new set of algorithms were developed allowing us to measure LOSVDs (Fourier Correlation Quotient, Bender 1990), and quantify deviations from pure single Gaussian (van der Marel & Franx 1993) and multiple Gaussian LOSVD with UGD (*Unresolved Gaussian Decomposition*, Kuijken & Merrifield 1993; Prada et al. 1996). Galactic kinematics, however, suffers from an important technical constraint: template mismatching. Stars are observed together with the object which kinematics we are interested in, to be used as spectral templates. However, it is difficult to choose the right star, since galaxy light comes from a wide range of stellar types. Although, for ellipticals in the V-band, it has been found that half of the light comes from G and K giants (Pickles 1985) and, therefore, those stellar types are good templates, this situation may change dramatically from galaxy to galaxy or even within a galaxy. Therefore kinematic parameters will be sensitive to the stellar template used. Much work has been devoted to address the template mismatch problem (Rix & White 1992; González 1993; Statler, Smecker-Hane & Cecil 1996; Statler & Smecker-Hane 1999).

In the last decade, new evolutionary stellar population synthesis models (Bruzual A. & Charlot 1993; Worthey et al. 1994; Buzzoni 1995; Tantalo et al. 1996; Vazdekis et al. 1996) have helped us to significantly increase our galaxy stellar populations knowledge. These models predict line strengths of a limited number of spectral features, such as those of the Lick/IDS system (i.e.Worthey et al. 1994; Vazdekis et al. 1996). However since these models were unable to predict full SEDs (Spectral Energy Distributions) at high enough resolution, they could not be used as templates for galaxy stellar kinematics. This situation has recently changed with the development of new SSP model SEDs in the blue and visual

at resolution 1.8 Å (FWHM) Vazdekis (1999) and in the near-IR Ca II triplet region at 1.5 Å (Vazdekis et al. 2003). In fact, Vazdekis (1999) and Vazdekis & Arimoto (1999) have shown the potential use of the SSP models as templates for determining the main kinematic parameters in the optical spectral range. In this chapter we are for the first time in position to determine galaxy kinematics using SSP templates in the near-IR Ca II spectral range. It is generally assumed, that kinematic stellar templates are required to be obtained with the same instrumental setting as the one used for the galaxy spectra (Sargent et al. 1977; Tonry & Davis 1979). In this paper we show that this is no longer a requirement, at least at the resolutions of the spectra considered here.

This chapter intends to be a first step in the exploration of SSP models as templates by comparing velocity profiles, for a sample of 19 galaxies, with those obtained with our best stellar or mixture of stellar templates. We show that in all cases SSP models produce kinematics of at least at the same level of quality, and are quite often better than the best stellar templates. In order to trace correlations between kinematic and population features along the galaxy minor axes, we measure the CaT* index (Cenarro et al. 2001a).

Section §2.2 summarizes the observations and data reduction. In §2.3 we describe the different types of template samples and the way the kinematical profiles have been determined, including a detailed comparison between stellar templates and SSP models. The obtained kinematics is discussed in §2.4. Kinematical profiles are graphically presented in Appendix C. Appendix D contains all the tables with the numerical values presented in appendix C.

2.2 Observations & Data Reduction

2.2.1 Sample

The sample comprises 20 galaxies of types S0–Sbc selected out of the Balcells & Peletier (1994) sample of bulges. The latter is a diameter-limited sample of galaxies with inclinations above 50 degree from the UGC catalog (Nilson 1995). The 20 objects were those we had observed with HST/WFPC2 and NICMOS, hence high-spatial resolution images are available for them at B, I, H bands (Peletier et al. 1999a). The main properties of the sample are presented in table 2.1.

2.2.2 Observations

We obtained long-slit spectra for our sample of galaxies at the 4.2m William Herschel Telescope of the Observatorio del Roque de los Muchachos at La Palma between 11 and 13 July 1997. Twenty galaxies were observed between 8360 - 9170 Å using the ISIS double spectrograph. We discarded NGC 5577 as the spectra did not have sufficient signal-to-noise. We are thus left with 19 objects (see Table 2.1). The red arm was equipped with the Tektronix (1024×1024) TEK2 CCD (0.36″per 24 μm pixel) and the R600R grating, providing a spectral resolution (FWHM of arc lines) of 1.74 Å (59.6 km/s) with a spectral dispersion of 0.8 Å/pix. We used the 6100 Å dichroic for simultaneous red and blue arm exposures. In this chapter we discuss the red arm spectra only. Typical exposure times per galaxy were 1500 sec. The slit width was 1.2″, matching the seeing at the time of the observations. Arc line exposures were taken before and after each target exposure. Tungsten continuum lamp exposures were taken with the red arm after each target exposure, for fringe calibration. Twilight sky exposures were taken every night for flat fielding. We also obtained spectra for 11 stellar templates of types A2 to M4, from the Lick list of stars (Worthey et al. 1994), listed in Table 2.2.

2.2.3 Data Reduction

The data were reduced following standard steps using the IRAF[1] package. Each individual frame was divided by a flatfield, taken at the same position, after a bias frame had been subtracted. We subtracted the sky using the outer regions of the 4′ long slit, and removed the cosmic rays using the $RED_M^{UC}E$ package (Cardiel 1999). The data were calibrated in wavelength, with an RMS error in the calibration solution of 0.1 Å in the blue and 0.02 Å in the red arm. Finally the data were calibrated in flux using standard stars BD+284211 (Oke 1990) and BD+174708 (Oke & Gunn 1983).

[1]IRAF is distributed by the National Optical Astronomy Observatories, which are operated by the Association of Universities for Research in Astronomy, Inc., under cooperative agreement with the National Science Foundation.

Table 2.1: Galaxy Sample

NGC	V_{LG} km/s	Scale kpc/″	Type	M_R^{tot} mag	M_R^{bul} mag	B/D	PA deg	Exp. Time sec	ϵ_D	ϵ_B	r_{bulge} ″	Best Templ.	S/N pix^{-1}
(1)	(2)	(3)	(4)	(5)	(6)	(7)	(8)	(9)	(10)	(11)	(12)	(13)	(14)
5326	2576	0.25	1	−22.16	−21.22	0.73	-138	1500	0.50	0.43	5.97	+0.2, 3.16	83
5389	1990	0.19	0	−21.32	−20.70	1.30	93	1500	0.80	0.46	2.85	M1 III / +0.2, 4.47	61
5422	1929	0.19	−2	−21.96	−21.33	1.28	64	1500	0.80	0.35	3.33	+0.2, 7.08	68
5443	2060	0.20	3	−21.53	−19.09	0.12	-52	1400	0.68	0.54	1.98	+0.2, 3.16	37
5475	1861	0.18	0	−20.98	−18.72	0.14	-101	1500	0.68	0.24	2.45	+0.2, 1.41	57
5587	2291	0.22	0	−21.07	−19.43	0.29	73	1500	0.70	0.47	1.51	−0.4, 14.12	36
5689	2290	0.22	0	−22.29	−21.47	0.89	-5	1500	0.75	0.48	2.04	0.0, 4.47	58
5707	2354	0.23	2	−21.43	−20.11	0.42	-59	1500	0.75	0.20	3.79	0.0, 2.51	51
5719	1684	0.16	2	−21.60	−20.00	0.30	5	1500	0.64	0.61	7.71	K3 Ib / −0.4, 3.55	51
5746	1677	0.16	3	−22.68	−21.70	0.68	-99	1200	0.84	0.52	2.37	M1 III / +0.2, 3.16	44
5838	1337	0.13	−3	−21.89	−20.93	0.71	134	1500	0.65	0.22	8.39	0.0, 12.59	86
5854	1708	0.17	−1	−21.43	−20.18	0.46	-33	1500	0.70	0.32	4.85	−0.7, 6.31	64
5879	1065	0.10	4	−20.30	−19.08	0.48	89	1500	0.62	0.32	0.85	−0.4, 3.16	41
5965	3603	0.35	3	−22.92	−21.76	0.53	-38	1500	0.84	0.50	2.32	−0.4, 5.01	46
6010	1923	0.19	0	−21.57	−19.88	0.27	12	1500	0.75	0.28	2.70	0.0, 14.12	67
6504	4680	0.46	2	−24.57	−23.30	0.45	135	1500	0.83	0.44	4.05	−0.4, 3.16	52
7331	1138	0.11	3	—	—	0.001[1]	80	1500	0.63[1]	0.62	4.57	−0.4, 15.85	117
7332	1550	0.15	−2	−21.86	−20.52	0.41	-114	1500	0.74	0.29	2.99	−0.4, 11.22	101
7457	1114	0.11	−3	−20.91	−20.91	10.00	35	1500	0.48	0.34	3.29	+0.2, 2.51	51

DESCRIPTION OF THE COLUMNS FOR TABLE 2.1:

(1): the NGC numbers of the galaxies.

(2): Recession velocity of each galaxy in km/s, corrected to the Local Group (Karachentsev & Makarov 1996), from optical heliocentric velocities given in the *Third Reference Catalogue of Bright Galaxies* (1991) (hereafter RC3).

(3): Scale in kpc/arcsec from Falcón-Barroso, Peletier & Balcells (2002).

(4): Type index T from the RC3.

(5) and (6): Absolute magnitudes, in R-band, from Peletier & Balcells (1997) (H_0=50 km/s/Mpc).

(7): Bulge-to-disk ratio from an R-band bulge-disk decomposition following Kent's (1984) method (Peletier & Balcells 1997).

(8): The position angle, in degrees, (N – E) of the dust-free minor axis (Peletier & Balcells 1997).

(9): Integration time, in sec, for each galaxy during the observations.

(10): Disk ellipticity from Peletier & Balcells (1997).

(11): Effective bulge ellipticity, from HST H-band ellipticity profiles, measured at the geometric effective radius (Balcells et al. 2003).

(12): Minor axis bulge radius, derived from Balcells et al. (2003) HST H-band profiles, as the radius at which the contribution from the disk and bulge light are equal, except for NGC 7332 for which a ground-based image was used instead (Peletier & Balcells 1997) (Alister W. Graham, private communication).

(13) Best template fit for each galaxy. The metallicity ([M/H]) and age (Gyr) of the best fit SSP models is shown. In those cases where the stellar template performed better, the adopted SSP best template is also given.

(14) Signal-to-noise ratio per pixel in the central aperture (1.2 x 0.36 arcsec^2).

[1] From Prada et al. (1996)

2.3 Data analysis

2.3.1 Stellar Templates

In Table 2.2 we list the observed stellar templates. A representative set of spectra is shown in figure 2.1. The wide range of spectral types covered allows us for an exploration of the best templates for matching galaxy spectra. The most apparent variation from top to bottom in figure 2.1 is the decrease of the Paschen lines toward later types. P14, in a region devoid of other features, is a strong discriminant of the presence of stars earlier than G. P13 and P15, when present, give characteristic asymmetric profiles to the second and third lines of the Ca II (Cenarro et al. 2001a). Following previous works in the literature (Rix & White 1992; Hau, Carter & Balcells 1999) we have included in our analysis a mix-template from a linear combination of stars in our sample. However we have used a different approach to derive our optimal mix-template. Given the importance of the continuum shape in this wavelength region (Cenarro et al. 2001a; Vazdekis et al. 2003), we have created an optimal template that provides the best fit to the overall continuum shape of each galaxy (i.e. fitting the regions outside the main Ca II features, but including the TiO bands), before broadening with the appropriate kinematics. It is important to perform this fit using a combination of unconvolved stellar spectra, since any input kinematics comes from a particular template and could bias our result. In most cases the optimal mix-template is formed by G8III, K3Ib and M4V stars. The importance of the M4V star in the final template is justified by its ability to match the TiO molecular bands. As we will show in 2.3.4, this mixture of stellar templates helps to alleviate the template mismatch problem and it is an ideal benchmark to test our SSP models.

2.3.2 SSP model templates

We have used 78 SSP synthetic models at FWHM=1.5 Å (0.85 Å/pix) in the Ca II triplet region, corresponding to a single-age, single-metallicity stellar populations of [Fe/H]=−0.7,−0.4, 0.0, and +0.2. For each metallicity, the age varies from 1 to 17 Gyr, except for [Fe/H]=−0.7 starting from 6 Gyr and for [Fe/H]=−0.4 starting 3 Gyr. These limitations arise from the limited coverage of atmospheric parameters of the stellar sample used by the models. More details can be found in Vazdekis et al. (2003). In order to adapt these models to the same instrumental

Table 2.2: STELLAR TEMPLATES

Name (1)	α (h m s) (2)	δ (d m s) (3)	Spectral Type (4)	M_V (5)
BARNARD[1]	17 57 48.50	+04 41 36.2	M4 Ve	9.54
GL818[2]	21 05 19.75	+07 04 09.5	K6 V	8.33
HR0072	00 18 41.87	−08 03 10.8	G0 V	6.46
HR4521	11 46 55.62	+55 37 41.5	K3 III	5.26
HR5340	14 15 39.67	+19 10 56.7	K3 Ib	1.23
HR5681	15 15 30.16	+33 18 53.4	G8 III	3.47
HR5826	15 31 24.93	+77 20 57.7	K5 III	5.00
HR5854	15 44 16.07	+06 25 32.3	K2 III	2.64
HR6685	17 55 25.19	+26 03 00.0	F2 Ibe	5.47
HR8334	21 45 26.93	+61 07 14.9	A2 Iab	4.31
HR8795	23 07 00.26	+09 24 34.2	M1 III	4.55

NOTES:
(1) HR names from the Bright Star Catalogue (Hoffleit & Warren 1995).
(2),(3) J2000 coordinates from SIMBAD
(4), spectral type from Worthey et al. (1994)
(5) from SIMBAD (http://simbad.u-strasbg.fr/Simbad)
[1] NSV 9910 from the New catalogue of suspected variable stars (Kukarkin & Kholopov 1982)
[2] HD 200779 from the Henry Draper Catalogue and Extension (Nesterov et al. 1995)

resolution of our data, we have convolved them with a Gaussian of σ=0.38 Å. This procedure relies on the assumption that a Gaussian represents a good match to the instrumental PSF (Point Spread Function) of the observations. We have tested whether the arclines followed a gaussian shape, finding that indeed they do, with only small deviations (below 0.01) in the h_3 and h_4 parameters, as described by van der Marel & Franx (1993). If h_3 and h_4 had been found to be significantly different from 0, we would have had to convolve the models with the line profile of the arc-lines. Additionally, since the library of SSP models is built from a large set of observations using different instrumental configurations, it is important to check whether the instrumental profile of the models depart from that of our observations. In order to perform this test we have convolved a set different stellar templates, i.e. K3Ib, K3III, M1III, K5III (typically the ones that resemble the SSP models), with different LOSVDs to simulate a galaxy spectrum. We have made use of a representative SSP model (i.e. [Fe/H]= 0.0, t= 5.01 Gyr) as the kinematic template to recover those LOSVDs. Our tests reveal a very good

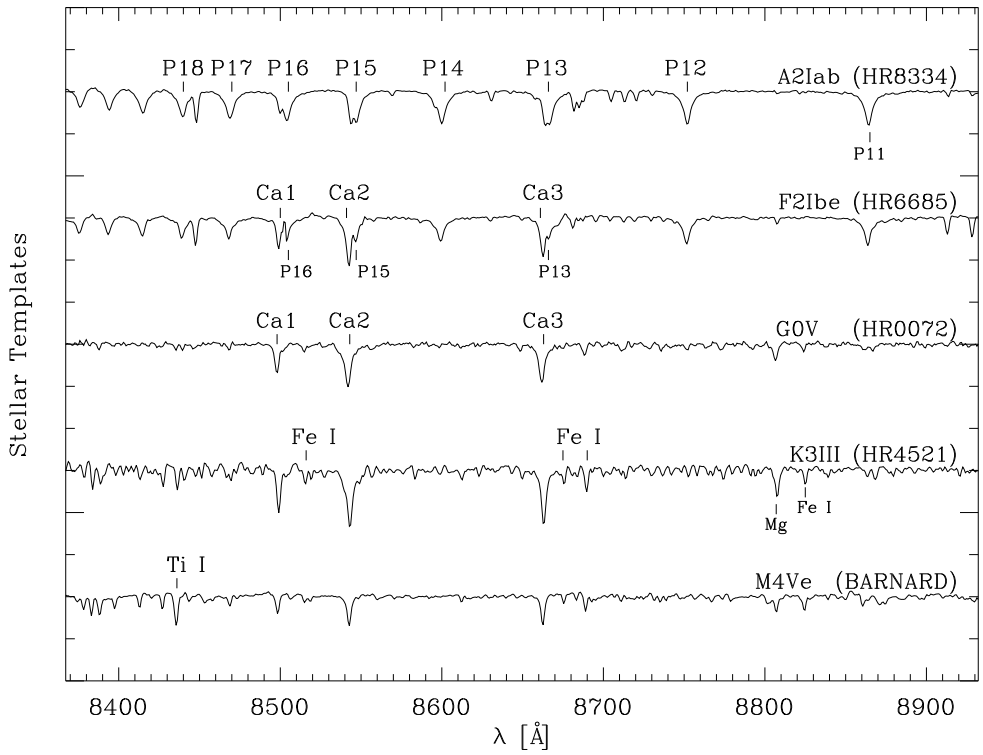

Figure 2.1: Representative sample of continuum subtracted stellar templates used in this paper. The most important features found in those spectra have been indicated: the Paschen series (from P11 to P18), the Ca II triplet (Ca1, Ca2 and Ca3) and several metal lines (Fe I, Mg I and Ti I).

agreement between the input and output parameters, confirming the SSP models from Vazdekis et al. (2003) as valid templates for our study.

2.3.3 Extraction of the kinematics

Kinematic profiles were derived from the data in the region of the near-IR Ca II triplet (8498 Å, 8542 Å, 8662 Å). For each galaxy, we generated two sets of coadded galaxy spectra, with minimum signal-to-noise ratios (S/N) of 33 and 20 per pixel, respectively. We made use of the program FOURFIT developed by van der Marel & Franx (1993), available from the first author's website. A Gauss-Hermite fit to the LOSVD was performed to obtain mean radial velocities, velocity dispersions, h_3 and h_4 moments for the data with signal-to-noise ratio above 33 per pix^{-1}. For data with signal-to-noise ratio between 33 and 20 per

pix^{-1} a pure gaussian fit was used. The choice of S/N is explained in Sec. 2.3.5.

2.3.4 Selection of the best fitting template

We have determined the kinematic profiles for our sample using each of the 90 templates we had available (78 SSP models, 11 stellar templates and the best mix-template for each galaxy). We have considered as our best fit template the one that minimized the χ^2, as defined in van der Marel & Franx (1993), for the central position of the galaxy profile, which has a S/N well above 33. One of the features of this code is the possibility of filtering the input spectra in fourier space so that any remaining low-order component not removed by the continuum subtraction or high-frequency noise can be filtered out. The resulting χ^2 is then evaluated over a finite range of wavenumbers determined by the filtering parameters. For our dataset the results from FOURFIT were weakly dependent on the lower cutoff and insensitive to the choice of the upper cutoff (given that we chose the same upper cutoff for all the galaxies and that this cut was well above the sigma of the galaxy). We also reduce the uncertainties in the derived kinematics by flux-calibrating the data and the template stars before applying the continuum subtraction because the normalizing polynomia for the data should be very similar to the ones used for the templates. Otherwise, the normalization procedure might introduce non-negligible variations in the spectra, including in the equivalent widths of the lines.

We establish whether SSP, stellar templates or mix-template provide better fits to the galaxy spectra by comparing the global reduced χ^2 of the fits. A typical distribution of χ^2 values is shown in figure 2.2. The lines trace reduced χ^2 for the SSP models, labeled by age and metallicity, while the crosses are the reduced χ^2 of the stellar templates labeled by their spectral types and combined stellar template. The patterns in this figure are representative of those found for all the galaxies in the sample. There is a group of stellar templates that do significantly better than the others; in particular, the A2, F2 and M4 templates consistently yield poor fits in all the galaxies. For the SSP models, the χ^2 distributions are fairly flat as a function of age for a given metallicity, except for ages below $\sim$2 Gyr, where the quality of the fits quickly degrades. This behavior is expected since, at younger ages, the Ca II equivalent widths significantly decrease and the Paschen series become noticeable (see Vazdekis et al. 2003). At each age, the fits

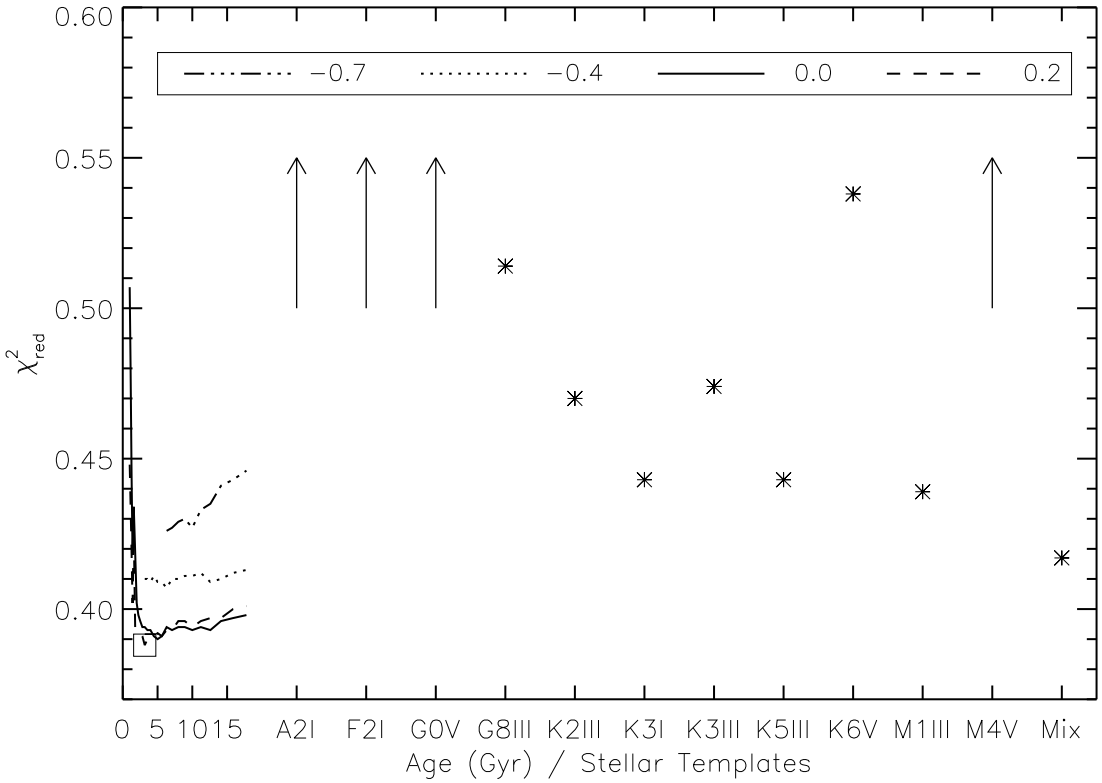

Figure 2.2: χ^2 distribution for NGC 5326. Open square indicates the minimum χ^2 for the best SSP fitting model, from which kinematics has been derived for this galaxy. χ^2 values for the stellar templates A2 Iab, F2 Ibe, G0 V and M4 Ve have been plotted with arrows indicating that they fall outside the plot limits. Their χ^2 values are: 2.197, 1.313, 0.613, 1.715 respectively.

are sensitive to metallicity.

For the spectrum used in figure 2.2, the best fit is obtained with a SSP model corresponding to [Fe/H]=+0.2 and 3.16 Gyr. It is worth noting that this SSP model should not necessarily be considered as the best fit to the stellar populations of this galaxy (see below). For the entire sample, the χ^2 for the best SSP model, best stellar template and mix-template are quite similar, and for 16 of the 19 objects the SSP templates provide marginally better fits. This result demonstrates that synthetic SSP spectra, convolved to the resolution of the data, can provide accurate templates for kinematic analysis of galaxy spectra. The high quality of the SSP fits is most-likely due to their ability to minimize the template mismatch problem. While the stellar populations of bulges are likely to contain a mixture of ages and a range of metallicities, the SSP models provide a better approximation to galaxy spectra than a single stellar spectrum. Our results indicate that late

KIII stars and early M stars provide a better approximation to the integrated light of bulges than A, F, and G stars in agreement with Vazdekis et al. (2003). Table 2.1, col. 13, lists the overall best template for each galaxy. Note that, for three galaxies (NGC 5389, NGC 5719, NGC 5746), the M1III and K3I stellar templates provide the overall best fit to the galaxy spectra.

In figure 2.3 we plot the central spectrum of NGC 5326 and the best-fitting stellar (M1 III), mix and SSP templates, convolved with their respective kinematic solutions. The SSP model represents a very good fit for the whole sample of galaxies spectrum. Fitted output parameters for the best template stars (G8III, K2III, K3I, K3III, K5III, K6V, M1III), mix-template and best SSP model are shown in Fig. 2.4 for the entire profile of NGC 5326. In figure 2.5 we show the central velocity dispersion for NGC 5326 as a function of the different templates. As expected the templates with highest χ^2 result in unrealistic velocity dispersions values. The results from the best templates show an excellent agreement. Therefore we adopt the solution from our best SSP template for each galaxy to obtain kinematic profiles.

A point to remark is that no inferences on the stellar population age and metallicity of the galaxies are presented here from the best-fitting SSP models. The reason is that an important relation has been shown to exist between the continuum shape and the stellar populations in this spectral region (Vazdekis et al. 2003; Cenarro et al. 2003). Since we remove this continuum, as required by FOURFIT, we neglect its valuable information for constraining galaxy stellar populations. Therefore the most useful information left in our spectra is the equivalent width of the Ca II feature, which does not vary much for SSPs of the age and metallicity regimes considered here. The wavelength region that we have used to derive the kinematics excludes the strong TiO molecular bands seen in this spectral range. Therefore we are left with an almost featureless continuum shape which is straightforward to subtract. A different methodology is required to be able to analyze their stellar populations on the basis of the SSP models. Methods for extracting useful information from the full SSP spectra are discussed in Vazdekis (1999) and Vazdekis & Arimoto (1999). The stellar population analysis of this galaxy sample will be presented elsewhere.

The use of SSP models has a potential to minimize the template mismatch problem that have traditionally affected galaxy kinematic measurements. Whereas the KIII stellar templates have been shown to provide reasonably good fits to

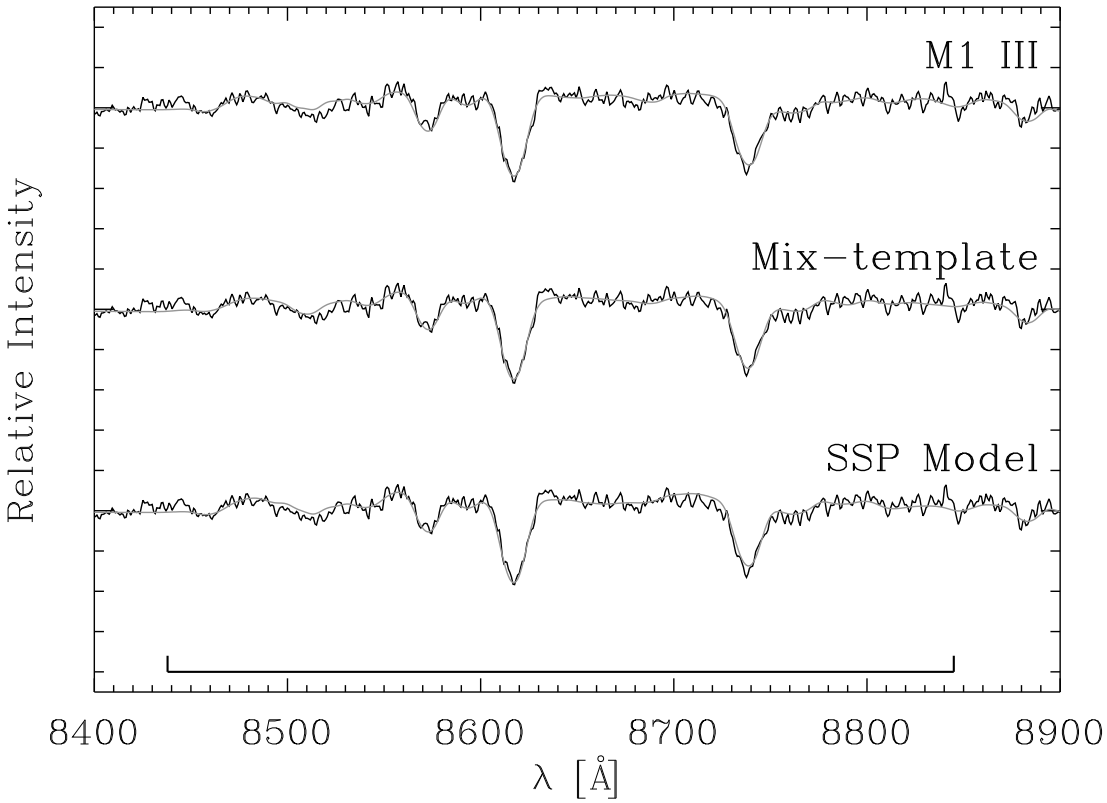

Figure 2.3: Comparison between our best stellar template, mix-template, and best SSP model fits, for the continuum subtracted and low-order filtered, binned central spectrum of NGC 5326. The fitting region has been indicated with a line at the bottom of the figure. In this case the best fitting template is the SSP model.

elliptical galaxy spectra in the optical region, one expects that the SSP models should significantly improve the kinematical fits. The blue and visible have been proven to have large sensitivities to the age, metallicity and abundance ratios (Rose et al. 1994; Worthey et al. 1994; Vazdekis et al. 1996; Vazdekis 1999). Our results suggest that the requirement of observing stellar template with the same instrumental setting as the galaxies is not compelling. The use of SSP models as templates allows us to use all of the available observing time for the targets, without the need to take spectra of template stars. An important application of SSP models should be in the field of high-redshift galaxy kinematics, where the measurement of the same spectral range in stars and target galaxies would require changing the instrumental setup, and where the redshift of the target objects is not generally known a priori.

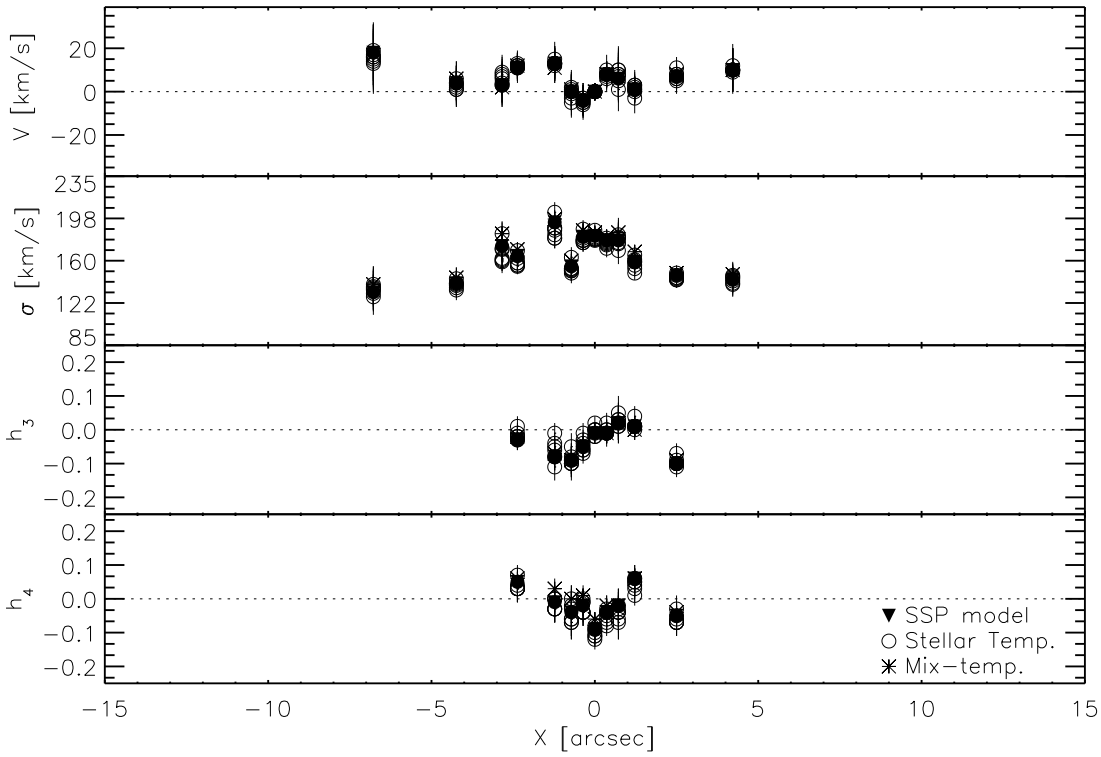

Figure 2.4: Comparison of the profiles obtained with our best stellar templates (G8III, K2III, K3I, K3III, K5III, K6V, M1III), mix-template and best SSP model fit of NGC 5326.

The main limitation of the use of SSP models is that it relies on a well designed stellar library to produce the full stellar population synthesis. However, the method is expandable to include combinations of SSP models to account for composite populations. Potential applications are the study of age differences between bulge and disk, or population signatures of kinematically-decoupled cores.

2.3.5 Errors & Simulations

Although FOURFIT gives the formal errors of the fit, we have performed simulations to establish the level of confidence the code can produce on (V, σ, h_3 and h_4) at S/N=33 pix^{-1}, and (V, σ) at S/N=20 pix^{-1}.

For the simulations, we convolved an SSP model ([Fe/H]= 0.0, t= 5.01 Gyr) with a wide range of LOSVDs to generate model galaxy spectra. The LOSVDs included several velocities, velocity dispersions, h_3 and h_4 mapping a representative parameter space covered by our sample of galaxies (V $\in$ [800, 2000], σ $\in$

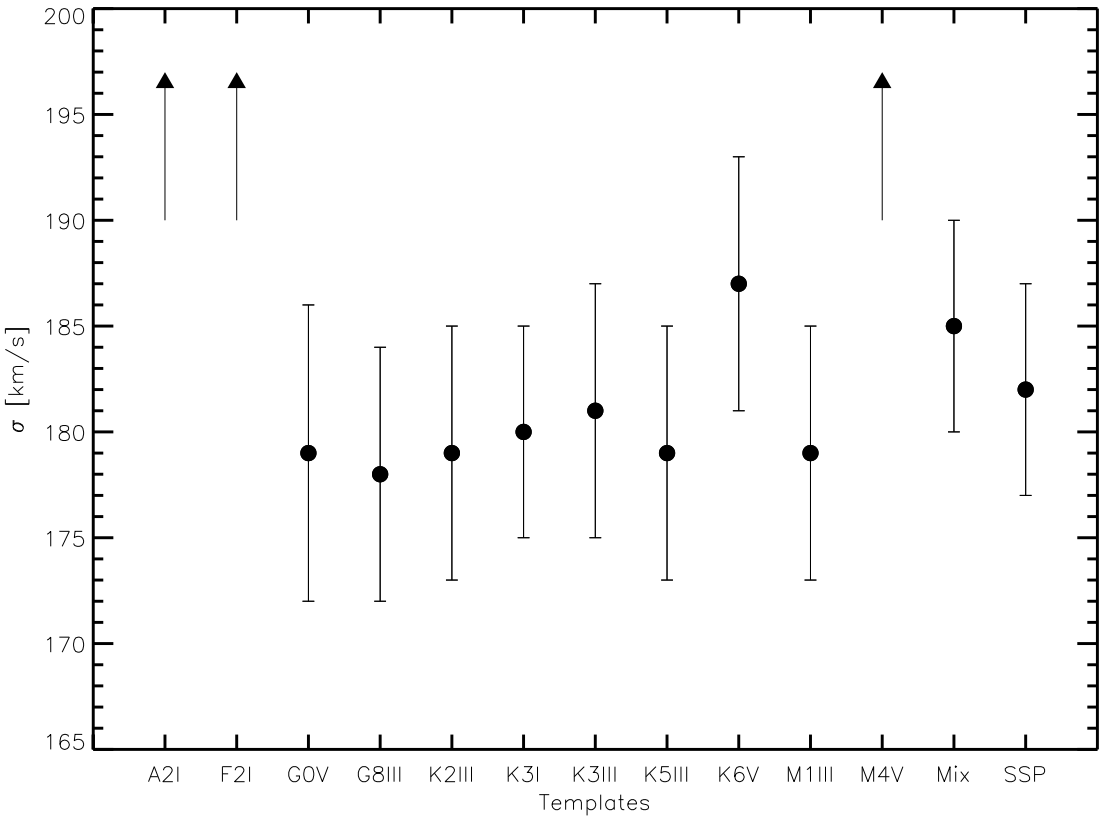

Figure 2.5: Comparison of the central velocity dispersion values for NGC 5326, obtained with the different templates (stellar templates, mix-template and best SSP model). Velocity dispersions for the stellar templates A2 Iab, F2 Ibe, and M4 Ve have been plotted with arrows indicating that they fall outside the plot limits.

[50,300], h_3 and $h_4 \in$ [-0.1,0.1]). The inclusion of higher velocities (up to 4000 km/s, to match our furthest galaxy) doesn't affect our results. White noise was added to our model galaxy spectra to yield S/N ratios of 20 and 33 pix^{-1}. Given the fact that all SSP models give very similar χ^2 values, only a representative subsample of 17 SSP models ([Fe/H]=-0.7,-0.4,0.0,0.2; Age=2,5.01,7.98, 10.00, 15.85 Gyr) were used to perform these simulations. We have simulated both Gaussian and non-Gaussian LOSVDs, however we only fitted pure gaussians to the spectra of S/N=20 pix^{-1}, for which we only modeled the V and σ errors due to LOSVD mismatching in the S/N=20 spectra. We have used for this purpose the SSP models.

The results of the simulations show two effects worth mentioning. First there is a systematic underestimate of the velocity dispersion for input velocity dispersions

Table 2.3: Errors from simulations

Param.	V [km s^{-1}]		σ [km s^{-1}]		h_3		h_4	
S/N	20	33	20	33	20	33	20	33
std	9	7	14	10	–	0.07	–	0.08

Notes: Standard deviations for each parameter at the different signal-to-noise ratios measured from the simulations.

below the instrumental resolution (typically $\Delta(\sigma) = -10$ km/s at $\sigma = 50$ km/s). This effect may bias our velocity dispersion curves for our two smallest bulges only, see Figure 2.8. Second, as we move towards larger velocity dispersions, the uncertainty in σ also increases (from 5 km/s at σ=50 km/s, to 8 km/s between σ=100-200 km/s and 12 km/s between σ=250-300 km/s), while the relative error in σ decreases. Hence, although the Gauss-Hermite expansion conforms a description of the LOSVD with a set of orthogonal functions and therefore we only expect major coupling between γ (the peak of the LOSVD) and σ (Larsen et al. 1983), V and h_3, and σ and h_4, we have detected other correlations when working at low signal-to-noise ratios. The expected coupling of V with h_3 and σ with h_4 appears in our simulations. Similar results have been found by authors who have performed similar tests (van der Marel & Franx 1993; Hau, Carter & Balcells 1999). In Table 2.3 we give the standard deviations of the distributions (parameter$_{out}$ - parameter$_{in}$), obtained from the simulations, for the full set of parameters. This is a measurement of the uncertainty when working at the mentioned S/N ratios. These uncertainties are also displayed as error bars on the right-hand side of each kinematic profile, see appendix C.

We have decided to impose a S/N=33 as the minimum level to determine h_3 and h_4. This is a slightly lower level than that suggested by the van der Marel (S/N$\simeq$40 pix^{-1}) to give a good estimation of the Gauss-Hermite higher order moments. Nevertheless in most cases we obtain S/N$\geq$40 for the profile central position (see Table 2.1).

2.3.6 Measurement of the CaT* index

We have measured the recently defined Paschen-free CaT* index (Cenarro et al. 2001a, see Appendix B), that measures the strength of the Ca II lines corrected from the contamination by Paschen lines, from our flux calibrated spectra. We

have made use of the FORTRAN routine `indexfits` (part of the R$_{\rm E}$D$^{\rm uc}_{\rm m}$E package), kindly made available to us by Javier Cenarro. No velocity dispersion correction and zero-point offset have been performed. Errors in the CaT* index include contributions from radial velocity uncertainties and from S/N. The first one is obtained by the CaT* index from 100 random simulations within the velocity range $[V - \Delta V, V + \Delta V]$. The latter is determined using eq. A37 from Cenarro et al. (2001a). Both terms are added in quadrature. The uncertainty from the S/N dominates the CaT* error.

2.3.7 External comparisons

We have compared our best SSP model fits with those in the literature. Unfortunately, published minor axis kinematic profiles are scarce. We present the comparison in figure 2.6 and 2.7 for NGC 5854 and NGC 7332 respectively. An excellent agreement is found for the two galaxies, with no major systematic deviations, supporting our approach of using synthetic SSP models. This agreement is particularly good for the velocity dispersion of NGC 5854, where our results follow the same trend obtained by Vega Beltrán et al. (2001). The comparison for NGC 7332 reveals also good agreement with Fisher, Illingworth & Franx (1994) and Simien & Prugniel (1997).

2.4 Results

Kinematic profiles for the 19 galaxies in the sample are shown in appendix C. For each galaxy we show profiles of mean heliocentric velocity V, velocity dispersion (σ), h_3 and h_4 Gauss-Hermite coefficients, and Ca II triplet index CaT*, along the galaxy's minor axis. Abscissae are centred on the brightness peak of the long-slit spectrum, i.e. on the photometric centre of the galaxy since we don't expect large centring errors. Negative abscissae correspond to the minor axis that projects away from the disk (the "dust-free" side), whose position angle on the sky is given at the top next to the galaxy's name. Circles are measurements derived from $S/N > 33$ pix^{-1} spectra, and triangles are V, σ and CaT* derived from $20 < S/N < 33$ spectra. Error bars in each point are the formal error estimates coming from FOURFIT code. Measurement uncertainties derived from the simulations described in Sec. 2.3.5 are shown with vertical bars on the right

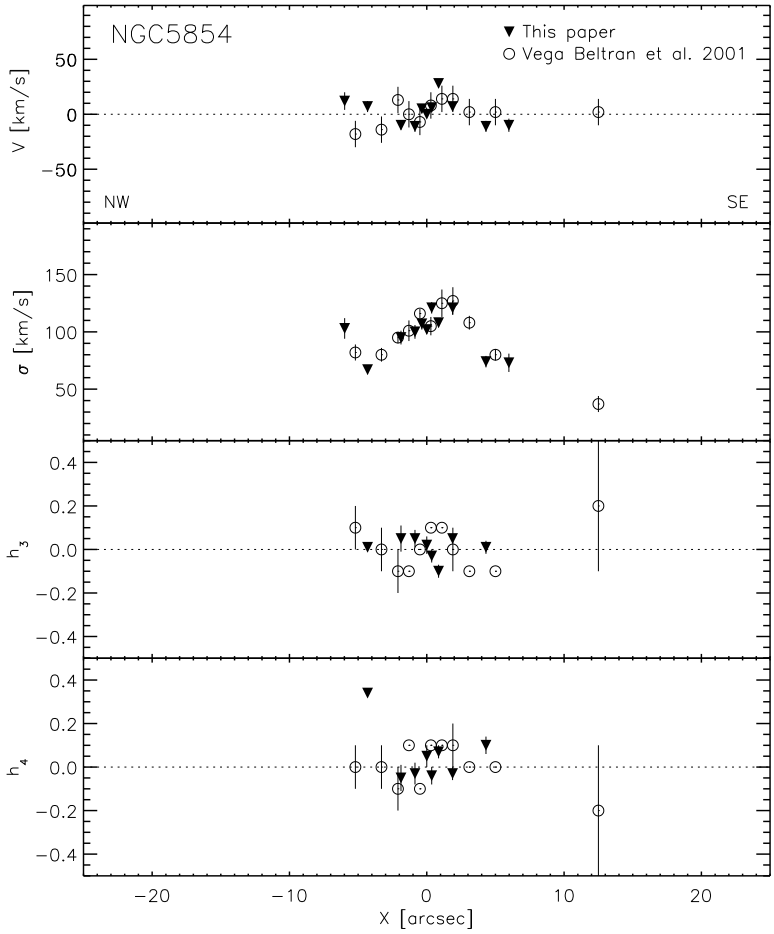

Figure 2.6: Comparison between our best SSP model fit and Vega Beltrán et al. (2001) for NGC 5854.

edge of each plot for the $S/N > 33$ spectra and, for V and σ, for $20 < S/N < 33$ as well (longest bar). The contour plot draws isophotes of the HST NICMOS F160W images (Peletier et al. 1999a), drawn to scale, with the area covered by the 1.2 arcsec slit indicated. The high spatial resolution of the NICMOS images (0.075 arcsec/pixel, PSF=0.18 arcsec FWHM) provides a clue on the level of substructure existing within the spectroscopic slit. Due to the lack of a NICMOS image for NGC 7332, a WFPC1 image, retrieved from the HST archive, has been used instead. Vertical dotted lines indicate the minor axis bulge radius and centre of the galaxy (see Table 2.1 for more details).

Owing to the short integration times and the S/N requirements for kinematic extractions derived from the simulations (Sec. 2.3.5), the kinematic profiles typically extend to 5-10 arcsec from the nucleus only. Only for the large galaxy

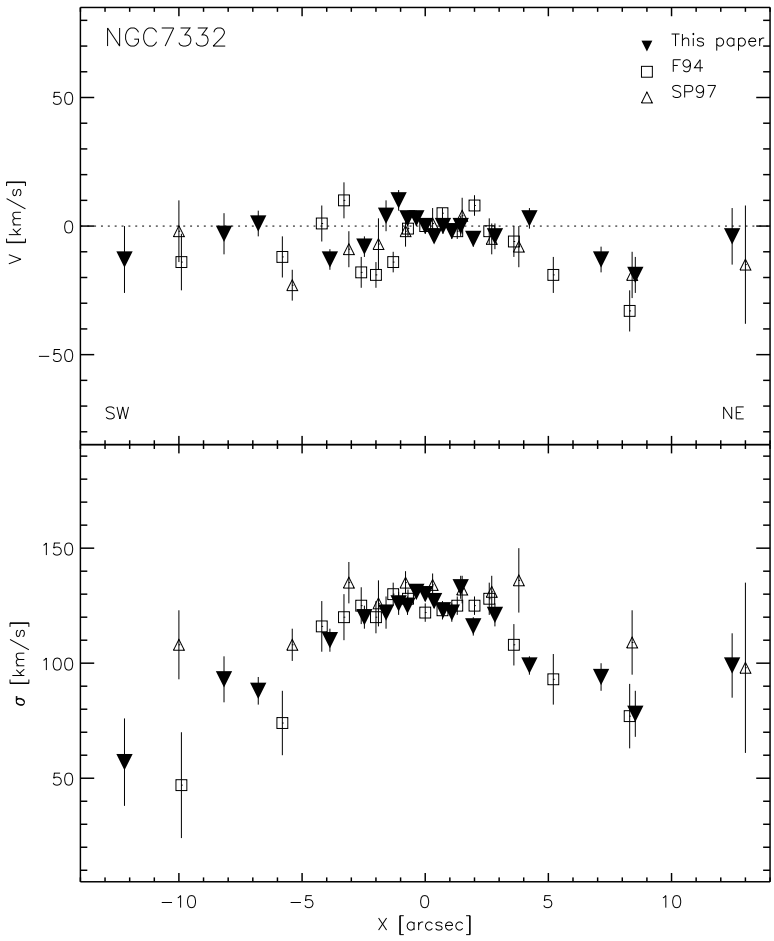

Figure 2.7: Comparison between our best SSP model fit with Fisher, Illingworth & Franx (1994) (F94) and Simien & Prugniel (1997) (SP97) for NGC 7332.

NGC 7331 do kinematic profiles extend over 20 arcsec on the dust-free side. All profiles are drawn to the same horizontal scale. In the following subsections we briefly address the global behavior of each kinematic parameter.

2.4.1 Velocity profiles

As expected for the minor-axis alignment of the slits, mean velocity profiles are fairly flat. However, the profiles are not entirely featureless. We note three types of features:

Rotation in the outer parts

We detect non-zero rotation in the outer parts of the profiles (opposite mean velocities at both sides of the centre, at the 2-σ level) in 6 out of the 19 galaxies (NGC 5389, 5689, 5746, 5838, 5854, 7457). Typical rotation amplitudes are in the range $10 < V < 20$ km s^{-1}. Such estimates of velocity amplitude and frequency of occurrence are highly dependent on the depth of the data. For two galaxies (NGC 5475, 5587) the profiles do not reach 5 arcsec and contain no information on rotation at large radii. Brighter galaxies in which the spectra extend farthest from the centre show the highest V at large radii. In most of these cases, the outer velocity measurements sample disk or bulge-disk transition regions. The non-zero velocities indicate that our spectroscopic slits were not perfectly aligned with the line of nodes. The slit was placed orthogonal to the major axis of the outer isophotes. Hence the misalignment might reflect an isophote twist in the outer parts sampled by the spectra, due e.g. to warps or spiral arms, or a distortion of the inner disk velocity field due to a bar or a spiral arm. Note that a misalignment of 5° or more could easily explain such amplitudes in velocity.

Inner rotation

We detect inner minor-axis rotation in 8 galaxies (NGC 5443, 5587, 5689, 5707, 5838, 5965, 6010, 7457) and possibly also in NGC 5389, 5422, 5854. Whenever the profiles extend beyond the nuclear region, inner rotation is delimited by a change in the velocity profile slope. These bulges thus contain kinematically distinct regions (hereafter KDR). We do not intend to set a link between these KDR and counterrotating or otherwise kinematically decoupled cores in ellipticals and bulges; full counterrotation cannot be established from our minor-axis kinematic profiles. Rather, we associate the velocity features to slight variations in the kinematic structure, related to inner components such as disks or bars.

Theoretically the simplest way to explain a minor-axis rotation in a bulge is to assume we are dealing with a triaxial object. In a triaxial object the position angle of the apparent minor axis can be different from that of the projected intrinsic short axis of the object (de Zeeuw & Franx 1991). Moreover, the photometric and kinematic minor axes may be misaligned as a result of the wide range of possible locations of the total angular momentum in a triaxial object (Binney 1985). In practice, whether minor-axis rotation traces a triaxial bulge can only

be checked using integral field spectrographs e.g. *SAURON* (Bacon et al. 2001), or measuring kinematics along different positions angles of the galaxy (Statler & Smecker-Hane 1999).

The typical minor-axis radial extent of the KDR is 2–3 arcsec, or 0.5 kpc at the median distance for the sample. In all of the eight galaxies listed above as KDR, isophotal analysis of the HST/NICMOS F160W images (our work, unpublished) reveals an inflection in the C_4 isophotal coefficient of the $\cos(4\theta)$ term that measures disky deviations of the isophotes from pure ellipses (e.g. Jørgensen, Franx & Kjærgaard 1992). C_4 amplitudes of the features are above 1% in all cases. This suggests the presence of flattened subcomponents in the inner regions of the bulges showing up as excesses in the bulge surface brightness profiles (Balcells et al. 2003). One probably sees a mixture of inner disks and inner bars. In four of the eight cases the isophotal analysis reveals changes in isophote position angle ($\Delta\mathrm{PA} \geq 10^\circ$) at the same radius, which are likely to correspond to inner bars but could also trace misaligned disks. The four remaining cases with no isophotal misalignment probably correspond to inner bars, as an aligned disk has its line of nodes parallel to the minor axis.

The most prominent nuclear KDR is that of NGC 5838. The nucleus of NGC 5838 harbors an ordered ring or disk of dust and young stars (Peletier et al. 1999a), which is oriented orthogonal to the slit. The dust may be responsible for the asymmetric rotation pattern.

It is worth noting that none of the KDR have distinct colors $B-I$ and $I-H$ (Peletier et al. 1999a) on the dust-free side of the galaxies, nor do they have corresponding features in the CaT* profiles (Appendix C). This may suggests that the velocity features are not associated to distinct stellar populations (e.g. Davies et al. 2001).

Kinematically offset nuclei

In two galaxies (NGC 5707, NGC 7331) the velocities at large radii appear offset in the same direction relative to the nuclear velocity. NGC 5707 has a nuclear disk or bar extending 1 arcsec, which is well aligned with the major axis of the outer disk and partially obscured by a dust lane; the dust might be responsible for the offset velocity measurement at the photometric centre of the galaxy. In NGC 7331, the entire region from -4 arcsec to +4 arcsec appears displaced 15-20 $\mathrm{km\,s^{-1}}$ from the

velocities further out. It is unclear whether dust extinction can be responsible for this structure, or whether the bulge might actually wander in the potential of the galaxy. The major-axis kinematics of this galaxy is complex (Prada et al. 1996), and its outer spiral structure is asymmetric; this could indicate a recent accretion event and/or the motion of the luminous material within the dark matter halo of the galaxy (Noordermeer, Sparke & Levine 2001).

2.4.2 Velocity dispersion profiles

Velocity dispersion profiles trace the dynamical temperature of the bulges and are key ingredients for dynamical modeling of the bulges. They also provide diagnostics for distinguishing between bulge and disk on the basis of the internal dynamics.

For our galaxies, the minor-axis velocity dispersion profiles show a wide diversity of shapes, from flat to strongly centrally peaked. Velocity dispersion gradients, ($\Delta\sigma$ per unit minor-axis r_e) were computed by fitting linear relations to the negative-abscissa dispersion profiles of figures in appendix C, which correspond to the dust-free side of the bulges. Minor-axis r_e were derived using the r_e values from Balcells et al. (2003), which derive from H-band surface brightness profiles from *HST*-NICMOS images, and ellipticities at the bulge effective radius $\epsilon_B(r_e)$ obtained from the ellipticity profiles in the same paper. Dispersion gradients range from 0 to -70 km/s/r_e, with a median of -21 km/s/r_e and a mode of only ~ -10 km/s/r_e.

Figure 2.8 displays all the velocity dispersion profiles, presented on two panels for clarity; the top/bottom panel shows the half sample with highest/lowest $\nabla(\sigma)$. In order to show whether the profiles sample only the bulge or extend to the disk region, we normalize each abscissa to r_{bulge}, the minor-axis radius where bulge and disk contribute equally to the surface brightness profile (listed in col. 12 of Table 2.1). Most profiles extend well beyond $r/r_{bulge} = 1$, indicating that the profiles reach to the region dominated by disk light according to the bulge-disk decomposition.

Three effects may influence the shape of the velocity dispersion profiles in our galaxies, (i) the intrinsic velocity structure of the bulge, (ii) the galaxy inclination, which determines which projection of the velocity ellipsoid is sampled by the data, and (iii) the brightness of the disk in the region sampled by the kinematic profiles.

Because most profiles reach the region where the surface brightness is dominated by the disk (Fig. 2.8), flat dispersion profiles imply similar dispersions for bulge and host disk. At the median inclination of the sample, $i = 73°$, minor-axis dispersion profiles preferentially sample the radial component of the velocity dispersion ellipsoid. Our flat profiles then indicate a surprisingly high *radial* velocity dispersions in the regions dominated by disk light, and an equally surprising continuity of the radial velocity dispersions into the region of the bulge. Steep dispersion profiles, in contrast, indicate distinct radial dispersions in the bulge and host disk, with dispersions increasing toward the centre as is expected in dynamically hot, self-gravitating ellipsoids.

The disk central surface brightness influences the velocity dispersion gradient. Figure 2.9a shows the distribution of $\nabla(\sigma)$ against the face-on disk central surface brightness μ_0. Bright disks have shallow dispersion profiles, while the steepest profiles are found in faint disks. We find it unlikely that this dependency arises from biases in the derivation of the kinematic profiles. Our simulations (Sec. 2.3.5) show that dispersions as low as $\sigma \sim 50$ km/s are well reproduced by the FOURFIT algorithm. Selection biases would hamper the detection of disk dispersions for faint disks first, but dispersion gradients of all values are found for these disks. The lack of steep dispersion profiles in bright disks appears therefore real.

Figure 2.9b shows the distribution of $\nabla(\sigma)$ against $\epsilon_B(r_e)$, the ellipticity measured at the bulge effective radius. A trend is found, in the sense that more flattened bulges show shallower dispersion profiles. This dependence does not arise from viewing-angle effects: Fig. 2.9c shows that $\nabla(\sigma)$ does not depend on the galaxy inclination. Shallow-profile objects may be kinematically described as thickened disks. In low-ellipticity bulges, the σ profiles increase toward the centre, again as expected from hot ellipsoids.

Kormendy (1993) discusses that some bulges share strong similarities with disks, on the basis of their low velocity dispersions, high $V_{\max}/\sigma_0$ for their ellipticity, and nuclear spiral structure. The disky nature of bulges is usually discussed in relation to late-type, low-mass bulges (Kormendy 1993). Our dispersion profiles indicate that this situation affects also early-types, including several S0's.

It appears that the disky nature of bulges cannot be established on the basis of spheroid luminosity; our velocity dispersion gradients do not correlate with bulge luminosity or with central velocity dispersion. Gradients do not correlate either

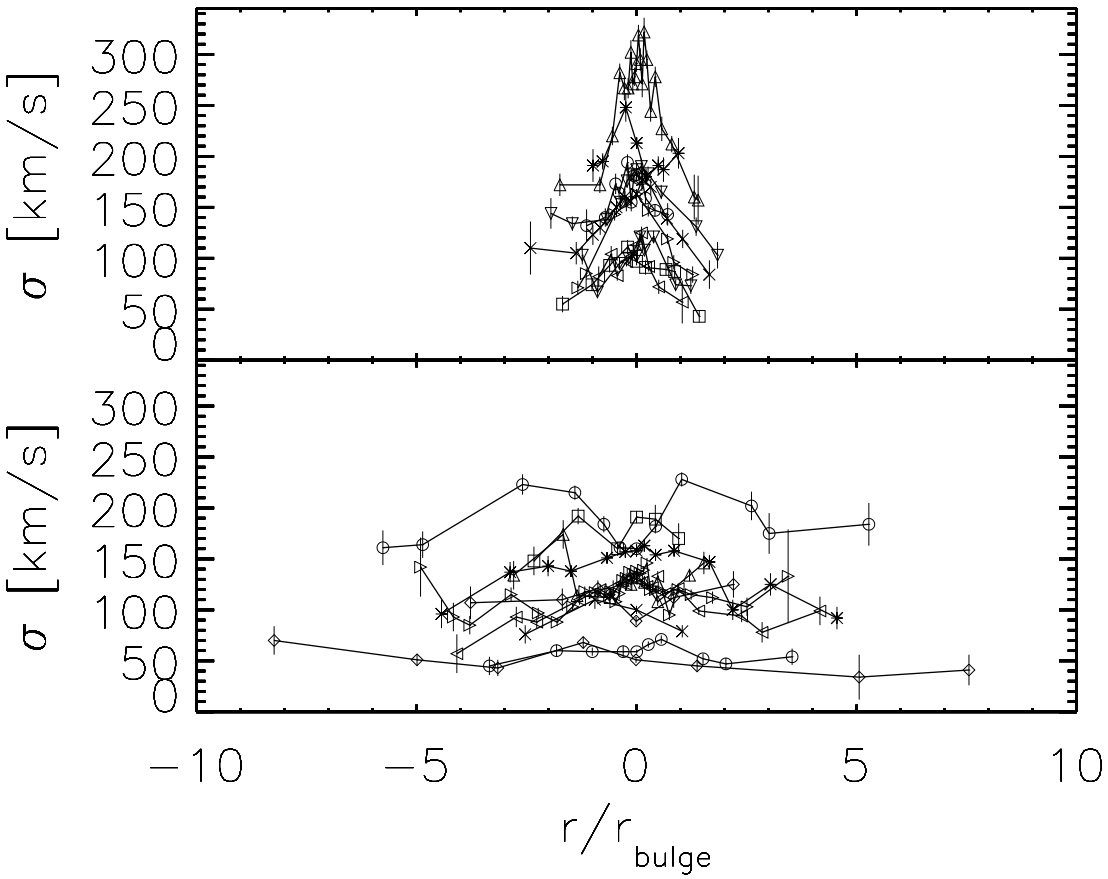

Figure 2.8: Velocity dispersion profiles for our sample of galaxies. Bulges with centrally-peaked velocity dispersions profiles are drawn in the top panel, whereas bulges with flat velocity dispersion profiles are plotted in the bottom panel. In the abscissa, radii have been normalized to the minor axis bulge radius (Table 2.1, col. 12), defined as the radius along the minor axis where bulge and disk have equal surface brightness.

with morphological type index, bulge Sérsic index n, bulge and disk scale lengths and bulge effective surface brightness. We have searched for a dependency on the presence of bars or box-peanut shaped bulge isophotes. Such galaxies are depicted with triangles in Figure 2.9. While bar detection is difficult at the inclinations of our sample galaxies, it is apparent that barred and box-peanut bulges do not occupy preferred regions in Figure 2.9.

The massive bulge of NGC 5746 (Sb) is the only object showing a strongly-defined central velocity dispersion minimum. A weak central minimum is also found in NGC 5443. Central velocity dispersion minima are generally understood as tracing embedded disks, bars, or low-mass spheroids. Therefore, given the

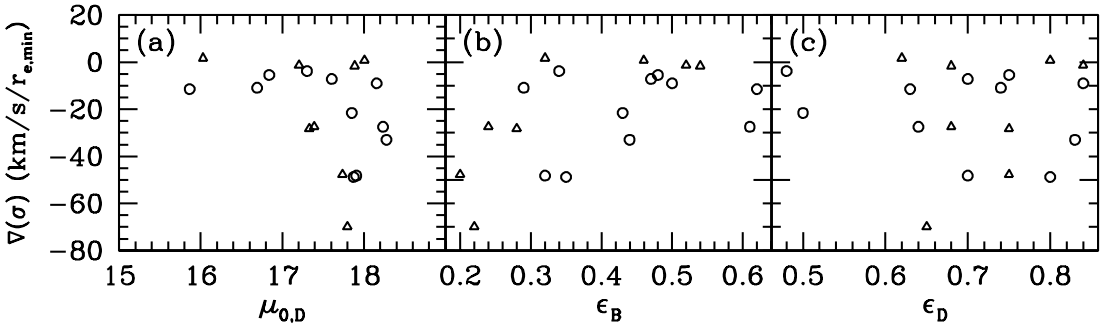

Figure 2.9: Dependency of the velocity dispersion gradient on galaxy parameters. (a) $\nabla\sigma$ against face-on H-band disk central surface brightness $\mu_{0,D}$. (b) $\nabla\sigma$ against bulge ellipticity ϵ_B. (c) $\nabla\sigma$ against disk ellipticity ϵ_D. Barred or box-peanut shaped galaxies in our sample are represented with open triangles.

abundance of isophotal substructure in the nuclei of these galaxies, it is surprising that central velocity dispersion minima are so infrequent among our objects. As mentioned above, our sample includes six box- or peanut-shaped bulges. For these objects, the bar producing the peanut may not reach the centre; or, alternatively, the central dispersion may be affected by the presence of secondary *nuclear* stellar bars/disks, with dispersion minima in bars being found for given viewing angles only. In NGC 5746 the local central minimum may be due to the main bar reaching all the way to the inner arcsecond, or to the presence of a secondary bar or nuclear disk.

2.4.3 High-order Gauss-Hermite terms

Profiles of the h_3 skewness term of the LOSVD are consistent with zero in most cases. In the few cases with significant non-zero h_3 (NGC 5475, 6010, 7331), h_3 does not have an opposite sign to the mean velocity that is typical of major axis profiles. This is reasonable as any rotation detected in the spectra is due to slight slit misalignment respect to the minor axis.

Similarly, the kurtosis profiles h_4 are generally flat and close to zero. In 12 galaxies however, h_4 is significantly positive above 0.1 somewhere in the profile, denoting centrally-peaked LOSVDs.

2.5 Conclusions

We have extracted minor-axis kinematic profiles from spectra in the Ca II near-IR region for a well-studied sample of early - to intermediate-type, inclined galaxies from the Balcells & Peletier (1994) sample. SSP models from Vazdekis et al. (2003) at 1.5 Å resolution have been used in addition to the traditional template stars. We have compared results obtained with the different templates and determined that synthetic models produce slightly better results than those from stellar templates, in the Ca II triplet region. We discuss the advantages/disadvantages of using SSP models instead of stellar templates. Our main conclusion is that synthetic models, when coming from a well constructed stellar library, help to reduce several drawbacks such as the template mismatch problem affecting all the traditional kinematical methods. We find a good agreement with high-quality kinematic profiles from the literature. SSP model spectra used as templates have clear applications for kinematic studies of galaxies at high redshift.

We find minor axis rotation in almost half of our galaxy sample. We discuss two types of minor axis rotation: rotation in the outer parts, probably due to slit misalignments, and inner rotation, which are associated to disky deviations of the isophotes from pure ellipses. We also find some cases of kinematically offset nuclei (NGC 5707 and NGC 7331) for which we do not find a clear explanation. We show that flattened bulges tend to show shallow velocity dispersion gradients and similar dispersions in bulge and inner disk, possibly indicating a thickened disk structure for these bulges. Finally, we find that our velocity dispersion gradients correlate with disk central surface brightness and with bulge ellipticity, but do not correlate with disk ellipticity. Gradients do not correlate either with bulge luminosity, bulge central velocity dispersion, bulge Sérsic index n, bulge effective surface brightness, galaxy morphological type, and disk or bulge effective radii.

Chapter 3

Bulges on the Fundamental Plane of Early-Type Galaxies*

* Falcón-Barroso, J., Peletier, R. F., Balcells, M., published in *Monthly Notices of the Royal Astronomical Society*

3.1 Introduction

It has been known for almost 15 years that early-type galaxies obey a tight relation linking their structure with their kinematics. Originally discovered by Djorgovski & Davis (1987) and Dressler et al. (1987), the Fundamental Plane (FP) establishes that the effective radius (r_e), the mean effective surface brightness (Σ_e) and the central velocity dispersion (σ_0) are related by

$$r_e = C \cdot \sigma_0^A \cdot \Sigma_e^B$$

The FP is one of the main scaling relations for early-type galaxies (e.g. Pahre, Djorgovski & de Carvalho 1998, hereafter P98). The fact that, compared to other relations, its scatter is so small, has made it a useful distance indicator (Jørgensen, Franx & Kjærgaard 1996, hereafter J96). Historically, the FP is a refinement of the Faber & Jackson (1976), relation between galaxy luminosity and σ_0, which includes the dependency of luminosity and σ_0 on surface brightness (Kormendy 1985).

Much work has been devoted to determining the exponents A and B. The virial theorem predicts $A = 2$ and $B = -1$. However, observations show lower values of A and higher values of B (Busarello et al. 1997). The value B has been well determined to be ~ -0.8 (P98, J96). A, usually referred to as the 'tilt' of the FP (P98), has values that vary significantly depending on the band employed. Several mechanisms are likely to produce the difference between observations and the Virial Theorem prediction: age and metallicity, shape of the light profiles (Caon, Capaccioli & D'Onofrio 1993; Graham & Colless 1997; Prugniel & Simien 1994, 1997) variations in the initial mass function (IMF) or even the dark matter distribution in galaxies (Guzman, Lucey & Bower 1993; Courteau, de Jong & Broeils 1996).

Beyond its value as a distance indicator, the FP contains useful clues on the physics of galactic systems. The position of galactic bulges on the FP of elliptical galaxies provides information about the differences in stellar populations, internal structure and kinematics of both types of galaxies. In a series of papers, Prugniel & Simien (1994, 1996, 1997) have gone into the details of using the FP for this purpose. Assuming that the FP is a representation of the Virial Theorem $\sigma_0^2 \propto \frac{M}{r_e}$, and that the mass-to-light ratio scales as $\frac{M}{L} \propto L^\beta$, these authors obtain

the relation between observables $\sigma_0^2 \propto \frac{1}{r_e} L^{1+\beta}$. In their picture, this relation is tight for old elliptical galaxies, since for them σ_0 is a good mass-indicator, and $\frac{M}{L}$ is a smooth function of L, probably metallicity-driven. Deviations to the relation can be due to the presence of young stellar populations (causing a change in $\frac{M}{L}$, see also Schweizer & Seitzer 1992a), rotational support (since in this case σ_0 gives an underestimate of the gravitational energy), or differences in structure, for example indicated by the shape of the surface brightness profile.

One of the first papers addressing the position of bulges on the FP is the study of Bender, Burstein & Faber (1992), (hereafter B92). They present B-band FP properties for a large sample of dynamically hot galaxies, which they divide into several groups, referred to as Es, intermediate Es, compact Es, bulges, bright dwarf ellipticals and dwarf spheroidals. B92 conclude that bulges lie preferentially below the FP of ellipticals, suggesting that, on average, bulges are younger than ellipticals. Most (17 out of 19) of the bulges in B92 are in lenticular galaxies. In a related study using a sample of galaxies from the Coma cluster Saglia, Bender & Dressler (1993) find a small shift in the same direction in the location of bulges when compared with Es and S0s (0.1 in $\log(r_e)$ in B-band). In contrast with these findings, J96, in their comparison between the FP of 10 clusters, find a negligible difference between E and S0 galaxies ($\Delta(E-S0) = 0.010 \pm 0.015$ in B-band), a result shared by Prugniel & Simien (1996).

The FP of bulges is more complicated to study than that of elliptical galaxies, since a determination of structural parameters requires a decomposition of the light into bulges and disks, as well as to take into account dust reddening and extinction. These problems only worsen as we move to later types. Perhaps as a result of this, very little information is available about the FP of bulges of types later than S0. This chapter intends to fill this gap by presenting a study of the FP of bulges for types ranging from S0 to Sbc. It belongs to a series of papers discussing the properties of galactic bulges. The first paper (Balcells & Peletier 1994) discusses optical colours and colour gradients of an optically selected, complete, sample of $\sim$ 50 bulges of type S0-Sbc. The galaxies were required to have an inclination i $>50^o$ to minimize the amount of disk light which projects onto the bulge and ensure that extinction from dust in the disk does not dominate the colours measured on one side of the bulge. Of this sample, 30 galaxies for which the colour profiles were smooth on one side of the bulge (i.e. where the colours were not significantly affected by dust extinction) were observed

in the near-infrared K-band at higher spatial resolution. Andredakis, Peletier & Balcells (1995) (hereafter APB95) present a photometric decomposition into bulge and disk, using Kent's 1986 model-independent method, after which Sersic (Sersic 1968) $r^{1/n}$ laws are fitted to the bulge. They find that the Sersic law generally fits very well, and that there is a good correlation between n and morphological type, such that bulges of early-type spiral galaxies follow the $r^{1/4}$ law, while profiles of late type spirals are more nearly exponential. Optical and near-infrared colours of bulges are presented in Peletier & Balcells (1996). Photometric data for this sample, including colour profiles along major and minor axis and fits of ellipticity and position angle as a function of radius, are presented in Peletier & Balcells (1997) (hereafter PB97). Central color profiles, based on HST/WFPC2 and NICMOS imaging of a subsample of 20 of our galaxies, are analysed in Peletier et al. (1999a). The latter paper concludes that all bulges, except those of Sbc's, are old with an age spread of less than 2 Gyr. The present chapter makes use of our own spectroscopy of the sample to address the position of bulges on the FP of elliptical galaxies. A full report of the kinematic properties derived from the spectroscopy is given in chapter 2.

When analyzing bulges, several authors have made the assumption that bulges' surface brightness profiles are either $r^{1/4}$ or exponential (Courteau, de Jong & Broeils 1996), a dichotomy of shapes that would suggest a dichotomy of formation processes. Carollo (1999) also divides bulges into $r^{1/4}$ and exponential classes in her study of galaxy nuclei. In our work we define and characterize a bulge on the basis of its signature in the galaxy's ellipticity profile, rather than on the shape of the surface brightness profile. We thus avoid having to assign each bulge to a given profile class, and indeed we find a continuum of profile shapes, which we model with Sersic's law with free index n, rather than two separate classes. Because our sample includes objects ranging from exponential to $r^{1/4}$, our FP study should uncover any structural and population signatures that depend on the shape of the surface brightness profile.

Section §3.2 summarises the observations and data reduction as well as procedures to derive the different structural and kinematic parameters. In §3.3 we show the FP in the different bands and compare the results with other authors. The Mg_2 - σ relation is analysed in §3.4. Possible correlations between observables and the residuals of the FP are studied in §3.5.1. Throughout the chapter we use a Hubble Constant of H_0=50 $\mathrm{km\,s^{-1}Mpc^{-1}}$.

3.2 Observations & Data Reduction

3.2.1 Observations

We obtained long-slit spectra of our sample galaxies at the 4.2m William Herschel Telescope of the Observatorio del Roque de los Muchachos at La Palma between 11 and 13 July 1997. Nineteen galaxies were observed (see Table 1). All galaxies were observed between 3660 - 5560 Å and between 8360 - 9170 Å using the ISIS blue and red arms, respectively. The red arm was equipped with the Tektronix (1024×1024) TEK2 CCD (0.36" per 24 μm pixel) and the R600R grating, giving a spectral resolution (FWHM of arc lines) of 1.74 Å (60 km/s). The blue arm was equipped with the Loral (2048×2048) LOR2 CCD, (15 μm pixels, 0.22 "/pixel) and the R300B grating, giving a spectral resolution of 4.1 Å. We used the 6100 Å dichroic for simultaneous red and blue arm exposures. Typical exposure times per galaxy were 1500 sec in both wavelength ranges. The slit width was 1.2", matching the seeing at the time of the observations. Arc line exposures were taken before and after each target exposure. Tungsten continuum lamp exposures were taken with the red arm after each target exposure, for fringe calibration. Twilight sky exposures were taken every night for flat fielding. We took spectra of spectral templates of types A2 to M5, from the Lick list of stars (Worthey et al. 1994).

3.2.2 Spectroscopic Parameters

Spectral Data Reduction

The data reduction was carried out using the IRAF package. The general standard procedures were applied to the data (bias subtraction, flat fielding, fringe correction in the red arm data, sky subtraction, wavelength and flux calibration), as described in Sec. 2.2.3. Cosmic ray removal was performed using the $\mathrm{R_ED^{uc}_mE}$ package (Cardiel 1999).

Derivation of kinematic parameters

Kinematic parameters were derived from data in the region of the IR Ca II triplet (8498 Å, 8542 Å, 8662 Å) in the red arm spectra. We worked with coadded spectra covering the central 3 pixels of each long-slit galaxy spectrum, roughly 1.1

Table 3.1: The Data Set.

NGC	V_{LG} km/s	Scale kpc/arcsec	$r_{e,K}$ arcsec	$<\mu>_{e,K}$ mag arcsec^{-2}	$r_{e,B}$ arcsec	$<\mu>_{e,B}$ mag arcsec^{-2}	$\log(\sigma_0/\mathrm{km\ s^{-1}})$	S/N pix^{-1}	n	T	ϵ_{disc}	$Mg_{2,0}$ mag
(1)	(2)	(3)	(4)	(5)	(6)	(7)	(8)	(9)	(10)	(11)	(12)	(13)
5326	2576	0.25	1.87	13.88	2.40	18.14	2.216	84	2.19	1	0.55	0.291
							(0.016)		(0.45)			
5389	1990	0.19	3.23	14.94	3.98	19.19	2.056	62	3.07	0	0.75	0.275
							(0.023)		(0.24)			
5422	1929	0.19	3.63	14.78	4.44	18.97	2.205	69	3.07	-2	0.80	0.307
							(0.016)		(0.20)			
5443	2060	0.20	3.85	15.69	4.94	19.80	1.881	38	2.86	3	0.72	0.240
							(0.046)		(0.35)			
5475	1861	0.18	2.43	14.83	3.12	18.91	1.960	57	2.52	1	0.71	0.239
							(0.029)		(0.25)			
5587	2291	0.22	1.76	15.13	2.05	19.02	1.967	36	1.53	0	0.70	0.259
							(0.038)		(0.21)			
5689	2290	0.22	6.86	15.39	9.77	20.04	2.155	59	5.90	0	0.75	0.275
							(0.018)		(0.62)			
5707	2354	0.23	3.10	14.71	3.49	18.50	2.149	52	1.30	2	0.75	0.257
							(0.019)		(0.27)			
5719	1684	0.16	2.77	14.69	4.47	19.98	2.034	52	2.26	2	0.68	0.212
							(0.024)		(0.10)			
5746	1677	0.16	11.00	15.57	17.43	20.55	2.144	45	4.10	3	0.83	0.324
							(0.025)		(0.43)			

NOTES: Photometric errors in columns (5) and (7) are 0.05 and 0.08 mag respectively (PB97). For definition of $\log(\sigma_0)$ and $Mg_{2,0}$ see text. Table continues in next page.

Table 3.1: The Data Set.[continuation]

NGC	V_{LG} km/s	Scale kpc/arcsec	$r_{e,K}$ arcsec	$<\mu>_{e,K}$ mag arcsec^{-2}	$r_{e,B}$ arcsec	$<\mu>_{e,B}$ mag arcsec^{-2}	$\log(\sigma_0/\mathrm{km\ s^{-1}})$	S/N pix^{-1}	n	T	ϵ_{disc}	$Mg_{2,0}$ mag
(1)	(2)	(3)	(4)	(5)	(6)	(7)	(8)	(9)	(10)	(11)	(12)	(13)
5838	1337	0.13	6.66	14.56	8.05	18.83	2.407	86	4.04	-3	0.63	0.319
							(0.010)		(0.34)			
5854	1708	0.17	5.04	15.53	5.09	19.14	1.986	65	4.12	-1	0.70	0.191
							(0.027)		(0.47)			
5879	1065	0.10	1.90	15.68	2.99	20.11	1.761	42	2.21	4	0.70	0.190
							(0.060)		(0.31)			
5965	3603	0.35	6.26	15.77	8.50	20.12	2.210	46	3.29	3	0.83	0.230
							(0.021)		(0.26)			
6010	1923	0.19	2.10	13.76	2.71	17.85	2.157	68	2.21	0	0.77	0.297
							(0.018)		(0.34)			
6504	4680	0.46	3.86	15.21	4.21	19.35	2.266	53	2.59	2	0.80	0.347
							(0.014)		(0.36)			
7332	1550	0.15	2.99	12.97	3.66	16.91	2.051	102	4.48	-2	0.75	0.259
							(0.015)		(0.27)			
7457	1114	0.11	6.68	16.50	8.28	20.53	1.749	52	6.24	-3	0.48	0.191
							(0.046)		(1.44)			
7537	2717	0.26	1.28	15.69	1.52	19.62	1.619	23	0.89	4	0.66	0.155
							(0.094)		(0.19)			

NOTES: Photometric errors in columns (5) and (7) are 0.05 and 0.08 mag respectively (PB97). For definition of $\log(\sigma_0)$ and $Mg_{2,0}$ see text.

arcsec, which is a good match to the seeing conditions during the observations. Signal-to-noise ratios per pixel for these spectra are listed in Table 3.1. We made use of the program FOURFIT developed by van der Marel & Franx (1993), available from the first author's website. A Gaussian fit to the line-of-sight velocity distribution (LOSVD) was performed to obtain mean radial velocities and velocity dispersions. Star templates of spectral types G8III, K1IIIb, K3III and K5III, gave dispersions with rms differences around 5 km/s. We took the median value of the 4 determinations as the best estimate of the central velocity dispersions of our galaxies. Velocity dispersions results are given in column (8) of Table 3.1. Aperture corrections have been applied to the central velocity dispersions. We have converted a rectangular aperture (1.1 x 1.2 arcsec^2) to an 'equivalent circular aperture'. Then we have corrected those values to a standard aperture, in this case defined to be 1.7 arcsec at the distance of Coma (see Jørgensen, Franx & Kjærgaard 1995a for more details)

The velocity dispersion errors in Table 3.1 are uncertainty estimates derived from simulations using FOURFIT. Simulated galaxy spectra were made by broadening a K3III star with different LOSVD, using Gaussian as well as non-Gaussian profiles, and adding white noise to yield S/N of 25, 33, 50 and 100. These simulated spectra were analyzed with three star templates of types G8III, G9VI and K3III. For each S/N we define the dispersion error as the rms of all the velocity dispersions coming from all templates as well as all LOSVDs. The error estimate thus includes contributions from S/N, template mismatch and non-Gaussian LOSVD. A complete report of the simulations that we performed will be given in a forthcoming paper that presents the full LOSVDs of the galaxies.

Derivation of $Mg_{2,0}$

The blue arm data was used exclusively to measure the central Mg_2 index, here indicated with $Mg_{2,0}$. We have measured the aperture corrected $Mg_{2,0}$ index (see Jørgensen, Franx & Kjærgaard 1995b for more details) and converted it to the Lick system Worthey et al. (1994) following the procedure in Vazdekis et al. (1997).

Derivation of distances

Distances to the galaxies were derived from optical recession velocities given in RC3 (de Vaucouleurs et al. 1991), corrected to the centroid of the Local Group (Karachentsev & Makarov 1996), and assuming a uniform Hubble flow. Distance errors are therefore significant, due to the Virgocentric flow and the possible influence of the Great Atractor. We have taken 150 km/s as the error in the distance-equivalent radial velocity. We have taken this value from the work of Aaronson et al. (1982) who studied the influence of bulk motions on a sample of spiral galaxies at distances comparable to our sample.

3.2.3 Photometric Parameters

Derivation of structural parameters in the K-Band

The derivation of the structural parameters in K-band was done as follows. The K-band effective radii in arcsec were obtained from APB95. These r_e therefore were derived from Sersic fits to K-band bulge profiles after an ellipticity-based bulge-disk decomposition (see APB95 for details). The APB95 major-axis r_e values were scaled to the geometric mean radius $r_e = \sqrt{r_{e,minor} \cdot r_{e,major}}$ for direct comparison with other authors (B92, J96, P98) using ellipticity profiles from the K-band ellipse fits published in PB97.

Derivation of structural parameters in the B-Band

For the B-band FP, our goal is to minimize the effects of dust extinction on the photometry. An $r_{e,B}$ derived from a direct ellipse fit to the B-band image is likely to be affected by the copious dust present on one side of the galaxy, and also in the nuclear area (Peletier et al. 1999a). We opt therefore to derive the dust-corrected B-band effective radius $r_{e,B}$ from the effective radius in K and the colour gradient determined on the minor axis. The conversion was done in the following way:
We assume that our profile is of the form:

$$I(r) = I_e \cdot 10^{(-b_n \cdot ([r/r_e]^{1/n} - 1))} \tag{3.1}$$

with $b_n = 0.868 \cdot n - 0.142$ (Caon, Capaccioli & D'Onofrio 1993). Differentiating $B - K = -2.5 \cdot log[I_B(r)/I_K(r)] + cst$ with respect to log(r) gives:

$$\frac{\mathrm{d}(B-K)}{\mathrm{d}\ \log(r)} = \frac{r}{\log(e)} \cdot \frac{\mathrm{d}(B-K)}{\mathrm{d}r} \tag{3.2}$$

Working this expression out, we get the relation between the effective radii in the two bands as:

$$r_{e,B} = \left\{1 - \frac{\nabla(B-K)}{\delta(n)}\right\}^n \cdot r_{e,K} \tag{3.3}$$

where $\nabla(B-K) = \mathrm{d}(B-K)/\mathrm{d}\log(r)$ is the colour gradient taken from PB97 and $\delta(n) = (2.5 \cdot b_n)/(n \cdot log(e))$. The ratio $r_{e,B}/r_{e,K}$ does not depend much on the power law used and depends mainly on the value of the colour gradient. Values of $r_{e,B}$ used in this paper are derived from eqn. 3.3.

Once the major and minor axis effective radii in both bands are known, we can determine the value of $I_{e,B}$ from the K-band surface brightness at $\mathrm{r}_{e,major,B}$ and the $B-K$ colour at $r_{e,minor,B}$ on the dust-free minor axis. This is valid since $B-K$ colour gradients on the minor axis are small (PB97). To convert from $I_{e,B}$ to the mean surface brightness within an effective radius we have used the relation:

$$< I_e >= 10^{[0.030 \cdot (\log[n])^2 + 0.441 \cdot \log(n) + 1.079]} \cdot \frac{I_e}{2\pi} \tag{3.4}$$

for an $\mathrm{r}^{1/n}$ law (Caon, Capaccioli & D'Onofrio 1993).

3.2.4 Presentation of the Data

In Table 3.1 we present the data used in the analysis of the FP. In column (1) we give the New General Catalogue number (Dreyer 1988). Column (2) lists the recession velocity of each galaxy in km/s, corrected to the Local Group (Karachentsev & Makarov 1996), from optical heliocentric velocities given in the RC3. Column (3) corresponds to the scale in kpc/arcsec. Column (4) gives the K-band geometric effective radius $r_e = \sqrt{r_{e,minor} \cdot r_{e,major}}$ in arcsec. Column (5) gives the K-band central surface brightness in mag/arcsec^2 within r_e, also from APB95, the photometric errors were assumed to be 0.05 (PB97). Column (6)

gives the B-band effective radius, in arcsec, from eqn. 3.3. Column (7) is the B-band mean central surface brightness within r_e in mag/arcsec^2, the photometric errors were assumed to be 0.08 (PB97). Column (8) is the logarithm of the aperture corrected central velocity dispersion in km/s and its error (see Section 3.2.2). Column (9) is the S/N per pixel of the spectrum used to determine the central velocity dispersion. Column (10) shows the parameter n of the Sersic profile and its error from APB95. Column (11) is the morphological type from the RC3. Column (12) is the disk ellipticity of the galaxy as given by APB95. Finally we tabulate in column (13) the aperture corrected central $Mg_{2,0}$ index in the Lick System (Worthey et al. 1994), in magnitudes.

3.3 Bulges on the Fundamental Plane

We determine the FP by means of an orthogonal fit to the function,

$$\log(r_e) = \alpha \cdot \log(\sigma_0) + \beta \cdot < \mu >_e + \gamma \tag{3.5}$$

We minimise the sum of the absolute deviations of the points orthogonally to the relation, using the program GAUSSFIT (Jefferys, Fitzpatrick & McArthur 1987). We have chosen this method since it is relatively insensitive to the presence of outliers (J96, P98) and is more robust than minimizing the sum of the squares of the absolute deviations of the points.

Because of the reduced size of our bulges sample, we are not obtaining a FP solution for our objects alone. Rather, we perform fits to various combinations of our sample and other samples in the literature, namely those of J96 in the B-band, and that of P98 in the K band. In order to avoid errors due to distance uncertainties between clusters, we take only a subsample of the galaxies of J96 and P98: the Es and S0s in the Coma cluster. FP differences when including our objects provide then a measure of the deviation of our bulges with respect to the FP of ellipticals and lenticulars. We minimise any dependency on the fitting method by performing our own fits to the data published by B92, J96 and P98, rather than using their FP solutions.

The results of the fits for B and K band data are given in Table 3.2. We list each parameter, its error, the number of objects employed, the rms of the solution and the rms of our bulges in each fit. We have also included in the last column the

Table 3.2: The Fundamental Plane coefficients

Sample	Band	α	β	γ	N	rms	
						$\mathrm{rms_{Bulges}}$	σ_{obs}
B92	B	1.63	0.27	-8.84	103	0.185	
		(0.09)	(0.02)			0.168	
J96(Coma)	B	1.20	0.34	-9.08	28	0.061	
		(0.12)	(0.02)			0.150	0.061
Common	B	1.15	0.31	-8.37	46	0.098	
fit		(0.15)	(0.02)			0.136	0.060
P98(Coma)	K	1.38	0.32	-7.85	64	0.083	
		(0.20)	(0.03)			0.128	0.060
Common	K	1.30	0.30	-7.31	82	0.092	
fit		(0.15)	(0.01)			0.125	0.063

dispersion expected from observational errors; the latter is computed as described in Sec. 3.3.1. Uncertainties in the coefficients have been calculated by performing a bootstrap analysis with 1000 iterations.

For the B band, the fit corresponding to the B92 sample excludes the dwarf spheroidals. "Common Fit" denotes the fit to the 28 galaxies of the Coma cluster from J96 [hereafter J96(Coma)] and our sample. Our fitted parameters agree well with the ones given by J96 , with slightly higher uncertainties due to the smaller number of points used.

The Coma cluster data from P98 [hereafter P98(Coma)] have been used to study the FP in the K-band. We performed a new FP fit to all 64 galaxies in P98, instead of the 60 used by the authors, given the lack of information about which ones had been excluded by P98. Our P98(Coma) FP is identical to that given by P98, including the errors in the fit. The "Common fits" to the FP have the added value of extending the FP of galactic spheroids to low $\log(\mathrm{r}_e)$ objects.

3.3.1 Error Determination

The FP fits are shown in figures 3.1 and 3.2. As usual, the errors in $\log(r_e)$ and $< \mu >_e$ are highly anticorrelated, with a linear correlation coefficient r of about 0.97 (Jørgensen, Franx & Kjærgaard 1995a), which implies that the error in the combination that enters the Fundamental Plane $log(r_e) - \beta < \mu >_e$ are much

smaller than the individual errors in $\log(r_e)$ and $< \mu >_e$. For this reason those errors are not plotted. The error in the combination $log(r_e) - \beta < \mu >_e$ was derived from a comparison with other authors (A. Graham, private communication). This gives us a mean value of $\sigma_{\log(r_e)-\beta<\mu>_e}$=0.036. The same value has been applied for both bands. The observational error on the FP, including the uncertainties in $\log(\sigma)$ and distance is then

$$\sigma^2_{obs} = \sigma^2_{(\log(r_e)-\beta<\mu>_e)} + (\alpha\sigma_{\log(\sigma_0)})^2 + \sigma^2_D \tag{3.6}$$

and the intrinsic scatter can be determined as

$$\sigma_{int} = [\sigma^2_{fit} - \sigma^2_{obs}]^{1/2}. \tag{3.7}$$

Observational errors are listed in column 8 of Table 3.2.

An independent estimate of the measurement errors comes from comparing our data with the literature. Unfortunately we have no objects in common with P98(Coma) and J96(Coma), and only one object in common with B92: NGC 7332. For this object, while the σ's are very similar, we measure $\log(r_e/\mathrm{kpc}) = -0.26 \pm 0.042$ whereas B92 give $\log(r_e/\mathrm{kpc})$=0.010. For the surface brightness $< \mu >_{e,B}$ the values are 16.91 and 18.30 respectively. The difference in $log(r_e) - \beta < \mu >_e$ between these measurements, 0.70, is much larger than the measurement errors in either our or B92's data. Since the effective radius of the bulge of NGC 7332 is small, one might think that a difference in seeing might have caused the difference. However, our sample contains several smaller bulges, which are lying very close to the FP, indicating that differences in seeing will not move objects away from the FP.

We decided not to consider NGC 7332 in any of the common fits since it seems to be a very peculiar object and its observational errors are not big enough to explain such deviation from the different FP relations. It hasn't been included either in the studies of residuals of the FP with other parameters presented in following sections. This galaxy is addressed again in chapters 2, 4, 5.

3.3.2 The B-band Fundamental Plane

The distribution of galaxies in B-band FP space is shown in Fig. 3.1. Two projections are given. Fig. 3.1(a) shows the view orthogonal to the J96(Coma) FP solution. Fig. 3.1(b) shows the view orthogonal to the Common Fit FP

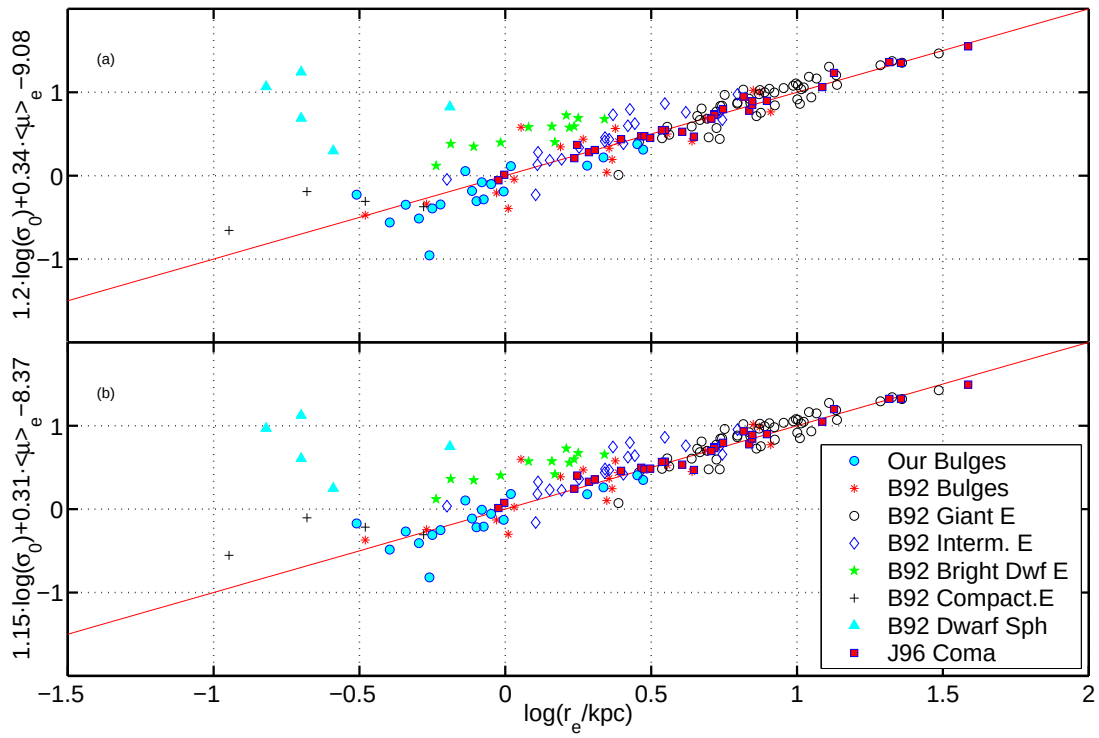

Figure 3.1: The B-Band FP. Velocity dispersions are in km/s, and surface brightness is in B mag/arcsec^2. We give two different fits to the FP. In Fig. 3.1(a) we have performed a fit to J96(Coma) galaxies and we have also plotted our bulges and B92 galaxies following J96(Coma) definition. Fig. 3.1(b) represents a common fit using all the points (J96(Coma) + our bulges - NGC7332).

(J96(Coma) plus this work minus NGC 7332). Substantial differences are found between the two distributions. Figure 3.1(a) shows that our bulges fall slightly below the relation defined by the Es and S0s of J96(Coma). Other classes of objects also show global displacements with respect to the FP, resulting in the apparent thickening of the galaxy distribution as we move on to smaller sizes. To analyse the behaviour of the different classes of galaxies we have computed the mean separation from the FP for each of the object groups, by measuring the mean deviation $\overline{x}$ along the $\log(r_e)$ direction ($x \equiv$ object $-$ FP), as well as the error in the mean ($\Delta\overline{x}$). Deviations from the FP are listed in Table 3.3 for each of the groups in Fig. 3.1, and for the two FP solutions (J96(Coma), and Common). Aperture corrections are essential to the determination of the offset. Earlier determinations by us of the FP offset of bulges, which did not

Table 3.3: Deviations from the B-band FP

Group	J96(Coma)		Common fit	
	$\overline{x}$	$\Delta\overline{x}$	$\overline{x}$	$\Delta\overline{x}$
Our Bulges	0.074	0.033	-0.008	0.032
B92 Bulges	0.015	0.049	-0.026	0.045
B92 Es	-0.049	0.018	-0.060	0.018
B92 DwfEs	-0.413	0.027	-0.406	0.026
B92 DwfSph	-1.423	0.217	-1.340	0.206
J96(Coma)	-0.003	0.012	-0.013	0.012

NOTES: $\overline{x}$ is the mean deviation in the $\log(r_e)$ direction ($x \equiv$ object $-$ FP). $\Delta\overline{x}$ is the error in the mean.

include aperture corrections for σ, yielded an insignificant offset of bulges wrt. J96(Coma) (Balcells 2002).

Table 3.3 shows that our bulges show a 2-sigma deviation with respect to the J96(Coma) FP. The lower r_e values for our bulge sample require a significant extrapolation of the J96(Coma) FP. The offset from the Common fit is insignificant, as expected since the bulge data are included in this fit. Interestingly, the bulges of B92 show insignificant deviations with respect to the J96(Coma), in apparent contradiction with B92's conclusion that bulges preferentially lie below the FP. We can trace the origin of this difference to the fact that the FP of B92, while very similar to the fits shown in this paper, is slightly above the J96(Coma) FP.

The decoupling of the bright dwarf ellipticals from the rest of galaxies (a 15σ result) is remarkable. This behaviour was noticed by B92 who referred to the degree of anisotropy as the trigger of the observed offset. The structural parameters of these objects are probably intermediate between larger ellipticals and dwarf spheroidals. The latter are known to be structurally different from ellipticals or bulges (Mateo 1998).

We have computed the intrinsic scatter of our sample around the Common fit, along the $\log(r_e)$ direction using equation 3.7. We find $\sigma_{int} = 0.122$, which is larger than what can be accounted for by observational errors (0.060) (see Table 3.2). This supports the idea of the existence of intrinsic scatter, not just for ellipticals, but also for bulges. We discuss clues on the origin of the intrinsic scatter in Sec. 3.5.

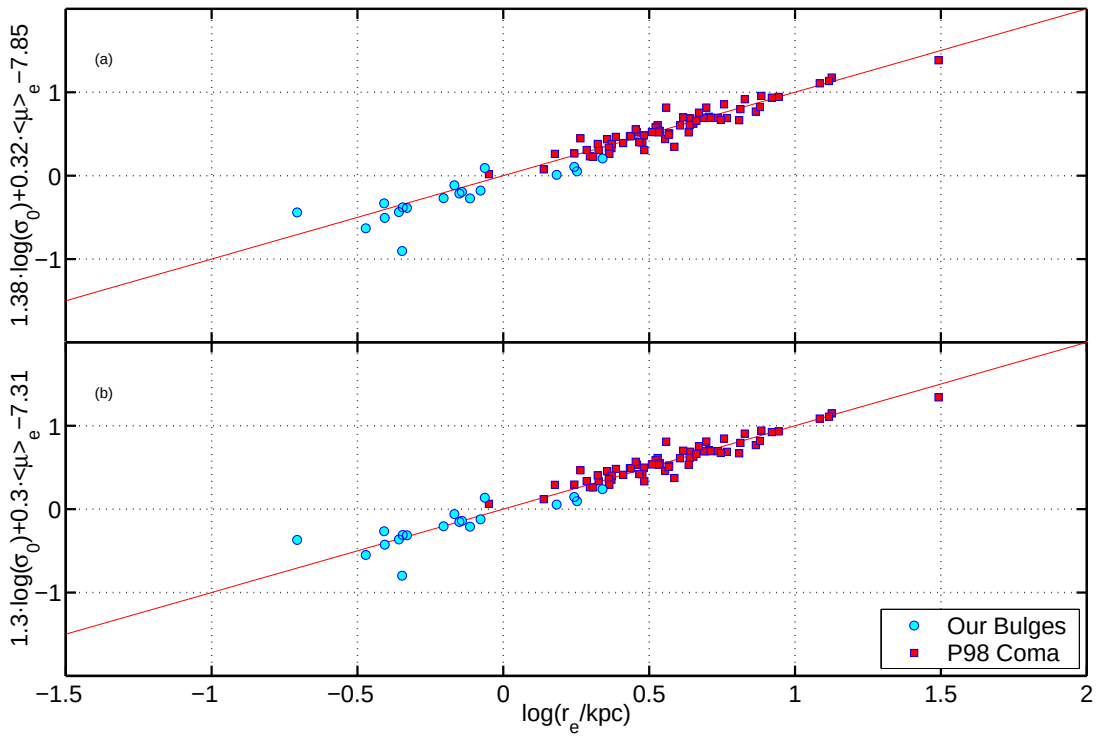

Figure 3.2: The K-Band FP. 2 different fits to the FP. In Fig. 3.2(a) we have performed a fit to P98(Coma) galaxies and we have also plotted our bulges. Fig. 3.2(b) represents a common fit using all the points (P98(Coma) + our bulges - NGC7332.).

3.3.3 The K-Band Fundamental Plane

We have obtained the position of bulges on the K-band FP following the same procedures used for the B-band FP. Our reference elliptical and S0 sample here is the Coma sample of P98 (P98(Coma)). The distribution of galaxies in FP space is shown in Fig. 3.2. As for the B-band FP, two projections are shown, one orthogonal to the P98(Coma) elliptical FP (Fig. 3.2a), and one orthogonal to the Common fit FP (P98(Coma) plus our bulges minus NGC 7332 (Fig. 3.2b).

Figure 3.2 shows that our bulges define a slightly displaced sequence with respect to the K-band FP of Coma ellipticals, extending the FP almost one decade in radius toward low-mass spheroids. The most deviant point is NGC 7332. Its offset with respect to the FP is unexplained by measurement errors.

The FP offsets of our bulges with respect to the P98(Coma) and the Common

Table 3.4: Deviations from the K-band FP

Group	P98(Coma)		Common fit	
	$\overline{x}$	$\Delta\overline{x}$	$\overline{x}$	$\Delta\overline{x}$
Our Bulges	0.054	0.029	-0.006	0.029
P98(Coma)	0.002	0.010	-0.007	0.010

NOTES: The mean separation ($\overline{x}$) has been determined by measuring the mean deviation $\overline{x}$ along the $\log(r_e)$ direction ($x \equiv$ object $-$ FP). $\Delta\overline{x}$ is the error in the mean.

FP's, computed as described in section 3.3.2, are given in Table 3.4. The deviations again are significant when using the P98(Coma) FP solution. These results highlight the displacement of bulges to cluster ellipticals in the K band.

Again, the scatter of our sample around the Common fit in the K-Band, along the $\log(r_e)$ direction turns out to be larger (0.125) than the dispersion of our bulges on the FP due to uncertainties in the observational parameters (0.063) (see section 3.3.1), implying that we find an intrinsic scatter in the K-band of 0.108. The fact that our intrinsic scatter in both bands is almost equal implies that for our sample stellar population differences are not responsible for most of the scatter, since this would lead to much larger scatter in B. We would like to remark that there is a strong paucity of FP data for low velocity dispersion galaxies ($\sigma < 100$ km/s), also ellipticals and S0s, and especially in the field, a likely consequence of the relatively recent arrival of large-format IR detectors. Measuring the intrinsic scatter of the FP in the K-band as well as better constraining any offsets of bulges with respect to the FP of ellipticals will require data for significantly larger samples.

In figure 3.3 we have plotted the residuals of the fundamental plane in the B-band against the residuals in the K-band for the J96(Coma) and P98(Coma) fits. Residuals are correlated, something which we expect from the way these quantities were calculated. The most extreme objects are NGC 7332 and NGC 5879. A third outlier is NGC 5719. If a deviation from the plane is caused by dust, the object in this diagram will lie on the left of the 1-to-1 diagonal line. Based on previous work, we don't think that dust extinction is affecting either of these 2 galaxies. The reason is the way that our fundamental plane parameters have been determined. Instead of measuring the effective radius and the surface brightness in B we used the values in K and corrected them using the $B-K$ colour at

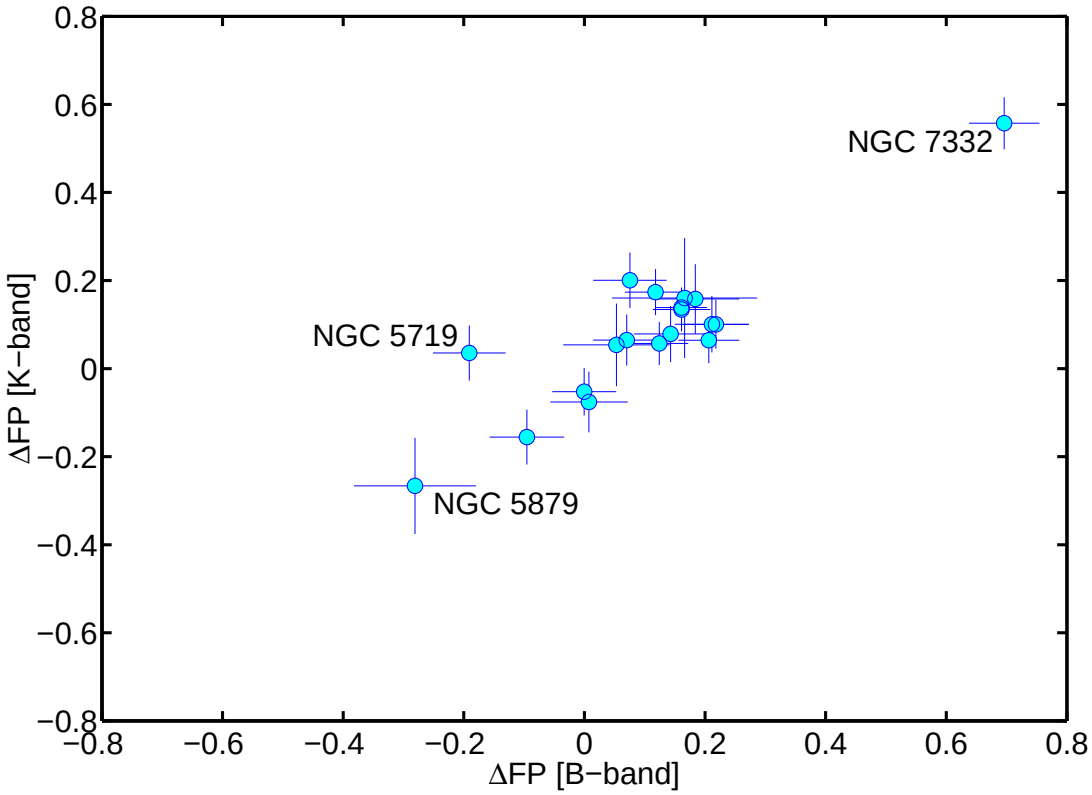

Figure 3.3: Residuals from the Fundamental Plane in B vs. those in K.

$r_{e,K}$ and a constant colour gradient (see section 3.2.3), determined in the region where we decided, based on the flatness of the colour profile, that extinction was not important. In PB97 this region was determined to be the region outside 3″ for NGC 5719 and outside 1.5″ in NGC 5879. This method should in principle work as long as $r_{e,K}$ would lie outside the dusty region. In fact, $r_{e,K} = 2.77''$ for NGC 5719 and 1.90″ for NGC 5879, both at the border of the dustfree regions, showing that the FP parameters for these 2 galaxies are barely affected. If the deviation is due to young stellar populations, the object would lie right of the 1-to-1 diagonal. The fact that there are no objects situated here shows that the sample does not contain object within significant amounts of young stars in the bulge. The fact that for NGC 7332 the deviations are so similar shows that the deviations might be related to the details of the stellar distribution, non-homology, or other factors. For NGC 5879, a small galaxy, the error in its velocity dispersion is so large that little can be concluded. (Section 3.2.2).

3.4 The $Mg_{2,0}$ - $\log(\sigma_0)$ Relation

It is well known that the absorption line index $Mg_{2,0}$ correlates strongly with velocity dispersion (Terlevich et al. 1981; Bender, Burstein & Faber 1993). This relation can be interpreted as a mass-metallicity dependence (e.g. Schweizer & Seitzer 1992a; Prugniel, Maubon & Simien 2001). Since, according to them, in early-type systems deviations are generally attributed to the presence of young stars, this relation can identify young stellar populations as producers of the scatter around the FP. We have determined this relation for our sample of bulges as well as for a number of samples in the literature (Fig. 3.4).

The thick solid line corresponds to a least squares fit to our points, while the thin solid line is a standard least squares fit to the bulges of B92 (solid squares). The dashed line is the fit given by J96 for Es and S0s. The coefficients of the fits are given in Table 3.5. We have also included the data of Prugniel, Maubon & Simien (2001, hereafter P01), a sample of 89 bulges, mostly of spiral i.e. non-S0 galaxies. These bulges can be split into 2 subsamples: open triangles are bulges with EW(OIII)$\geq$1, filled triangles are bulges with EW(OIII)$<$1. Finally we have also added the bulges from Jablonka, Martin & Arimoto (1996, hereafter JMA96) (asterisks).

We first try to explain the difference between the position of our bulges and the ellipticals and S0s of J96. In the picture that the $Mg_2 - \sigma$ relation describes the dependence of metal enrichment on the depth of the gravitational potential, the position of bulges above the relation of ellipticals may be taken as a horizontal offset to the left – σ_0^2 underestimating the binding energy by not including the rotation. The contribution of rotation to $\log(\sigma_0)$ may be estimated as $0.5\ \log(1 + 0.62V_0^2/\sigma_0^2)$ (Prugniel & Simien 1994). An offset of 0.014 in Mg_2 can be brought back onto the J96 relation by an offset of 0.071 in $\log(\sigma_0)$. A mean V/σ of 0.5 suffices to bring the points back on the Mg_2 - σ relation. We conclude that non-inclusion of the rotation alone could explain the offset of our bulges sample from the Mg-sigma relation of old ellipticals.

Fig. 3.4 also shows that there are significant differences between the various samples of bulges. To establish the nature of them we have compared the observables for objects in common with these authors (see Table 3.6). For Mg_2 the average differences are 0.010 (RMS=0.006) for B93, -0.013 (RMS=0.013) for T98 and -0.024 (RMS=0.006) for Golev et al. The first 2 are consistent with the

systematic error of the Lick system of 0.008 (see Table B.1 in appendix B). We conclude that the Mg_2 values of P01 might be underestimated, leading to an offset in Fig. 3.4. One should note that, although the data of Golev et al. (1999) and Prugniel & Simien (1997), used in Table 3.6, were calculated in the large Lick-aperture, the data of Fig. 3.4 have been corrected to the much smaller physical aperture of 0.4 kpc, so that the real difference between our sample and P01 in Fig. 3.4 is probably larger. Subtle differences in sample selection may contribute to the differences in $Mg_2 - \sigma$, despite the similar Hubble-type distributions and the ranges in σ in our and P01's bulges. Our sample selection did exclude very dusty bulges (Balcells & Peletier 1994; Peletier et al. 1999a). This might have biased our sample toward bulges without ongoing star formation. On the other hand, our sample is less affected by dust optical depth effects on Mg_2 and on σ, as well as from disk contamination, which probably affected the measurements of P01. Thus our sample allows more accurate measurements of stellar population diagnostics, but at the price of potentially excluding the youngest objects. We note nevertheless that our two Sbc bulges, at the low-σ end of the distribution, fall right on the relation of old ellipticals; these objects are moderately dusty. For $\log(\sigma)$ the average differences are 0.066 (RMS=0.013) for B92, 0.084 (RMS=0.074) for T98 and 0.070 (RMS=0.025) for Golev et al.. It appears that our velocity dispersions are consistently lower that the values in the literature. We think this might be due to the fact that our dispersions were calculated using minor axis spectra, while all others used major axis spectra. This means that in our case we did not suffer from possible rotation, which would tend to broaden the spectra. The shift of 0.07 in the $\log(\sigma)$ direction proposed above to bring the bulges onto the J96 relation would bring our datapoints toward those of P01, but a much larger shift would be required to explain the whole difference. The data of JMA96 fall in between us and P01, and could be considered consistent with us (given the uncertainties in the zero point of the Lick system and the above mentioned shift of 0.07 in the $\log(\sigma)$ direction).

Another important point to see from Fig. 3.4 is that the slope of all three bulge samples seems to be steeper than that of J96 for Es and S0s, although statistically they are equivalent within 1-σ. The traditional way to explain this is that low velocity dispersion galaxies contain a larger fraction of young stellar populations (P01). This can be confirmed if, e.g., the galaxies furthest away from the FP of ellipticals have the latest morphological type. For our sample the answer is

Table 3.5: The $Mg_{2,0}$ - $\log(\sigma_0)$ Relation

Group	a	Δa	b	Δb
J96	0.196	0.016	0.257	
B92 Bulges	0.247	0.045	0.258	0.008
Our Bulges	0.237	0.030	0.271	0.006
P01 (OIII$\geq$1)	0.447	0.060	0.183	0.007
P01 (OIII<1)	0.238	0.033	0.201	0.006

NOTES: Different fitting coefficients of the $Mg_{2,0}$ - $\log(\sigma_0)$ relation, defined as $Mg_{2,0}$=a $\cdot$ [$\log(\sigma_0)$ $-$ 2.1]+b

not clear. While the 2 galaxies with type 4 are situated the most below the FP, no trend is visible for the others. For the bulges of P01, the $Mg_{2,0}$ deficit with respect to ellipticals is very pronounced, especially so for galaxies with strong [OIII] emission, indicating significant amounts of ionised gas. If one assumes that ionised gas traces ongoing star formation one can understand their position in the $Mg_2 - \sigma$ relation as due to young stars diluting the Mg_2 index. For this reason P01 called the $Mg_{2,0} - \sigma$ relation a mass-metallicity relation for bright ellipticals, becoming gradually a mass-age relation as one goes to fainter objects. Under this view of the $Mg_2 - \sigma$ relation, figure 3.4 is interpreted as indicating that the young-star contents of our bulges is much lower than in the P01 sample, and comparable to that of S0's of B92. If indeed low Mg_2 values are due to dilution by a young stellar continuum, the $Mg_2 - \sigma$ distribution for our bulges argues against a mass-age relation for small objects.

3.5 Discussion

In the past bulges of spirals have been difficult galactic components to study. This has been due to the presence of dust, the accompanying disk, and the fact they are generally small, so that very often ground-based observations are affected by lack of resolution. The appearance of the Hubble Space Telescope in the 1990s has vastly improved the situation. Peletier et al. (1999a) performed a detailed study of galactic bulges using NICMOS observations, giving as a result a much more detailed insight of ages and dust in these objects than was known before. The main conclusions from this work are that early-type bulges (S0-Sb) behave like ellipticals and seem to be as old as cluster Es with very little spread in age

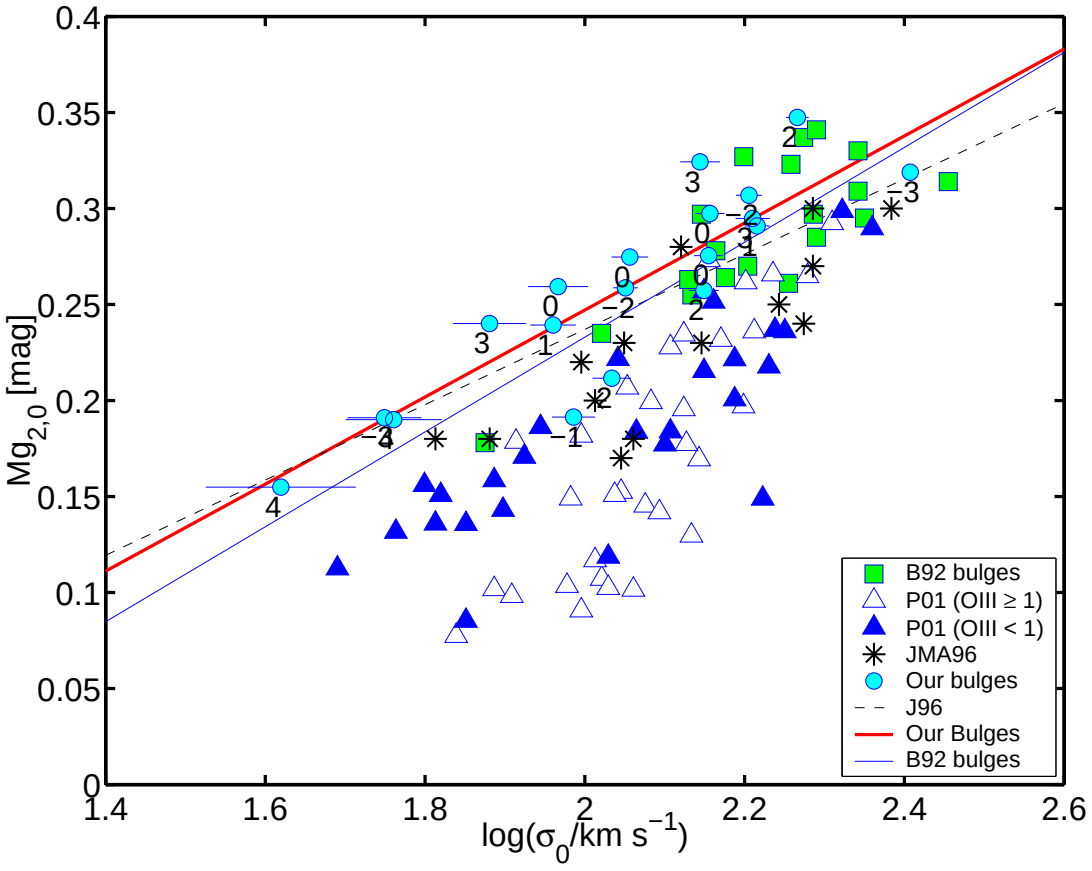

Figure 3.4: The $Mg_{2,0}$ - $\log(\sigma_0)$ Relation. Filled circles correspond to our sample of bulges while solid squares represent the sample of bulges of B92. Morphological types of the galaxies of our sample are indicated. Open triangles are bulges with EW(OIII)≥1, while filled triangles are bulges with EW(OIII)<1 both from Prugniel, Maubon & Simien (2001). Asterisks correspond to the sample of bulges of Jablonka, Martin & Arimoto (1996). Errorbars of $\log(\sigma_0)$ for our sample are also plotted.

(∼ 2 Gyr). This supports the hypothesis of an early formation for bulges and ellipticals, via either dissipational collapse or early mergers. Late-type bulges (Sbc onwards) show hints of youth with respect to the early-types and could belong to a class of objects formed or transformed by secular disk evolution. In general they are smaller, younger and have lower central surface brightness. The question then is whether they fall on the same Fundamental Plane described by Es and S0s.

We have measured the mean separation of our bulges with respect to the FP

Table 3.6: Comparison with other authors

Galaxy	Parameter	Us	B93	T98	G99/SP97
NGC 5422	Mg_2	0.307	0.323		
NGC 5854	Mg_2	0.191		0.160	0.174
NGC 7332	Mg_2	0.259	0.263	0.253	0.225
NGC 7457	Mg_2	0.191		0.189	0.171
NGC 5422	$\log(\sigma_0)$	2.205	2.258		
NGC 5854	$\log(\sigma_0)$	1.986		2.170	2.017
NGC 7332	$\log(\sigma_0)$	2.051	2.130	2.114	2.117
NGC 7457	$\log(\sigma_0)$	1.749		1.756	1.863

NOTES: B93: Bender, Burstein, & Faber 1993.
T98: Trager et al. 1998.
G99: Golev et al. 1999 [for Mg_2]
SP97: Simien & Prugniel 1997 [for $\log(\sigma_0)$]

of Es and S0s (as defined by the Es/S0s of J96(Coma)) and found a small but non-negligible offset of 0.074 $\pm$ 0.033 in the B-band and 0.054 $\pm$ 0.029 in the K-band. In agreement with other authors (J96,P98) we find that the FP has intrinsic scatter, not explained by observational uncertainties.

The strong proximity of bulges to the FP of ellipticals and S0s reinforces the conclusions of Peletier et al. (1999a) that early-to-intermediate bulges are homogeneously old and structurally similar to elliptical galaxies. It is useful in any event to investigate the origin of the intrinsic scatter and the offset. We first analyse the intrinsic scatter by showing the FP residuals with respect to various galaxy observables. Then, we discuss the roles of populations, kinematics and homology in creating the offset with respect to Coma ellipticals.

3.5.1 Analysis of the Residuals

The existence of this intrinsic scatter has been a matter of debate for the last decade. For ellipticals, Mobasher et al. (1999) have proposed the population of AGB stars as one of the sources of the intrinsic scatter of the FP in the K-band. Structural and dynamical non-homology may be responsible, at least in part, for the intrinsic scatter (Graham & Colless 1997). Recent studies suggest that the intrinsic scatter is probably a combination of age/metallicity variations and

dynamical deviations from homology (P98 and references therein). For bulges differences in s stellar populations might account for even larger scatter (e.g. Prugniel, Maubon & Simien 2001).

To obtain clues on the origin of the intrinsic scatter of our bulges in the FP, we analyse correlations between the residuals of the FP, defined as $\Delta FP \equiv \log(r_e)$-fit, using the Common fits, and different observables for our sample of bulges: ΔMg_2, Galaxy Type, inclination of the galaxy and Sersic index n. These correlations should give us ideas whether the distribution of our bulges along the sequence described by Es and S0s depends on the presence of young stars [$\Delta FP - \Delta Mg_2$], homology or light profile shape [ΔFP - Galaxy Type, ΔFP - Index of the Sersic profile (n)] or the degree of anisotropy of the object [ΔFP - Inclination of the galaxy (i)].

We perform this study for the 2 bands using the Spearman rank order correlation coefficients in each case. We find that there is no correlation between the residuals of the FP and any of the 3 FP parameters in either B or K, as can be expected from section 3.3. Figure 3.5 shows the distributions of FP residuals as a function of global galaxy parameters in the B and K-band. Points are labeled with the morphological type of the galaxy T. The probability of a null correlation is given within parenthesis in each panel, next to the correlation coefficient. The point labeled "-2" near the top of each panel corresponds to NGC 7332. This point is not included in the computation of correlation coefficients (see section 3.3).

No signs of correlations are found of ΔFP and ΔMg_2 (96% and 31%, in B and K band respectively). The same is true if the deviations are taken from the fit of J96. If the deviations, both to the FP and the $\mathrm{Mg}_2 - \sigma$ relation, are due to young stellar populations, or even to non-inclusion of rotational support, a correlation is expected (P01). However, for our sample the deviations from both relations are small, and this fact combined with the relatively small size of the sample makes us not see the correlation.

A weak trend is found with galaxy type (12%) in the K-band and negligible in the B-band. While weak, the distribution of galaxy types (within our bulges) gives a suggestion that the FP residuals may depend on galaxy type, in the sense that late type bulges tend to be below the FP, and early types above.

We don't find a relation between ΔFP and n, the Sersic index. The same conclusion was reached by Graham & Colless (1997) for Virgo cluster galaxies studied

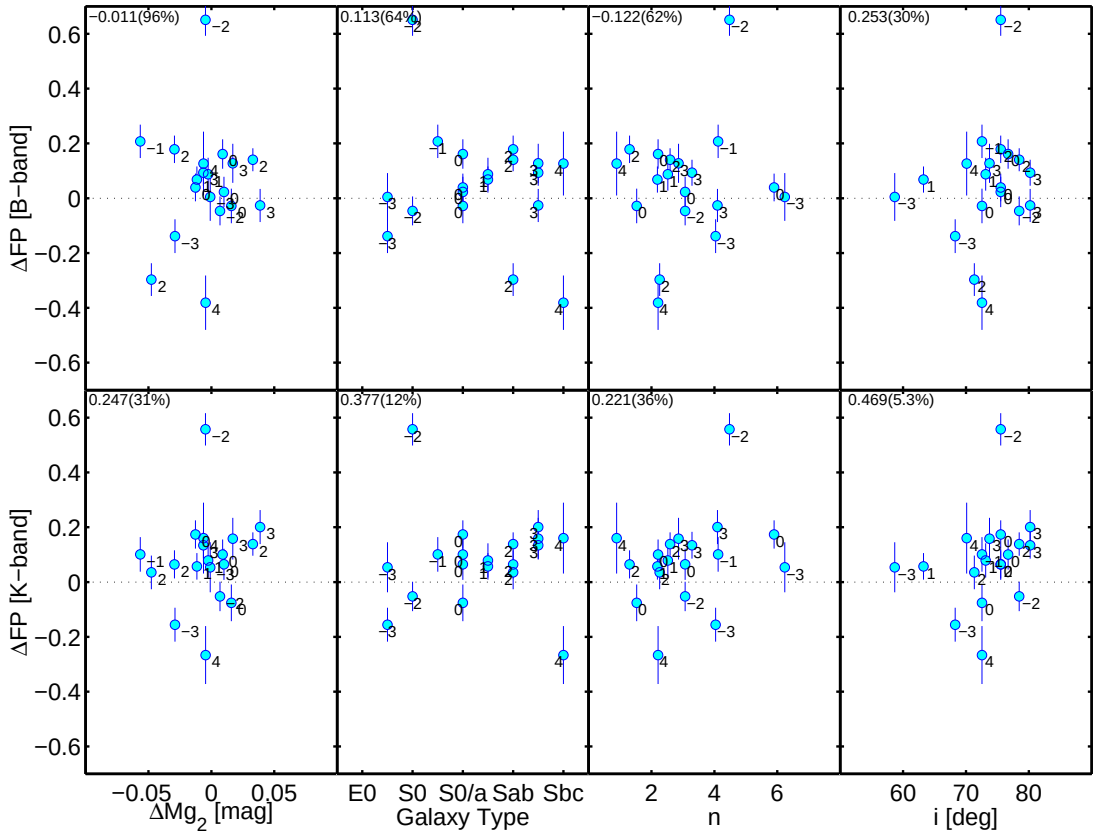

Figure 3.5: Correlations of the $\Delta FP = log(r_e) - fit$ with global galaxy parameters. Points are labeled with the morphological type of the galaxy T. The number at the top left of each panel is the Spearman rank correlation coefficient. The number within parenthesis is the probability of a null correlation.

in the V band at high S/N. Such a correlation, however, could be hidden, in part, by stellar populations effects. Prugniel & Simien (1997) found a correlation between the residuals of the FP and n after removing the scatter induced by the stellar populations. Here again think the small size of the sample prevents us from seeing this correlation.

Next we analyse possible correlations between ΔFP and the inclination of the galaxy (i). Projection effects and the presence of disks are both likely sources of scatter in the FP (Saglia, Bender & Dressler 1993). Despite the limited range in ellipticities, we find that the probability for a significant correlation is 70% and 95%, in the B and K bands respectively. J96 found that galaxies with a large ellipticity (presumably edge-ons) have a slight tendency to lie below the FP. The

residual, for $\epsilon = 0.6$ - $0.8 \approx$ 0.10 in $\log(r_e)$, similar to ours. The ΔFP dependence on inclination can contribute to the global offset of our inclined sample w.r.t. the J96(Coma) FP. We address this in section 3.5.2.

3.5.2 Offsets with respect to ellipticals

Population age/metallicity differences, internal kinematics and non-homology each can in principle shift bulges with respect to the FP of old ellipticals. We discuss each in turn.

The position of bulges below the FP of ellipticals could have been produced if bulges are on average younger than elliptical galaxies (Schweizer & Seitzer 1992a; Prugniel & Simien 1996). Taking the models of Vazdekis et al. (1996) one finds that for solar metallicity a decrease in age from 12.5 to 10.0 Gyr gives a shift in the $\log(r_e)$ direction of 0.06 in B and 0.04 in K, consistent with the results presented here. This means that possibly the offset could be explained if our sample on the average would be about 2.5 Gyr younger than the Coma cluster samples used by J96 and P98.

The effect of rotational support, although small, has been detected by other authors Bender, Burstein & Faber (1992); Prugniel & Simien (1994). Following Prugniel & Simien 1994, the rotational kinetic energy may be introduced in the FP via a 'rotational support term' S to be added to $\log(\sigma_0^2)$. Using our definition of FP and after accounting for the inclination range for our sample, we approximate S as

$$S = \alpha\, 0.5\, \log(1 + 0.62 \frac{V_{max}^2}{\sigma_0^2}) \tag{3.8}$$

with α is from Eqn. 3.5. Since our spectra were obtained along the minor axis of the galaxies, we have not been able to measure S for our sample. We can nevertheless estimate the amount of rotation needed to generate the observed offset. Non-inclusion of the rotation term offsets points *downward* on the FP diagram. A sample average of $V_{max}/\sigma_0 = 0.66$ produces the observed FP offset. Within this model, the observed offset of our bulges sample with respect to Coma ellipticals can be explained by the non-inclusion of rotation data for our bulges.

The effect of non-homology, i.e. that bulges do not all follow the $R^{1/4}$ law, has not been found in our data, given that ΔFP does not correlate with n, the

Sersic index. As noted in section 3.5.1, Prugniel & Simien 1997 did find such a correlation once the scatter by population effects had been taken into account.

Finally, in section 3.5.1 we have identified galaxy inclination as a potential origin for FP offsets. J96 model the inclination effect by considering the effect of rotation on the measurement of the central velocity dispersion. This effect is independent of the rotation support term described above.

The previous analysis suggests that any combination of age and kinematics contribution to the FP can explain the offsets of our sample with respect to Coma ellipticals, whereas we fail to identify the effects of non-homology. Most plausibly, not a single one of the two processes is responsible for the entire offset. The latter probably results from a combination of the two. Nevertheless, we note that, while the population contribution rests on a model determination of ages, the kinematic offset is sure to be there; indeed, bulges rotate and our sample is selected to be inclined.

3.6 Conclusions

We have analysed the position of bulges of early-type spirals (type S0-Sbc) on the Fundamental Plane of early-type galaxies. A few conclusions can be drawn from our study:

- We find that our sample of bulges early-type spirals lies slightly below the FP, as defined by E and S0 galaxies, both in the B and K bands. The fact that bulges lie so close to the FP of ellipticals and S0s implies that their formation epoch must have been similar to that of cluster Es and S0s.

- Both age and the unaccounted rotation effects are likely to contribute to the offset observed. Any single one of these effects can account for the observed offset, by assuming either an age on average 2.5 Gyr younger than the cluster ellipticals and S0s, or by assuming an average $V_{max}/\sigma_0 \sim 0.66$. Because rotation must contribute to the FP offset, the age differential between bulges and cluster ellipticals must be significantly smaller than the mentioned 2.5 Gyr.

- We find that there is a hint that bulges of later morphological type are situated below the other bulges in our sample, indicating that they have

slightly younger ages, again consistent with our results from HST colours.

- We confirm the result of P01 that bulges seem to have a steeper $Mg_{2,0}$ – $\log(\sigma)$ relation than ellipticals or S0s. Contrary to current lore, the $Mg_{2,0}$ – σ is not a mass-metallicity relation only, at least for bulges: Younger objects seem to increase the slope of the relation (P01). For our sample, however, the slope is shallower than for P01, much closer to that of the ellipticals.

Chapter 4

The near-IR Ca II - σ relation in bulges of early-type galaxies*

* Falcón-Barroso, J., Peletier, R.F., Vazdekis, A., Balcells, M., to be submitted to *Astrophysical Journal Letters*

4.1 Introduction

A very powerful way to study the physical properties of galaxies is by using scaling relations. Apart from linking internal structure and dynamics through e.g. the fundamental plane (Djorgovski & Davis 1987) they are also very powerful in linking these properties with stellar populations. For example, the colour-magnitude relation (e.g. Sandage & Visvanathan 1978) shows that brighter galaxies are redder, something which is commonly interpreted by assuming that brighter galaxies are more metal rich. Since colours are a very crude way to represent stellar populations in galaxies, one often uses relations between line strength and luminosity, or central velocity dispersion. The most popular relation here is the Mg_2 - σ relation (Terlevich et al. 1981), which shows that the Mg_2 line index increases with luminosity. Generally one prefers to use relations with velocity dispersion, rather than luminosity, because of the smaller scatter. The colour - σ and Mg_2 - σ relation are very powerful tools to detect small amounts of young stars in an otherwise old stellar population. Schweizer & Seitzer (1992b), e.g. showed that for a sample of ellipticals and S0's all galaxies that deviated from the main relation had a significant population of young stars, as deduced through independent means. Both relations can be used in this way to study the evolution of stellar populations as a function of redshift (e.g. Ellis et al. 1997). They can also be used to study whether e.g. bulges are younger than elliptical galaxies. In chapter 3 we studied the ages of our sample of bulges using the fundamental plane and the Mg_2 - σ relation and found that the bulges in this sample were generally as old as the ellipticals, with maybe some younger ages for the galaxies of type Sbc.

In reality, however, the situation might be more complex. Stellar population studies in the region of the Mg_2 index (Trager et al. 2000; Kuntschner 2000) indicate that Mg_2 is affected by age and metallicity, that Mg is overabundant w.r.t Fe in bright galaxies, and that therefore the Mg_2 - σ relation for ellipticals not necessarily is a relation for old galaxies (see also Vazdekis et al. 2001). If this is the case the conclusions about scaling relations in high-redshift clusters will have to be considerably revised. It is therefore useful to investigate an element that possibly is not affected by element overabundance, calcium.

The Ca II triplet at 8500 Å is a bright atomic feature that can easily be studied with modern detectors. It has been used in the past to analyse stellar populations (e.g. Carter, Visvanathan & Pickles 1986; Terlevich, Diaz & Terlevich 1990;

Olszewski et al. 1991; Bica et al. 1998). Recently, a series of papers have been published describing a new stellar library that is used to make a thorough calibration of the Ca II triplet and other features in its spectral region in terms of stellar parameters (Cenarro et al. 2001a,b, 2002). A followup paper (Vazdekis et al. 2003, hereafter VAZ03) presents the behaviour of these features for single stellar populations as predicted by recent evolutionary synthesis models. Recently 2 letters have been published to study the Ca II triplet in samples of elliptical galaxies using this calibration. A first paper (Saglia et al. 2002) (hereafter SAG02) finds that CaT* is constant with σ, while in a second paper (Cenarro et al. 2003) (hereafter CEN03) finds that there is a decreasing trend. Both works find that for bright galaxies CaT* is much lower than predicted by the models, something which could be due to either a dwarf-enhanced IMF or low Ca/Fe abundance ratios.

Here in this chapter we analyse a sample of galactic bulges using the same calibration. This sample offers an opportunity to find out if stellar populations in bulges of early-type galaxies are similar to those in ellipticals, and in particular whether calcium behaves in the same way. For example, one might expect that abundance ratios in bulges are different, since the formation history has not been the same. It also offers an opportunity to see whether CaT* really might be decreasing as a function of σ, or whether it remains constant. If, as predicted by the models, the CaT* - σ relation is very tight, and independent on galaxy type, it could be used, like the Fundamental Plane, for things like distance determinations, measuring evolution in clusters etc. In this chapter these questions, as well as the origin of Ca in galaxies, are addressed. In §4.2 we present our observations and data analysis. A number of relations of line strength and σ are presented in §4.3. Possible interpretations of the results are given in Sec. §4.4.

4.2 Observations & Data Analysis

4.2.1 Observations

A set of nineteen early-type galaxies, ranging from S0 to Sbc, from a sample defined by Balcells & Peletier (1994) were observed using the ISIS double spectrograph at the 4.2m William Herschel Telescope of the Observatorio del Roque de los Muchachos at La Palma between 11 and 13 July 1997. Spectra were obtain

between 8360 - 9170 Å, along the minor axis of the galaxies, at 1.74 Å spectral resolution (FWHM of the arc lines). The slit width was 1.2″ to match the seeing at the time of the observations. A more detailed summary of the observations and data reduction can be found in chapters 2 and 3.

4.2.2 Kinematics

Kinematic parameters were derived using FOURFIT developed by van der Marel & Franx (1993). A gaussian fit to the LOSVD was performed to obtain mean radial velocities and velocity dispersions. We have made use of a single-age, single-metallicity synthetic model ([Fe/H]=0.0, t=6.31 Gyr) from VAZ03 as a kinematic template. This procedure has proven to be very effective in reducing template mismatch and produces as good results as the best stellar templates in this wavelength domain (see chapter 2).

4.2.3 Measurement of the Line Strength

In order to explore the dependence of the relation of line-strength and velocity dispersion on aperture we measured the 4 line-strength indices in three different apertures (r_{eff}, $r_{eff}/2$, 1.2 x 4 arcsec^2). The signal-to-noise ratios for the different apertures range from 67 to 256, 55 to 232 and 75 to 244 per angstrom, respectively. K-band effective radii were taken from Table 3.1 in chapter 3 and converted to the minor axis using high-spatial resolution H-band ellipticity profiles from Balcells et al. (2003). For a large number of our bulges it was not possible to accurately measure the index at aperture sizes $< r_{eff}/2$ due to its size and seeing conditions. At the same time, we are also not able to reproduce exactly Cenarro (2002) (hereafter CEN02b) aperture (2 x 4 arcsec^2) given that the slit width was just 1.2″ to match the seeing at the time of the observations. The difference at smaller apertures, however, should be minor since the Ca II triplet depend very little with the size of the aperture (see Fig. 4.2).

We measured the recently defined line-strength indices CaT*, CaT, PaT (Cenarro et al. 2001a) and Mg I (CEN02b) for the three different apertures on the flux calibrated spectra. Note that the Mg I index is completely independent of previous index definitions based on Mg lines in the blue wavelength range (see Appendix B for more details). The main advantages of these new definitions

Table 4.1: Calibration Stars

HD (1)	Sp.Type (2)	T_{eff} (3)	Property (4)	Selected Stars
1461	G0 V	5816	High Proper Motion	*
102328	K3 III	4395	Normal	*
103095	G8 Vp	5025	Flare	
113226	G8 III	4983	High Proper Motion	*
122563	F8 IV	4566	Variable	
124897	K2 IIIp	4361	Variable	*
125560	K3 III	4381	Variable	*
129312	G8 III	4880	Variable	
135722	G8 III	4847	Variable	
139669	K5 III	3917	Variable	
140573	K2 III	4528	Binary	
163506	F2 Ibe	6491	Post AGB	
188056	K3 III	4244	Variable	*
199478	B8 Iae	10800	Emission-Line	
200779	K6 V	4252	High Proper Motion	*
207260	A2 Ia	9100	Variable	
217476	G4 Ia	5100	Binary	
218329	M1 IIIab	3810	Variable	*
219734	M2 III	3730	High Proper Motion	*
221148	K3 IIIvar	4643	Variable	*

NOTE:
(1) HD names from the Henry Draper Catalogue (Nesterov et al. 1995).
(2) Spectral Type from (Cenarro et al. 2001a).
(3) Effective temperature in Kelvin (Cenarro et al. 2001a).
(4) Property from SIMBAD (http://simbad.u-strasbg.fr/Simbad).

over the previous ones (e.g. Armandroff & Zinn 1988; Díaz, Terlevich & Terlevich 1989; Rutledge, Hesser & Stetson 1997) are that they have been designed to ease problems in the definition of the continuum bands, the contamination of the Paschen lines, and the sensitivity to the S/N ratio and velocity dispersion (see Cenarro et al. 2001a for more details). In order to compare the galaxies with each other, we broadened all the spectra to 300 km s^{-1}, slightly higher than the largest velocity dispersion in our sample (291 km $s^{-1}$for NGC 5838 in the central aperture). This correction is small for the CaT* index, which has shown to be fairly constant with velocity dispersion up to 300 km s^{-1} (VAZ03). Errors in the indices include contributions from radial velocity uncertainties and Poisson errors

Table 4.2: Index calibration offsets

Index	Offsets at 300 km s^{-1}	Offsets at 400 km s^{-1}
(1)	(2)	(3)
CaT*	0.178±0.032	0.175±0.029
CaT	0.205±0.027	0.199±0.025
Mg I	-0.001±0.022	0.010±0.021
PaT	0.029±0.007	0.026±0.006

(see chapter 2 for more details). The uncertainty from S/N dominates the errors in the indices.

4.2.4 Spectrophotometric corrections

In order to be able to make a direct comparison of our measured indices with the model predictions, it is necessary to determined to what extent our spectrophotometric system is similar to the one from which the SSP models are based on. During our observation campaign, spectra for 20 stars from the Lick system (Worthey et al. 1994) were obtained. Details of the list of stars can be found in Table 4.1. The same stars were also observed by Cenarro et al. (2001a) as part of their stellar library in the Ca II triplet region from which VAZ03 developed the SSP models.

In the following paragraph we describe the necessary steps to obtain the desired offsets.

- First, we need to flux calibrate our stellar spectra. This is a compulsory step to be taken not only in this case but every time we want to measure line strength indices (see appendix B).
- Second, we have to zero-redshift our spectra by cross-correlating the spectra of each of our stars with the spectra of the same star in the stellar library. This will allow us to measure the line-strengths at the same redshift, and therefore avoid the introduction of spurious errors into the measurement of the equivalent width of the indices.
- In our case we are interested in measuring the indices at 300 km s^{-1} and 400 km s^{-1} spectral resolution. Given that the two sets of data are at a

different spectral resolution, it is necessary to convolve each one of them with the appropriate Gaussian functions to match the required resolution. This is done in quadrature as described by the equation:

$$\sigma = \frac{\sqrt{\sigma_2^2 - \sigma_1^2}}{\Delta v} \tag{4.1}$$

where σ_1 is the instrumental resolution of the input system (i.e. our data or the stellar library), σ_2 the final instrumental resolution we want to achieve and Δv is is a conversion factor km/s/pix.

- Once we have performed the three previous steps we just need to measured the line-strength indices from all the spectra.

- In Fig. 4.1 we present the plots from which the desired offsets, at 300 km s^{-1} resolution, have been computed. Although not shown here a similar picture is found for the 400 km s^{-1} resolution. We obtained the offsets by taking the mean value on the y-axis, considering only the red points. Results are summarised in Table 4.2.

The choice of the stars to be considered for the offset estimation was based on the properties of the stars. We avoided all the stars which could potentially affect the final result (Flare, binary, Post AGB, emission-line stars). Variable stars were selected only if their effective temperatures were below $\sim$ 4500 K and more importantly if their values for the different indices were in the range of values observed for our sample of galaxies. The final selection of stars is indicated with red solid circles in Fig. 4.1 and marked in Table 4.1. Given that the offsets found for some indices are significant at the 2 or 3 σ level, we suspect that flux calibration errors might be responsible for such values. Although in principle we had 2 flux standard stars available from our observations (see chapter 2), one of them (BD+174708) was not really useful since the reference spectrophotometric calibration curve provided just one point in the wavelength range that was covered.

The values of the different indices in the different apertures, without the offset corrections, can be found in appendix E. In Fig. 4.2 the offsets have been applied to the data.

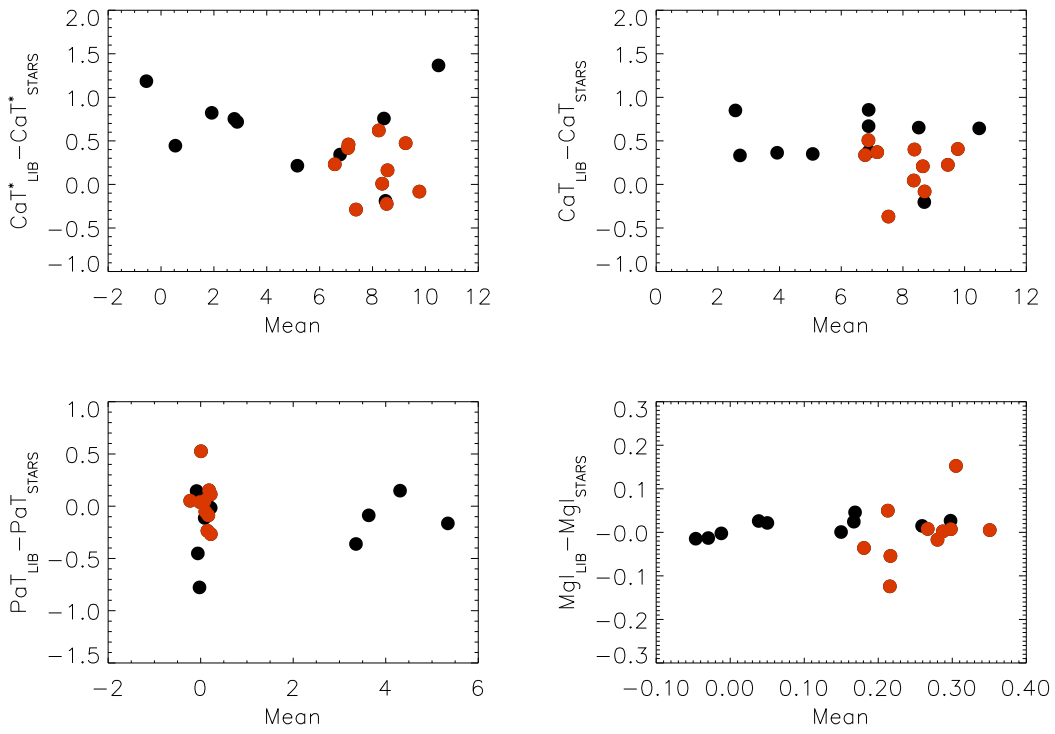

Figure 4.1: Line strength offsets due to spectrophotometric differences between our data and the stellar library in which the models are based on. The final adopted offsets, in Table 4.2, have been measured using the red points only.

4.3 The index - log(σ) relations

The relations of the line-strength indices CaT*, CaT, PaT, Mg I and velocity dispersion are shown in figure 4.2. We present each relation for the three aperture sizes described in §4.2.3 (labeled on the top boxes). Early-type spirals (T $\leq$ 0) are depicted as filled symbols, and late type (T>0) as open ones. Index values for a range of SSP models at the resolution of the data are shown in the fourth-column panels. Linear least-squares fits are plotted for some of the relations, with fit coefficients given in Table 4.3.

A strong anti-correlation exists between the CaT and CaT* indices and log(σ) in all apertures. This is reflected in the low value of the significance levels of the Spearman rank-order tests (Table 4.3, column 8), which give the probability of a null correlation, and the rms values about the best fit for the three indices. The anti-correlation of the CaT* index with σ shown here for bulges is similar to that

Table 4.3: Fitting Parameters

Index	a	Δa	b	Δb	r^2	r_s	$\alpha(r_s)$	rms
(1)	(2)	(3)	(4)	(5)	(6)	(7)	(8)	(9)
				1.2 x 4				
CaT*	8.72	0.38	-0.80	0.17	0.51	-0.71	7.4E-04	0.09
CaT	8.98	0.40	-0.70	0.19	0.41	-0.58	8.6E-03	0.07
MgI	0.00	0.08	0.11	0.04	0.13	0.20	4.2E-01	0.03
				$r_{eff}/2$				
CaT*	8.13	0.44	-0.97	0.20	0.36	-0.62	4.4E-03	0.11
CaT	9.48	0.47	-0.88	0.22	0.41	-0.71	6.2E-04	0.07
MgI	0.11	0.10	0.07	0.04	0.10	0.21	3.8E-01	0.02
				r_{eff}				
CaT*	9.44	0.39	-1.14	0.18	0.52	-0.76	1.7E-04	0.11
CaT	9.76	0.42	-1.06	0.20	0.63	-0.80	4.2E-05	0.07
MgI	0.04	0.09	0.10	0.04	0.13	0.22	3.6E-01	0.02

NOTE: Parameters of the error-weighted least-squares linear fits to the index - $\log(\sigma)$ relation, defined as $I = a + b \cdot \log(\sigma)$ at 300 km s^{-1} resolution. Columns 2,3,4,5 show the fitted parameters and their errors. Columns 6,7,8 give the linear correlation coefficient (r), the Spearman rank-order correlation coefficient (r_s) and significance level ($\alpha(r_s)$). The last column shows the rms around the best fit.

recently found by CEN03 for elliptical galaxies (which was, if at all, marginally detected also for ellipticals by SAG02). CaT* is the first metallic line index that is found to anticorrelate with σ. The Mg I index, in contrast, shows a positive trend with σ as expected from the behaviour of the Mg*b* and Mg_2 indices in the optical range (e.g. Terlevich et al. 1981).

We have investigated whether different apertures would lead to significant differences in the index–σ relations. No major difference is found between the gradients of any index at each aperture: the slopes and zero-points agree within the errors (see Table 4.3). It is interesting to see that none of our bulges give a measurement of the CaT or CaT* indices that lies above the predictions of the models (VAZ03). This result agrees with the model predictions that the CaT and CaT* indices tend to saturate for metallicity above [M/H]$\sim$-0.4 (VAZ03), which is also supported by the data of CEN03 and SAG02.

Given that our sample contains bulges from S0 to Sbc, we have looked whether the index–σ relations depend on morphological type (see Fig. 4.2). Due to our

limited number of galaxies, we split the sample in just two groups: one of them containing galaxies of types E, S0, S0/a (T $\leq$ 0) and a second group with the Sa to Sbc galaxies (T>0). No differences are found for any of the relations given very similar fitting parameters when the two groups of galaxies were fitted independently.

4.3.1 Comparison with CEN02b

Finally, we have compared our index–σ relations with those found by CEN02b in an aperture of 1.2x4 arcsec^2. An accurate comparison with SAG02 is not possible since their aperture is four times smaller than the smallest we can get given the size of some of our bulges. We perform the comparison with CEN02b at a similar aperture size (2x4 arcsec^2) and at the same spectral resolution (400 km s^{-1}). In figure 4.3 we show the comparison of the CaT*, CaT, Mg I and PaT indices. Results are in good agreement at 1-σ level for all the indices, with the slopes agreeing within the errors(i.e. b[CaT*(Us)]=-0.69$\pm$0.18, b[CaT*(CEN02b)]=-0.56 $\pm$0.15). For the CaT* - σ relation the exclusion of one of our low-velocity dispersion galaxies (NGC 7457) provides an even better agreement in the slope values (b[CaT*(Us)]=-0.52$\pm$0.19). The other relations, however, are not significantly affected if the same galaxy is left out. On the other hand, the RMS of our data around the best fit is much smaller (RMS[CaT*(Us)]=0.14) than the one measured by CEN02b (RMS[CaT*(CEN02b)]= 0.28), certainly because of the lack of bulges with velocity dispersions as high as CEN02b.

Our galaxy sample shows values for the PaT index slightly higher than those of CEN02b for ellipticals ($\sim$0.03 Å at 400 km s^{-1} resolution). The offset w.r.t. ellipticals could indicate that mean population ages for bulges are somewhat lower than those of ellipticals. Recent studies of the same sample, using deviations of bulges from the FP of ellipticals and S0s (see chapter 3) or color-color diagrams (Peletier et al. 1999a), conclude that bulge populations are old, but could be younger than ellipticals by up to 2.5 Gyr. The higher PaT values, and correspondingly younger ages for bulges could also be due to younger stars in the centre of our galaxies. Finally, small calibration errors are not out of the question, since the young ages for some galaxies inferred from PaT are not consistent with the ages from CaT* measurements (i.e. higher PaT values, if coming from young populations would produce a decrease in the CaT* values, not an increase as we

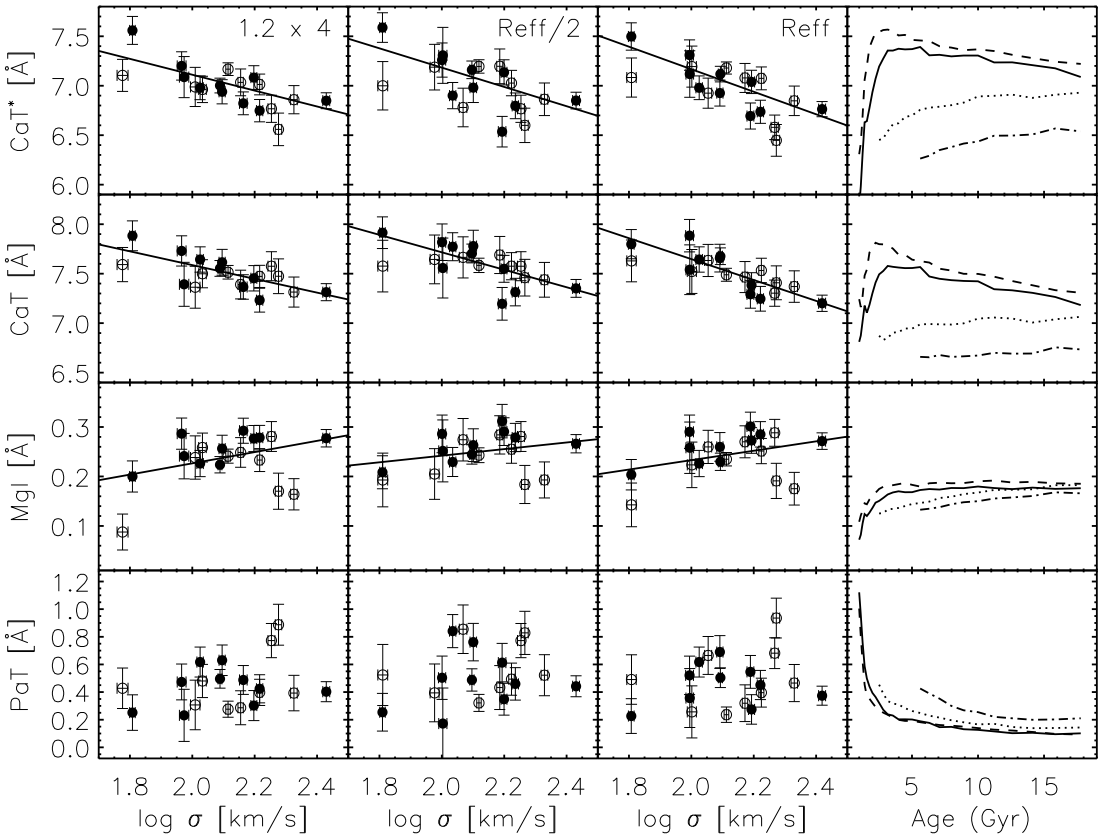

Figure 4.2: The CaT*, CaT, MgI and PaT index relations with $\log(\sigma)$ for different apertures. The data has been convolved to a spectral resolution of 300 km s^{-1}. Solid circles are early-type bulges (T $\leq$ 0), while later-type bulges (T>0) are represented by open circles. Solid lines represent an error-weighted least-squares fit to the all the points. See Table 4.3 for more details. The last column shows SSP model predictions for different ages and metallicities, for a Salpeter IMF, for each index. Dashed, solid, dotted and dash-dotted lines in the last column represent SSP models of [M/H]=0.2,0.0,-0.4,-0.7 metallicities respectively.

find here). For the most extreme cases in our sample (NGC 5965, PaT=0.86 Å and NGC 5746, PaT=0.74 with the 1.2x4 arcsec^2 aperture) their value could be due to star formation induced by the presence of strong bars in these galaxies (Kuijken & Merrifield 1995). Interestingly, five out of the seven galaxies in our sample that have been classified as barred galaxies (de Vaucouleurs et al. 1991), show PaT values above the sample mean value. Finally, we find no correlation of the PaT index with σ, a result supported by CEN03 for Es, and contrary to the strong trend found by SAG02. An explanation for that difference could be in the velocity dispersion correction they have applied to each galaxy in their sample.

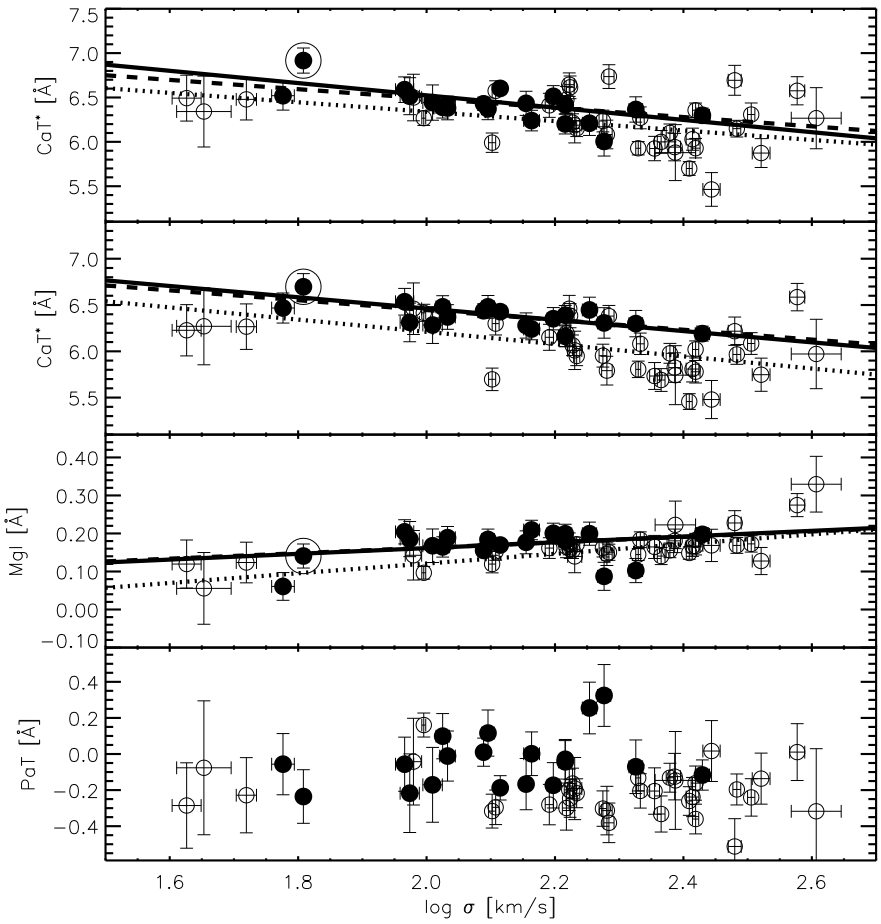

Figure 4.3: Comparison of the CaT*, CaT, Mg I and PaT vs log(σ) relations between our sample of bulges and early-type galaxies from CEN02b. Solid circles and line represent our sample of galaxies and an error-weighted least-squares linear fit to it. Open circles and dotted line represent CEN02b sample and its fit. The dashed line is an error-weighted least-squares linear fit to our sample excluding the galaxy marked with a circle ($\sim$1.8 in log(σ)). In order to compare our results we have degraded the resolution of our data to 400 km s^{-1}.

A large velocity dispersion correction for more massive galaxies could explain the positive correlation of the PaT index and the flatness of the CaT* index as a function of velocity dispersion.

In summary, the small differences between CEN02b and our sample are likely to be due to calibration errors and possibly by the way the two datasets are sampled as a function of velocity dispersion. More observations are required to address this question.

4.4 Discussion

The origin and abundance evolution of the atomic element Ca has been a matter of debate. Due to its nature as an α element, an evolution history similar to that of Mg is predicted (Woosley & Weaver 1995). However several observations reveal a more complex picture where Ca and Mg originate and evolve differently. The problem has resuscitated again recently in the light of the results of two publications (CEN03; SAG02).

In our own Galaxy, Ca seems to follow Mg: [Ca/Fe] is high in the halo and metal-poor bulge stars, but it is close to zero in the solar neighborhood (Timmes, Woosley & Weaver 1995). For early-type galaxies, the Ca abundance does not follow Mg. Evidence now comes from measurements of the Ca4227 line (Vazdekis et al. 1997, 2001) and from the Ca II triplet (VAZ03; CEN03). In fact there are indications that Ca abundance is not even enhanced compared to Fe in elliptical galaxies (O'Connell 1976; Peletier et al. 1999b; Proctor & Sansom 2002). Although scarce, some work has been published about the Ca content in late-type galaxies (Bica & Alloin 1987; Proctor & Sansom 2002). These papers conclude that spiral galaxies show similar Ca equivalent widths (from Ca II triplet measurements) as luminous ellipticals.

The Mg - $\log(\sigma)$ relation has been interpreted as a mass-metallicity relation for early-type galaxies (Terlevich, Diaz & Terlevich 1990). In the light of the new results obtained by CEN03 and model predictions (VAZ03), such statement does not hold for the Ca II triplet - $\log(\sigma)$ relation. An anti-correlation between CaT* and velocity dispersion could be interpreted as an underabundance of Ca w.r.t. Mg in more massive galaxies. Other possibilities are: 1) Composite Stellar Populations including a low metallicity component or a young and old population of the same metallicity, and 2) An IMF biased towards low-mass stars. We discuss the advantages/disadvantages of each one of these possible explanations in turn.

4.4.1 Ca underabundance

The problem of the Ca underabundance is not new, and it has been previously reported by several authors (McWilliam & Rich 1994; Vazdekis et al. 1997; Peletier et al. 1999b; Vazdekis et al. 2001, VAZ03). There is no clear explanation why Ca should be underabundant in massive galaxies. The actual nucleosyn-

thesis theory (Woosley & Weaver 1995) predicts two "flavours" of SNe: one in which more massive stars (20-40 $M_{\odot}$) produce Mg before ($\approx$2.6 Myr) Ca, which is generated in less massive stars, 12-30 $M_{\odot}$. This picture could explain the small discrepancy in abundances between Mg and Ca (Mollá & García-Vargas 2000). However, large abundance ratio differences are hard to obtain in this way, and impossible to get for real galaxies, for which the formation timescale is much larger than a few Myr.

4.4.2 Non-Solar Abundance Ratios

Is it possible that our model predictions are wrong because we don't use the right isochrones? If we would use α-enhanced isochrones (Salasnich et al. 2000; VandenBerg et al. 2000,VAZ03), required to get the correct [Mg/Fe] ratios in giant ellipticals, assuming a solar-like element partition for the the [Mg/Ca], would predict even larger Ca indices (VAZ03), increasing the discrepancy. Therefore using these isochrones will only make matters worse.

4.4.3 IMF variations

Next we discuss the apparent Ca underabundance at large velocity dispersions in terms of a dwarf-enhanced IMF. The universality of the IMF has been a matter of controversy in the last decades (see Gilmore 2001 and Eisenhauer 2001 for current reviews of observational keys in favour and against this statement). IMF time variations among ellipticals have been studied by CEN03 in detail. An advantage of this approach is its ability to explain the [Mg/Fe] overabundance problem (Vazdekis et al. 1996). The effect of a dwarf-dominated IMF is a weakening of the CaT* index (CEN03; VAZ03). This effect is stronger at high metallicities. As also mentioned in SAG02, there are four observational drawbacks against this theory: first: indications of an IMF flatter than Salpeter in the bulge of our own Galaxy (Zoccali et al. 2000), second: the fact that the predicted FeH 9916 Å feature is significantly stronger than what it is observed (Carter, Visvanathan & Pickles 1986), third: the discrepancy between visual M/L ratios (M/L>10) and dynamical estimates M/L$\approx$6 (Gerhard et al. 2001). An additional drawback is that visual-infrared $(V-K)$ colors are just at the verge of what it is observed in Es, as pointed out by CEN03.

4.4.4 Composite stellar populations

The use of composite stellar populations is analysed by SAG02. Given the lack of measurements of blue indices (i.e. Hβ) and CaT* simultaneously for bulges, we decided to use the well studied elliptical galaxy NGC 4365 as an example. Vazdekis et al. (2001) measured a Hβ value of 1.5 Å, whereas VAZ03 found a CaT* value of 6.3 Å. The velocity dispersion of this galaxy is σ= 255 km s^{-1} (Vazdekis et al. 2001).

The use of composite stellar populations is analysed by SAG02. We have performed a similar study by combining two populations: a young component (t=1 Gyr, [M/H]=0.0, IMF=1.3) and an old component (t=16 Gyr, [M/H]=0.0, IMF= 1.3). We use the E3 galaxy NGC 4365 as an example. Vazdekis et al. (2001) measured a Hβ value of 1.5 Å, whereas VAZ03 found a CaT* value of 6.3 Å. If one includes a young population that consist of 2% of the light in V, one gets a good fit to the observed Hβ value, whereas it overestimates (7.3 Å) the expected CaT* value. On the other hand a 50% old population is necessary to match the measured CaT* index, but then the Hβ index would be significantly overestimated (3.7 Å). Alternatively we have checked whether the same old population but with a more metal-poor old population (t=16 Gyr, [M/H]=-0.7, IMF=1.3) would provide better fits. We find that any fraction of the metal-rich population produces reasonable fits, within the errors, to the Hβ index but it is unable to reproduce CaT* index at the same time.

4.4.5 Ca Depletion

Ca is known to be highly depleted onto dust in the interstellar medium (Crinklaw, Federman & Joseph 1994). Could it be that it is also depleted in stars? The evidence is not strong. Such depletion in stars would require that, during star formation, interstellar dust is recycled less than interstellar gas. Moreover, depletion would have to be stronger in more dusty galaxies, so one would expect a large scatter in the CaT* - σ relation due to depletion. At least, the scatter for bulges of spirals, which are generally more dusty than ellipticals, should be larger. Since this is not seen, we argue that depletion can be excluded to be the cause of the low CaT* values.

In summary, many mechanisms can be used to explain the apparent underabun-

dance of Ca for massive galaxies. However none of them alone seems to be able to explain all the observations. In the light of the discrepancies found between all the possibilities, a combination of several effects could be in place. In any case much work is still needed to provide an answer to this problem.

Chapter 5

The formation of S0 galaxies: the case of NGC 7332*

* Falcón-Barroso, J., Peletier, R. F. and the *SAURON* team, to be published in *Monthly Notices of the Royal Astronomical Society*

5.1 Introduction

The nature of S0 galaxies has been a matter of controversy since their appearance in the first morphology classification schemes (Hubble 1936; de Vaucouleurs 1959; van den Bergh 1960a,b). Their location on the crossroads of the Hubble diagram, dividing galaxies up between early-type and late-type, gives them an important role in the understanding of galaxy formation and evolution. One of the biggest unknowns is whether they form an unique class of objects on their own or whether they are just simply a transient state in which they evolve from one morphological type of to another.

Many papers in the literature have addressed this question. Some authors refer to the S0 galaxies as normal spiral galaxies that have been stripped of their gas (Sandage & Visvanathan 1978; Dressler 1980). Studies of S0 galaxies in clusters suggest that interactions between galaxies could lead to the loss of interstellar matter in the disk and convert spirals into S0s. Some other theories are more in favour of gas loss through ram-pressure stripping from the intergalactic medium (Gunn & Gott 1972) or gas removal via galactic winds (Faber & Gallagher 1976). On the other hand there are authors who are more inclined to think that S0 galaxies are a set of primordial galaxies which have consumed their gas due to a rather high star formation rate (Larson, Tinsley & Caldwell 1980).

When studying the formation of S0 galaxies, one has to study the formation of both the bulge and the disk. Initial formation models predicted the formation of the bulge before the disk. This idea has been supported by several photometric studies (Caldwell 1983; Gregg 1989; Bothun & Gregg 1990). However some more recent simulations show evidence of the contrary (Pfenniger 1993). In their models of galaxy formation bulges of galaxies are formed via secular evolution after their disks (Pfenniger & Norman 1990; Emsellem 2001). On the other hand S0s behave like ellipticals in the widely known scaling relations (i.e. Color-Magnitude, Mg_2-σ or Fundamental Plane) and therefore they are thought to be old galaxies. It appears that dissipation has played a key role in the formation of these galaxies.

The role of mergers in the formation history of early-type galaxies is more and more believed to be important with the discovery of kinematically decoupled components in the centres of these galaxies (i.e. Franx & Illingworth 1988). The study of multiple-component kinematic structure in early-type galaxies has been a matter of extensive study in the last decade. Many discoveries have populated the

literature showing evidence for early-type galaxies with dynamically decoupled cores (i.e. NGC4621, Wernli, Emsellem & Copin 2001, NGC 4365, Davies et al. 2001 and NGC 4406, Bender (1988), see Wernli 2002 for an overview). Such cores are generally revealed using long-slit measurements, which introduces an a priori assumption on the geometry of the central structures. Several works have tried to overcome this limitation by mapping the galaxies with multiple slits at different positions angles (Fisher, Illingworth & Franx 1994; Fisher 1997; Statler & Smecker-Hane 1999). Despite these methods, there is still a large fraction of undetected cores still to be found. The arrival of a new generation of Integral Field Units (IFUs), such as OASIS or *SAURON*, has proved to be able to substantially increase the number of detections of such structures.

Unusual characteristics found in galaxies can provide, and have provided, extremely valuable clues for elucidating some of the key processes at work during galaxy formation. These galaxies become the ideal benchmark to test the predictions of theories of galaxy formation and evolution. NGC7332, an edge-on S0 galaxy, has been extensively studied in the past. Knapp, Kerr & Williams (1978) detected a small amount of H I in NGC 7332. However, more significant amounts of H I has been found in the neighbour galaxy NGC 7339, a Sbc galaxy that lies $5.2'$ away from NGC 7332 (Martin 1998). The X-ray detection is noteworthy since detections have only been made in 36% of the normal, noninteracting S0 and SB0s, in the Roberts et al. (1991) catalogue. Nevertheless, the galaxy is mainly known for a significant counter-rotating and a faint co-rotating [O III] gas components w.r.t. the stars (Bertola, Buson & Zeilinger 1992; Fisher, Illingworth & Franx 1994). Plana & Boulesteix (1996) later confirmed these gas disks by looking at the emission in Hα. They found two distinct gas components: a strong one counterrotating w.r.t the stars and a secondary faint one co-rotating w.r.t. the stars. This picture seems to disagree with the undisturbed photometry (Peletier & Balcells 1997). Broad band colours (Balcells & Peletier 1994) show that the colours of NGC 7332 ($B-R=1.4$) are somewhat bluer than colours of elliptical galaxies of the same luminosity. This result is confirmed by a spectral analysis showing that the galaxy has a luminosity weighted age of about 6 Gyr (Vazdekis & Arimoto 1999). Recently, a two-integral dynamical model for this galaxy has set an upper limit for the black-hole mass of the galaxy ($\log \mathrm{M}_{BH}/\mathrm{M}_{Sun} \leq 6.845$, see Magorrian et al. 1998). The first attempt of integral field spectroscopy on this galaxy (Sil'Chenko 1999) has revealed a core (R$\leq 5''$), younger than the sur-

rounding bulge (R>5″). Finally, the location of NGC 7332 on the fundamental plane of early-type galaxies has been reviewed in chapter 3, and it was found that this galaxy lies significantly below the relation (i.e. surface brightness is too high for its velocity dispersion), and that the displacement can not be explained by uncertainties in our measurements. In the light of these results it appears that putting all these pieces together to form a unique formation scenario for NGC 7332 is far from being an easy task.

Here in this last chapter we have made use of *SAURON* observations to add new evidence for peculiarities in NGC 7332. We show the discovery of a kinematically decoupled core (hereafter KDC), kinematic signatures of a central disk and disturbed 2D gas kinematics. This galaxy has turned out to be one of those cases where previous multiple long-slit studies have missed the KDC, strengthening the need for IFU units to accurately measure 2D kinematics in galaxies.

The main parameters of the galaxy are shown in Table 5.1. Section §5.2 summarises the observations and data reduction. A photometry analysis and comparison with the literature is done in §5.3. In sections §5.4 and §5.5 we show the kinematic maps of stars and gas, as well as give details about the innovative methods to derive such maps. A detailed line strength analysis is given in § 5.6. In the light of the new results we discuss possible formation scenarios for NGC 7332 in §5.7.

5.2 Observations & Data Reduction

5.2.1 *SAURON* observations

We observed NGC 7332 with *SAURON* at the 4.2m William Herschel Telescope of the Observatorio del Roque de los Muchachos at La Palma on 13 Oct 1999. We obtained 4 exposure frames of 1800 s. each, producing a total of 1431 simultaneous spectra per frame at a spectral resolution of 3.6 Å (FWHM) between 4790 and 5370 Å. The sky level is measured 1.9′ away from the main field, in a separate set of 146 lenses. The combination of the 4 exposures delivers a field of view of ≈ 34″ x 46″. The small offsets between the exposures enable us to resample the final datacube onto 0.8″ x 0.8″ pixels (drizzling technique, see Mutchler & Fruchter 1997 for more details). *SAURON* is equipped with an EEV12 CCD (2148x4200 px, 0.19″ per 13.5 μ pixel). The seeing at the time of the observations was stable

Table 5.1: Galaxy Parameters

Parameter	Value	Source
Morphological Type	S0 pec	de Vaucouleurs et al. 1991
Distance Modulus	31.81	Tonry et al. 2001
M_R [mag]	-21.86	Balcells & Peletier 1994
$B-R$ [mag]	1.40	Balcells & Peletier 1994
Ellipticity	0.75	Andredakis, Peletier & Balcells 1995
Scale [kpc/arcsec]	0.15	Falcón-Barroso, Peletier & Balcells 2002
Heliocentric Velocity [km/s]	1218	Falco et al. 1999

at 1.1″. Flux, velocity and line strength standard stars were observed during the same night for calibration purposes. Arc line exposures were taken before and after each target frame for wavelength calibration. A tungsten lamp frame was also taken at the end of the night in order to compute the mask that allow us to extract the data from the CCD frames.

5.2.2 *SAURON* data reduction

We have followed the procedures described in Bacon et al. (2001) for the extraction and reduction of the data. We have also performed 2D-binning to our final datacube using a dedicated software included in the *SAURON* package. We have chosen the Voronoi-tesselation implementation (Cappellari & Copin 2001, 2002) to a signal-to-noise ratio of 20 per pixel to present our results. This method has the advantage of binning the data in such a way that we obtain the same signal-to-noise in each bin in our maps.

5.2.3 STIS observations & Data reduction

We have retrieved STIS data from the HST archive in order to obtain high spatial resolution spectroscopy of the centre of the galaxy. The data is part of the observations in proposal ID 7566. The wavelength range covers the region between 8282 Å and 8835 Å. The grating used was the G750M that together with the aperture 52X0.2 provides a spectral dispersion of 0.56 Å/pix and a spatial resolution of 0.05″/pix. The dataset consist of 4 target frames plus calibration frames (fringe flats). The data was partially reduced when retrieved from the archive. However,

fringing corrections were needed to be applied as well as cosmic rays rejection. Fringing corrections where applied using the prescriptions in Goudfrooij, Baum & Walsh (1997), whereas we made use of the R$_{\rm E}$D$^{\rm uc}_{\rm m}$E package (Cardiel 1999) to perform the cosmic ray rejection procedure. A K0III template star (HR7615) from the same data set was retrieved to be used as template star for kinematic purposes. The star has also undergone the same reduction processes.

5.2.4 HST & ground-based imaging

Photometric data has been retrieved from several archives to perform a structural analysis. We have retrieved a set of WFPC−I images from the HST archive as part of an observation program, designed by T. Lauer and S. Faber (Prop. ID 2600). The observations were made using the F555W filter. The data set consist of 3 target frames with exposure times 35, 140, 140 sec respectively. The spatial resolution given by the instrument is 0.044″ per pixel. A cosmic ray rejection procedure, using the IRAF[1] routine *crrej*, was applied to the set of images to produce a fully reduced frame ready to use.

Finally, we have also made use of a fully-reduced ground-based Cousins I-band image from Peletier & Balcells (1997), available at the first author's website, taken at the Isaac Newton telescope located in the Observatorio del Roque de los Muchachos at La Palma. The exposure time of the frame was 200 sec and the spatial sampling is 0.549″ per pixel.

5.3 Photometric Analysis

We have analysed the WFPC−I data retrieved from the archive in order to study the photometric structures in NGC 7332. We have compared our photometric analysis with that obtained by Fisher, Illingworth & Franx (1994) from a R-band image (Fig. 5.1). The agreement between the two analysis in the overlapping region is quite good.

The isophotal analysis of the HST image reveals an inflection in the C_4 parameter. The maximum C_4 amplitude of the feature reaches 3% and extends up to

[1]IRAF is distributed by the National Optical Astronomy Observatories, which are operated by the Association of Universities for Research in Astronomy, Inc., under cooperative agreement with the National Science Foundation.

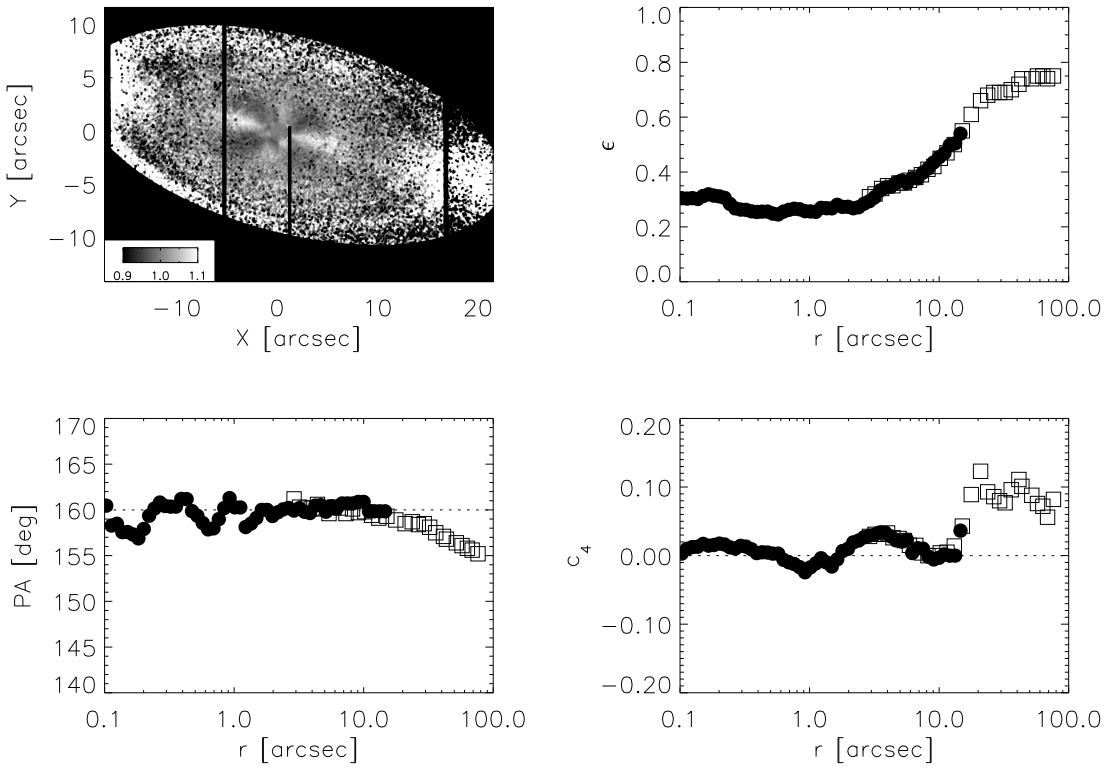

Figure 5.1: Photometric analysis of NGC 7332. The ratio between the WFPC1 image and a model image from our best ellipse fit is shown in the top left corner. PA, C_4, ϵ profiles along the geometric radius of the galaxy. Solid circles represent our WFPC1 analysis, whereas open squares show Fisher, Illingworth & Franx (1994) profile.

8″. A complementary representation is shown in Fig. 5.1 (top left corner) by dividing our image by a 2-dimensional model image from our best fitting elliptical isophotes. The results confirm an excess of light in the centre on the galaxy above 10% and therefore the presence of a central disk with a major axis position angle of 160°, previously reported by Seifert & Scorza 1996. On the other hand there are hints of a boxy component between 1″ and 2″ (C_4 <0), although not as significant as the disky feature mentioned above. There are also hints of another boxy component at ∼10″. Since our photometric bulge radius[2], from Peletier & Balcells (1997) is around 4″ (Alister Graham, private communication), which is much smaller than the location of that secondary boxy component, we can rule out the presence of strong boxiness in the bulge of NGC 7332. Edge-on,

[2]We define the bulge radius as the location in the surface brightness profile where the light from the disk starts to dominate over the bulge's light.

box/peanut shaped bulges might harbour a bar (Merrifield & Kuijken 1999), although kinematical evidence (a figure of eight in the Position-velocity diagram, see Fig. 1.2) is also necessary to confirm such result (Kuijken & Merrifield 1995; Bureau & Freeman 1999). On the other hand the ellipticity profile increases as we move towards the outer regions. This is consistent with the picture of an edge-on galaxy where ellipticity raises as we leave the bulge region and move into the disk. The same effect is seen in the C_4 profile.

Another striking feature is a position angle twist from the centre to the outer regions of the galaxy. The magnitude of the twist is about 5°. This change in the position angle is consistent with a projection effect. If we assume that NGC 7332 consists of aligned ellipsoids with different ellipticities, which is probably the case given the fact that it has a bulge and a disk, but with the same position angle, then a change of the viewing angle produces the effect of position angles moving away from the intrinsic one (Binney, Kormendy & White 1984).

5.4 Stellar Kinematics

We have measured the stellar kinematics of NGC 7332 using the Fourier correlation quotient method (Bender 1990). This method is based on the deconvolution of the galaxy-template correlation function with the peak of the autocorrelation of the template star. A gauss-hermite expansion (van der Marel & Franx 1993) has been fitted to obtain the higher order moments h_3 and h_4. We have computed the errors by means of 100 Montecarlo simulations using a synthetic single-age, singe-metallicity (SSP) model from Vazdekis (1999) as the simulated galaxy and the model itself as the template. From the simulations we estimate our errors to be below 10% for the mean velocity, and 20% for the velocity dispersion. This procedure will trace only errors due to signal-to-noise ratio and not the ones produced by template mismatching. However we are reducing the template mismatch as well due to the particular procedure we have used to derive the stellar kinematics (see Sect. 5.4.1). Kinematics has also been measured from the STIS data using van der Marel & Franx (1993)'s code although, due to the poor quality of the data retrieved, we have fitted a standard Gaussian and no higher order terms. In order to make it easier for the reader to understand the extend of the *SAURON* maps, we have plotted the contours from the *SAURON* reconstructed total intensity map in Fig. 5.2, on top of a contour map of the I-band ground

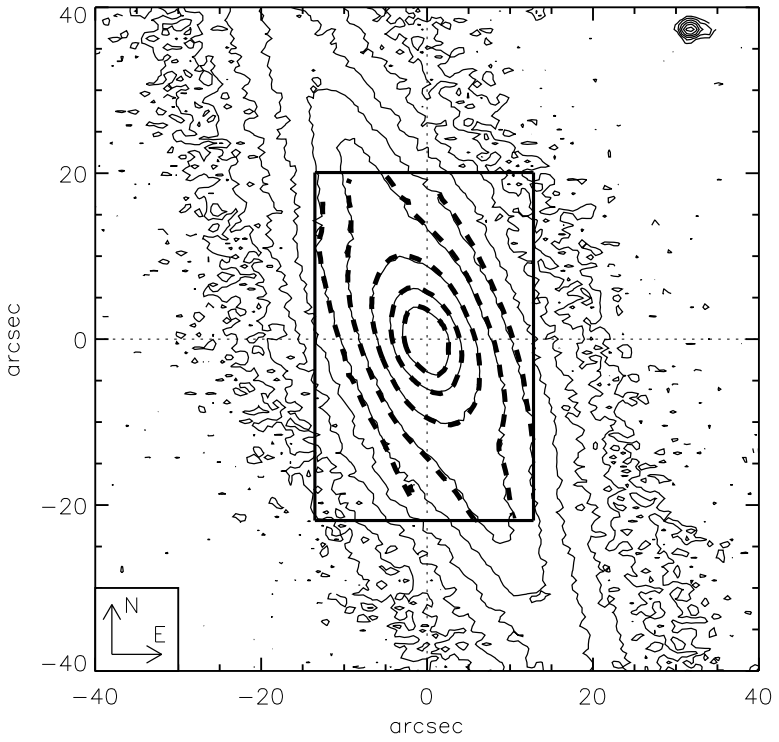

Figure 5.2: *SAURON* field, dashed contours, on top of the I-band image from Peletier & Balcells (1997). The orientation is the same as the shown in the *SAURON* kinematic maps (i.e. fig. 5.4). Contour levels are set at intervals of 0.25 mag.

based image from Peletier & Balcells (1997).

5.4.1 Measurement of emission-free stellar kinematics

NGC 7332 presents the following emission lines in the wavelength range we are working with (4790 - 5370 Å): Hβ (4861 Å) , [O III] (4959 and 5007 Å) and [N I] (5199 Å). Therefore some caution is needed to derive the stellar kinematics, due to nebular contamination. In order to obtain a clean stellar spectrum from which we can determine kinematic parameters, we have made use of a slightly modified version of the procedure described in Sect. 4.1 in de Zeeuw et al. (2002). A summary of the process follows:

- We first obtain an initial estimate of the stellar kinematics by fitting a region in the spectra with very little or no emission signatures. In this case we have fitted the wavelength range between 5060 Å and 5280 Å that, although

it includes the [N I] emission line, serves as a very good initial estimate.

- We then built a library of synthetic stellar spectra with different ages and metallicities from the library of Vazdekis (1999) convolved to our instrumental resolution.

- Third, we fit a linear combination of models, convolved with the kinematics we determined in step 1, to the full spectral range of our spectra, except those regions where emission is expected.

- The subtraction of the fit to the original data results in a pure emission spectrum that will be used to extract the gas kinematics.

- We then fit a the emission spectra with a Gaussian and remove such fit from the original data, obtaining a clean spectrum from which we can safely obtain stellar kinematics

- The final step is to re-measure the stellar kinematics, but this time using a larger wavelength range and the best fitting combination of models from step 2 as the comparison template.

This method has proved to be very powerful and allows us to recover faint emission line profiles such as the [N I] doublet at 5199 Å. An example of how this method works can be found in Fig. 5.8.

5.4.2 A KDC & a central disk in NGC 7332

NGC 7332's kinematics reveals a smooth uniform stellar velocity field rotating along the major axis of the galaxy (see Fig. 5.4). The velocity field appears consistent with cylindrical rotation, although this result will have to be confirmed with some detailed modelling. Furthermore, we have discovered a KDC in NGC 7332. This result is shown in Fig. 5.4 as a 'S-shape' feature of the zero-velocity contour line in the velocity map and is confirmed by the long-slit STIS data retrieved from the archive. Figure 5.3 shows an enlarged comparison of the *SAURON* data and the STIS velocity profile along a PA$\approx$ 160°. This indicates that the angular momentum of this structure sits in a different plane w.r.t. the one defined by the overall kinematics and therefore its position angle is also rotated with respect to the major axis of the galaxy (PA=155°). In order to obtain an estimate of the

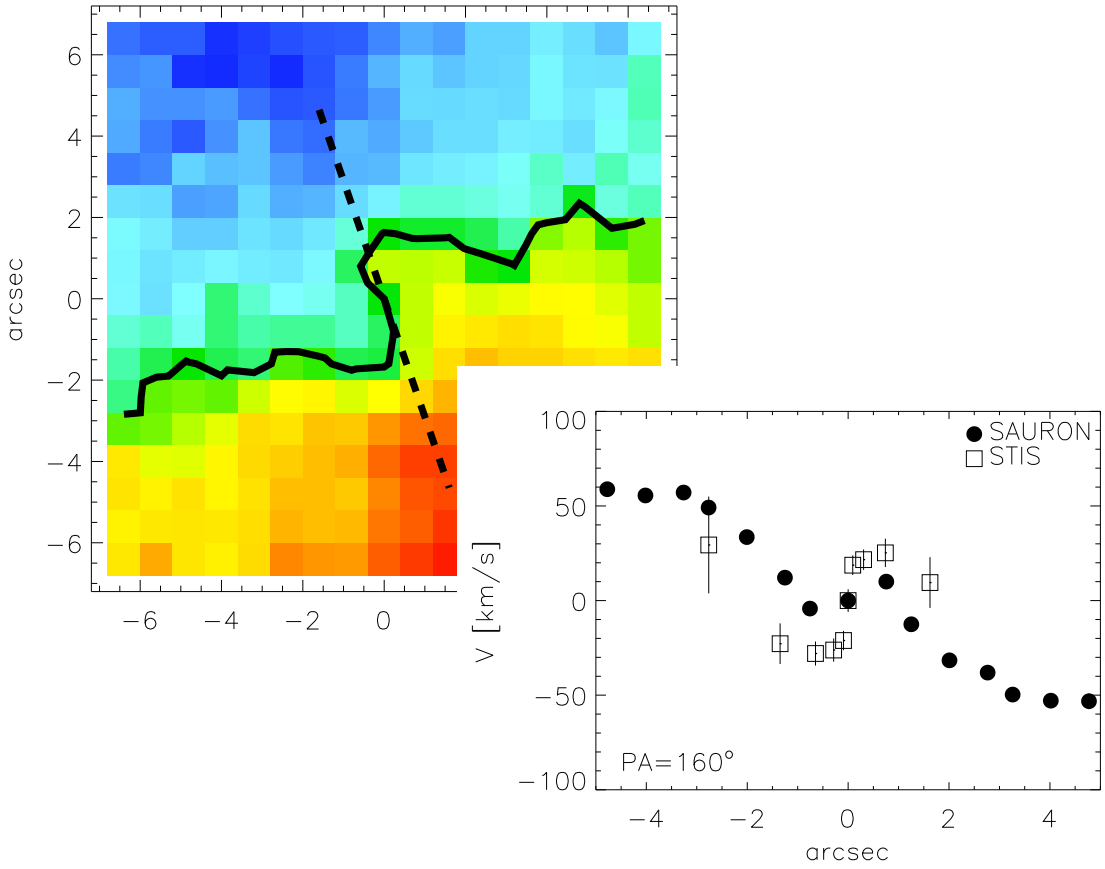

Figure 5.3: Comparison of the *SAURON* and STIS velocity profiles at a position angle of 160°. Color scheme and scale as in Fig. 5.4.

position angle of the KDC, we have modelled our velocity field on large scales with an isothermal thin disk (Freeman 1970). We have excluded from the fit the central 2.5″ to avoid biases in the fitting model because of the KDC. The results of our analysis is shown in Fig. 5.5. Our best model fit gives a major axis position angle for the galaxy of 159.9° which is consistent with the major axis photometric PA within the *SAURON* field. The residual image highlights the KDC component (within the circle). Measuring the position angle of the highest and the lowest residual points, within that circle, we can get an estimate of the KDC position angle. In this case the KDC appears to be ∼25° misaligned w.r.t. the galaxy's major axis (PA=155°). Examples of KDCs that are resolved in 2D are becoming more numerous in the literature, mainly because of the arrival of the IFUs (e.g. NGC 4365, NGC 4406, NGC 5813, Peletier et al. 2001). The existence of KDCs in early-type galaxies is strong evidence that mergers play an important

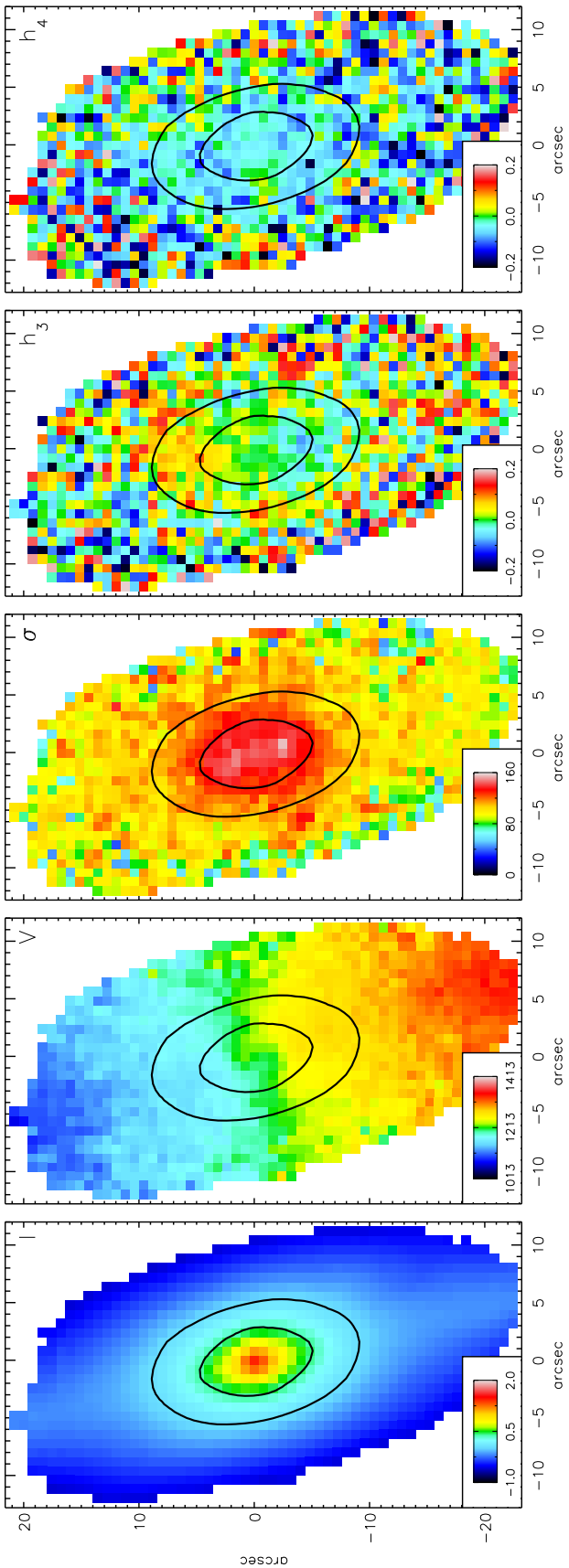

Figure 5.4: Stellar kinematics for NGC 7332. a) the reconstructed total intensity in $\log_{10}$ scale, b) stellar mean velocity (in km s^{-1}), c) velocity dispersion (in km s^{-1}), d), e) Gauss-Hermite moments (h_3 and h_4).

role in the formation and evolution of these systems (e.g. de Zeeuw & Franx 1991).

The velocity dispersion map shows a dip along the major axis of the galaxy (see fig. 5.4). Central velocity dispersion minima are generally understood as tracing embedded disks, bars, or low-mass spheroids (i.e. Emsellem et al. 2001). In our photometric analysis (sec. 5.3) we showed that indeed this is the case for NGC 7332. Moreover, the same analysis reveals that this disk is also misaligned with respect to the major axis of the galaxy (PA=155°) in ≈5°. An independent confirmation comes from our kinematic analysis. First, the Gauss-Hermite moment h_3 shows a change of behavior (∼0.2 in amplitude) in the region where the central disk is expected. This is consistent with an asymmetrical drift were the superposition of a moderately rotating spheroid (i.e. the bulge) and a fast-rotating disk. Furthermore the residual image in Fig.5.5 reveals an excess of velocity at same location described by the photometry, velocity dispersion and h_3 maps.

Therefore we have discovered a remarkably unusual situation in the core of NGC 7332, with a misaligned central disk (PA∼160°, and a kinematically decoupled core rotating at an angle of 25° w.r.t. the main body of the galaxy.

5.4.3 Comparison with Fisher, Illingworth & Franx (1994)

In order to check the accuracy of our results, we have compared our results with the best work up to date on the stellar kinematics of this galaxy (Fisher, Illingworth & Franx 1994). In their paper they measured stellar kinematics along several position angles of the galaxy.

In Fig.5.6 we show a comparison of our results with those by Fisher, Illingworth & Franx (1994) along two position angles (PA=155°, 65°), the major and minor axis of the galaxy respectively. The agreement is very good in general, but specially in the velocity profile along the major axis. We seem to be able to reproduce the rotation velocity profiles on both axes. We have checked whether we find the counter-rotating core from Fisher's and our own profile at PA=155°, but there is very little evidence for it at that position angle, strengthening the importance of Integral Field units. Finally we find a very good agreement between the velocity dispersion profiles for both axes.

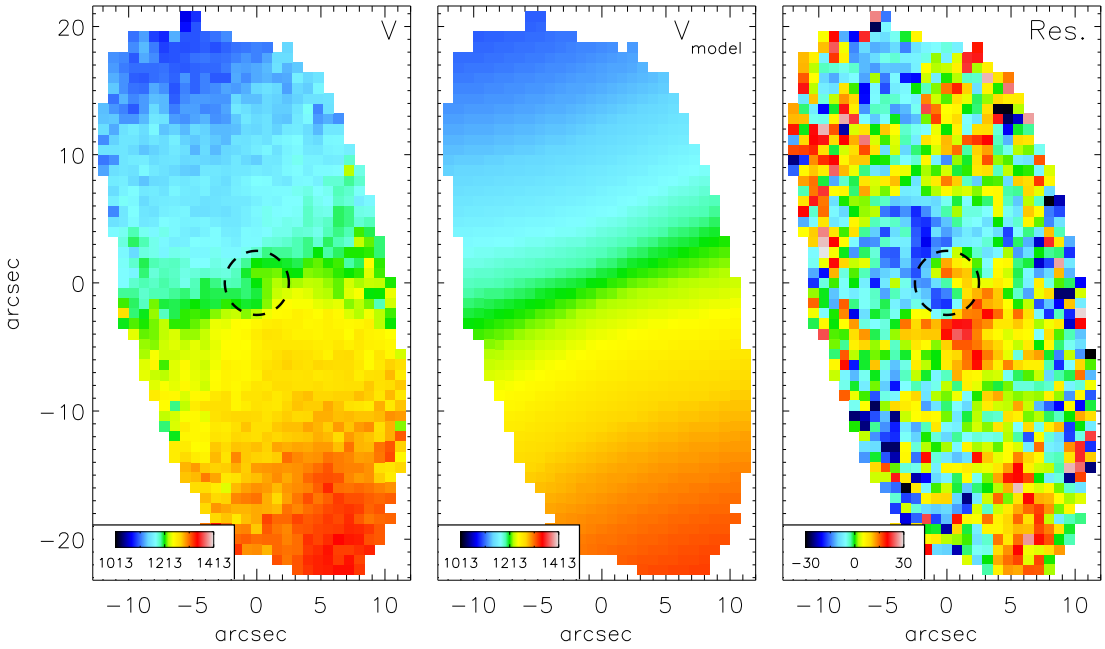

Figure 5.5: Fitting of our velocity field by an isothermal thin disk model (Freeman 1970). a) the velocity field (as presented in Fig. 5.4), b) the fitted model, c) the residual image (V-V_{model}). All the maps are in units of km s^{-1}.

5.5 Gas Kinematics

This galaxy is best known for its peculiar gas structure. The only references up to date on this matter are those of Bertola, Buson & Zeilinger (1992), Fisher, Illingworth & Franx (1994) and Plana & Boulesteix (1996), where they observed 2 kinematically different gas components. Fisher, Illingworth & Franx (1994) measured the [O III] emission using several slits along different position angles, whereas Plana & Boulesteix (1996) obtained complete 2D emission maps from using the Hα line. In our case we are able to measure up to 3 different emission lines within the wavelength region covered by *SAURON* (Hβ, [O III], [N I]). A pure emission line spectra datacube has been obtained using the procedure described in Sect. 5.4.1.

We have measured the Hβ, [O III] and [N I] kinematics by fitting a single Gaussian to the three lines simultaneously. This relies on the assumption that all the lines have the same velocity and velocity dispersion. In our analysis this assumption seems to be generally true. We have found a main counter-rotating component and very small traces of a much fainter co-rotating one. We were able to easily

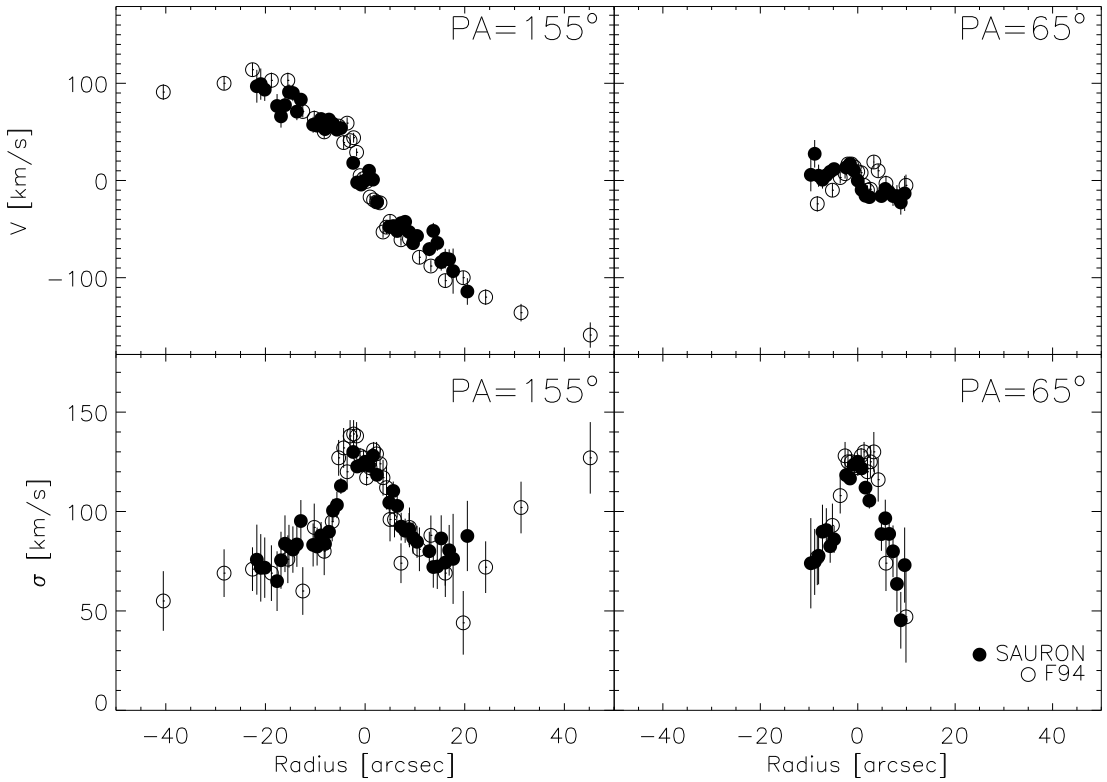

Figure 5.6: Comparison of the NGC 7332 kinematic profiles from *SAURON* (solid symbols) and Fisher, Illingworth & Franx 1994 (F94, open symbols) at two position angles (PA=155° and 65°).

obtain [O III] intensity values for the main component. However the second component was much more difficult to resolve, not only because of its low intensity value but also because of our limited spectral resolution (3.6 Å FWHM). Given the fact that Plana & Boulesteix (1996) and Fisher, Illingworth & Franx (1994) already detected 2 components, there is no doubt that the co-rotating component is real. In Fig. 5.7 we present the Hβ, [O III] and [N I] gas intensity maps as well as their kinematics in the form of mean radial velocity and velocity dispersion maps. The intensity distribution of the Hβ and [O III] lines appear to be similar, although the Hβ intensity is somewhat fainter and can not be fully mapped. The velocity and velocity dispersion maps show quite unusual kinematics, with almost no signs of circular motions. Furthermore we find an unexpected localised blob (350 km s^{-1} relative to the central velocity) at around 7″ SW from the centre of the galaxy that coincides with an increase in [O III] intensity. Sitting on the right wing of the Mgb (5170 Å), the [N I] intensity distribution is very difficult to detect. Our analysis shows very small amounts of [N I] emission within the

SAURON field. All these results are consistent with the picture described by Fisher, Illingworth & Franx (1994) from their multiple slits. Here, however, it is much easier to see that the gas is in a stream, not centrered on the galaxy nucleus.

As we mentioned in Sec. 5.4.1 we have made use of a novel technique to remove the contribution of gas to the galaxy's spectra. An example of how this method works is shown in Fig. 5.8. There, we show the fitted combination of models (red line) on top to the underlying galaxy spectra (black line). Below we show the difference between the two. This residual spectrum has been offset for displaying purposes. We show the results of our fitting procedure at 4 different locations of the galaxy. The main spectral features have been also noted. Our analysis reveals an excellent fit to the galaxy's spectra. The residual spectra, used here to derive gas kinematics, present a nearly flat continuum and highlight the gas emission found. [O III] appears to be strongly present everywhere in the galaxy, as shown in Fig.5.7. The Hβ and [N I] emission, although present, are much fainter than the [O III]. Since we have found traces of the second component only in a reduced region of our field, we have not attempted to derive its velocity field. Instead we show the location where we find the co-rotating component and an example of its line profile (Fig. 5.8, bottom right panel).

Contrary to the stellar velocity fields, were the stars in disk components rotate around a certain axis, gas velocity fields may also experience inflows and outflows of material. The emission line maps are really puzzling. First of all the intensity distribution of the main component appears to be somehow warped, but only towards one end of the galaxy. The major axis of the bulk of [O III] is clearly misaligned with respect to the main stellar disk. The velocity field seems quite disturbed, with no apparent signatures of ordered motions. If any, we find an important concentration of gas to the SW of the galaxy centre moving faster than the surrounding material. This feature could have its counterpart on the SE from the centre. This is indeed a very complicated picture with no easy interpretation. What we can say, however, is that there is a large amount of ionised gas in this, apparently gas-free galaxy.

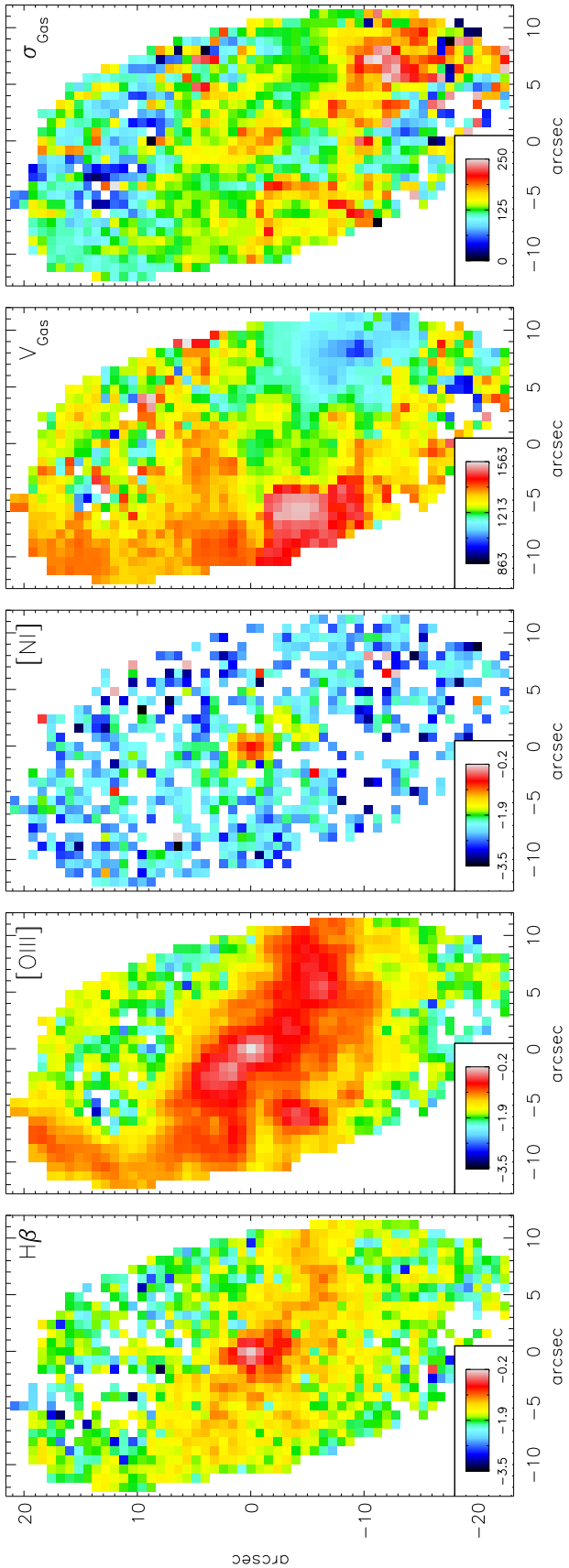

Figure 5.7: The Hβ, [O III] and [N I] doublet gas distribution and kinematics. The intensities are in $\log_{10}$ scale, velocity and velocity dispersion are expressed in km s^{-1}.

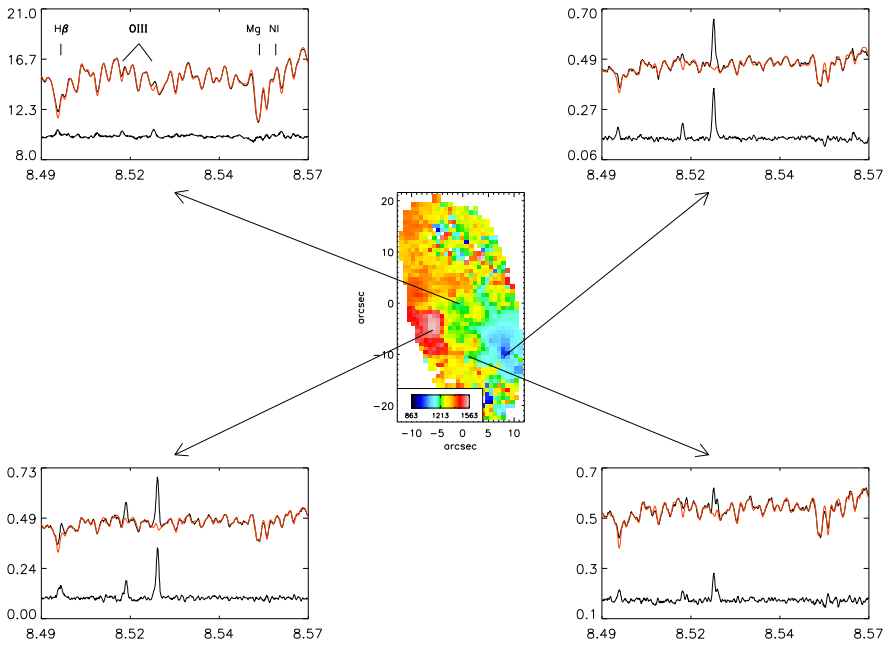

Figure 5.8: Optimal template fitting for NGC 7332. The red line represents our best fitting template (see Sect. 5.4.1) for the underlying galaxy spectra (black line). The residual spectra, is also shown below and offset for displaying purposes. The central panel represents the gas velocity field as shown in Fig. 5.7. Small traces of a secondary co-rotating [O III] component are shown in the bottom right panel.

5.6 Stellar Populations

We have made use of our flux calibrated *SAURON* datacube to measure the line-strength indices available in our wavelength domain (Hβ, Fe5015, Mgb and Fe5270) in the Lick/IDS system (Worthey et al. 1994). We have measured the absorption line-strength indices following the procedures described in §4.1 of de Zeeuw et al. (2002). The Fe5270 index cannot be fully mapped due to instrumental limitations at the redshift of the galaxy.

We have measured the indices before and after applying our emission cleaning procedure. We present the resultant line-strength maps in Fig. 5.9. In the original data we find that Hβ and Fe5015 maps are affected by emission (Fig. 5.9, top row). These regions are directly connected to the presence of significant amounts of nebular emission and therefore is not surprising that the Hβ line has been filled-up with emission as well as Fe5015 has been affected by its proximity to the [O III] emission line.

The emission-free datacubes reveal a significantly different picture (Fig.5.9, bottom row). Whereas the regions seriously affected by emission in the Hβ and Fe5015 maps have virtually disappear, the Mgb and Fe5270 line strength maps show the same behavior as before the emission cleaning procedure. If the picture shown here is consistent with previous works in the literature, this is a strong evidence that the optimal template fitting method is a very powerful tool to detect the gas contribution in galactic spectra.

After the cleaning process, we find that the Hβ distribution remains nearly constant over the field, whereas the Mgb and Fe5270 indices increase in the inner regions. There are 2 scenarios likely to produce this behaviour (Bender & Paquet 1999): a) The bulge is older than the disk but has a similar metallicity, b) The bulge is more metal rich and younger than the disk. The first case explains the Mgb map, but it cannot explain the Hβ strength. Our Hβ index is much weaker than it should be if the disk were younger than the bulge. Nebular emission could play an important role here, but, as suggested by Bender & Paquet (1999), this would require an uniform increase of the emission distribution as we move outwards from the centre to compensate for the expected high Hβ value of a young disk. Since this is not the case we can rule out this option. The second option, however, explains our result naturally and more importantly agrees with previous results in the literature. Colors (Balcells & Peletier 1994) and spectroscopy (Vazdekis & Arimoto 1999; Terlevich & Forbes 2002), find a young bulge in NGC 7332 and give it a central luminosity weighted age between 4 to 6 Gyr. Determining ages and metallicities can be achieved if one has enough and accurate line-strength measurements. Traditionally index-index diagrams, such as Hβ vs <Mgb· Fe5270>, together with models predictions are used to estimate such values (i.e. Davies et al. 2001). In our case we are limited by the fact that the spatial coverage for the Fe5270 index is not complete with *SAURON*, and more importantly at least two out of the four indices are clearly affected by emission in some regions of the galaxy. However, the fact that we map the line strength in 2D and that we have also obtained emission free spectra, allows us to test our ages and metallicities predictions in different locations of the galaxy.

Since we can not fully measure the Fe5270 index in 2D, we have defined a new index <Mgb· Fe5015>= $\sqrt{\text{Mg}b \cdot \text{Fe5015}}$, in order to minimize the effect of Mg/Fe abundance ratios everywhere in the galaxy. In Fig. 5.10a we show the results of our analysis averaging 1.6$''$ around the 4 positions selected in Fig. 5.8. Fig. 5.10b

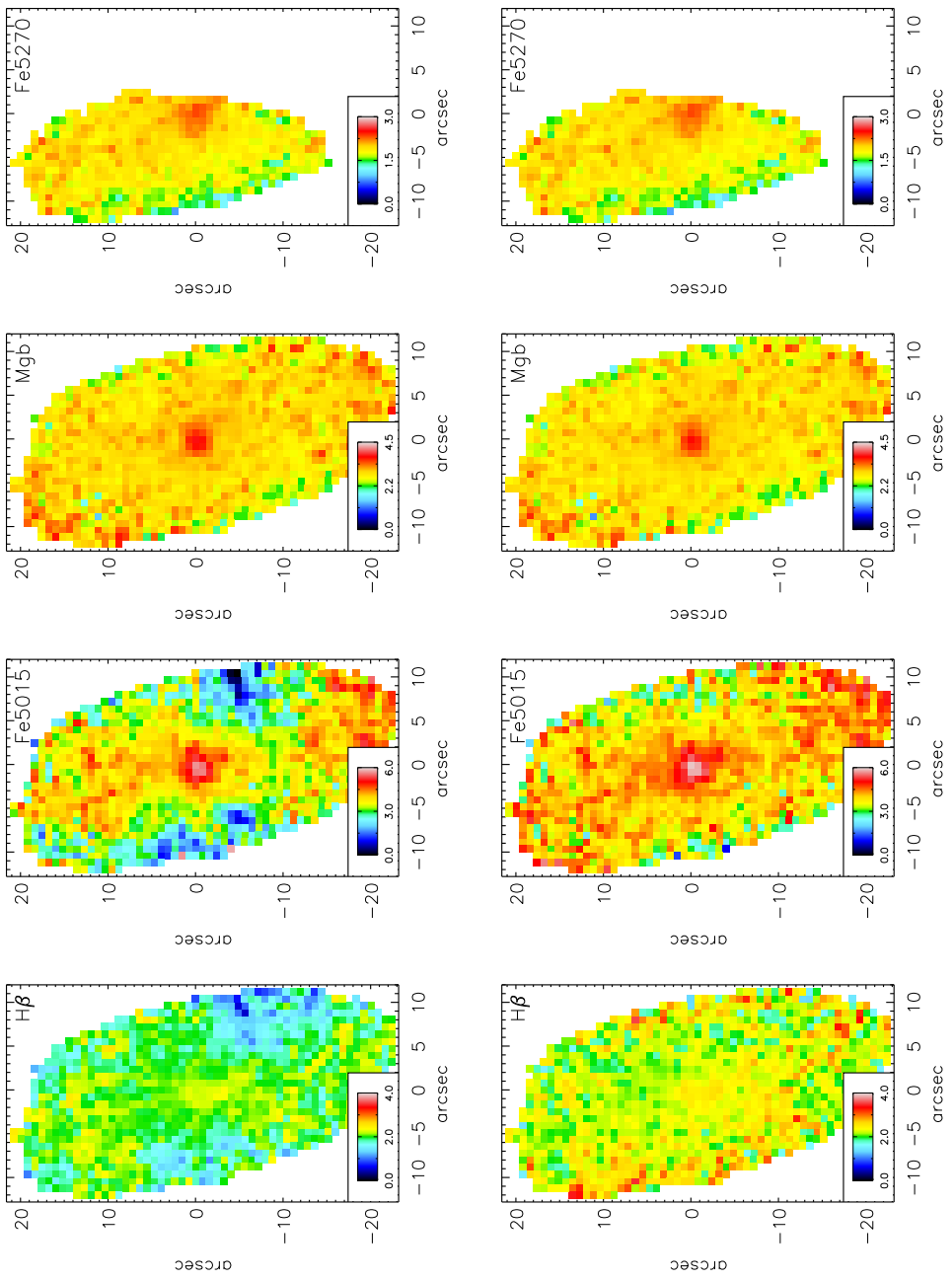

Figure 5.9: Hβ Fe5015, Mgb and Fe5270 line-strength maps from the *SAURON* data. The indices have been corrected to the Lick/IDS system (Worthey et al. 1994). In the top row we display the raw indices. In the bottom row they have been corrected for nebular emission.

gives the <Mg$b\cdot$ Fe5270> index measurements in those 2 regions for which <Mg$b\cdot$ Fe5270> is available. Solid symbols represent measurements from the *cleaned* datacube, whereas open symbols represent measurements from the original datacube, and therefore affected by nebular contamination. Circles represent the centre of the galaxy (i.e. the KDC), triangles represent the localised knob of gas SW of the galaxy (Fig. 5.8, bottom left panel), squares show the location shown in Fig. 5.8 (top left panel). Finally diamonds represent the faint, co-rotating [O III] component (Fig. 5.8, bottom right panel). The influence of nebular emission on the indices becomes clear in the figure by looking at the differences between the original and *clean* and clean versions. Noteworthy is the remarkable difference found for the squares and triangles. While those affected by emission are clearly outside the grid of models, the *clean* ones provide at least a solution within the range of parameters. Interesting is the fact that the estimated luminosity weigthed age for those regions, that belong to the disk of NGC 7332, provide an averaged age between 6 and 7 Gyr and metallicity below solar. A similar picture is found in Fig. 5.10b. The centre of NGC 7332 (i.e. the KDC) shows an mean luminosity weigthed age between 4 and 5 Gyr in the original set of data, and $\sim$3 Gyr in the *cleaned* one. This picture is remarkably similar to other works found in the literature. The nucleus of NGC 7332 has been reported to host a young population of luminosity weighted age between 4 and 6 Gyr, depending on authors (Vazdekis & Arimoto 1999; Terlevich & Forbes 2002). The color gradients are also small, in the disk and bulge (Peletier & Balcells 1997), which in our case implies that the age of the whole galaxy cannot vary wildly across the galaxy. This argument also supports our analysis here from the *cleaned* data points where the luminosity weigthed age ranges from 3 to 8 Gyr. It is important to note that the estimations of age from the *cleaned* data depend on the particular set of models used in the library to create the optimal template. Because of the way the *clean* galaxy spectra is determined, the obtained luminosity weigthed age will be given by the combination of models used. Therefore estimations of ages from the *clean* Hβ index are uncertain. A possible way out is the use of age-sensitive absorption lines not significantly affected by emission (i.e. Hγ, Hδ), something not achievable with *SAURON*.

At this moment we are working on a paper in which we will give a more detailed analysis of the stellar populations, including colors and more indices.

5.7 Discussion

KDCs and multiple gaseous components are common in the literature all along the Hubble sequence (see Merrifield, Fisher & Kuijken 1996). In recent years with the arrival of a new generation of spectrographs (Integral Field Units) significant improvements have been made towards the interpretation and understanding of such structures. As we have shown in previous sections, NGC 7332 presents all kind of features. Such features are not new and wouldn't be a surprise if found on itself in a galaxy. The unusual picture is to find them all together coexisting in one galaxy. Therefore this galaxy, like many others in the literature (i.e. NGC 4550, Rix et al. 1992 and NGC 7331, Prada et al. 1996), serves as the perfect benchmark to test theories of galaxy formation and evolution.

5.7.1 The observational evidence

NGC 7332 has revealed several peculiar structures. In the present paper we have found a KDC (inner 2.5″) rotating at an axis ∼25° w.r.t. the galaxy's major axis as well as a kinematical evidence for a central disk extending up to r=8″ also misaligned w.r.t the major axis defined in the outer parts ($\Delta \approx 5°$). Multiple gaseous systems are also found: a disturbed main [O III] component counter-rotating w.r.t. to the stars and small evidence of co-rotating [O III] gas. Our line strength analysis reveals a young galaxy showing small age differences between the centre and the inner disk, in agreement with others (Peletier & Balcells 1996; Vazdekis & Arimoto 1999; Terlevich & Forbes 2002). Several other works in the literature have addressed different aspects of this galaxy. Photometrically its light profile can be decomposed into a bulge, central disk, an exponential main disk and a fourth flat structure seen between 14″ to 25″ (Seifert & Scorza 1996). The color gradients, in the disk and the bulge, are also small, implying that the age of the whole galaxy has to be similar (Peletier & Balcells 1996). H I is present in NGC 7339 (Haynes 1981) (the neighbor galaxy), but its detection is very weak in NGC 7332 (Knapp, Kerr & Williams 1978). The amount of X-ray emission gas has been estimated to be $\sim 10^{8.8}$ $M_\odot$ (Roberts et al. 1991, considering the galaxy as a point source). The total amount of ISM mass, from the H I and the X-ray masses, has also been estimated to be $\sim 10^{8-9}$ $M_\odot$ (Fisher, Illingworth & Franx 1994), which is a small fraction compared to the galaxy's total mass (10^{11} $M_\odot$ Roberts et al. 1991). The ratio of the IRAS flux at 60 and 100 μm, although

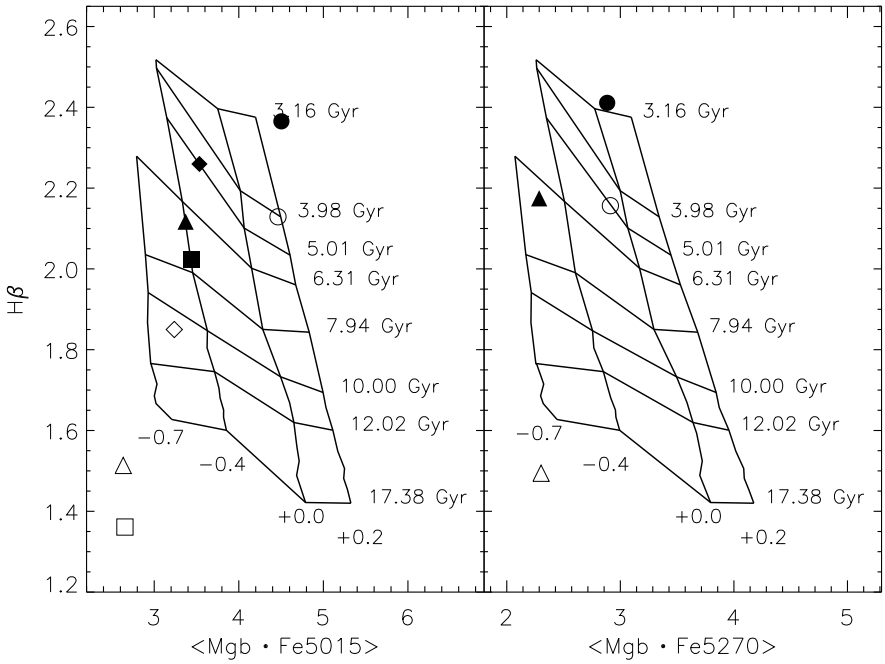

Figure 5.10: The Hβ vs <Mgb · Fe5015> and Hβ vs <Mgb · Fe5270> equivalent width diagrams. Solid symbols represent measurements from the *clean* datacube, whereas open symbols represent measurements from the original datacube. Circles represent the inner 1.6″ of the galaxy, triangles represent the localised blob of gas SW of the galaxy, squares show the location shown in Fig.5.8 (top right panel) and diamonds represent the faint, co-rotating [O III] component (see Sec. 5.6 for more details).

marginal, suggests that some current level star formation must be still going on (Fisher, Illingworth & Franx 1994).

None of the previous works seem to be able to draw the perfect picture that fully explains the formation history of NGC7332. This is partly because every new study on this galaxy adds new surprising features which changes the simple picture one has of the formation of this galaxy.

5.7.2 Formation Scenarios

Our current knowledge of formation of decoupled cores is mainly understood in the framework of the hierarchical model (Kauffmann, Guiderdoni & White 1994), which involves single or multiple merging steps. The KDC would correspond to the last major burst of star formation (Davies et al. 2001). On the other hand central disks in S0 galaxies are not scarce, and they turn out to be frequent

among galaxies of this Hubble type (Emsellem et al. 1996; Seifert & Scorza 1996), although it is not clear yet what mechanism triggers their formation. Counter-rotating gas w.r.t the stars has been found to be significant among S0s and it is mainly understood to have external origin (Bertola, Buson & Zeilinger 1992). Now that we have presented the most important observational features of the galaxies, we will discuss a number of possible explanations for the origin of this galaxy.

Secular evolution

It is generally assumed that boxy profiles in edge-on galaxies are produced by bars (Kuijken & Merrifield 1995; Bureau & Freeman 1999; Merrifield & Kuijken 1999). The presence of a bar NGC 7332 has been discussed in the literature by Fisher, Illingworth & Franx (1994) in the light of the existence of a plateau in the surface brightness profile and a boxy bulge. We argue, however, that we are not dealing with a boxy bulge, but a boxy component at $\sim 10''$ since our photometric analysis gives a bulge radius $\sim 4''$ (see Sect. 5.3). The detection of bars in edge-on galaxies is always difficult. Our analysis of the stellar kinematics do not show any strong evidence for the presence of a bar in NGC 7332 (i.e. figure of eight in the Position-Velocity diagram), which we should be able to detect in our *SAURON* field. Therefore, although our results are inconclusive, there is no indication of a formation scenario driven by secular evolution in this galaxy.

Mergers

Given the large number of peculiar features this galaxy presents, a sequence of minor mergers is a very likely explanation for the recent formation history of NGC 7332. Photometrically the galaxy is a regular edge-on S0 galaxy with no signs of shells, filaments or arcs. Nebular emission is present everywhere in the galaxy with signatures of irregular motions. This is suggestive of gas infall at the present time. The stellar populations are found to be young (3-8 Gyrs). The galaxy has no dust (Peletier & Balcells 1997) and very little gas, which is not atypical for S0 galaxies in general. Given the absence of dust, the large amount of ionised gas is surprising. Hierarchical models predict that the bulge forms before the disk. Under this picture the disk is most likely younger than the bulge since it is assumed to be part of the last major accretion of material in the hierarchical

formation process. If a small satellite, not big enough to disrupt the disk, is accreted by the galaxy it could provide the necessary gas to fuel a burst of star formation in the centre of the galaxy producing an effect of rejuvenation. It is also possible that such merger event would be responsible for the KDC observed and the irregular gas distribution across the galaxy. This fact could also explain the current level of star formation. However the dynamical timescale for the settling of gas is $\approx 10^8$ yr in this galaxy, which is much smaller than the 4-6 Gyr we find from its stellar populations. Therefore a different process is required to explain the origin of the amount of gas we find today in NGC 7332.

On the other hand one could argue that S0 galaxies do not conform a unique set of galaxies, but are more like a transient state in which they evolve from one morphological type of galaxies to another. Is it a case of a fading disk?. This line of argument this does not appear to be the case for NGC 7332, since the disk surface brightness corrected for inclination ($< \mu >_{B,0}$=18.48 mag, Peletier & Balcells 1997) is higher than spirals ($< \mu >_{B,0}$=21.7 mag, Freeman 1970).

Interaction with NGC 7339

New light can be shed on the evolution of NGC 7332 by considering the interaction with its neighbour galaxy NGC 7339. This is a spiral galaxy redshifted by $\sim$55 km s^{-1} (Burbidge & Burbidge 1959) w.r.t NGC 7332. Some interaction could indeed have occurred between these two galaxies providing NGC 7332 the necessary gas that we see today in NGC 7332 counter-rotating. Bertola, Buson & Zeilinger (1992), as mentioned above, found an important amount of S0 galaxies in which extended emission was found in counter-rotation and discussed the external origin of gas in S0 galaxies. If some kind of interaction is due to be found between the two galaxies, given the young age of NGC 7332, some kind of tracer should remain between the two galaxies. At this moment we have not been able to find evidence of such link, although we are already on our way to obtain observations to estimate the H I content in this pair of galaxies.

In Fig.5.11 we present a sketch of a sequence of events likely to have happened during the formation and evolution of NGC 7332. The bulge and disk of the galaxy were the first to form through some unknown major star formation event about 8 Gyr ago. An important amount of gas is required to produce the central disk we find in this galaxy. Given the kinematics shown by the central disk, it is

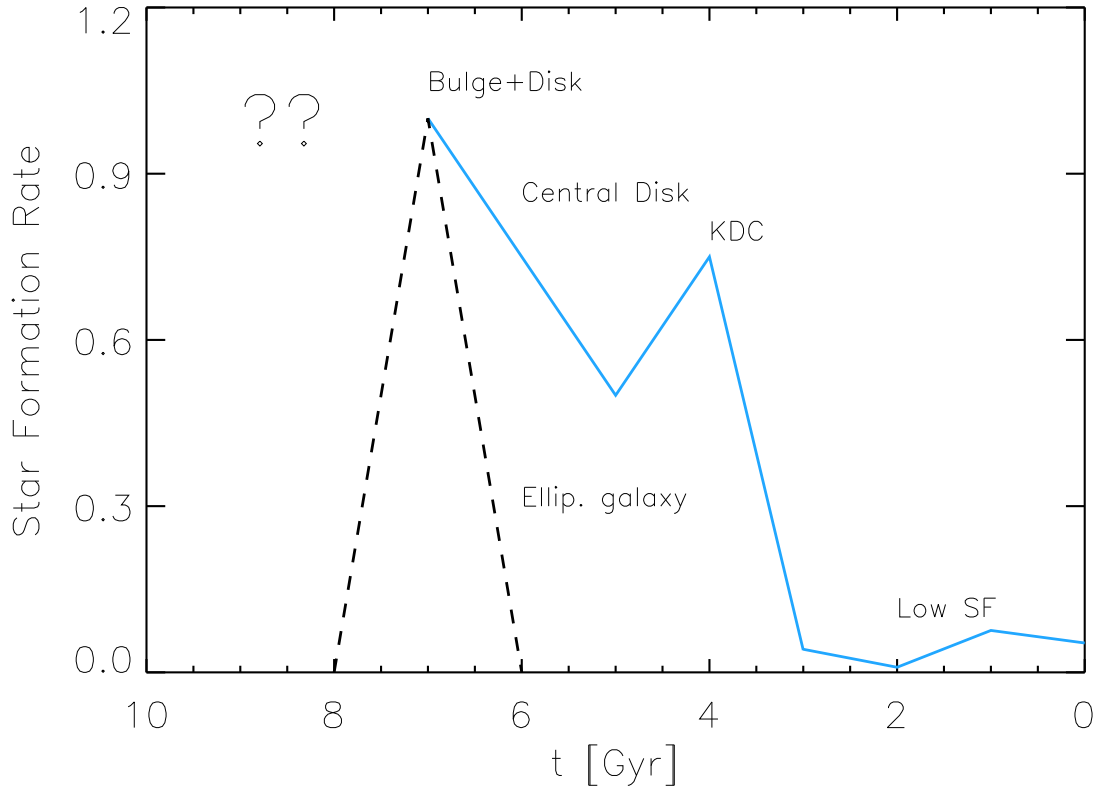

Figure 5.11: Schematic view of the formation and evolution of NGC 7332. Note that the timescales for the different formation stages are not necessarily as drawn.

likely that the necessary gas is part of the last stages of this major event. It seems likely that the process that originated the galaxy was a major merger leading to the production of a large number of stars. On the other hand, what seems to be clear is that, this process is unlikely to have generated the misaligned KDC that we have discovered in the galaxy. In that respect, a recent minor merger not only would explain the KDC but also the recent burst of star formation necessary to make the bulge look younger (∼3-4 Gyr) than the rest of the galaxy. Finally the remaining ionised gas that we still find infalling in the galaxy, is probably due to its interaction with NGC 7339.

In the light of the results found on NGC 7332 and our discussion of possible formation scenarios, it looks like a sequence of events is the most likely explanation for the formation and evolution of this galaxy. The initial major event would be responsible for the formation of the central disk and a minor merger could explain the KDC we see today.

5.8 Conclusions

In this chapter we have shown new results of the edge-on S0 galaxy NGC 7332 using integral field spectroscopy. We have made use of the large set of unusual phenomena taking place in this galaxy simultaneously, to test the current lore of formation and evolution theories.

We present the discovery of a Kinematically Decoupled Core misaligned ($\approx$25°) w.r.t the galaxy's kinematical major axis. We also provide kinematic evidence, showing in the velocity dispersion and h_3 maps, of the presence of a central disk. This structure is also shown in our model of the velocity field, assumed to behave like an isothermal thin disk (Freeman 1970).

NGC 7332 is a galaxy that presents significant emission in the spectral range we are working on. In particular Hβ (4861 Å) , [O III] (4959 and 5007 Å) and [N I] (5199 Å). In order to *clean* the emission present in the spectra, which would affect our stellar kinematics, we have made use of a novel technique to remove the gas contribution and obtain pure stellar kinematics. At the same time this method allows us to obtain a pure emission datacube from which we have extracted the gas kinematics.

The emission maps, measured from the Hβ, [O III] and [N I] lines, reveal a unique picture, showing a disturbed gas distribution, specially in [O III], counter-rotating w.r.t the stars and with signs of non circular motions. Furthermore, we have found traces of a faint co-rotating component w.r.t the main body of the galaxy.

The analysis of its stellar populations shows that NGC 7332 is young object ($\sim$6 Gyr), not only in the disk but also in the bulge, as previous works (Balcells & Peletier 1994; Vazdekis et al. 1996; Terlevich & Forbes 2002) have found. Similar color gradients (Peletier & Balcells 1996) in the disk and the bulge also support this result.

We have shown that a sequence of events is the most likely explanation for all the peculiar features we find in NGC 7332. A major event must have taken place building up the galaxy we see today. The central disk is is likely to have been produced at the final stages of such event. An interaction with the neighbour galaxy NGC 7339 seems to be responsible for the amount of ionised gas still infalling in the galaxy. Furthermore the formation of the KDC is more likely to be produced by a minor merger occurred 3-4 Gyr ago, providing the rejuvenation

of the inner parts of the galaxy (i.e. bulge). All these processes support the hierarchical merger picture for the formation of NGC 7332.

Chapter 6

Conclusions

The aims of this thesis were the investigation of the internal kinematics and stellar populations of bulges in nearby galaxies. In order to do that we have reduced and analysed minor axis spectroscopic data of a subset of 19 of the well-defined sample of bulges of galaxies ranging from S0 to Sbc from Balcells & Peletier (1994). The galaxies were required to have an inclination i $>50^{\circ}$ to minimize the amount of disk light which projects onto the bulge and ensure that extinction from dust in the disk would not dominate the colours measured on one side of the bulge. Our study of this sample has highlighted the galaxy NGC 7332 as a peculiar object, not only for its unsual stellar and gas kinematics (Fisher, Illingworth & Franx 1994; Plana & Boulesteix 1996) but also, because this object lies significantly away from the Fundamental Plane (FP) defined by early-type galaxies and the rest of our sample (see chapter 3). In order to understand the origin of this behavior we have obtained Integral Field Spectroscopy data for this galaxy using *SAURON*. The data reveals a significant amount of new features that, together with previous studies, allows us to use this object as a perfect benchmark to test theories of galaxy formation and evolution.

The overall conclusions in this thesis are that bulges, in the range of morphological types we are dealing with, are as old as elliptical galaxies and if younger they cannot differ more than 2.5 Gyr w.r.t. the ellipticals (as derived from offsets from the FP). We have also discovered a significant anti-correlation between the CaT* line strength and the central velocity dispersion for our sample of bulges. The same result has been recently found by two independent groups (Cenarro et al. 2003; Saglia et al. 2002) for elliptical galaxies . This finding is surprising since it is the first evidence of a metal line index anticorelating with σ. On the other

hand, we have studied the possibility of using SSP models (Single-age, single-metallicity) as kinematical templates to extract mean velocities, velocity dispersions and higher order moments (h_3,h_4) instead the traditionally used template stars. Our analysis shows that SSP models, at least in the Ca II triplet region, are as effective and often provide better kinematics estimates than stellar templates. The kinematic results reveal that bulges in this sample are not featureless. We have distinguished two kinds of minor axis rotation: one due to misalignments of the slit w.r.t. the line of nodes, and the other showing velocity features due to slight variations in the kinematic structure, related to inner components such as disks or bars. The velocity dispersion profiles of the sample are also intriguing, showing two kinds of shapes: flat or cuspy profiles. Contrary to what has been found before (Kormendy 1993), we do not find a direct correlation between the velocity dispersion gradients and morphological types, although we do find correlations with the central surface brightness of the disk and the bulge ellipticity. Our two-dimensional spectroscopic study of NGC 7332 has revealed a Kinematically Decoupled Core (KDC) whose major axis is misaligned $\approx$75° from the galaxy's major axis. We have also found kinematical evidence of a fast rotating central disk slighlty misaligned as well w.r.t. the galaxy's major axis. The gas kinematics, from the Hβ, [O III], and [N I] emission lines, shows signatures of irregular rotation and non uniform distribution. The stellar population analysis shows that the galaxy is young everywhere. We have evidence for a sequence of events taken place in NGC 7332 forming the central disk, KDC and infalling gas we have found in the galaxy.

We will proceed to list, in more detailed, the main conclusions from this work:

1. We have made use of SSP models from Vazdekis et al. (2003) at 1.5 Å resolution, together with the traditional template stars, to measure minor axis stellar kinematics in our sample of galaxies. We have compared the results obtained with the different templates and determined that synthetic models produce slightly better results than those from stellar templates in the Ca II triplet region. We find that synthetic models help to reduce several drawbacks such as the template mismatch problem affecting all the traditional kinematical methods. A good agreement is found with previous high-quality kinematic profiles from the literature.

2. Our kinematic analysis shows small amounts of minor axis rotation in al-

most half of our galaxy sample. We find two types of minor axis rotation: rotation in the outer parts, probably due to slit misalignments, and inner rotation, which is associated to small disks, as evidenced by disky deviations of the isophotes from pure ellipses.

3. We have found some cases of kinematically offset nuclei (NGC 5707 and NGC 7331). For NGC 5707 a nuclear disk or bar extending 1 arcsec, which is well aligned with the major axis of the outer disk and partially obscured by a dust lane might be responsible for the offset velocity at the photometric centre of the galaxy. For NGC 7331 it is unclear what the cause of such offset is. In any case the kinematics of this galaxy has shown to be complex (Prada et al. 1996).

4. We show that flattened bulges tend to show shallow velocity dispersion gradients and similar dispersions in bulge and inner disk, possibly indicating a thickened disk structure for these bulges. We also find that our velocity dispersion gradients correlate with the central surface brightness of the disk and the bulge ellipticity, but do not correlate with disk ellipticity. Gradients do not correlate either with bulge luminosity, bulge central velocity dispersion, bulge Sérsic index n, bulge effecitive surface brightness, galaxy morphological type, and disk or bulge effective radii.

5. We find that our sample of bulges of early-type spirals lies slightly below the FP, as defined by E and S0 galaxies, both in the B and K bands. The fact that bulges lie so close to the FP of ellipticals and S0s implies that their formation epoch must have been similar to that of cluster Es and S0s. There is one object, however, that lies significantly away from the relation (NGC 7332). Our observational errors do not seem to be able to explain its offset.

6. Both age and unaccounted rotation effects are likely to contribute to the offset observed between bulges and ellipticals. Any single one of these effects can account for the observed offset, by assuming either an age on average 2.5 Gyr younger than the cluster ellipticals and S0s, or by assuming an average $V_{max}/\sigma_0 \sim 0.66$. Because rotation must contribute to the FP offset, the age differential between bulges and cluster ellipticals must be significantly smaller than the mentioned 2.5 Gyr.

7. We find that there is a hint that bulges of later morphological type are situated below the other bulges in our sample, indicating that they have slightly younger ages, again consistent with results from HST colours (Peletier et al. 1999a).

8. We confirm the result of Prugniel, Maubon & Simien (2001) that bulges have a steeper $Mg_{2,0}$ – $\log(\sigma)$ relation than ellipticals or S0s. Contrary to current lore, the $Mg_{2,0} - \sigma$ is not a mass-metallicity relation only, at least for bulges: Younger objects seem to increase the slope of the relation Prugniel, Maubon & Simien (2001). For our sample, however, the slope is shallower than for Prugniel, Maubon & Simien (2001), much closer to that of the ellipticals.

9. We have looked at the Index - σ relation for the Ca II triplet spectral region for our sample of bulges. We confirm a positive correlation between the Mg I index and velocity dispersion, as expected from the behaviour of the Mg_2 index in the optical range found in chapter 3.

10. On the other hand we find a significant anti-correlation between the CaT and CaT* indices with $\log(\sigma)$, in agreement with the results found by Cenarro et al. (2003) for elliptical galaxies. An anti-correlation between CaT* and velocity dispersion can be interpreted as an underabundance of Ca w.r.t. Mg and Fe in more massive galaxies. In principle composite stellar populations including a two different ages (young and old) with the same metallicity or a composite population with an old low metallicity component could also be in place. However we have found that this hypothesis is unlikely to expain the CaT* values since is not able to reproduce the line strength measurements found in the literature for high velocity dispersion galaxies. Finally, an IMF biased towards low-mass stars provides an alternative explanation. In any case none of those explanations alone seem to be able to explain all the observations.

11. Making use of *SAURON* we have studied the two-dimensional stellar, gas kinematics and stellar populations of the S0 NGC 7332. We have found a Kinematically Decoupled Core misaligned ($\approx 25°$) w.r.t the galaxy's kinematical major axis.

12. We have also confirmed previous photometric evidence of the presence of a

central disk, and found kinematical evidence of it in the velocity dispersion and h_3 maps, as well as in our model of the velocity field, assumed to behave like an isothermal thin disk (Freeman 1970).

13. NGC 7332 is a galaxy that presents emission lines in the spectral range we are working in. In particular Hβ (4861 Å) , [O III] (4959 and 5007 Å) and [N I] (5199 Å). Therefore stellar kinematic measurements will be affected by the nebular contamination. In this thesis we have made use of a novel technique to remove the gas contribution in our galaxy spectra and obtain pure stellar kinematics. At the same time this method produces a pure emission datacube from which we have extracted the gas kinematics.

14. The emission maps, measured from the Hβ, [O III] and [N I] lines, reveal a unique picture, showing a disturbed gas distribution, specially in [O III], counter-rotating w.r.t the stars and with signs of non circular motions. Furthermore, we have found traces of a faint co-rotating component.

15. The analysis of its stellar populations shows that NGC 7332 is a young object overall ($\sim$6 Gyr). This is true not only in the centre, where previous works (Balcells & Peletier 1994; Vazdekis et al. 1996; Terlevich & Forbes 2002) have found the same results, but also in the disk.

16. Finally our results, together with more evidence from previous works in the literature, suggest a sequence of events as the most likely explanation for all the peculiar features we find in NGC 7332. Some kind of interaction with the neighbour galaxy NGC 7339 seems to be responsbile for the gas we see today infalling in the galaxy. On the other hand the formation of the KDC is more likely to be produced by a minor merger ocurred 3-4 Gyr ago, providing the rejuvenation of the inner parts of the galaxy (i.e. bulge). The central disk is more likely to have been produced in the last stages of the major event that led to the formation of the galaxy itself. All these processes support the hierarchical merger picture for the formation of NGC 7332.

6.1 Future Work

6.1.1 Short term projects

The analysis and results presented here have led to some small projects which have already started but were not ready to be included in this thesis:

Puzzled by the significant deviation of NGC 7332 on the Fundametal Plane, we have performed tests to check whether the now evident existence of a central disk has produced an overestimation of the photometric parameters and therefore explain this offset. This seems to be the case. Therefore it in the light of the decomposition of the light profiles by Balcells et al. (2003), it would be interesting to see how the new modelling of inner components in the light profiles modify our current view of bulges on the Fundamental Plane. At the same time it would be worthwhile to check the location of known barred galaxies in the FP, but also in the near-IR relations presented in chapter 4 and see the implications for galaxy formation and evolution.

The stellar population analysis we have presented in this thesis for NGC 7332 is the first step of a more detalied analysis we are preparing for this galaxy. We intend to make use of all the data avaliable (spectra and colors) to give an accurate picture of the stellar populations in this galaxy in the two dimensions. To the data we have presented here we will add new major axis long slit observations, that cover a larger wavelength range in the blue, and colors from Peletier & Balcells (1997).

6.1.2 Long term projects

My future research plans include the study of the link between stellar populations of early-type galaxies and the state-of-the-art kinematic data coming from *SAURON* to study the 2D distribution of the different spectral indices. The new IFUs (Integral Field Units) allow us to obtain a 2 dimensional representation of galaxies. Therefore it is possible to study kinematical and population properties across the whole field of those galaxies. A new stellar library project, in which I am involved, is being developed to produce a set of models will help us to determine ages and metallicities at each point by fitting the full spectra, instead of the often hard to use Lick indices (see Kauffmann et al. 2002 for an example of the

application using such a powerful library). Unfortunately, as we have discovered with the *SAURON* survey, emission line contamination is often present not only in late-type galxies (i.e. spirals), but in Es and S0s as well. This introduces a new difficulty to overcome. By using the technique, mentioned above for NGC 7332, we should be able to deal with this problem. It is, therefore very important to explore the use of the forthcoming models to separate emission from absorption and therefore extract clean line strength maps. Applying this technique to the *SAURON* sample will also allow us to study the different structural components in galaxies (bulges, disks, etc) as a function of the enviroment (i.e. field, clusters). Once we have performed this analysis it would be relatively easy to extend this results to new datasets at higher redshifts using the upcoming surveys (i.e. *EDisCs, 2dFGRS*).

Appendix A

Kinematic Extraction Methods

The spectrum extracted from a galaxy is the superposition of the individual spectra of each star in that region of the galaxy, along the line of sight. As the line of sight of each star is different , the spectra of the stars with respect to the others will be shifted by a certain amount in wavelength. The net effect is a broadening in the galaxy spectrum owing to these shifts. In other words. the galaxy spectrum is the convolution of the spectrum of the stars with an appropriate velocity distribution along the line of sight.

In order to quantify these offsets and broadening *Line of Sight Velocity Distribution* (LOSVD, $F(v_{los})$) has been defined as the fraction of stars contributing to the spectrum with a line of sight between v_{los} and v_{los}+dv_{los}. Assuming that all the stellar spectra are identical ($S(u)$), with u the stellar velocity, the galaxy spectrum can be given by the equation:

$$G(u) \approx \int F(v_{los}) \cdot S(u - v_{los}) \cdot dv_{los} \tag{A.1}$$

This is the most important equation in the analysis of galactic kinematics. In order to obtain the kinematics of a particular galaxy we need to make use of a '*stellar template*', whose spectrum is required to be a good approximation of the galaxy's spectrum. From this point, the better selection of the template star, the more accurate the fit to the galaxy spectrum and therefore the better kinematics we will get. The simplest properties of the LOSVD are its mean velocity and velocity dispersion:

$$\overline{v} = \int F(v_{los}) \cdot v_{los} \cdot dv_{los} \tag{A.2}$$

$$\sigma^2_{los} = \int F(v_{los}) \cdot (v_{los} - \overline{v}_{los})^2 \cdot dv_{los} \tag{A.3}$$

To first approximation, it is assumed that the LOSVD of the stars is Gaussian. However the improvements of the detectors has made it possible to measure deviations from Gaussian shape through a new set of algorithms. We review the most relevant methods in the literature in the following paragraphs. All the methods shown here take advantage of the fact that the convolution shown in A.1 becomes a multiplication in '*Fourier space*' and therefore it is easier to extract and analyse the LOSVD there. Note that there is no distinction between a function and its Fourier transform. The main advantage of working if Fourier space is the possibility of *filtering* residual low-order and high frequency components in the original spectrum that are due to an imperfect continuum subtraction and Poisson noise respectively. Some computer codes have been developed to fit the LOSVD in '*Real space*' (Rix & White 1992; van der Marel & Franx 1993), although they won't be discussed here.

• Fourier Quotient (Sargent et al. 1977)
Sargent et al. (1977) based their algorithm on the assumption that the $F(v_{los})$ has a Gaussian shape. Under this consideration they fit a Gaussian to the quotient between the galaxy spectra and the template spectra in Fourier space:

$$F(k) = \frac{G(k)}{S(k)} \approx \gamma \cdot exp\Big[-\frac{1}{2}\frac{2\pi k\sigma}{N} + \frac{2\pi vki}{N} \Big] \tag{A.4}$$

where $F(k), G(k)$ and $S(k)$ are the fourier transforms of the $F(v_{los}), G(v)$ and $S(v)$ respectively, γ is the mean relative line-strength, σ is the velocity dispersion and v is the mean radial velocity of the assumed Gaussian. N is the number of pixels in the input spectra.

• Cross-Correlation Method (Simkin 1974; Tonry & Davis 1979)
The Cross-Correlation approach, initiated by Simkin (1974) and improved by Tonry & Davis (1979), is a simple method based on the fitting of the cross-correlation peak defined by the functions: $G(k)$ and $S(k)$

$$C(k) = \frac{1}{N\Delta_g\Delta_t}\, G(k) \cdot S^*(k) \tag{A.5}$$

where Δ_g and Δ_t are the rms of the galaxy and template respectively and * indicates complex conjugation. Cross-correlating a template spectrum with the galaxy spectrum then produces a function $C(k)$ with a peak at the redshift of the galaxy with a width related to the dispersion of the galaxy. The resultant function is then fitted with a Gaussian in Fourier space.

• Fourier Correlation Quotient (Bender 1990)
The two previous methods were based on the assumption that the broadening function was a Gaussian. The Fourier Correlation Quotient (FCQ) is an improvement of the two and a generalization of the problem because it provides the full LOSVD function instead of the results of a specific parametrisation. The main advantage of this procedure lies in the fact that one can choose the most appropriate function to fit the LOSVD *a posteriori* rather than *a priori*. This approach is based on the deconvolution of the peak of the template-galaxy correlation function with the autocorrelation function of the template star:

$$F(k) = \frac{G(k) \cdot S^*(k)}{S(k) \cdot S^*(k)} \tag{A.6}$$

Compared to previous methods (i.e. Fourier Quotient) FCQ is less sensitive to template mismatch because the LOSVD comes from the ratio of template-galaxy correlation and template autocorrelation functions which are smooth functions, instead of the division of 2 spectra.

• Unresolved Gaussian Decomposition (Kuijken & Merrifield 1993)
This method assumes deviations from pure gaussian are due to the composition of several gaussians uniformly distributed in mean velocity and velocity dispersion, but not in amplitude:

$$F(k) \approx \sum_{k=1}^{N} a_k \cdot exp\Big[- \frac{(v_{los} - v_k)^2}{2\sigma_k} \Big] \tag{A.7}$$

where a_k, v_k, σ_k represents the amplitude, mean velocity and velocity dispersion of each gaussian. The algorithm, under certain physical constraints, determines the different amplitudes a_k for each component that best fit the galaxy spectrum in the least square sense. Those physical constraints are:

- The LOSVD must be non-negative everywhere
- The LOSVD is expected to be smoothly varying on small scales
- The LOSVD is expected to be non-zero over only a fairly small range in velocity

The Rayleigh criterium is also required to define the separation between 2 adjacent peaks. This should be less than 2σ in order to avoid dips between 2 peaks.

• Gauss-Hermite Expansion (van der Marel & Franx 1993)
This approach defines the LOSVD as the product of a normal Gaussian and a truncated expansion of the Hermite polynomials:

$$F(v_{los}) \approx \left[\frac{\gamma\alpha(w)}{\sigma}\right] \cdot \left[1 + \sum_{j=3}^{n} h_j H_j(w)\right] \tag{A.8}$$

$$w = \frac{(v_{los} - v)}{\sigma}$$

where γ, v, σ characterise the line-strength, mean velocity and velocity dispersion of the traditional Gaussian and the Hermite coefficients (h_j) describe deviations from the gaussian shape (i.e. h_3 measures asymmetries and h_4 symmetries) of the LOSVD. $\alpha(w)$ is the standard Gaussian.

For most of the work presented in this thesis we have made use of FOURFIT, a computer code developed by van der Marel & Franx (1993) (chapters 2, 3, 4). In chapter 5 we also use an adapted implementation of Bender (1990) that deals with SAURON data.

Appendix B

Line-Strength Extraction Methods

As we have been mentioned in previous sections, a spectrum is the key to discover intrinsic properties (metallicity, gravity, temperature) of the object studied. In order to perform that analysis we define spectral indices. The aim of these indices is to give a measurement of the strength of a certain feature.

Each index is defined by a central band, where the feature is placed, plus 2 side bands on each side of this central band that represents a pseudocontinuum. We talk about pseudo-continuum and not real continuum due to the depletion of it because of the large number of metal absorption lines. Atomic features are measured in equivalent width (EW) while molecular ones are described as magnitudes of the average unabsorbed flux.

$$EW = \int_{\lambda_1}^{\lambda_2} \left(1 - \frac{F_I(\lambda)}{F_C(\lambda)}\right) \cdot d\lambda \tag{B.1}$$

$$Mag = -2.5 \cdot log\Big[\frac{1}{\lambda_2 - \lambda_1} \cdot \int_{\lambda_1}^{\lambda_2} \frac{F_I(\lambda)}{F_C(\lambda)} \cdot d\lambda\Big] \tag{B.2}$$

where λ_1 and λ_2 represents the wavelength limits of the feature passband, $F_C(\lambda)$ is the straight line connecting the middle points of the sidebands and $F_I(\lambda)$ is the observed flux per unit wavelength.

In the early 70' s Faber and collaborators started a collection of spectra of an extensive library of galaxies with globular clusters and stars in the wavelength range between 4000 - 6400 Å and with a mean resolution of 8 Å (see Worthey

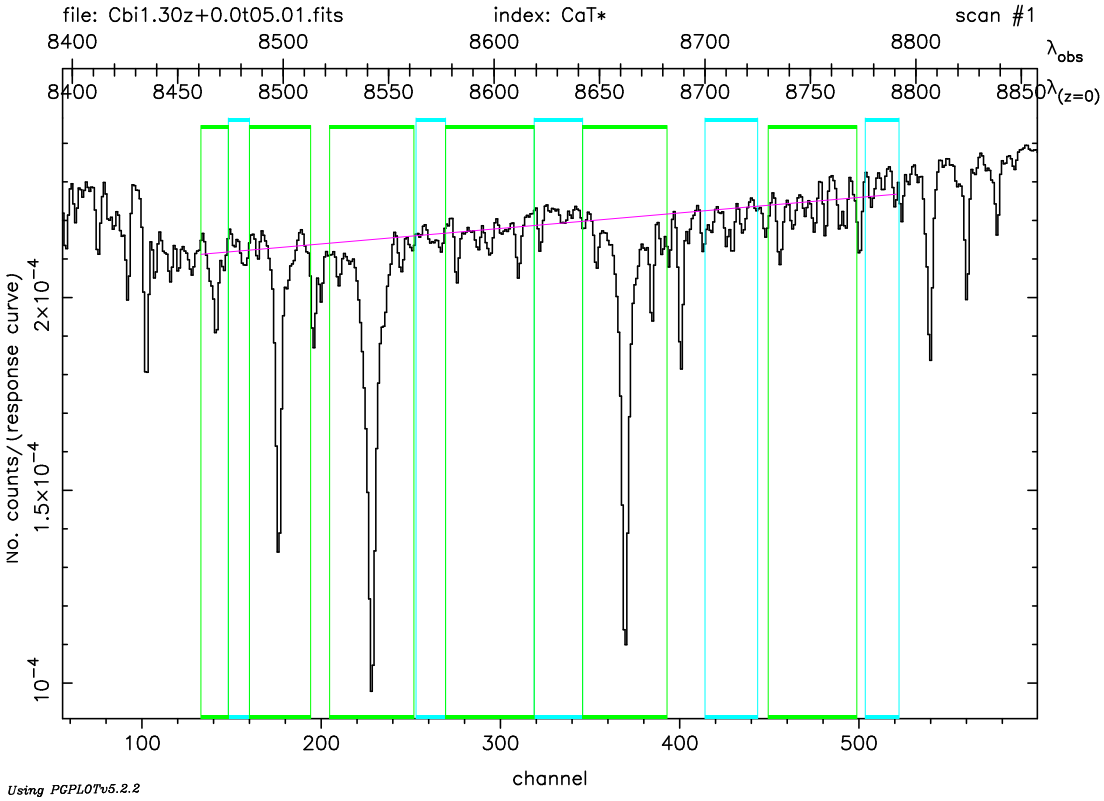

Figure B.1: Representative example of the Line-Strength measurement. A synthetic model from Vazdekis et al. (2003) has been used to measure the CaT* index (Cenarro et al. 2001a). Pseudo-continuum bands are shown in cyan, whereas central bands are plotted in green.

& Ottaviani (1997) for further details) using the Shane Telescope at Lick Observatory. This work led to the definition of the Lick/IDS absorption line index System. In Table B.1 we present the extended version of this system, adding new definitions, given by Worthey et al. (1994). At optical wavelengths there are also different line index systems, e.g. Rose et al. (1994).

Subsequent projects opened the field of study leading to the description of new indices at larger wavelengths (Table B.2).

To interpret observations of galaxies, several corrections have to be applied to be able to perform an appropriate comparison of the results with different authors:

- Convolution to the same instrumental resolution.
- Velocity Dispersion Correction.
- Offset Correction (non flux-calibrated systems).

Table B.1: Definitions of Lick/IDS Indices

Name	Central bandpass	Pseudo-continuum	Units	Element Measured	Error
CN1	4142.125 4177.125	4142.125 4177.125	Mag	C, N, (0), (Mg)	0.018
		4244.125 4284.125			
CN2	4142.125 4177.125	4083.875 4096.375	Mag	C, N, (0), (Mg)	0.019
		4244.125 4284.125			
Ca4227	4222.250 4234.750	4211.000 4219.750	Å	(C), Ca, O	0.25
		4241.000 4250.000			
G4300	4281.376 4316.375	4266.375 4282.625	Å	C, (O), Ti	0.33
		4318.875 4335.125			
Fe4383	4369.125 4420.375	4359.125 4370.375	Å	Fe, C, (Mg)	0.46
		4442.875 4455.375			
Ca4455	4452.125 4474.625	4445.875 4454.625	Å	(Fe), (C), Cr	0.22
		4477.125 4492.125			
Fe4531	4514.250 4559.250	4504.250 4514.250	Å	Ti, (Si), Cr	0.37
		4560.500 4579.250			
C24668	4634.000 4720.250	4611.500 4630.250	Å	C, (O), (Si)	0.57
		4742.750 4756.500			
Hβ	4847.850 4876.625	4287.875 4847.875	Å	Hb,,(Mg)	0.19
		4876.625 4891.625			
Fe5015	4977.750 5054.000	4946.500 4977.750	Å	(Mg), Ti, Fe	0.41
		5054.000 5065.250			
Mg_1	5069.125 5134.125	4895.125 4957.625	Mag	C, Mg, (O),(Fe),(Si)	0.006
		5301.125 5366.125			
Mg_2	5154.125 5196.625	4895.125 4957.625	Mag	C, Mg, (O),(Fe),(Si)	0.008
		5301.125 5366.125			
Mg*b*	5160.125 5192.625	5142.625 5161.375	Å	Mg, (C), (Cr),(Fe)	0.20
		5191.375 5276.375			
Fe5270	5245.650 5285.650	5233.150 5248.150	Å	Fe, C, (Mg)	0.24
		5285.650 5318.150			
Fe5335	5312.125 5352.125	5304.625 5315.875	Å	Fe, (C), (Mg)	0.22
		5353.375 5363.375			
Fe5406	5387.500 5415.000	5376.250 5387.500	Å	Fe	0.18
		5415.000 5425.000			
Fe5709	5696.625 5720.375	5672.875 5696.625	Å	(C), Fe	0.16
		5722.875 5736.625			
Fe5782	5776.625 5796.625	5765.375 5775.375	Å	Cr	0.19
		5797.875 5811.625			

Convolution to the same instrumental resolution

Since we do not always observe at the same telescope, instruments, detectors used by the person to whom we are going to compare our results with, it is important to degrade our data to the comparing author's resolution. Doing this is as simple as to convolve our spectrum with a gaussian of width σ.

$$\sigma = \frac{\sqrt{\sigma_2^2 - \sigma_1^2}}{\Delta v} \tag{B.3}$$

where σ_1 is the instrumental resolution of our system (telescope, instrument, detector), σ_2 the comparison author's instrumental resolution and Δv is the conversion factor km/s/pix. For the measurement of σ_1 a comparison arc lamp is used (assuming unblended lines with a gaussian profile).

Velocity Dispersion Correction

In order to correct the line strength in the galaxy for the broadening due to its velocity dispersion a correction needs to be made. This correction takes the form C(i)=i(σ)/i(0), where i(σ) corresponds to a certain index at the velocity dispersion of our galaxy whereas i(0) is the index in which no broadening has been applied. In the case of indices in magnitudes the correction factor is C(i)=i(σ)-i(0). This procedure is performed from the same kind of stars, that the galaxy is presumed to be made of, for each index.

Offset Correction (non flux-calibrated systems)

This is the last effect we need to correct for to get our data ready for comparison with other results. It is very important to remark that this step only needs to be made if either one of the systems use non flux calibrated data. If this is not the case NO offset corrections has to be made.

This correction factor is defined as the offset between the comparison index values for stars measured in one system (Lick/IDS System for instance) and Us. A constant value, if appropriate, is expected as the offset, but one could also take into account a straight line with some slope. See Sec. 3.2 in Kuntschner (1998) for typical values of these offsets.

Table B.2: Other index definitions

Name	Central bandpass [Å]		Pseudo-continuum [Å]		Reference
D4000	4050.000	4250.000	3750.000	3950.000	1
$OIII_1$	4948.920	4978.920	4885.000	4935.000	2
			5030.000	5070.000	
$OIII_2$	4996.850	5016.850	4885.000	4935.000	2
			5030.000	5070.000	
Ca 1	8483.000	8513.000	8447.500	8462.500	3
			8842.500	8857.500	
Ca 2	8527.000	8557.000	8447.500	8462.500	3
			8842.500	8857.500	
Ca3	8647.000	8677.000	8447.500	8462.500	3
			8842.500	8857.500	
Mg I	8799.500	8814.500	8775.000	8787.000	3
			8845.000	8855.000	
Ca1 A&Z	8490.000	8506.000	8474.000	8489.000	4
			8521.000	8531.000	
Ca2 A&Z	8532.000	8552.000	8521.000	8531.000	4
			8555.000	8595.000	
Ca3 A&Z	8653.000	8671.000	8626.000	8650.000	4
			8695.000	8725.000	
PaT	8461.000	8474.000	8474.000	8484.000	5
	8577.000	8619.000	8563.000	8577.000	
	8730.000	8772.000	8619.000	8642.000	
			8700.000	8725.000	
			8776.000	8792.000	
CaT	8484.000	8513.000	8474.000	8484.000	5
	8522.000	8562.000	8563.000	8577.000	
	8642.000	8682.000	8619.000	8642.000	
			8700.000	8725.000	
			8776.000	8792.000	
CaT*	See caption				5
Mg I	8781.000	8789.000	8831.000	8835.500	5
			8841.500	8846.000	
			8802.500	8811.000	

Notes:
The CaT* index can be measured as: CaT*=CaT− 0.93·PaT (see Cenarro et al. (2001a) for more details).
(1) Bruzual A. & Charlot (1993)
(2) González (1993)
(3) Díaz, Terlevich & Terlevich (1989)
(4) Armandroff & Zinn (1988)
(5) Cenarro et al. (2001a)

Appendix C

Kinematic Profiles - Figures

In this section we present kinematic profiles for each galaxy (heliocentric velocity, velocity dispersion, h_3, h_4, together with an H-band NICMOS (F160W) contour map from Peletier et al. (1999a) (except for NGC 7332 for which a WFPC1 image, taken from the archive, is plotted instead). The area covered by the 1.2 arcsec wide slit has been indicated. The CaT* index (see Sec. 2.3.6) is shown in the bottom panel. Filled circles represent data points with signal to noise ratio above 33, whereas filled triangles represent data points with signal to noise between 20 and 33. Contour levels have 0.5 mag difference. The left hand side of the profiles, for all galaxies, corresponds the dust-free side, while the right hand side corresponds to the dusty side. The PA (on top of the figure) is the position angle (N-E) of the dust-free minor axis. Error bars determined in the simulation for each S/N (see sec. 2.3.5) are located on the right hand side of each panel, S/N=33 (short bar) and S/N=20 (long bar). A dotted line has been drawn, on each panel, at the level of the central value for the velocity, velocity dispersion and CaT* index and it is at the zero value for the h_3 and h_4 parameters. Vertical dotted lines indicate the minor axis bulge radius and center of the galaxy (see table 2.1 for more details).

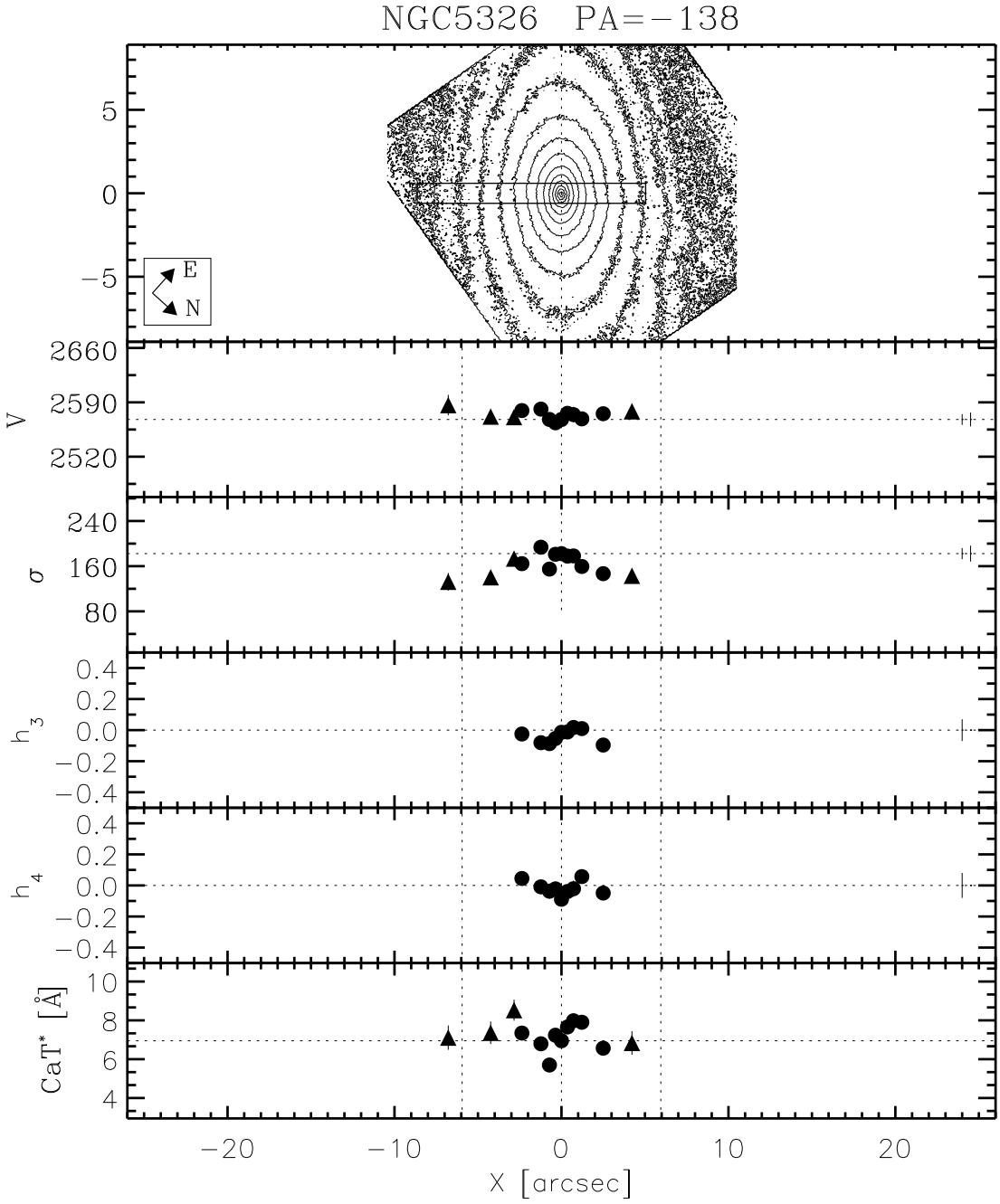
NGC5326 PA=−138
E
N
V
σ
h3
h4
CaT* [Å]
X [arcsec]

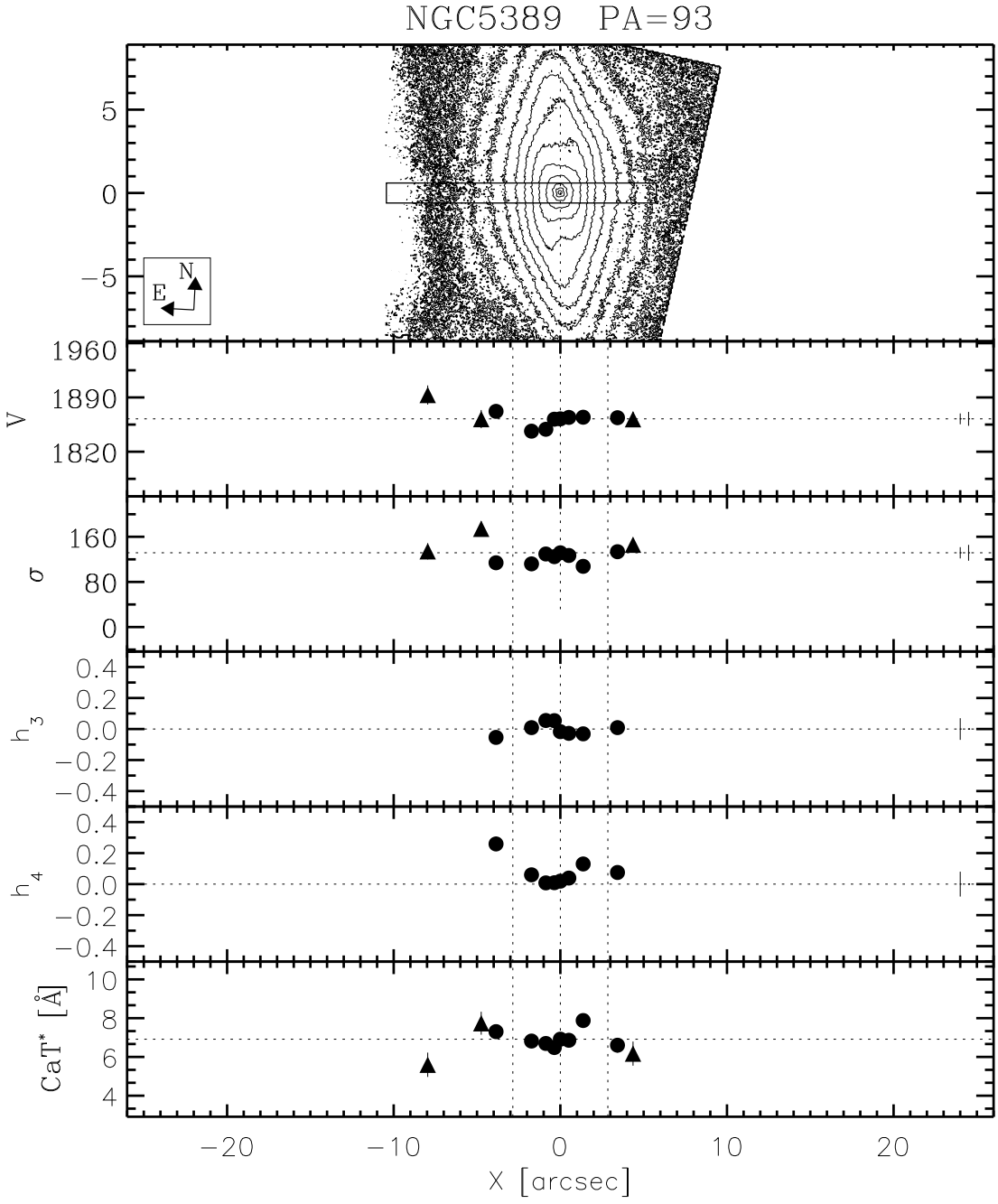
NGC5389 PA=93
N
E
V
σ
h3
h4
CaT* [Å]
X [arcsec]

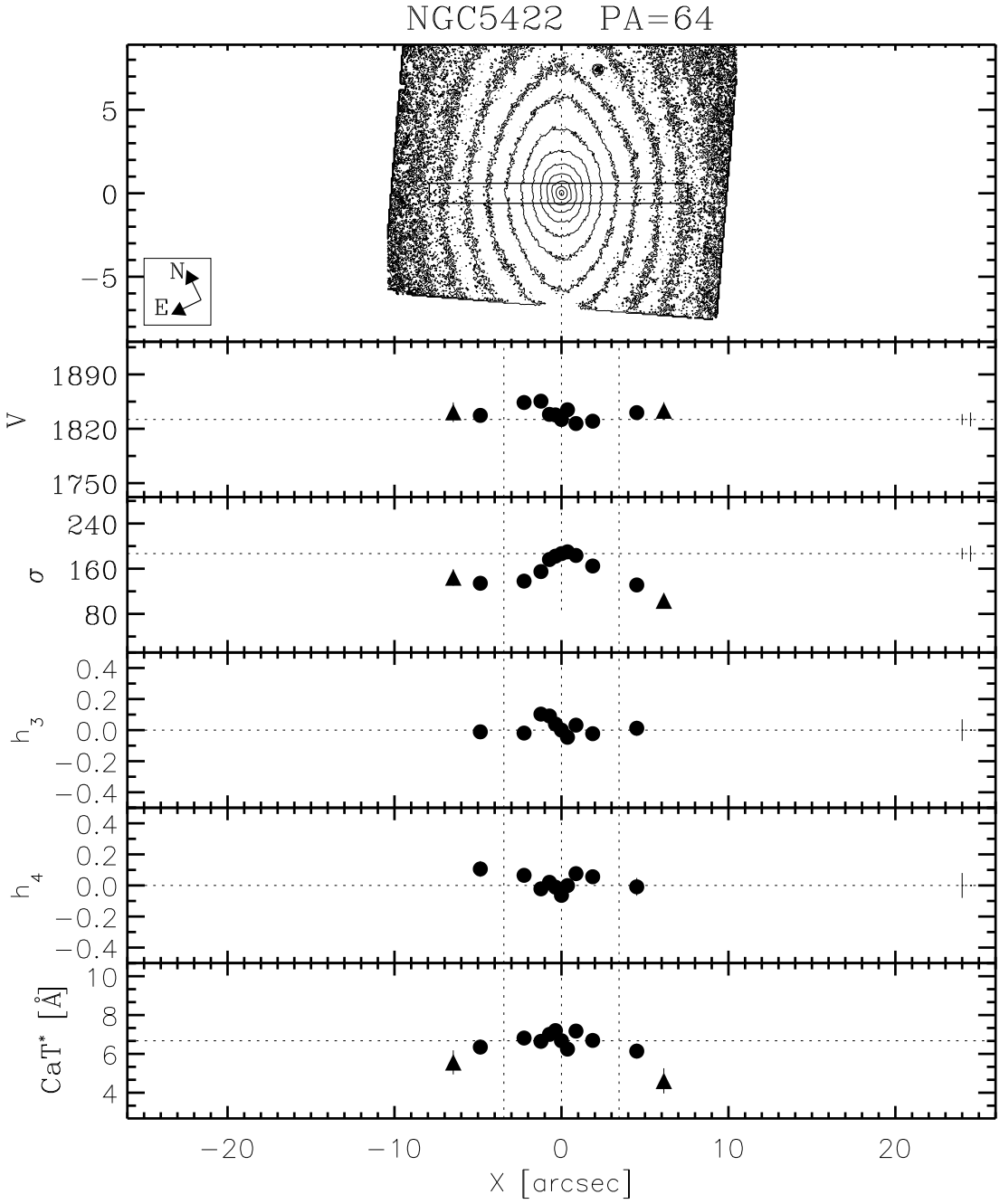
NGC5422 PA=64
N
E
V
σ
h3
h4
CaT* [Å]
X [arcsec]

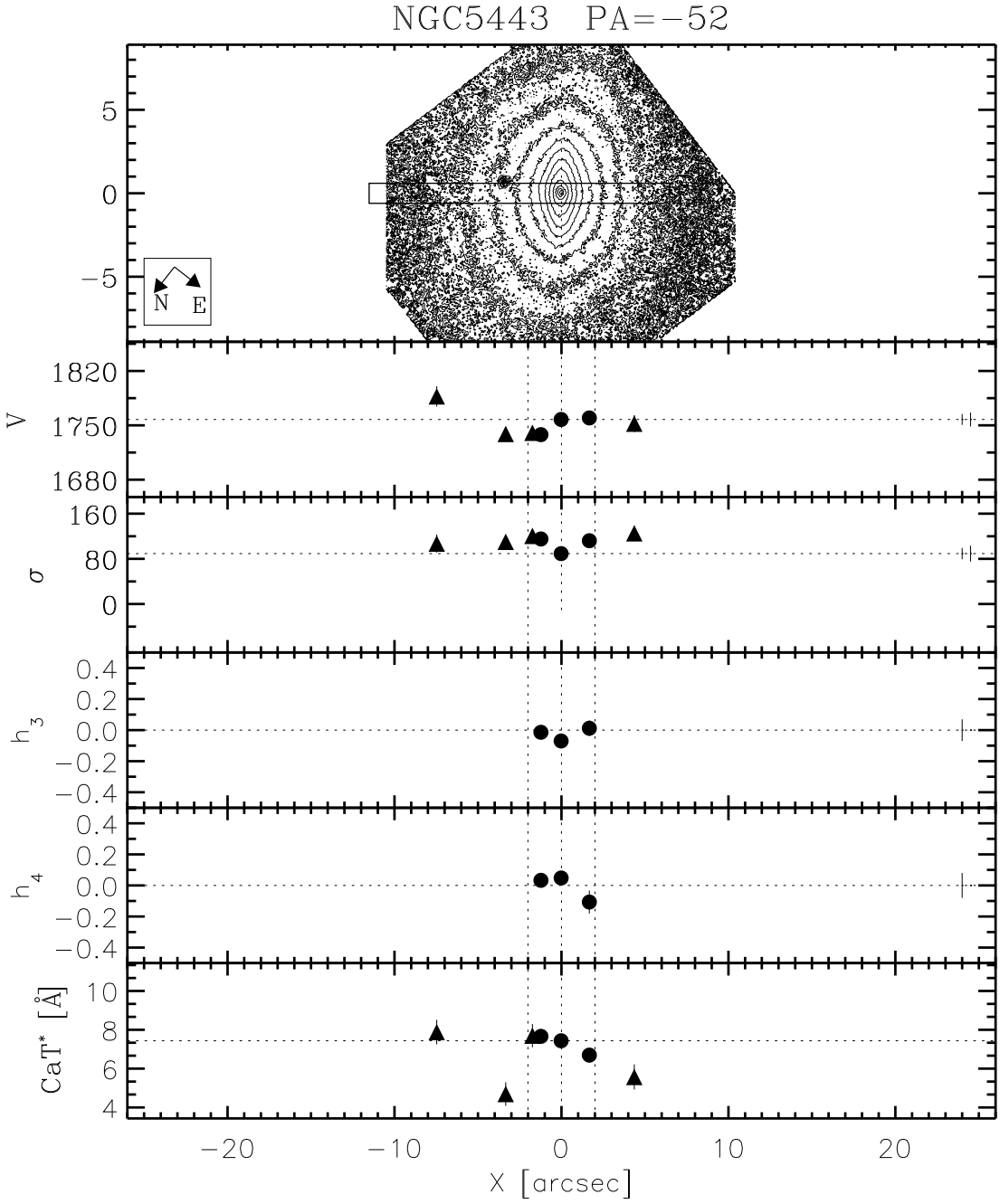
NGC5443 PA=−52
N
E
V
σ
h3
h4
CaT* [Å]
X [arcsec]

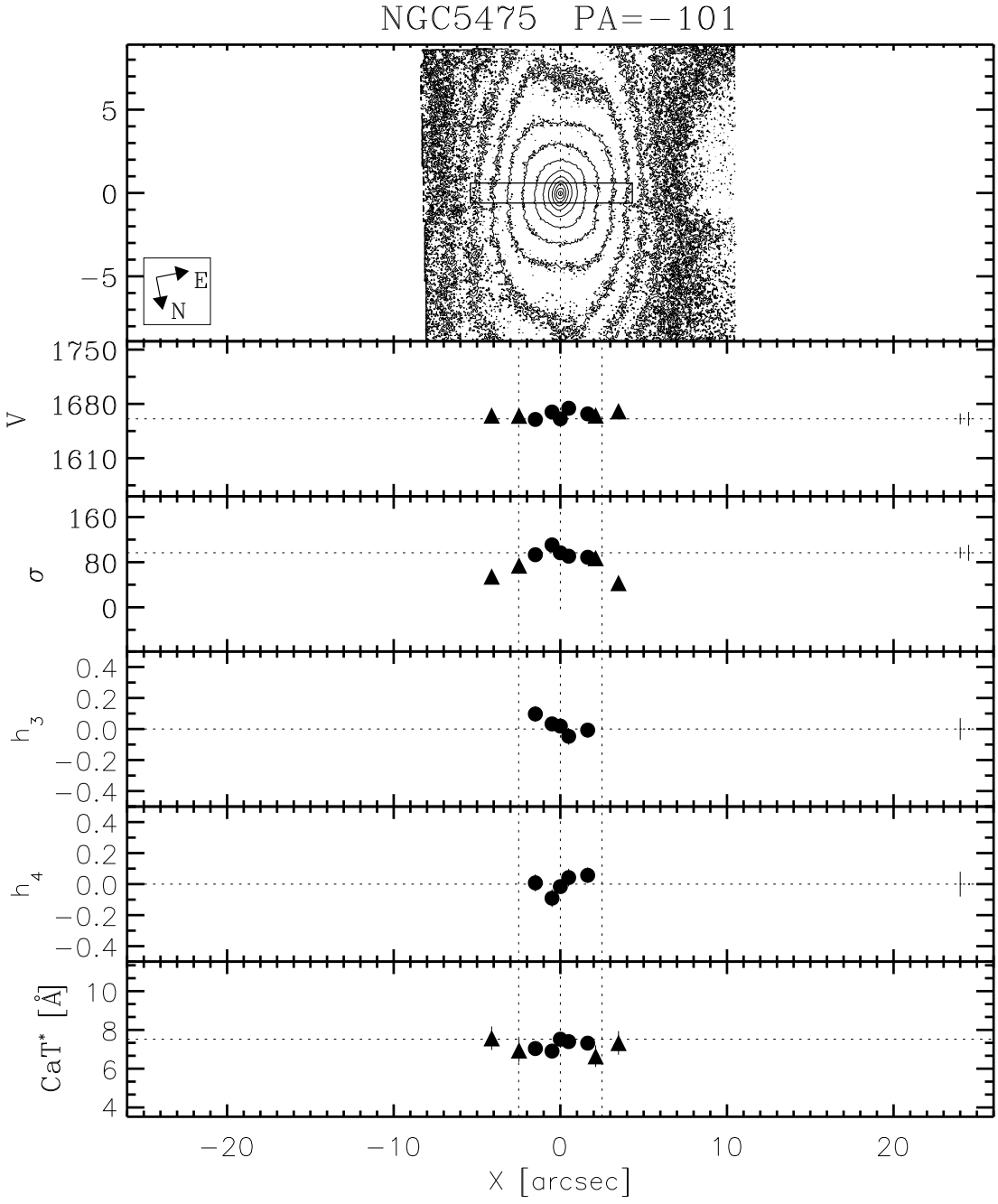
NGC5475 PA=−101
5
0
−5
E
N
1750
1680
1610
V
160
80
0
σ
0.4
0.2
0.0
−0.2
−0.4
h3
0.4
0.2
0.0
−0.2
−0.4
h4
10
8
6
4
CaT* [Å]
−20
−10
0
10
20
X [arcsec]

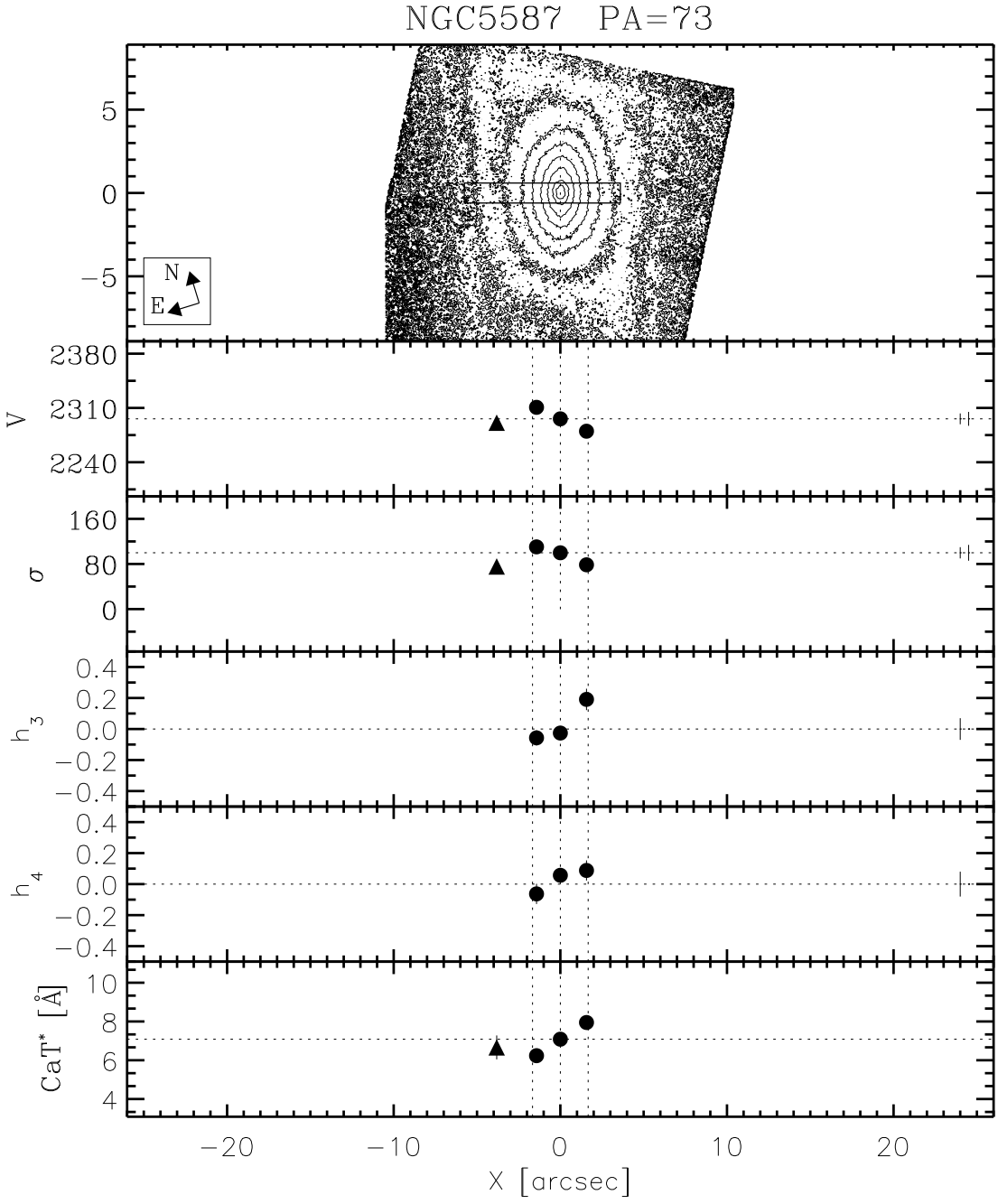
NGC5587 PA=73
N
E
V
σ
h3
h4
CaT* [Å]
X [arcsec]

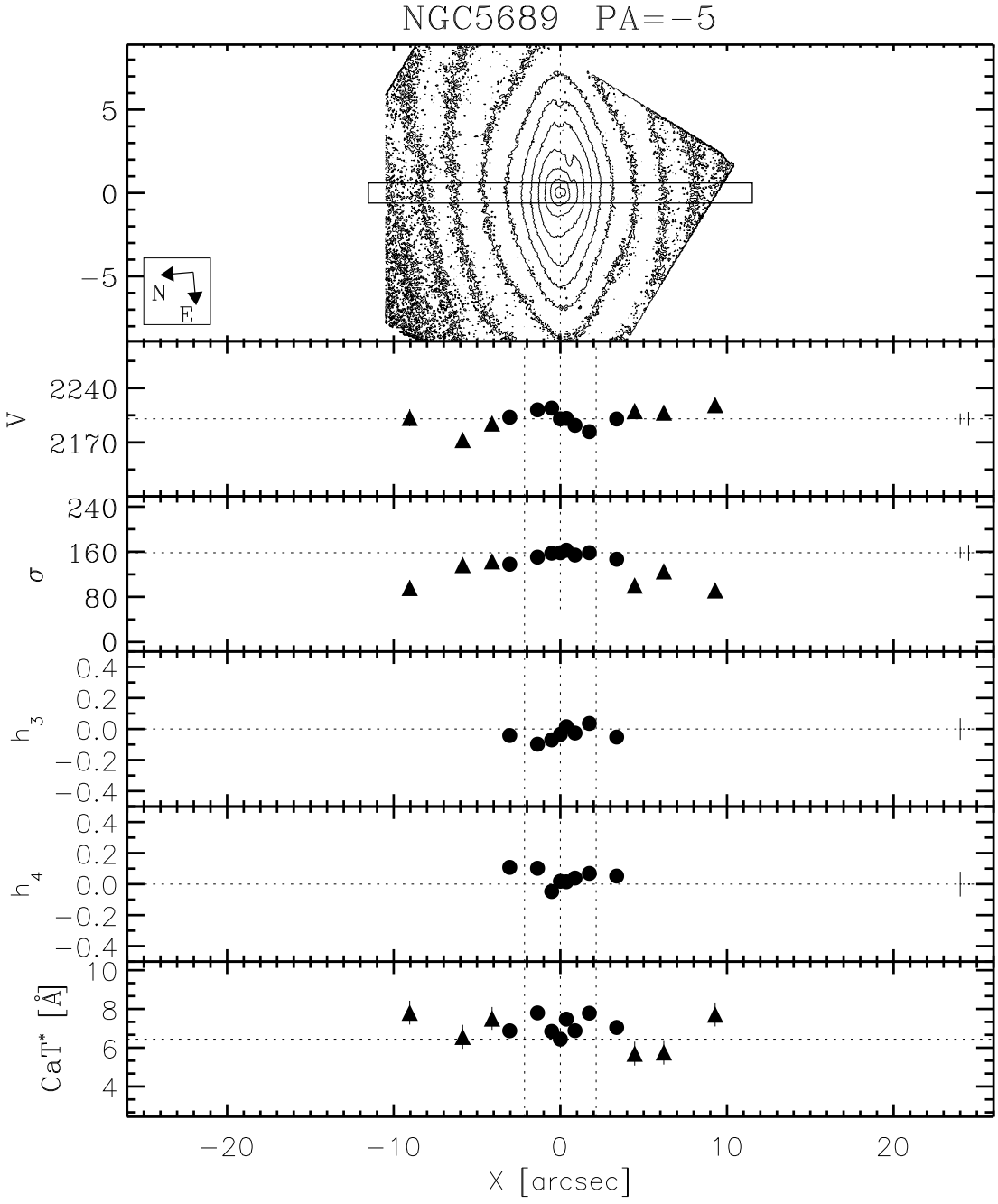
NGC5689 PA=−5
N
E
V
σ
h3
h4
CaT* [Å]
X [arcsec]

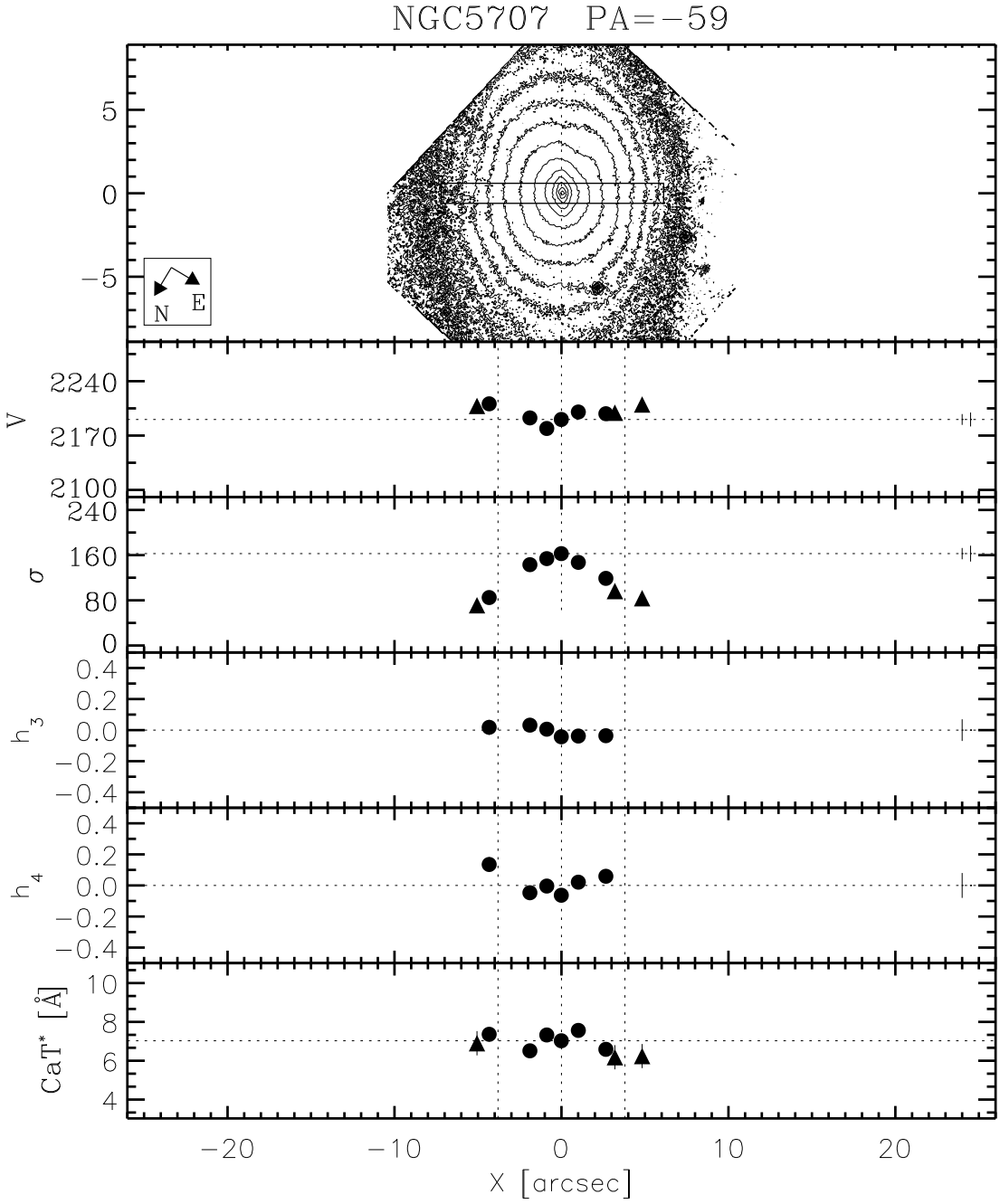
NGC5707 PA=−59
N
E
V
σ
h3
h4
CaT* [Å]
X [arcsec]

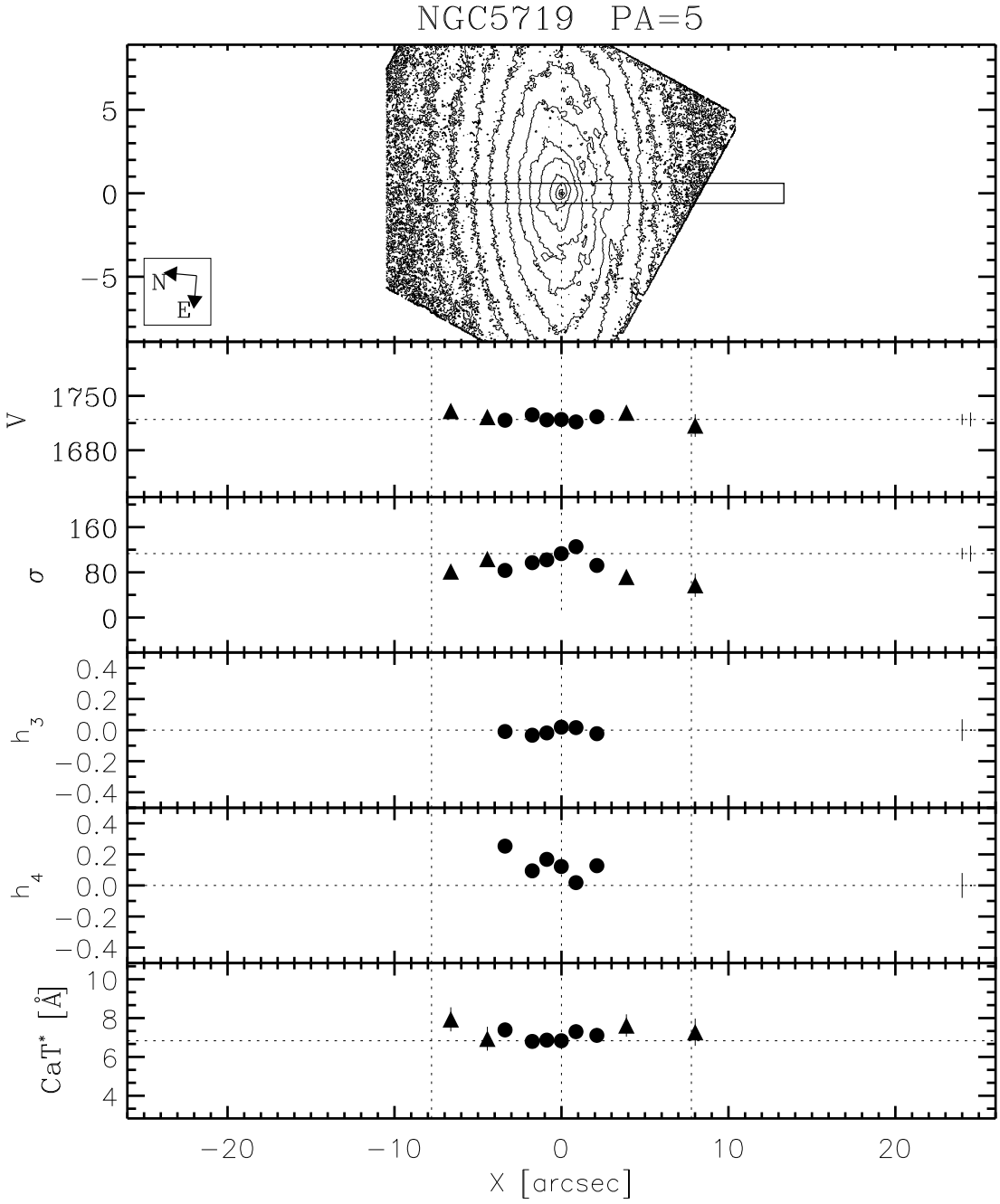
NGC5719 PA=5
N
E
V
1750
1680
σ
160
80
0
h3
h4
0.4
0.2
0.0
−0.2
−0.4
CaT* [Å]
10
8
6
4
−20
−10
0
10
20
X [arcsec]

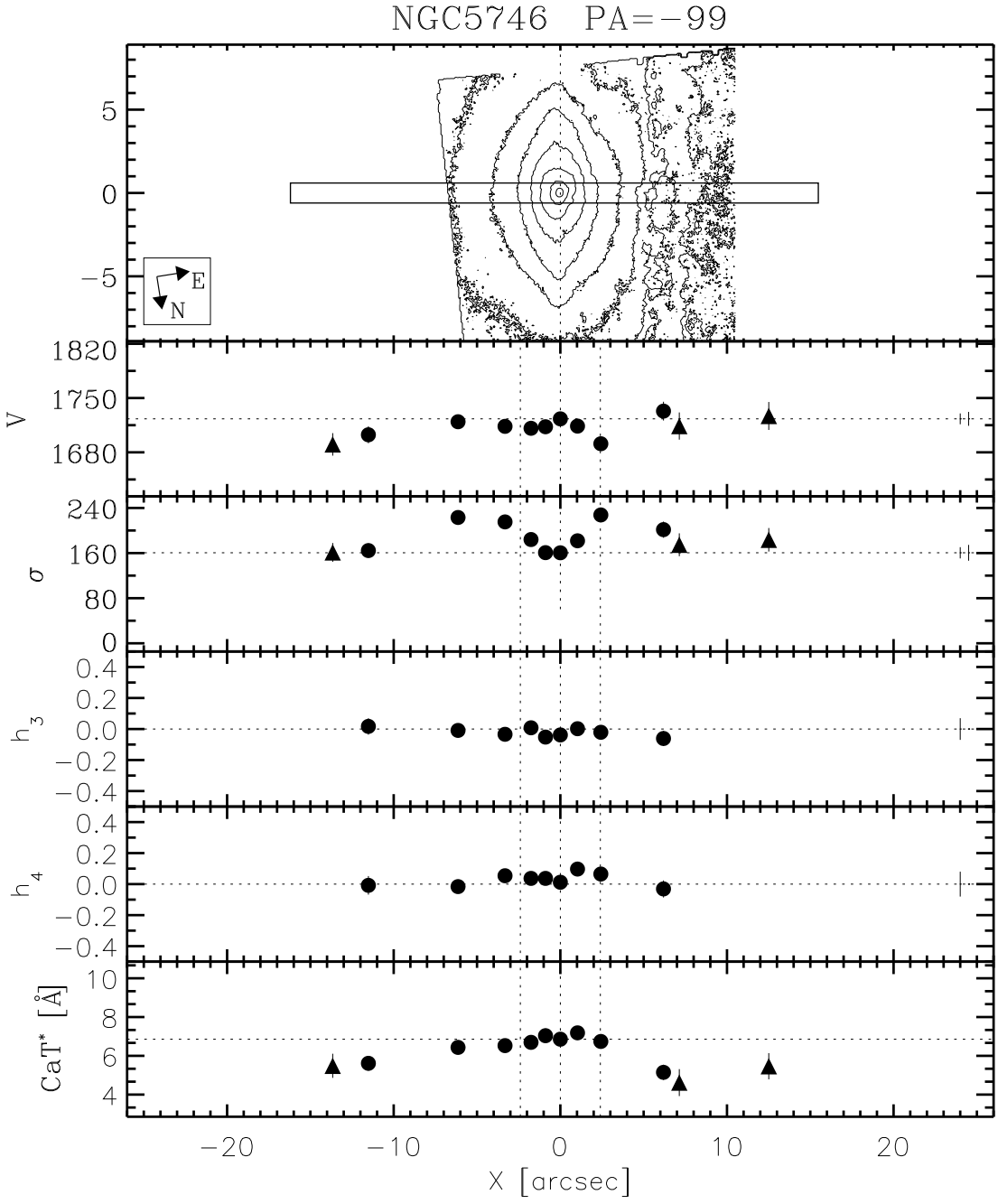
NGC5746 PA=−99
E
N
V
σ
h3
h4
CaT* [Å]
X [arcsec]

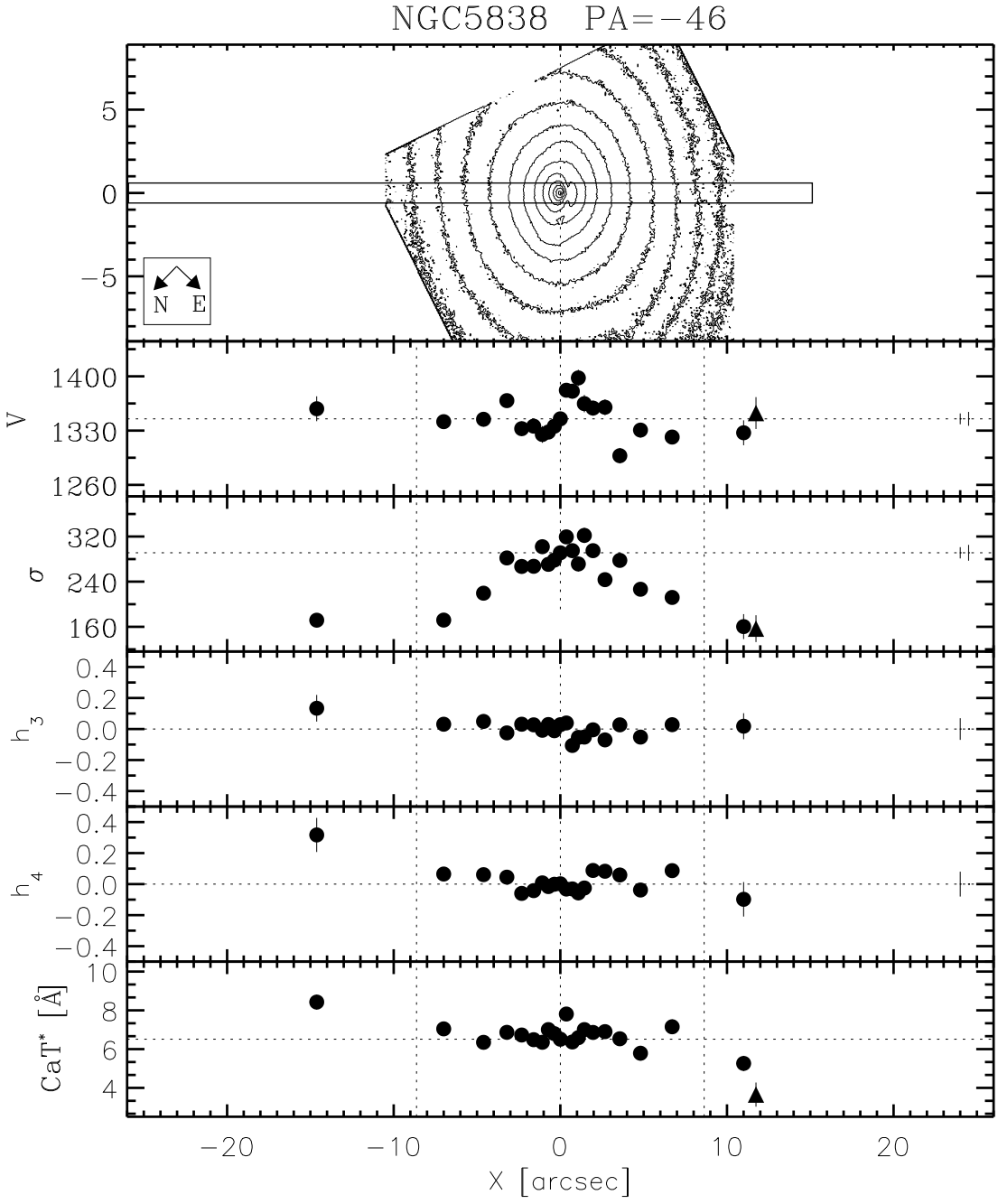
NGC5838 PA=−46
N E
V
σ
h3
h4
CaT* [Å]
X [arcsec]

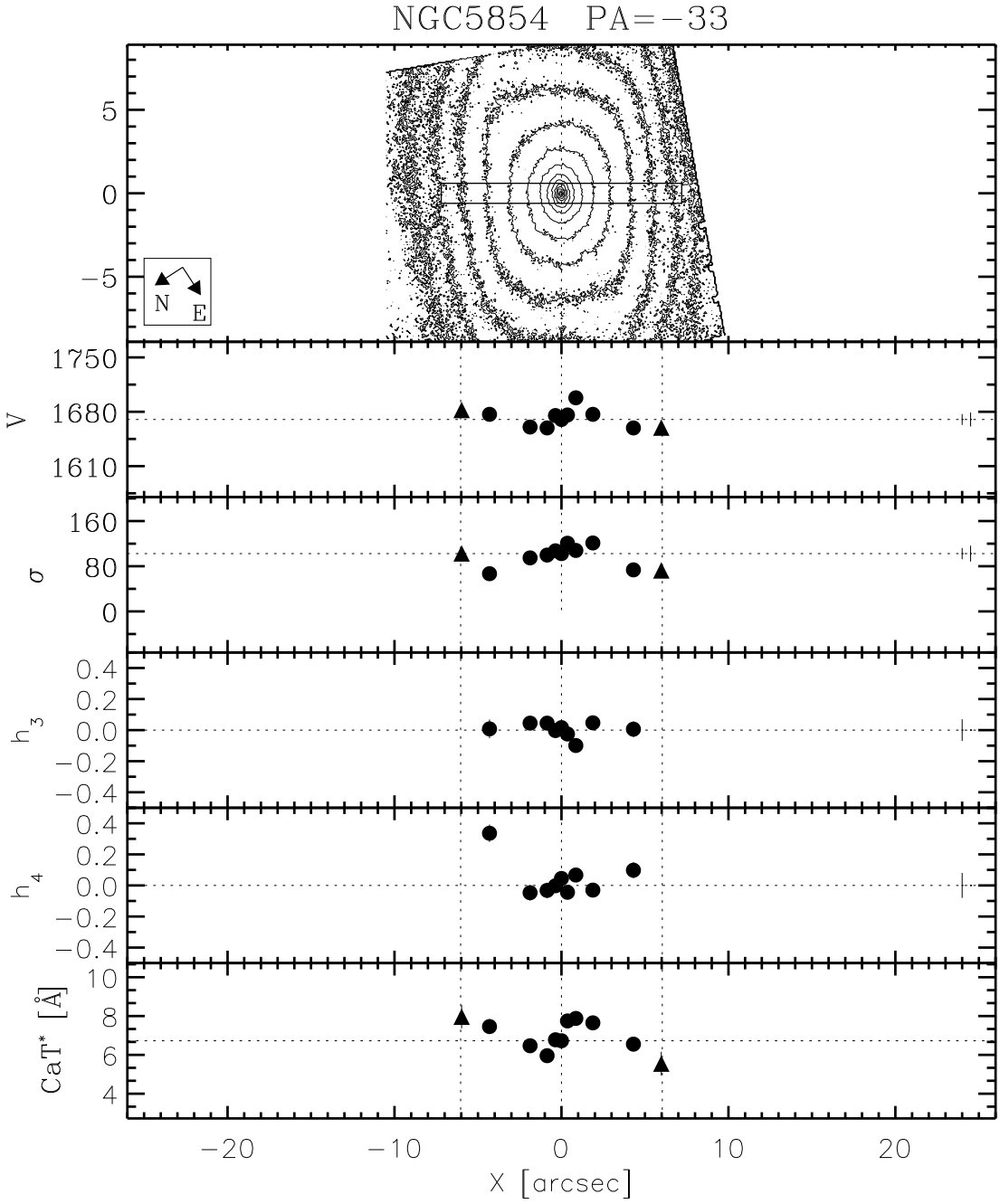
NGC5854 PA=−33
N
E
V
σ
h3
h4
CaT* [Å]
X [arcsec]

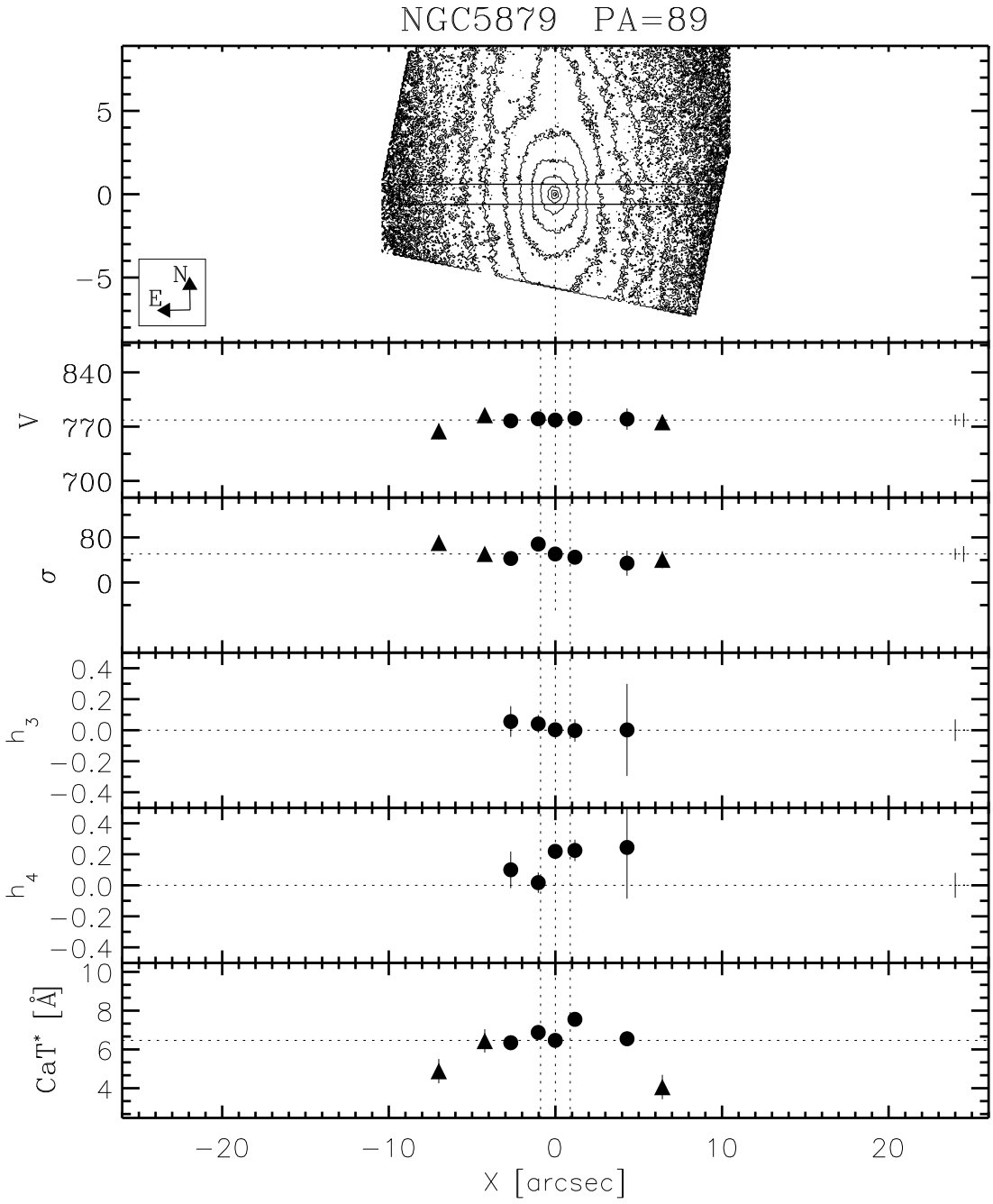
NGC5879 PA=89
N
E
V
σ
h3
h4
CaT* [Å]
X [arcsec]

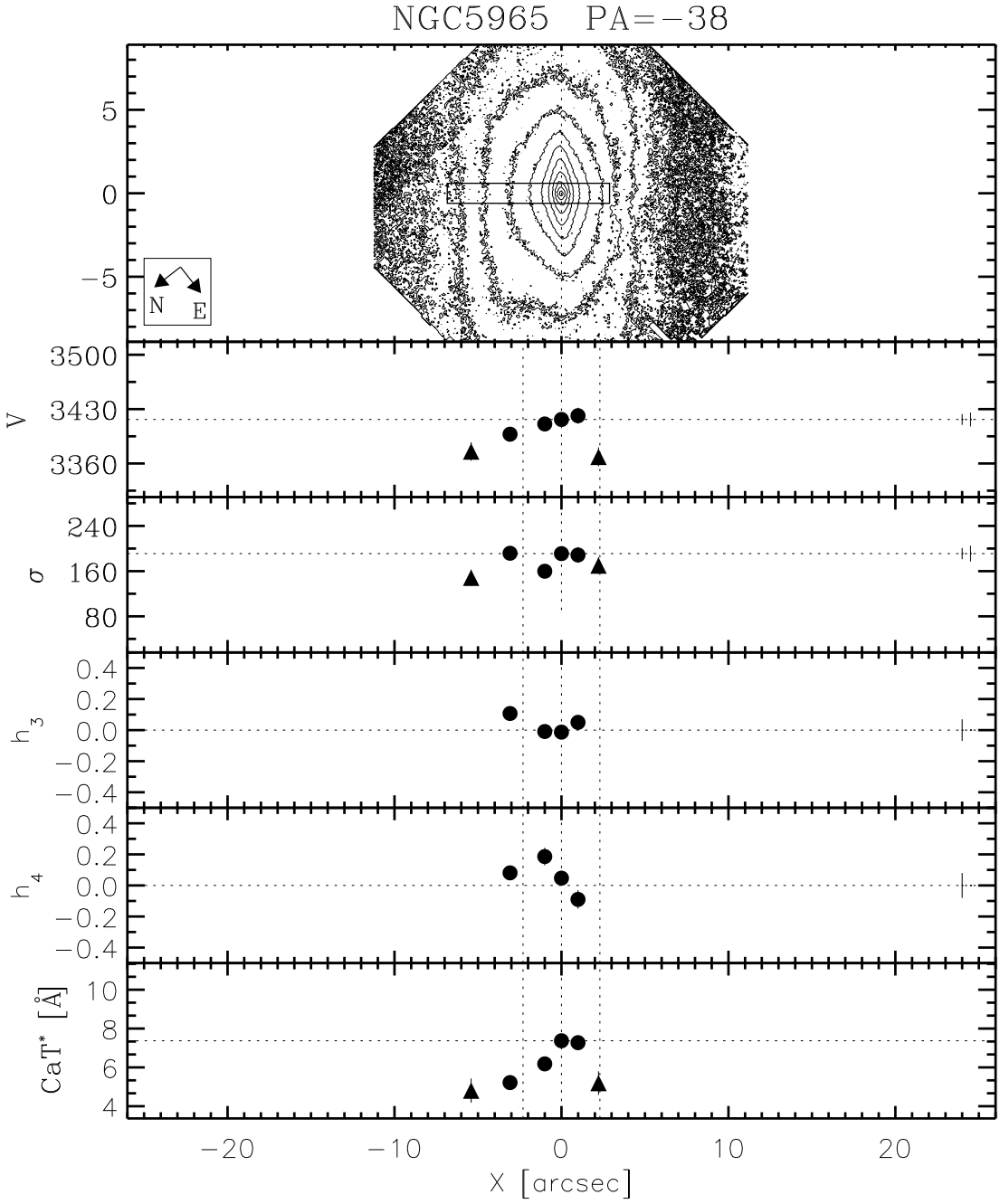
NGC5965 PA=−38
N
E
V
σ
h3
h4
CaT* [Å]
X [arcsec]

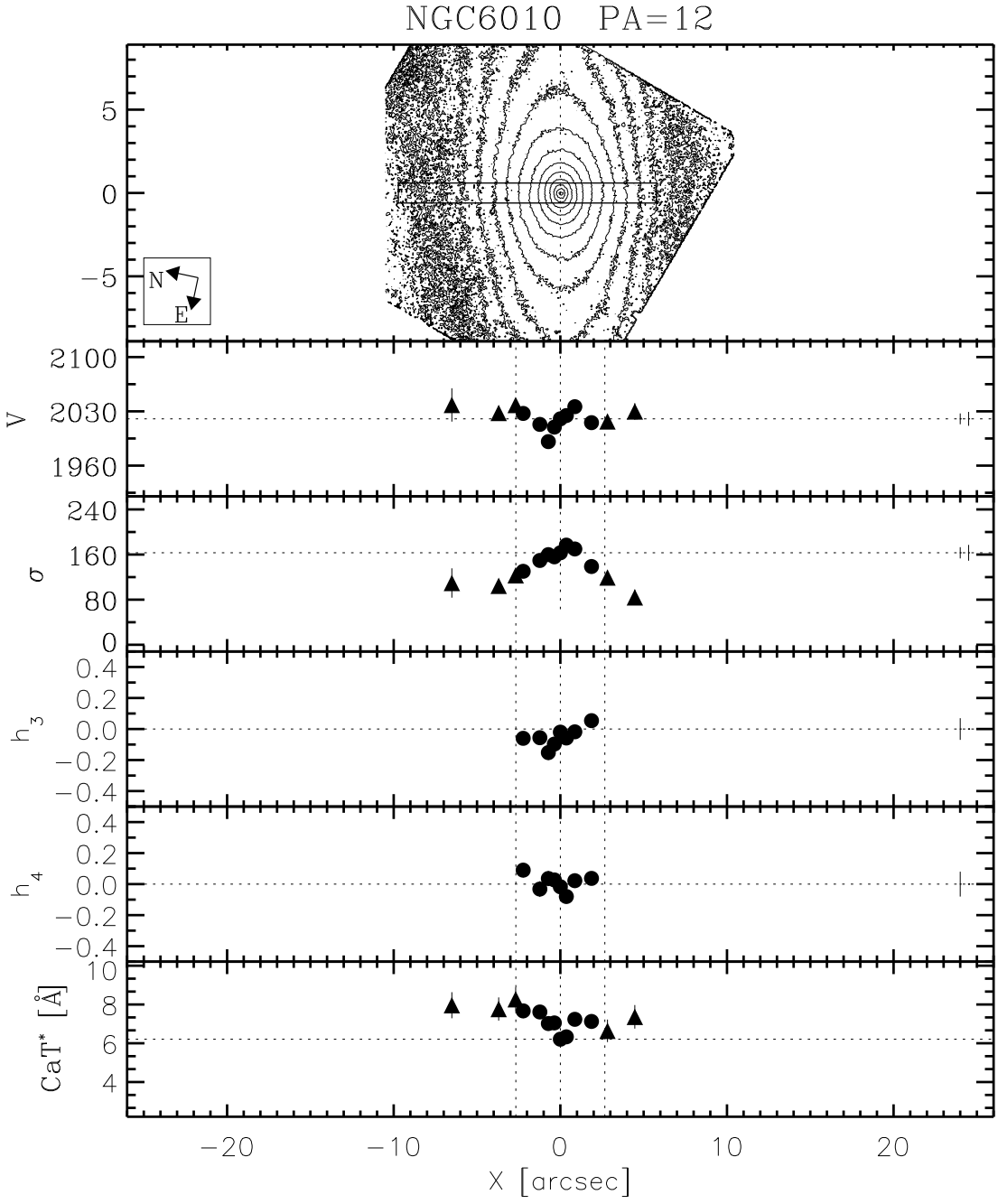
NGC6010 PA=12
N
E
V
σ
h3
h4
CaT* [Å]
X [arcsec]

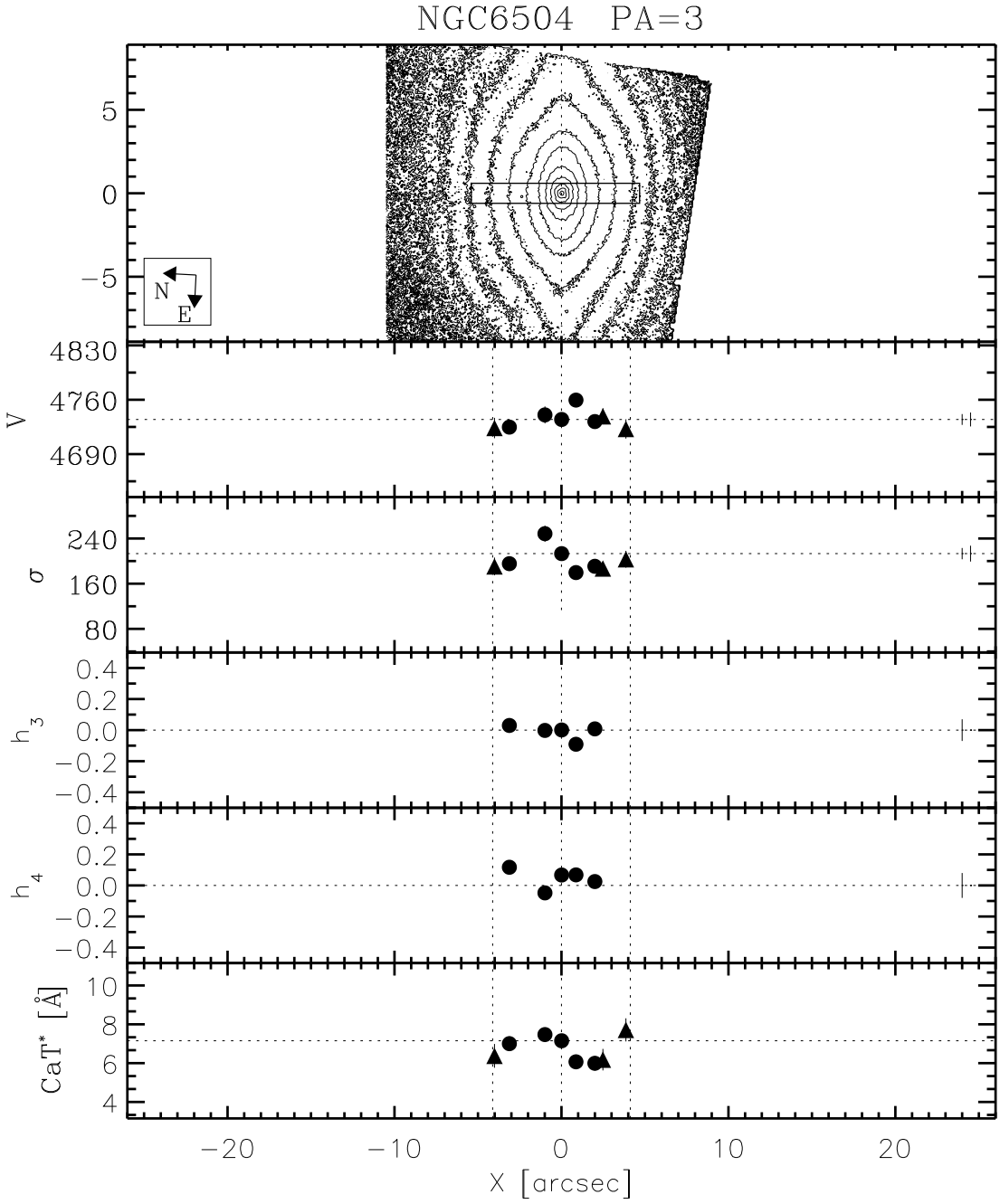
NGC6504 PA=3
N
E
V
σ
h3
h4
CaT* [Å]
X [arcsec]

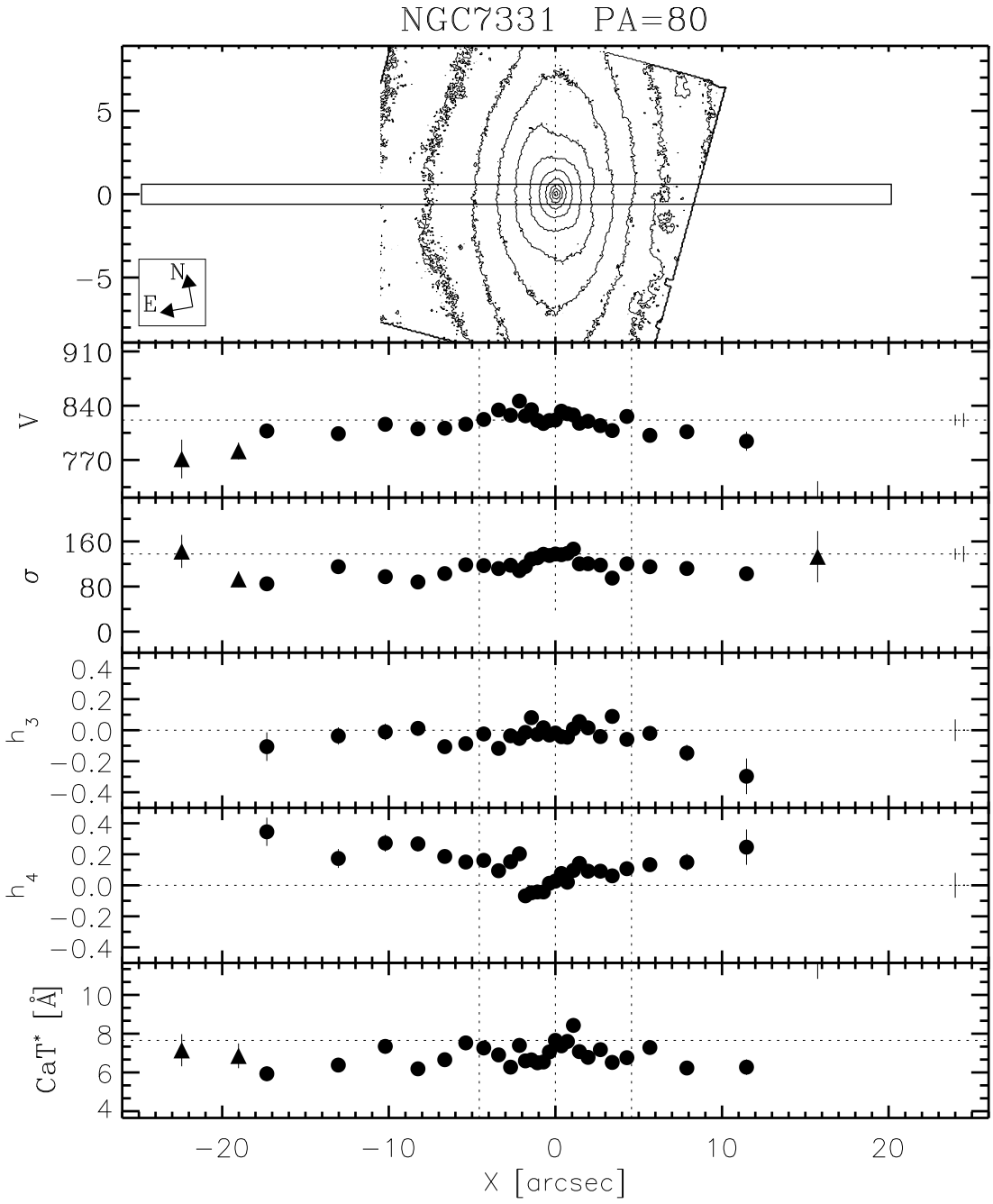
NGC7331 PA=80
N
E
V
σ
h3
h4
CaT* [Å]
X [arcsec]

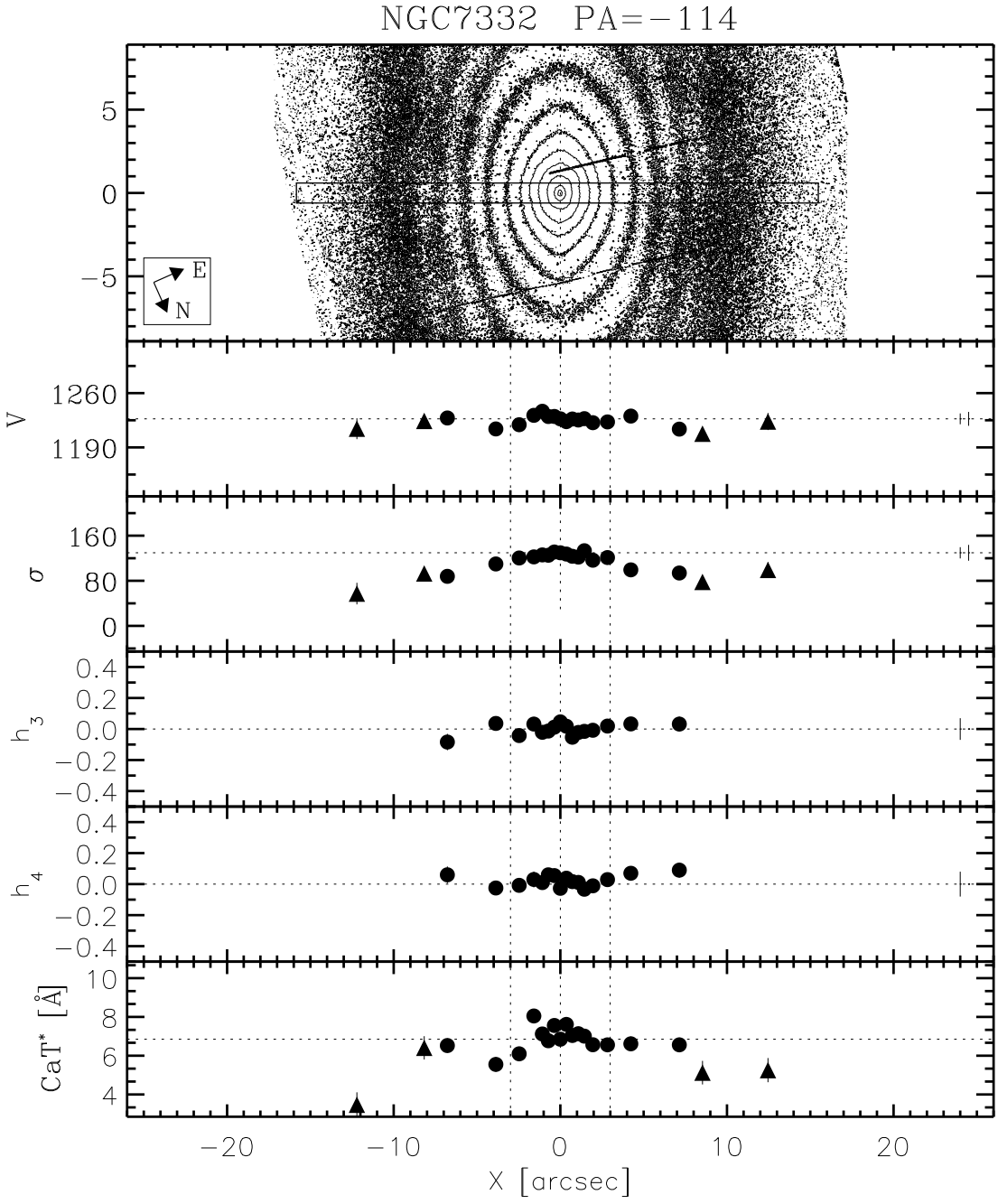
NGC7332 PA=−114
E
N
V
1260
1190
σ
160
80
0
h3
h4
0.4
0.2
0.0
−0.2
−0.4
CaT* [Å]
10
8
6
4
−20
−10
0
10
20
X [arcsec]

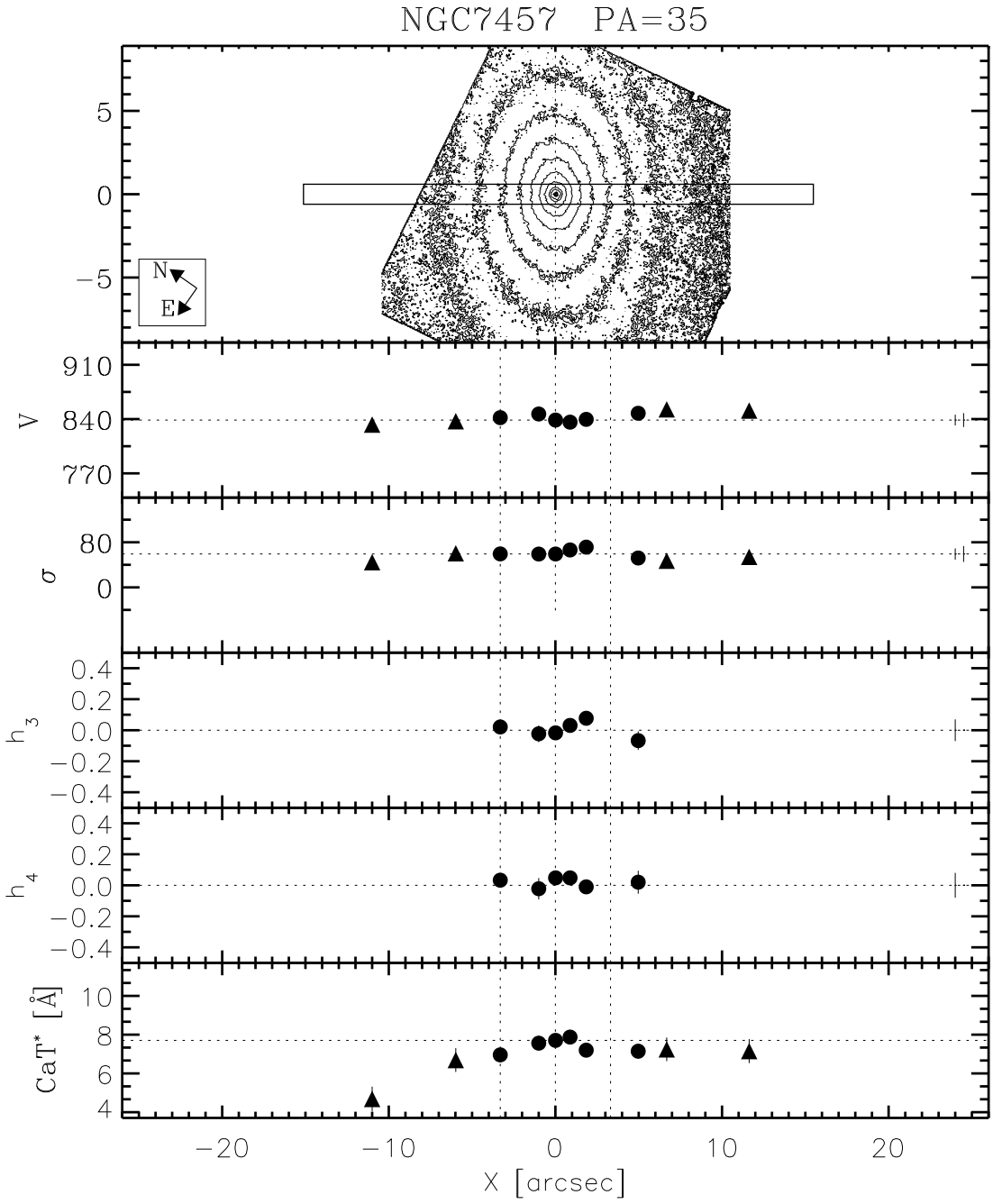
NGC7457 PA=35
N
E
V
σ
h3
h4
CaT* [Å]
X [arcsec]

Appendix D

Kinematic Profiles - Tables

In this appendix we tabulate for each galaxy the heliocentric velocities, velocity dispersions and their errors are expressed in km/s whereas the values for the CaT* index, and their uncertainties, are given in Å.

Table D.1: NGC 5326

x[″]	V	ΔV	σ	$\Delta\sigma$	h_3	Δh_3	h_4	Δh_4	CaT*	ΔCaT*
-6.78	2586	13	132	16	0.00	0.00	0.00	0.00	7.11	0.62
-4.24	2572	8	140	9	0.00	0.00	0.00	0.00	7.36	0.58
-2.84	2571	8	173	10	0.00	0.00	0.00	0.00	8.53	0.54
-2.37	2579	6	164	6	-0.03	0.03	0.05	0.03	7.34	0.37
-1.23	2581	8	194	8	-0.08	0.03	-0.01	0.04	6.79	0.37
-0.72	2568	8	155	9	-0.09	0.04	-0.04	0.05	5.70	0.36
-0.36	2564	7	181	8	-0.05	0.03	-0.02	0.03	7.24	0.26
0.00	2568	4	182	5	-0.01	0.02	-0.09	0.02	6.95	0.24
0.36	2576	6	178	7	-0.01	0.03	-0.04	0.03	7.66	0.28
0.72	2574	10	178	12	0.02	0.05	-0.02	0.05	7.98	0.37
1.22	2569	6	159	6	0.01	0.03	0.06	0.03	7.90	0.37
2.50	2575	5	147	6	-0.10	0.03	-0.05	0.04	6.57	0.37
4.22	2578	10	143	11	0.00	0.00	0.00	0.00	6.84	0.61

Table D.2: NGC 5389

x[″]	V	ΔV	σ	$\Delta\sigma$	h_3	Δh_3	h_4	Δh_4	CaT*	ΔCaT*
-7.96	1893	12	134	14	0.00	0.00	0.00	0.00	5.60	0.63
-4.75	1862	12	174	14	0.00	0.00	0.00	0.00	7.74	0.59
-3.86	1872	6	114	4	-0.05	0.04	0.26	0.05	7.30	0.37
-1.73	1847	4	112	5	0.01	0.03	0.06	0.04	6.82	0.35
-0.87	1849	5	129	6	0.05	0.03	0.01	0.04	6.70	0.29
-0.36	1862	3	125	4	0.05	0.02	0.01	0.03	6.49	0.35
-0.00	1862	4	132	4	-0.02	0.02	0.02	0.03	6.91	0.34
0.51	1864	4	127	5	-0.03	0.03	0.04	0.03	6.86	0.29
1.37	1865	4	108	4	-0.03	0.03	0.13	0.03	7.88	0.35
3.43	1864	6	134	6	0.01	0.04	0.08	0.04	6.61	0.38
4.36	1862	10	146	11	0.00	0.00	0.00	0.00	6.17	0.62

Table D.3: NGC 5422

x[″]	V	ΔV	σ	$\Delta\sigma$	h_3	Δh_3	h_4	Δh_4	CaT*	ΔCaT*
-6.48	1841	13	144	15	0.00	0.00	0.00	0.00	5.56	0.62
-4.86	1837	7	134	7	-0.01	0.05	0.11	0.05	6.35	0.38
-2.24	1854	5	138	5	-0.02	0.03	0.06	0.03	6.82	0.36
-1.23	1856	6	155	7	0.10	0.03	-0.02	0.04	6.65	0.33
-0.72	1839	7	176	7	0.09	0.03	0.02	0.04	7.01	0.36
-0.36	1838	5	182	6	0.04	0.02	-0.01	0.02	7.20	0.31
-0.00	1832	5	187	7	0.00	0.02	-0.06	0.03	6.68	0.30
0.36	1844	7	190	8	-0.05	0.03	-0.00	0.03	6.25	0.35
0.87	1827	7	183	7	0.03	0.03	0.08	0.03	7.18	0.32
1.87	1830	7	165	7	-0.02	0.03	0.06	0.04	6.70	0.36
4.51	1841	7	131	9	0.01	0.05	-0.01	0.06	6.14	0.38
6.13	1843	11	103	13	0.00	0.00	0.00	0.00	4.61	0.65

Table D.4: NGC 5443

x[″]	V	ΔV	σ	$\Delta\sigma$	h_3	Δh_3	h_4	Δh_4	CaT*	ΔCaT*
-7.47	1787	13	107	16	0.00	0.00	0.00	0.00	7.88	0.63
-3.34	1739	9	110	11	0.00	0.00	0.00	0.00	4.69	0.61
-1.74	1740	7	121	8	0.00	0.00	0.00	0.00	7.70	0.60
-1.23	1738	5	115	6	-0.01	0.04	0.03	0.05	7.66	0.37
-0.02	1758	3	89	4	-0.07	0.03	0.05	0.04	7.43	0.33
1.67	1760	6	112	10	0.01	0.05	-0.11	0.07	6.70	0.38
4.36	1752	11	125	13	0.00	0.00	0.00	0.00	5.57	0.65

Table D.5: NGC 5475

x[″]	V	ΔV	σ	$\Delta\sigma$	h_3	Δh_3	h_4	Δh_4	CaT*	ΔCaT*
-4.12	1665	5	55	8	0.00	0.00	0.00	0.00	7.57	0.60
-2.48	1665	5	74	6	0.00	0.00	0.00	0.00	6.94	0.60
-1.50	1660	5	93	7	0.10	0.05	0.01	0.05	7.04	0.38
-0.50	1669	5	111	7	0.03	0.04	-0.09	0.06	6.91	0.30
0.00	1661	3	97	4	0.02	0.03	-0.02	0.04	7.52	0.36
0.50	1674	6	91	7	-0.05	0.05	0.04	0.06	7.40	0.32
1.64	1667	5	89	6	-0.01	0.05	0.06	0.05	7.32	0.37
2.12	1665	5	87	7	0.00	0.00	0.00	0.00	6.65	0.55
3.49	1671	4	43	6	0.00	0.00	0.00	0.00	7.33	0.61

Table D.6: NGC 5587

x[″]	V	ΔV	σ	$\Delta\sigma$	h_3	Δh_3	h_4	Δh_4	CaT*	ΔCaT*
-3.82	2291	6	76	9	0.00	0.00	0.00	0.00	6.66	0.62
-1.43	2311	6	110	9	-0.06	0.05	-0.06	0.06	6.24	0.37
-0.00	2296	3	100	4	-0.03	0.03	0.06	0.03	7.09	0.35
1.57	2280	6	79	6	0.19	0.07	0.09	0.06	7.95	0.37

Table D.7: NGC 5689

x[″]	V	ΔV	σ	$\Delta\sigma$	h_3	Δh_3	h_4	Δh_4	CaT*	ΔCaT*
-9.04	2202	11	96	14	0.00	0.00	0.00	0.00	7.81	0.61
-5.86	2173	9	137	10	0.00	0.00	0.00	0.00	6.57	0.62
-4.10	2195	8	143	10	0.00	0.00	0.00	0.00	7.51	0.59
-3.04	2202	5	138	5	-0.04	0.03	0.11	0.04	6.87	0.37
-1.37	2212	5	151	4	-0.10	0.03	0.10	0.03	7.80	0.33
-0.52	2214	4	157	5	-0.07	0.02	-0.05	0.03	6.84	0.28
0.00	2200	5	158	5	-0.04	0.02	0.02	0.03	6.44	0.36
0.36	2201	5	163	5	0.01	0.02	0.01	0.03	7.48	0.37
0.88	2192	5	154	5	-0.03	0.02	0.04	0.03	6.88	0.30
1.74	2184	5	158	5	0.04	0.02	0.07	0.03	7.78	0.33
3.38	2200	6	147	7	-0.05	0.04	0.05	0.04	7.05	0.38
4.46	2211	8	100	10	0.00	0.00	0.00	0.00	5.70	0.62
6.21	2209	9	125	11	0.00	0.00	0.00	0.00	5.76	0.63
9.29	2218	9	92	11	0.00	0.00	0.00	0.00	7.72	0.62

Table D.8: NGC 5707

x[″]	V	ΔV	σ	$\Delta\sigma$	h_3	Δh_3	h_4	Δh_4	CaT*	ΔCaT*
-5.06	2208	5	71	7	0.00	0.00	0.00	0.00	6.90	0.62
-4.33	2211	5	85	5	0.02	0.05	0.14	0.05	7.36	0.37
-1.89	2193	5	143	6	0.03	0.03	-0.05	0.04	6.51	0.35
-0.88	2179	6	154	8	0.01	0.03	-0.00	0.04	7.33	0.34
-0.01	2191	3	163	4	-0.04	0.02	-0.06	0.02	7.03	0.24
1.01	2200	5	147	6	-0.04	0.03	0.02	0.03	7.56	0.34
2.66	2198	5	119	5	-0.04	0.03	0.06	0.04	6.59	0.37
3.20	2199	6	96	7	0.00	0.00	0.00	0.00	6.18	0.62
4.83	2210	6	84	8	0.00	0.00	0.00	0.00	6.24	0.62

Table D.9: NGC 5719

x[″]	V	ΔV	σ	$\Delta\sigma$	h_3	Δh_3	h_4	Δh_4	CaT*	ΔCaT*
-6.63	1731	8	82	10	0.00	0.00	0.00	0.00	7.93	0.62
-4.44	1723	7	104	8	0.00	0.00	0.00	0.00	6.94	0.62
-3.38	1719	4	83	5	-0.01	0.04	0.25	0.04	7.39	0.37
-1.75	1726	5	97	5	-0.03	0.04	0.09	0.04	6.80	0.35
-0.88	1719	4	102	4	-0.02	0.03	0.17	0.03	6.86	0.33
-0.01	1720	3	113	2	0.02	0.02	0.12	0.02	6.83	0.24
0.87	1717	5	125	6	0.02	0.03	0.02	0.04	7.30	0.36
2.12	1723	5	92	5	-0.02	0.04	0.13	0.04	7.11	0.37
3.89	1728	5	72	7	0.00	0.00	0.00	0.00	7.62	0.58
8.01	1712	15	57	21	0.00	0.00	0.00	0.00	7.28	0.70

Table D.10: NGC 5746

x[″]	V	ΔV	σ	$\Delta\sigma$	h_3	Δh_3	h_4	Δh_4	CaT*	ΔCaT*
-13.66	1690	15	161	17	0.00	0.00	0.00	0.00	5.49	0.62
-11.52	1703	11	164	13	0.02	0.05	-0.01	0.06	5.61	0.38
-6.14	1719	9	223	10	-0.01	0.03	-0.02	0.04	6.43	0.37
-3.32	1713	7	215	7	-0.03	0.03	0.05	0.03	6.53	0.35
-1.76	1711	7	184	8	0.01	0.03	0.04	0.03	6.70	0.37
-0.89	1713	5	161	5	-0.05	0.03	0.04	0.03	7.04	0.37
-0.00	1723	4	160	5	-0.04	0.02	0.01	0.03	6.86	0.28
1.03	1714	6	182	5	0.00	0.03	0.10	0.03	7.19	0.32
2.43	1691	7	228	7	-0.02	0.02	0.06	0.03	6.74	0.36
6.19	1733	12	202	14	-0.06	0.05	-0.03	0.05	5.15	0.39
7.14	1714	18	175	20	0.00	0.00	0.00	0.00	4.62	0.70
12.51	1727	18	184	21	0.00	0.00	0.00	0.00	5.47	0.68

Table D.11: NGC 5838

x[″]	V	ΔV	σ	$\Delta\sigma$	h_3	Δh_3	h_4	Δh_4	CaT*	ΔCaT*
-14.62	1358	16	172	11	0.13	0.09	0.32	0.11	8.43	0.38
-7.00	1341	8	172	8	0.03	0.04	0.06	0.04	7.04	0.37
-4.61	1345	9	220	9	0.05	0.03	0.06	0.04	6.35	0.35
-3.21	1369	9	282	9	-0.03	0.02	0.05	0.03	6.86	0.36
-2.32	1332	9	267	12	0.03	0.03	-0.06	0.03	6.73	0.36
-1.60	1336	8	267	10	0.03	0.02	-0.04	0.03	6.49	0.29
-1.08	1325	11	302	12	-0.01	0.03	0.01	0.03	6.35	0.33
-0.72	1328	8	271	9	0.03	0.02	-0.02	0.03	7.01	0.29
-0.36	1336	7	278	9	-0.01	0.02	-0.00	0.02	6.80	0.26
0.00	1345	7	291	8	0.03	0.02	0.00	0.02	6.51	0.25
0.36	1382	8	319	10	0.04	0.02	-0.03	0.02	7.81	0.25
0.72	1381	10	295	11	-0.11	0.03	-0.03	0.03	6.37	0.27
1.08	1398	11	271	13	-0.05	0.03	-0.06	0.04	6.59	0.32
1.44	1365	11	322	14	-0.05	0.03	-0.03	0.03	7.01	0.37
1.96	1359	10	295	9	-0.00	0.03	0.09	0.03	6.86	0.30
2.68	1360	10	244	10	-0.07	0.03	0.08	0.04	6.90	0.35
3.57	1298	10	278	10	0.03	0.03	0.06	0.03	6.53	0.35
4.81	1331	10	227	12	-0.05	0.04	-0.04	0.04	5.79	0.38
6.71	1322	9	212	8	0.03	0.03	0.09	0.04	7.15	0.38
11.00	1327	16	160	22	0.02	0.08	-0.10	0.11	5.26	0.39
11.74	1353	21	157	24	0.00	0.00	0.00	0.00	3.65	0.62

Table D.12: NGC 5854

x[″]	V	ΔV	σ	$\Delta\sigma$	h_3	Δh_3	h_4	Δh_4	CaT*	ΔCaT*
-5.98	1682	8	103	9	0.00	0.00	0.00	0.00	7.97	0.60
-4.31	1677	5	67	4	0.01	0.06	0.34	0.06	7.46	0.37
-1.88	1660	4	95	6	0.05	0.04	-0.05	0.05	6.47	0.37
-0.86	1659	5	100	6	0.05	0.04	-0.03	0.05	5.96	0.31
-0.36	1675	4	107	5	-0.00	0.03	-0.00	0.04	6.78	0.35
0.00	1670	3	102	4	0.02	0.03	0.05	0.03	6.73	0.33
0.36	1676	3	121	5	-0.03	0.02	-0.04	0.03	7.75	0.33
0.86	1698	4	108	4	-0.10	0.03	0.07	0.04	7.88	0.30
1.88	1677	4	121	6	0.05	0.03	-0.03	0.04	7.65	0.36
4.31	1659	5	74	5	0.01	0.05	0.10	0.05	6.55	0.38
5.98	1660	6	73	8	0.00	0.00	0.00	0.00	5.55	0.61

Table D.13: NGC 5879

x[″]	V	ΔV	σ	$\Delta\sigma$	h_3	Δh_3	h_4	Δh_4	CaT*	ΔCaT*
-7.00	764	10	70	14	0.00	0.00	0.00	0.00	4.88	0.63
-4.24	785	4	51	6	0.00	0.00	0.00	0.00	6.44	0.60
-2.68	777	5	43	8	0.06	0.10	0.10	0.12	6.35	0.38
-1.03	780	5	68	6	0.04	0.06	0.02	0.07	6.88	0.36
-0.01	779	3	51	3	0.00	0.04	0.22	0.04	6.47	0.30
1.17	781	4	45	5	-0.00	0.07	0.22	0.07	7.55	0.34
4.30	780	14	34	22	0.00	0.30	0.24	0.33	6.55	0.38
6.42	776	10	41	15	0.00	0.00	0.00	0.00	4.06	0.63

Table D.14: NGC 5965

x[″]	V	ΔV	σ	$\Delta\sigma$	h_3	Δh_3	h_4	Δh_4	CaT*	ΔCaT*
-5.41	3375	12	148	14	0.00	0.00	0.00	0.00	4.80	0.62
-3.08	3398	9	192	8	0.11	0.04	0.08	0.04	5.22	0.38
-1.00	3411	9	160	7	-0.01	0.05	0.19	0.06	6.18	0.37
0.00	3417	5	191	6	-0.01	0.02	0.05	0.03	7.37	0.27
0.99	3421	10	189	14	0.05	0.05	-0.09	0.06	7.27	0.38
2.22	3368	12	170	15	0.00	0.00	0.00	0.00	5.19	0.61

Table D.15: NGC 6010

x[″]	V	ΔV	σ	$\Delta\sigma$	h_3	Δh_3	h_4	Δh_4	CaT*	ΔCaT*
-6.51	2038	22	110	26	0.00	0.00	0.00	0.00	7.96	0.67
-3.70	2028	9	105	11	0.00	0.00	0.00	0.00	7.76	0.60
-2.68	2038	8	123	10	0.00	0.00	0.00	0.00	8.27	0.61
-2.23	2027	7	130	7	-0.06	0.04	0.09	0.05	7.67	0.38
-1.23	2013	8	150	9	-0.06	0.04	-0.03	0.05	7.61	0.34
-0.72	1991	9	160	8	-0.15	0.05	0.04	0.05	7.02	0.37
-0.36	2010	5	156	5	-0.10	0.03	0.03	0.03	7.05	0.32
-0.00	2020	4	163	5	-0.02	0.02	-0.02	0.02	6.21	0.31
0.36	2025	7	177	9	-0.06	0.03	-0.08	0.04	6.33	0.35
0.87	2036	7	170	8	-0.02	0.03	0.02	0.04	7.23	0.32
1.87	2015	5	139	6	0.05	0.03	0.04	0.04	7.12	0.36
2.83	2017	8	119	9	0.00	0.00	0.00	0.00	6.64	0.58
4.47	2030	11	84	14	0.00	0.00	0.00	0.00	7.36	0.61

Table D.16: NGC 6504

x[″]	V	ΔV	σ	$\Delta\sigma$	h_3	Δh_3	h_4	Δh_4	CaT*	ΔCaT*
-4.01	4724	13	191	16	0.00	0.00	0.00	0.00	6.38	0.61
-3.12	4725	8	195	8	0.03	0.03	0.12	0.04	7.00	0.38
-0.99	4740	11	248	14	-0.00	0.04	-0.05	0.04	7.47	0.34
0.01	4735	5	213	5	0.00	0.02	0.07	0.02	7.15	0.24
0.87	4760	8	180	8	-0.09	0.04	0.07	0.04	6.07	0.35
2.00	4732	8	191	9	0.01	0.03	0.03	0.04	5.99	0.37
2.48	4739	10	187	12	0.00	0.00	0.00	0.00	6.18	0.55
3.86	4722	12	203	15	0.00	0.00	0.00	0.00	7.71	0.59

Table D.17: NGC 7331

x[″]	V	ΔV	σ	$\Delta\sigma$	h_3	Δh_3	h_4	Δh_4	CaT*	ΔCaT*
-22.43	771	25	142	29	0.00	0.00	0.00	0.00	7.15	0.83
-19.02	781	11	93	14	0.00	0.00	0.00	0.00	6.86	0.64
-17.32	807	9	85	9	-0.11	0.09	0.34	0.09	5.93	0.37
-13.03	804	8	115	7	-0.04	0.06	0.17	0.06	6.38	0.37
-10.21	816	6	97	5	-0.01	0.05	0.27	0.05	7.34	0.37
-8.25	810	5	88	4	0.01	0.05	0.27	0.05	6.19	0.36
-6.64	811	5	103	4	-0.11	0.04	0.19	0.04	6.66	0.36
-5.38	816	5	118	5	-0.09	0.04	0.15	0.04	7.53	0.37
-4.30	822	4	117	4	-0.02	0.03	0.16	0.03	7.26	0.32
-3.41	834	4	112	4	-0.12	0.03	0.09	0.03	6.91	0.34
-2.69	828	3	118	3	-0.04	0.02	0.15	0.03	6.27	0.30
-2.16	846	4	108	3	-0.05	0.03	0.20	0.03	7.39	0.37
-1.80	827	4	116	6	-0.01	0.03	-0.07	0.05	6.60	0.34
-1.44	835	4	129	5	0.08	0.03	-0.05	0.04	6.65	0.30
-1.08	821	3	131	5	-0.03	0.02	-0.04	0.03	6.50	0.26
-0.72	817	3	137	4	0.02	0.02	-0.04	0.03	6.54	0.22
-0.36	821	3	135	3	-0.03	0.02	0.01	0.02	7.06	0.18
-0.00	821	2	138	3	-0.02	0.01	0.03	0.02	7.65	0.18
0.36	833	3	136	3	-0.04	0.02	0.08	0.02	7.37	0.20
0.72	830	3	139	4	-0.05	0.02	0.02	0.02	7.60	0.24
1.08	828	5	146	5	0.01	0.03	0.10	0.03	8.43	0.29
1.44	817	4	120	4	0.06	0.03	0.14	0.03	7.07	0.35
1.96	820	4	120	4	0.01	0.03	0.09	0.03	6.78	0.30
2.70	814	4	118	4	-0.04	0.03	0.09	0.03	7.18	0.34
3.41	808	4	95	5	0.09	0.04	0.06	0.04	6.52	0.37
4.29	826	5	120	5	-0.06	0.03	0.11	0.04	6.76	0.36
5.67	802	5	115	5	-0.02	0.04	0.13	0.04	7.29	0.36
7.89	806	7	112	6	-0.15	0.05	0.15	0.05	6.23	0.36
11.47	794	12	103	9	-0.30	0.12	0.25	0.11	6.27	0.40
15.74	704	39	133	46	0.00	0.00	0.00	0.00	12.04	1.21

Table D.18: NGC 7332

x[″]	V	ΔV	σ	$\Delta\sigma$	h_3	Δh_3	h_4	Δh_4	CaT*	ΔCaT*
-12.21	1214	13	57	19	0.00	0.00	0.00	0.00	3.47	0.64
-8.17	1224	8	93	10	0.00	0.00	0.00	0.00	6.41	0.60
-6.78	1228	5	88	6	-0.08	0.05	0.06	0.05	6.53	0.37
-3.87	1214	4	110	5	0.04	0.03	-0.03	0.04	5.55	0.38
-2.47	1219	4	120	5	-0.04	0.03	-0.01	0.04	6.10	0.36
-1.59	1231	6	122	7	0.03	0.05	0.03	0.05	8.05	0.31
-1.08	1237	4	126	5	-0.02	0.03	0.01	0.03	7.12	0.33
-0.72	1230	3	125	4	-0.01	0.02	0.06	0.03	6.77	0.26
-0.36	1230	3	131	3	0.01	0.02	0.05	0.02	7.56	0.22
0.00	1227	2	130	3	0.05	0.02	-0.03	0.02	6.85	0.21
0.36	1223	2	127	3	0.02	0.02	0.04	0.02	7.62	0.21
0.72	1227	3	123	3	-0.05	0.02	0.02	0.02	7.04	0.22
1.08	1225	3	122	4	-0.02	0.02	0.01	0.03	7.14	0.25
1.44	1227	4	133	5	-0.01	0.03	-0.03	0.03	7.01	0.32
1.95	1222	3	116	4	-0.01	0.03	-0.01	0.03	6.57	0.31
2.83	1223	5	121	5	0.02	0.03	0.03	0.04	6.56	0.36
4.23	1230	4	99	4	0.03	0.04	0.07	0.04	6.61	0.38
7.14	1214	5	94	6	0.03	0.05	0.09	0.05	6.56	0.37
8.53	1208	7	78	10	0.00	0.00	0.00	0.00	5.13	0.61
12.46	1223	11	99	14	0.00	0.00	0.00	0.00	5.26	0.62

Table D.19: NGC 7457

x[″]	V	ΔV	σ	$\Delta\sigma$	h_3	Δh_3	h_4	Δh_4	CaT*	ΔCaT*
-11.00	833	6	45	9	0.00	0.00	0.00	0.00	4.68	0.63
-5.98	837	4	60	6	0.00	0.00	0.00	0.00	6.69	0.62
-3.31	842	3	59	4	0.02	0.04	0.03	0.05	6.96	0.37
-1.00	847	4	59	6	-0.02	0.05	-0.02	0.07	7.56	0.37
0.01	839	2	59	2	-0.02	0.03	0.05	0.03	7.70	0.24
0.88	836	3	66	3	0.03	0.03	0.05	0.04	7.88	0.32
1.85	840	3	71	4	0.08	0.04	-0.01	0.04	7.20	0.37
4.97	848	4	52	5	-0.07	0.06	0.02	0.07	7.15	0.38
6.68	853	4	47	6	0.00	0.00	0.00	0.00	7.24	0.61
11.63	851	6	54	8	0.00	0.00	0.00	0.00	7.15	0.62

Appendix E

The near-IR Ca II triplet - σ relations - Tables

In this appendix we tabulate for each galaxy the velocity dispersion and near-IR Ca II triplet indices presented in chapter 4. Velocity dispersions and their errors are expressed in km/s whereas the values for the CaT*, CaT, Mg I and PaT indices, and their uncertainties, are given in Å.

Table E.1: INDEX - σ RELATION [R_{eff} APERTURE]

Galaxy	log(σ)	Δlog(σ)	CaT*	ΔCaT*	CaT	ΔCaT	Mg I	ΔMg I	PaT	ΔPaT	S/N [pix^{-1}]
NGC 5326	2.224	0.008	6.897	0.116	7.238	0.124	0.252	0.026	0.367	0.105	108
NGC 5389	2.091	0.010	6.748	0.132	7.363	0.141	0.260	0.029	0.661	0.119	95
NGC 5422	2.221	0.010	6.559	0.117	6.951	0.125	0.286	0.026	0.422	0.106	107
NGC 5443	2.002	0.015	7.016	0.208	7.227	0.223	0.224	0.046	0.228	0.189	60
NGC 5475	1.994	0.013	7.132	0.154	7.589	0.164	0.291	0.034	0.492	0.139	81
NGC 5587	1.995	0.012	6.940	0.235	7.245	0.252	0.259	0.052	0.328	0.213	53
NGC 5689	2.193	0.010	6.861	0.118	7.089	0.126	0.273	0.026	0.245	0.107	106
NGC 5707	2.172	0.009	6.901	0.147	7.171	0.157	0.271	0.032	0.290	0.133	85
NGC 5719	2.054	0.011	6.747	0.152	7.339	0.163	0.260	0.034	0.636	0.137	82
NGC 5746	2.267	0.012	6.402	0.124	7.008	0.133	0.289	0.027	0.652	0.112	101
NGC 5838	2.419	0.011	6.586	0.077	6.906	0.082	0.272	0.017	0.345	0.069	164
NGC 5854	2.025	0.010	6.801	0.120	7.348	0.128	0.227	0.027	0.588	0.108	104
NGC 5879	1.808	0.015	6.905	0.198	7.334	0.212	0.143	0.044	0.461	0.179	63
NGC 5965	2.272	0.011	6.270	0.161	7.113	0.172	0.192	0.036	0.906	0.144	78
NGC 6010	2.189	0.011	6.516	0.132	6.997	0.141	0.302	0.029	0.517	0.119	95
NGC 6504	2.330	0.010	6.670	0.149	7.075	0.160	0.176	0.033	0.436	0.134	84
NGC 7331	2.112	0.007	7.002	0.061	7.194	0.066	0.235	0.014	0.207	0.056	203
NGC 7332	2.093	0.007	6.940	0.079	7.381	0.085	0.230	0.017	0.475	0.071	158
NGC 7457	1.807	0.009	7.320	0.138	7.503	0.148	0.204	0.031	0.197	0.126	90

Table E.2: INDEX - σ RELATION [$R_{eff}/2$ APERTURE]

Galaxy	log(σ)	Δlog(σ)	CaT*	ΔCaT*	CaT	ΔCaT	Mg I	ΔMg I	PaT	ΔPaT	S/N [pix^{-1}]
NGC 5326	2.223	0.009	6.849	0.129	7.281	0.138	0.256	0.028	0.464	0.116	97
NGC 5389	2.101	0.010	6.803	0.150	7.484	0.161	0.264	0.033	0.732	0.136	83
NGC 5422	2.236	0.010	6.619	0.130	7.019	0.140	0.279	0.029	0.430	0.118	96
NGC 5443	1.977	0.014	7.010	0.231	7.349	0.247	0.206	0.051	0.365	0.209	54
NGC 5475	2.001	0.012	7.082	0.173	7.523	0.185	0.287	0.038	0.475	0.157	72
NGC 5587	2.003	0.013	7.129	0.283	7.262	0.304	0.252	0.063	0.143	0.257	44
NGC 5689	2.199	0.009	6.957	0.127	7.254	0.136	0.291	0.028	0.319	0.115	98
NGC 5707	2.186	0.010	7.018	0.176	7.394	0.188	0.285	0.039	0.404	0.159	71
NGC 5719	2.068	0.012	6.602	0.195	7.370	0.209	0.275	0.043	0.826	0.176	64
NGC 5746	2.254	0.011	6.589	0.137	7.281	0.147	0.281	0.030	0.743	0.124	91
NGC 5838	2.430	0.011	6.672	0.084	7.056	0.091	0.267	0.018	0.413	0.076	149
NGC 5854	2.035	0.010	6.722	0.133	7.478	0.142	0.230	0.029	0.812	0.120	94
NGC 5879	1.811	0.016	6.822	0.245	7.282	0.262	0.193	0.054	0.495	0.221	51
NGC 5965	2.266	0.011	6.422	0.174	7.165	0.186	0.184	0.039	0.799	0.156	72
NGC 6010	2.193	0.012	6.358	0.155	6.901	0.166	0.312	0.034	0.584	0.139	81
NGC 6504	2.329	0.011	6.685	0.165	7.143	0.176	0.194	0.036	0.493	0.149	76
NGC 7331	2.119	0.007	7.017	0.068	7.289	0.073	0.244	0.015	0.292	0.061	184
NGC 7332	2.096	0.007	6.983	0.089	7.410	0.095	0.245	0.020	0.459	0.081	140
NGC 7457	1.810	0.009	7.410	0.150	7.619	0.160	0.209	0.033	0.225	0.136	83

Table E.3: INDEX - σ RELATION [1.2x4 ARCSEC^2 APERTURE]

Galaxy	log(σ)	Δlog(σ)	CaT*	ΔCaT*	CaT	ΔCaT	Mg I	ΔMg I	PaT	ΔPaT	S/N [pix^{-1}]
NGC 5326	2.216	0.008	6.835	0.105	7.178	0.112	0.234	0.023	0.369	0.095	119
NGC 5389	2.096	0.010	6.761	0.122	7.320	0.131	0.257	0.027	0.601	0.110	102
NGC 5422	2.216	0.010	6.570	0.113	6.937	0.121	0.279	0.025	0.395	0.102	111
NGC 5443	2.009	0.015	6.810	0.198	7.068	0.213	0.239	0.044	0.278	0.179	63
NGC 5475	1.966	0.014	7.022	0.143	7.435	0.153	0.287	0.032	0.444	0.130	87
NGC 5587	1.974	0.015	6.909	0.208	7.098	0.223	0.242	0.046	0.202	0.189	60
NGC 5689	2.197	0.009	6.905	0.120	7.159	0.129	0.277	0.026	0.273	0.109	104
NGC 5707	2.155	0.008	6.856	0.136	7.095	0.146	0.249	0.030	0.257	0.123	92
NGC 5719	2.033	0.012	6.785	0.133	7.204	0.142	0.259	0.029	0.451	0.120	94
NGC 5746	2.254	0.011	6.589	0.137	7.281	0.147	0.281	0.030	0.743	0.124	91
NGC 5838	2.429	0.011	6.671	0.081	7.018	0.086	0.278	0.018	0.374	0.072	156
NGC 5854	2.025	0.010	6.801	0.120	7.348	0.128	0.227	0.027	0.588	0.108	104
NGC 5879	1.776	0.018	6.927	0.162	7.297	0.173	0.088	0.036	0.398	0.147	77
NGC 5965	2.276	0.010	6.381	0.165	7.179	0.176	0.171	0.037	0.858	0.148	76
NGC 6010	2.164	0.012	6.644	0.116	7.071	0.124	0.293	0.025	0.458	0.104	108
NGC 6504	2.326	0.011	6.681	0.143	7.019	0.152	0.165	0.032	0.364	0.128	88
NGC 7331	2.115	0.007	6.990	0.064	7.220	0.069	0.242	0.014	0.247	0.058	194
NGC 7332	2.089	0.006	6.824	0.075	7.258	0.080	0.224	0.017	0.467	0.068	167
NGC 7457	1.808	0.009	7.381	0.141	7.588	0.151	0.201	0.031	0.222	0.129	88

Bibliography

Aaronson, M., Huchra, J., Mould, J., Schechter, P. L., Tully, R. B., 1982, ApJ, **258**, 64.

Abraham, R. G., Merrifield, M. R., Ellis, R. S., Tanvir, N. R., Brinchmann, J., 1999, MNRAS, **308**, 569.

Andredakis, Y. C., Sanders, R. H., 1994, MNRAS, **267**, 283.

Andredakis, Y. C., Peletier, R. F., Balcells, M., 1995, MNRAS, **275**, 874 (APB95).

Armandroff, T. E., Zinn, R., 1988, AJ, **96**, 92.

Arsenault, R., Boulesteix, J., Georgelin, Y., Roy, J.-R., 1988, A&A, **200**, 29.

Athanassoula, E., Bureau, M., 1999, ApJ, **522**, 699.

Bacon, R., Adam, G., Baranne, A., Courtes, G., Dubet, D., Dubois, J. P., Emsellem, E., Ferruit, P., Georgelin, Y., Monnet, G., Pecontal, E., Rousset, A., Say, F., 1995, A&AS, **113**, 347.

Bacon, R., Copin, Y., Monnet, G., Miller, B. W., Allington-Smith, J. R., Bureau, M., Carollo, C. M., Davies, R. L., Emsellem, E., Kuntschner, H., Peletier, R. F., Verolme, E. K., de Zeeuw, P. T., 2001, MNRAS, **326**, 23.

Bacon, R., Bureau, M., Cappellari, M., Copin, Y., Davies, R. L., Emsellem, E., Kuntschner, H., McDermid, R., Miller, B. W., Peletier, R. F., Verolme, E. K., de Zeeuw, P. T., 2002, astro-ph/0204129.

Balcells, M., 2002. . In *ASP Conf. Series. Disks of Galaxies: Kinematics, Dynamics and Perturbations*, volume 275.

Balcells, M., Peletier, R. F., 1994, AJ, **107**, 135.

Balcells, M., Graham, A. W., Domínguez-Palmero, L., Peletier, R. F., 2003, ApJ, **582**, L79.

Baugh, C. M., Cole, S., Frenk, C. S., 1996, MNRAS, **283**, 1361.

Bender, R., 1988, A&A, **202**, L5.

Bender, R., 1990, A&A, **229**, 441.

Bender, R., Nieto, J.-L., 1990, A&A, **239**, 97.

Bender, R., Paquet, A., 1999, Ap&SS, **267**, 283.

Bender, R., Burstein, D., Faber, S. M., 1992, ApJ, **399**, 462 (B92).

Bender, R., Burstein, D., Faber, S. M., 1993, ApJ, **411**, 153.

Bender, R., Saglia, R. P., Gerhard, O. E., 1994, MNRAS, **269**, 785.

Bertola, F., Zeilinger, W. W., Rubin, V. C., 1989, ApJ, **345**, L29.

Bertola, F., Vietri, M., Zeilinger, W. W., 1991, ApJ, **374**, L13.

Bertola, F., Buson, L. M., Zeilinger, W. W., 1992, ApJ, **401**, L79.

Bica, E., Alloin, D., 1987, A&A, **186**, 49.

Bica, E., Claria, J. J., Piatti, A. E., Bonatto, C., 1998, A&AS, **131**, 483.

Binney, J., 1976, MNRAS, **177**, 19.

Binney, J., 1985, MNRAS, **212**, 767.

Binney, J., Kormendy, J., White, S. D. M., editors, 1982. *Morphology an dynamics of galaxies.*

Binney, J., Kormendy, J., White, S., 1984, Mercury, **13**, 92.

Bothun, G. D., Gregg, M. D., 1990, ApJ, **350**, 73.

Bruzual A., G., Charlot, S., 1993, ApJ, **405**, 538.

Burbidge, E. M., Burbidge, G. R., 1959, ApJ, **130**, 20.

Burbidge, E. M., Burbidge, G. R., 1968, ApJ, **154**, 857.

Bureau, M., Athanassoula, E., 1999, ApJ, **522**, 686.

Bureau, M., Freeman, K. C., 1999, AJ, **118**, 126.

Burstein, D., Faber, S. M., Gaskell, C. M., Krumm, N., 1984, ApJ, **287**, 586.

Busarello, G., Capaccioli, M., Capozziello, S., Longo, G., Puddu, E., 1997, A&A, **320**, 415.

Buzzoni, A., 1995, ApJS, **98**, 69.

Caldwell, N., 1983, ApJ, **268**, 90.

Caon, N., Capaccioli, M., D'Onofrio, M., 1993, MNRAS, **265**, 1013.

Caon, N., Macchetto, D., Pastoriza, M., 2000, ApJS, **127**, 39.

Cappellari, M., Copin, Y., 2001. Adaptive 2D-Binning. In *Galaxies: the Third Dimension. Edited by Margarita Rosado, Luc Binette, and Lorena Arias.*

Cappellari, M., Copin, Y., 2002, submitted to MNRAS.

Cardiel, N., 1999, Ph.D. Thesis. Universidad Complutense de Madrid.

Carollo, C. M., 1999, ApJ, **523**, 566.

Carollo, C. M., Stiavelli, M., de Zeeuw, P. T., Seigar, M., Dejonghe, H., 2001, ApJ, **546**, 216.

Carollo, C. M., Stiavelli, M., Seigar, M., de Zeeuw, P. T., Dejonghe, H., 2002, AJ, **123**, 159.

Carter, D., Visvanathan, N., Pickles, A. J., 1986, ApJ, **311**, 637.

Cenarro, A. J., Cardiel, N., Gorgas, J., Peletier, R. F., Vazdekis, A., Prada, F., 2001a, MNRAS, **326**, 959.

Cenarro, A. J., Gorgas, J., Cardiel, N., Pedraz, S., Peletier, R. F., Vazdekis, A., 2001b, MNRAS, **326**, 981.

Cenarro, A. J., Gorgas, J., Cardiel, N., Vazdekis, A., Peletier, R. F., 2002, MNRAS, **329**, 863.

Cenarro, A. J., Gorgas, J., Vazdekis, A., Cardiel, N., Peletier, R. F., 2003, MNRAS, **339**, L12.

Cenarro, J., 2002, Ph.D. Thesis. Universidad Complutense de Madrid. (CEN02b).

Courteau, S., de Jong, R. S., Broeils, A. H., 1996, ApJ, **457**, L73.

Crinklaw, G., Federman, S. R., Joseph, C. L., 1994, ApJ, **424**, 748.

Davies, R. L., Efstathiou, G., Fall, S. M., Illingworth, G., Schechter, P. L., 1983, ApJ, **266**, 41.

Davies, R. L., Kuntschner, H., Emsellem, E., Bacon, R., Bureau, M., Carollo, C. M., Copin, Y., Miller, B. W., Monnet, G., Peletier, R. F., Verolme, E. K., de Zeeuw, P. T., 2001, ApJ, **548**, L33.

de Jong, R. S., 1996, A&A, **313**, 45.

de Vaucouleurs, G., 1948, Annales d'Astrophysique, **11**, 247.

de Vaucouleurs, G., 1959, Handbuch der Physik, **53**, 275.

de Vaucouleurs, G., de Vaucouleurs, A., Corwin, H. G., Buta, R. J., Paturel, G., Fouque, P., 1991, S&T, **82**, 621 (RC3).

de Zeeuw, P. T., Bureau, M., Emsellem, E., Bacon, R., Marcella Carollo, C., Copin, Y., Davies, R. L., Kuntschner, H., Miller, B. W., Monnet, G., Peletier, R. F., Verolme, E. K., 2002, MNRAS, **329**, 513.

de Zeeuw, T., Franx, M., 1991, ARA&A, **29**, 239.

Díaz, A. I., Terlevich, E., Terlevich, R., 1989, MNRAS, **239**, 325.

Djorgovski, S., Davis, M., 1987, ApJ, **313**, 59.

Dressler, A., 1980, ApJ, **236**, 351.

Dressler, A., Lynden-Bell, D., Burstein, D., Davies, R. L., Faber, S. M., Terlevich, R., Wegner, G., 1987, ApJ, **313**, 42.

Dressler, A., Oemler, A. J., Couch, W. J., Smail, I., Ellis, R. S., Barger, A., Butcher, H., Poggianti, B. M., Sharples, R. M., 1997, ApJ, **490**, 577.

Dreyer, J., 1988. *The Complete New General Catalogue and Index Catalogue of Nebulae and Star Clusters*. Sky Publ. Corp., Cambridge, MA.

Dreyer, J. L. E., 1888, MmRAS, **49**.

Eggen, O. J., Lynden-Bell, D., Sandage, A. R., 1962, ApJ, **136**, 748.

Eisenhauer, F., 2001. Evidence in Favour of IMF Variations. In *Starburst Galaxies: Near and Far*, page 24.

Ellis, R. S., Smail, I., Dressler, A., Couch, W. J., Oemler, A. J., Butcher, H., Sharples, R. M., 1997, ApJ, **483**, 582.

Ellis, R. S., Abraham, R. G., Dickinson, M., 2001, ApJ, **551**, 111.

Emsellem, E., 2001. Secular Evolution in the central regions of galaxies. In *SF2A-2001: Semaine de l'Astrophysique Francaise*, page 283.

Emsellem, E., Bacon, R., Monnet, G., Poulain, P., 1996, A&A, **312**, 777.

Emsellem, E., Greusard, D., Combes, F., Friedli, D., Leon, S., Pécontal, E., Wozniak, H., 2001, A&A, **368**, 52.

Faber, S. M., Gallagher, J. S., 1976, ApJ, **204**, 365.

Faber, S. M., Jackson, R. E., 1976, ApJ, **204**, 668.

Faber, S. M., Burstein, D., Dressler, A., 1977, AJ, **82**, 941.

Falcón-Barroso, J. ., Peletier, R. F., Balcells, M., 2002, MNRAS, **335**, 741.

Falco, E. E., Kurtz, M. J., Geller, M. J., Huchra, J. P., Peters, J., Berlind, P., Mink, D. J., Tokarz, S. P., Elwell, B., 1999, VizieR Online Data Catalog, **611**, 10438.

Fathi, K., Peletier, R. F., 2003, submitted to A&A.

Fisher, D., 1997, AJ, **113**, 950.

Fisher, D., Illingworth, G., Franx, M., 1994, AJ, **107**, 160.

Fisher, D., Franx, M., Illingworth, G., 1996, ApJ, **459**, 110.

Franx, M., Illingworth, G. D., 1988, ApJ, **327**, L55.

Freeman, K. C., 1970, ApJ, **160**, 811.

Gerhard, O., Kronawitter, A., Saglia, R. P., Bender, R., 2001, AJ, **121**, 1936.

Gilmore, G., 2001. Evidence Supporting the Universality of the IMF. In *Starburst Galaxies: Near and Far*, page 34.

Gilmore, G., Wyse, R. F. G., 1998, AJ, **116**, 748.

Golev, V., Prugniel, P., Simien, F., Longhetti, M., 1999, A&AS, **136**, 519.

González, J. J., 1993, Ph.D. Thesis. Universidad of California Santa Cruz.

Gorgas, J., Pedraz, S., Guzman, R., Cardiel, N., Gonzalez, J. J., 1997, ApJ, **481**, L19.

Goudfrooij, P., Emsellem, E., 1996, Bulletin of the American Astronomical Society, **28**, 840.

Goudfrooij, P., Baum, S. A., Walsh, J. R., 1997. Fringe correction for STIS near-IR long-slit spectra using contemporaneous tungsten flat fields. In *The 1997 HST Calibration Workshop with a New Generation of Instruments, p. 100*, page 100.

Goudfrooij, P., Gorgas, J., Jablonka, P., 1999, Ap&SS, **269**, 109.

Graham, A., Colless, M., 1997, MNRAS, **287**, 221.

Graham, A. W., 2001, AJ, **121**, 820.

Gregg, M. D., 1989, ApJ, **337**, 45.

Gunn, J. E., Gott, J. R. I., 1972, ApJ, **176**, 1.

Guzman, R., Lucey, J. R., Bower, R. G., 1993, MNRAS, **265**, 731.

Hau, G., 1998, Ph.D. Thesis.

Hau, G. K. T., Carter, D., Balcells, M., 1999, MNRAS, **306**, 437.

Haynes, M. P., 1981, AJ, **86**, 1126.

Hoffleit, D., Warren, W. H., 1995, VizieR Online Data Catalog, **5050**.

Hubble, E. P., 1927, The Observatory, **50**, 276.

Hubble, E. P., 1936, Yale University Press.

Jablonka, P., Martin, P., Arimoto, N., 1996, AJ, **112**, 1415 (JMA96).

Jefferys, W. H., Fitzpatrick, M. J., McArthur, B. E., 1987, Celestial Mechanics, **41**, 39.

Jørgensen, I., Franx, M., Kjærgaard, P., 1992, A&AS, **95**, 489.

Jørgensen, I., Franx, M., Kjærgaard, P., 1995a, MNRAS, **273**, 1097.

Jørgensen, I., Franx, M., Kjærgaard, P., 1995b, MNRAS, **276**, 1341.

Jørgensen, I., Franx, M., Kjærgaard, P., 1996, MNRAS, **280**, 167 (J96).

Karachentsev, I. D., Makarov, D. A., 1996, AJ, **111**, 794.

Kauffmann, G., Guiderdoni, B., White, S. D. M., 1994, MNRAS, **267**, 981.

Kauffmann et al., 2002, astro-ph/0204055.

Kent, S. M., 1984, ApJS, **56**, 105.

Kent, S. M., 1986, AJ, **91**, 1301.

Knapen, J. H., Shlosman, I., Peletier, R. F., 2000, ApJ, **529**, 93.

Knapp, G. R., Kerr, F. J., Williams, B. A., 1978, ApJ, **222**, 800.

Kormendy, J., 1985, ApJ, **295**, 73.

Kormendy, J., 1993. Kinematics of extragalactic bulges: evidence that some bulges are really disks. In *IAU Symp. 153: Galactic Bulges*, volume 153, page 209.

Kormendy, J., Bender, R., 1996, ApJ, **464**, L119.

Kormendy, J., Illingworth, G., 1982, ApJ, **256**, 460.

Kuijken, K., Merrifield, M. R., 1993, MNRAS, **264**, 712.

Kuijken, K., Merrifield, M. R., 1995, ApJ, **443**, L13.

Kukarkin, B. V., Kholopov, P. N., 1982. *New catalogue of suspected variable stars.* Moscow: Publication Office "Nauka", 1982.

Kuntschner, H., 1998, Ph.D. Thesis. University of Durham.

Kuntschner, H., 2000, MNRAS, **315**, 184.

Larsen, N., Norgaard-Nielsen, H. U., Kjærgaard, P., Dickens, R. J., 1983, A&A, **117**, 257.

Larson, R. B., Tinsley, B. M., Caldwell, C. N., 1980, ApJ, **237**, 692.

Lauer, T. R., Ajhar, E. A., Byun, Y.-I., Dressler, A., Faber, S. M., Grillmair, C., Kormendy, J., Richstone, D., Tremaine, S., 1995, AJ, **110**, 2622.

Lindblad, B., 1956, Stockholms Observatoriums Annaler, **2**.

Magorrian, J., Tremaine, S., Richstone, D., Bender, R., Bower, G., Dressler, A., Faber, S. M., Gebhardt, K., Green, R., Grillmair, C., Kormendy, J., Lauer, T., 1998, AJ, **115**, 2285.

Martin, M. C., 1998, A&AS, **131**, 73.

Mateo, M. L., 1998, ARA&A, **36**, 435.

McWilliam, A., Rich, R. M., 1994, ApJS, **91**, 749.

Merrifield, M. R., Kuijken, K., 1994, ApJ, **432**, 575.

Merrifield, M. R., Kuijken, K., 1999, A&A, **345**, L47.

Merrifield, M. R., Fisher, D., Kuijken, K., 1996, Bulletin of the American Astronomical Society, **28**, 1345.

Mobasher, B., Guzman, R., Aragon-Salamanca, A., Zepf, S., 1999, MNRAS, **304**, 225.

Mollá, M., García-Vargas, M. L., 2000, A&A, **359**, 18.

Morgan, W. W., 1971, AJ, **76**, 1000.

Mutchler, M., Fruchter, A., 1997, American Astronomical Society Meeting, **29**, 1271.

Nesterov, V. V., Kuzmin, A. V., Ashimbaeva, N. T., Volchkov, A. A., Röser, S., Bastian, U., 1995, A&AS, **110**, 367.

Nilson, P., 1995, VizieR Online Data Catalog, **7026**.

Noordermeer, E., Sparke, L. S., Levine, S. E., 2001, MNRAS, **328**, 1064.

O'Connell, R., 1976, ApJ, **206**, 370.

O'Connell, R. W., 1980, ApJ, **236**, 430.

Oke, J. B., 1990, AJ, **99**, 1621.

Oke, J. B., Gunn, J. E., 1983, ApJ, **266**, 713.

Olszewski, E. W., Schommer, R. A., Suntzeff, N. B., Harris, H. C., 1991, AJ, **101**, 515.

Pahre, M. A., Djorgovski, S. G., de Carvalho, R. R., 1998, AJ, **116**, 1591 (P98).

Peletier, R. F., Balcells, M., 1996, AJ, **111**, 2238.

Peletier, R. F., Balcells, M., 1997, New Astronomy, **1**, 349 (PB97).

Peletier, R. F., Valentijn, E. A., Jameson, R. F., 1990, A&A, **233**, 62.

Peletier, R. F., Balcells, M., Davies, R. L., Andredakis, Y., Vazdekis, A., Burkert, A., Prada, F., 1999a, MNRAS, **310**, 703.

Peletier, R. F., Vazdekis, A., Arribas, S., del Burgo, C., García-Lorenzo, B., Gutiérrez, C., Mediavilla, E., Prada, F., 1999b, MNRAS, **310**, 863.

Peletier, R. F., Bacon, R., Bureau, M., Cappellari, M., Copin, Y., Davies, R. L., Emsellem, E., Falcon-Barroso, J., Krajnovic, D., Kuntschner, H., McDermid, R., Miller, B. W., Verolme, E. K., Wernli, F., de Zeeuw, P. T., 2001, The Newsletter of the Isaac Newton Group of Telescopes (ING Newsl.), issue no. 5, p. 5-9., **5**, 5.

Pfenniger, D., 1993. Delayed formation of bulges by dynamical processes. In *IAU Symp. 153: Galactic Bulges*, volume 153, page 387.

Pfenniger, D., Norman, C., 1990, ApJ, **363**, 391.

Pickles, A. J., 1985, ApJ, **296**, 340.

Plana, H., Boulesteix, J., 1996, A&A, **307**, 391.

Prada, F., Gutierrez, C. M., Peletier, R. F., McKeith, C. D., 1996, ApJ, **463**, L9.

Proctor, R. N., Sansom, A. E., 2002, MNRAS, **333**, 517.

Prugniel, P., Simien, F., 1994, A&A, **282**, L1.

Prugniel, P., Simien, F., 1996, A&A, **309**, 749.

Prugniel, P., Simien, F., 1997, A&A, **321**, 111.

Prugniel, P., Maubon, G., Simien, F., 2001, A&A, **366**, 68 (P01).

Rix, H., White, S. D. M., 1992, MNRAS, **254**, 389.

Rix, H., Franx, M., Fisher, D., Illingworth, G., 1992, ApJ, **400**, L5.

Roberts, M. S., Hogg, D. E., Bregman, J. N., Forman, W. R., Jones, C., 1991, ApJS, **75**, 751.

Rose, J. A., Bower, R. G., Caldwell, N., Ellis, R. S., Sharples, R. M., Teague, P., 1994, AJ, **108**, 2054.

Rubin, V. C., 2000, PASP, **112**, 747.

Rutledge, G. A., Hesser, J. E., Stetson, P. B., 1997, PASP, **109**, 907.

Saglia, R. P., Bender, R., Dressler, A., 1993, A&A, **279**, 75.

Saglia, R. P., Maraston, C., Thomas, D., Bender, R., Colless, M., 2002, ApJ, **579**, L13 (SAG02).

Salasnich, B., Girardi, L., Weiss, A., Chiosi, C., 2000, A&A, **361**, 1023.

Sandage, A., Visvanathan, N., 1978, ApJ, **225**, 742.

Sargent, W. L. W., Schechter, P. L., Boksenberg, A., Shortridge, K., 1977, ApJ, **212**, 326.

Schweizer, F., Seitzer, P., 1992a, AJ, **104**, 1039.

Schweizer, F., Seitzer, P., 1992b, AJ, **104**, 1039.

Schweizer, F., Seitzer, P., Faber, S. M., Burstein, D., Dalle Ore, C. M., Gonzalez, J. J., 1990, ApJ, **364**, L33.

Seifert, W., Scorza, C., 1996, A&A, **310**, 75.

Sellwood, J., Wilkinson, A., 1993, Reports of Progress in Physics, **56**, 653.

Sersic, J. L., 1968. Atlas de Galaxes Australes. In *Atlas de Galaxes Australes; Vol. Book; Page 1.*

Sil'Chenko, O. K., 1999, AJ, **117**, 2725.

Simien, F., Prugniel, P., 1997, A&AS, **126**, 15.

Simkin, S. M., 1974, A&A, **31**, 129.

Slipher, V. M., 1914, Lowell Observatory Bulletin, **2**, 6.

Spinrad, H., 1961, PASP, **73**, 336.

Statler, T. S., 1991, ApJ, **382**, L11.

Statler, T. S., 1994, AJ, **108**, 111.

Statler, T. S., Smecker-Hane, T., 1999, AJ, **117**, 839.

Statler, T. S., Smecker-Hane, T., Cecil, G. N., 1996, AJ, **111**, 1512.

Tantalo, R., Chiosi, C., Bressan, A., Fagotto, F., 1996, A&A, **311**, 361.

Terlevich, A. I., Forbes, D. A., 2002, MNRAS, **330**, 547.

Terlevich, E., Diaz, A. I., Terlevich, R., 1990, MNRAS, **242**, 271.

Terlevich, R., Davies, R. L., Faber, S. M., Burstein, D., 1981, MNRAS, **196**, 381.

Terndrup, D. M., Davies, R. L., Frogel, J. A., Depoy, D. L., Wells, L. A., 1994, ApJ, **432**, 518.

Timmes, F. X., Woosley, S. E., Weaver, T. A., 1995, ApJS, **98**, 617.

Tinsley, B. M., Gunn, J. E., 1976, ApJ, **206**, 525.

Tonry, J., Davis, M., 1979, AJ, **84**, 1511.

Tonry, J. L., Dressler, A., Blakeslee, J. P., Ajhar, E. A., Fletcher, A. ., Luppino, G. A., Metzger, M. R., Moore, C. B., 2001, ApJ, **546**, 681.

Trager, S. C., Faber, S. M., Worthey, G., González, J. J. ., 2000, AJ, **120**, 165.

Tully, R. B., Fisher, J. R., 1977, A&A, **54**, 661.

van den Bergh, S., 1960a, ApJ, **131**, 558.

van den Bergh, S., 1960b, ApJ, **131**, 215.

van den Bergh, S., 2002, PASP, **114**, 797.

van den Bergh, S., Cohen, J. G., Hogg, D. W., Blandford, R., 2000, AJ, **120**, 2190.

van der Marel, R. P., Franx, M., 1993, ApJ, **407**, 525.

VandenBerg, D. A., Swenson, F. J., Rogers, F. J., Iglesias, C. A., Alexander, D. R., 2000, ApJ, **532**, 430.

Vanderriest, C., 1980, PASP, **92**, 858.

Vazdekis, A., 1999, ApJ, **513**, 224.

Vazdekis, A., Arimoto, N., 1999, ApJ, **525**, 144.

Vazdekis, A., Casuso, E., Peletier, R. F., Beckman, J. E., 1996, ApJS, **106**, 307.

Vazdekis, A., Peletier, R. F., Beckman, J. E., Casuso, E., 1997, ApJS, **111**, 203.

Vazdekis, A., Kuntschner, H., Davies, R. L., Arimoto, N., Nakamura, O., Peletier, R., 2001, ApJ, **551**, L127.

Vazdekis, A., Cenarro, A. J., Gorgas, J., Cardiel, N., Peletier, R. F., 2003, accepted for publication in MNRAS (VAZ03).

Vega Beltrán, J. C., Pizzella, A., Corsini, E. M., Funes, J. G., Zeilinger, W. W., Beckman, J. E., Bertola, F., 2001, A&A, **374**, 394.

Verolme, E. K., Cappellari, M., Copin, Y., van der Marel, R. P., Bacon, R., Bureau, M., Davies, R. L., Miller, B. M., de Zeeuw, P. T., 2002, MNRAS, **335**, 517.

Visvanathan, N., Sandage, A., 1977, ApJ, **216**, 214.

Weiss, A., Peletier, R. F., Matteucci, F., 1995, A&A, **296**, 73.

Wernli, F., 2002, Ph.D. Thesis. University of Lyon.

Wernli, F., Emsellem, E., Copin, Y., 2001. NGC 4621 - a micro counter-rotating core. In *SF2A-2001: Semaine de l'Astrophysique Francaise*, page 327.

Wolf, M., 1914, Vierteljahresschr. Astron. Ges., **49**, 162.

Woosley, S. E., Weaver, T. A., 1995, ApJS, **101**, 181.

Worthey, G., Ottaviani, D. L., 1997, ApJS, **111**, 377.

Worthey, G., Faber, S. M., Gonzalez, J. J., Burstein, D., 1994, ApJS, **94**, 687.

Wyse, R. F. G., Gilmore, G., Franx, M., 1997, ARA&A, **35**, 637.

Zoccali, M., Cassisi, S., Frogel, J. A., Gould, A., Ortolani, S., Renzini, A., Rich, R. M., Stephens, A. W., 2000, ApJ, **530**, 418.

Acknowledgements

No thesis is exclusive of his author and this one is no exemption. During the last three years I have had the opportunity to spend great moments with lots of new people. Every smile, tear, discussion, idea that I have shared with them has had an influence some way or another in the final result of this thesis. I'd like to acknowledge all of those who in one way or another has contributed to make this thesis possible. In particular I would like to thank the following:

In the first place, I would like to give a special thanks to my parents, whose constant support and encouragement have made possible the great experience that it has been developing my thesis in a foreign country. My sisters and brother, whose numerous phone calls and visits remind me that there is always someone out there that cares for you. Of course, I could not forget my grandma, who never forgot to prepare one of her delicious *tortillas* every time I came back home.

I am indebted to my supervisor, Reynier Peletier, for his continuous support and understanding, not only on the scientific side, but especially on the personal side. For breaking the barriers student-supervisor and becoming a good friend. I am also very grateful to his family, Ayvur and Lambert, for their immeasurable kindness and hospitality.

At the IAC, I am very grateful to Antonio Jimenez and Pere Lluis Pallé for giving me my first opportunity in research and allowing me to enjoy fantastic moments at '*La Pirámide*'. Special thanks to Marc Balcells for his hospitality, many discussions and advice during the numerous visits I have paid to the IAC in the last three years.

Antonio, Aurora, Hector, David y Ana for their friendship and many fantastic trips (and many more to come!). The '*Papping Fellowship*', for making of lunchtime at the IAC a whole experience. Marta, David y Laura for keeping our friendship through the years and endless gatherings every time we get all together

in Tenerife.

Here in Nottingham I would like to thank to all the staff for the formidable group of people they form and the great atmosphere surrounding the department. I am very honoured to be part of the first generation of astronomers from the University of Nottingham. Of course I cannot forget my office mates: Bo, Ed, Pan, Simon and Pepe (the parrot) for sharing so many great moments during our quest for a PhD. Kambiz for many talks about life, love, and science. Nikos, Ilias, Vanessa, Dino, Fred, Juan and Laura for delightful evenings and '*Coffee*' on Saturdays.

I would like to thank the SAURON team for their phenomenal support, great science and fantastic meetings at the Lorentz Centre in Leiden. I am really grateful with the opportunity I am having of being involved in such a great and exciting project.

Finally, I would like to thank very specially my wife Auxi. Her understanding and immeasurable support, in the distance, during the first years and now that we are together, has been vital in the completion of this work.

My last words are in the memory of Luis Francisco Delgado Cedres, a good friend whose passion for Physics and science in general was as big as his devotion for his friends and family.